# A spectroscopic study of a large sample of L/T transition brown dwarfs

— **Federico Marocco** —

Centre for Astrophysics Research
Science and Technology Research Institute
— University of Hertfordshire —

Submitted to the University of Hertfordshire in partial fulfilment of the requirements of the degree of Ph.D.

**Principal Supervisor:** Prof Hugh R. A. Jones

— May 2014 —

*"Theories crumble, but good observations never fade."*

– Harlow Shapey

# Acknowledgements

First of all I wish to thank my principal supervisor, Prof. Hugh R. A. Jones, for his precious guidance, his constant encouragements, and his infinite patience. Without his help and his teachings I could have never made it this far. I would also like to thank my other two supervisors, Dr. Avril C. Day-Jones and Prof. David J. Pinfield, for their help, and for giving me the great opportunity to work on such a fruitful project.

I am grateful to Dr. Richard L. Smart, the man who more than everybody else has supported me in my pursuit of my passion for astronomy. Thanks to him and the IPERCOOL collaboration that he created, I had the opportunity to work with great colleagues like Alex Andrei, Bruno Coelho, and Youfen Wang. And I am thankful to Ben Burningham, Phil Lucas, and Leigh Smith for their help and the useful discussions we had.

The last three and a half years wouldn't have been the same without some great friends, whose company has been fundamental for me to get through the stress of a PhD. First of all, the Horsa Gardens people (in rigorous alphabetical order) Andrés, Andy, Emma, Hugo, Hywel (the best house mate one can ask for), Neil, Roberto, and ZengHua. Living with you has been great fun, and our parties will never be forgotten!

A big thanks goes to my friends in Italy (again in rigorous alphabetical order) Ale, Alfio, Cinzia, Emilia, Fabio, Fede, Fra, Fralaltro, Ivo, Mario, Mimma, Ramo, Silvio, Tralla, and Veronica, because you always find a way to cheer me up and make me laugh, and no matter how far away you are I always feel you are next to me.

Then of course I would like to thank the many great people I met here in England. Thanks to Carla and Joana (my two portuguese teachers) and the rest of the "portuguese family", Catarina, João, and Bruno. Thanks to my office mates, Gaius, Giulio, Graham, Gulay, Mike, and Nancy, for making my hours in the office nicer. And of course thanks to Kieran, Silvia, Geert, Carlos, Noemi, James, Maria, Nick, Nicole, Alex, Beatriz, Ged, Ylvi, Emrah, Cátia, James C, Lientjie, Veronica, John, Liz, Ian, Lisette, Aga, Manuel, Nicky, Craig, Alberto, Luvi, Gianluca, Alessandro, Ariane, Anais, Yanping, Christoph, Joan, Antoine, Sandra, Angelo, Martin, Ismael, Maria, Hagen, Luisa, Chiara, Iolanda, Hanifa, Michele, Maricruz, Beth, Nadine, Gemma, Simon, Simona, Brigitta, Gabor, Hieke, Richard, Jacquelin, and to all those I have forgotten in this list. You have all been part of my life, and I have good memories of all of you that I will take with me wherever I will go.

A special thanks goes to my first astronomy teachers: my cousin Milena with her colourful lessons, and Piero Angela, whose TV show I would not miss for any reason. Thank you to my physics teacher Paolo Gallizio and my astronomy professor Mario Lattanzi, because their passion for science has been inspirational.

Finally, the biggest thanks goes to my family for their constant support. In particular, I am thankful to my parents, Marina and Eraldo, for their unconditional love and infinite patience. My gratitude for them is beyond words. This thesis is dedicated to them.

# Abstract

In this thesis I present the spectroscopic analysis of a large sample of L and T dwarfs, in order to constrain the sub-stellar initial mass function and formation history. The main points I tried to address are the development of a better spectral type to distance calibration and of a better spectral type to effective temperature calibration, and the identification of a statistically complete sample of brown dwarf to be used to measure the luminosity function, and therefore to constrain the initial mass function and formation history.

To achieve the first goal I conducted the spectroscopic follow-up of brown dwarfs from the PARallaxes of Southern Extremely Cool objects (PARSEC) program. This is a large astrometric campaign to measure the parallaxes and proper motions of ∼120 L and T dwarfs in the southern hemisphere. I combined the astrometric results with the near infra-red spectra I obtained using the Ohio State Infra-Red Imager/Spectrometer (OSIRIS) on the SOuthern Astrophysical Research telescope (SOAR). That allowed me to investigate the nature of some unresolved binaries and common proper motion companion in the sample, as well as sub-dwarfs candidates, and potential members of young moving groups. Combining the spectra with the astrometric information and the available photometry I derived the bolometric luminosity and effective temperature for the targets, and determined a new polynomial conversion between spectral type and effective temperature of a brown dwarfs. This is a fundamental step to compare the results of empirical observations to numerical simulations of the sub-stellar luminosity function.

Once refined the type to temperature calibration, I measured the luminosity function. In order to do so my collaborators and I have selected a sample of ∼250 brown dwarfs candidates from the United Kingdom Deep Infra-red Sky Survey (UKIDSS) Large Area Survey (LAS) and followed them up with the echelle spectrograph X-shooter on the Very Large Telescope. I present in this thesis the results of the observations of 196 of the brown dwarfs candidates. Using the X-shooter spectra I determined their spectral types, and I identified a number of unresolved binary candidates and peculiar objects.

One of the peculiar objects in the sample, ULAS J222711−004547, turned out to be the reddest brown dwarf observed so far, and I therefore proceeded to analyse further its spectrum. Applying a de-reddening technique to its spectrum suggests that the most likely reason for its redness is an excess of dust in its photosphere, and that can account for the differences seen between objects of similar spectral type.

By comparing the results of the spectroscopic campaign to numerical simulations, I found that it is currently impossible to constrain robustly the initial mass function and formation history of sub-stellar objects, because of our limited knowledge of the binary fraction among brown dwarfs. The sample of binary candidates identified in this thesis can be used to place a better constraint on the binary fraction, but in order to do that the candidates need to be followed-up via high resolution imaging or radial velocity monitoring to confirm their binary nature.

# Contents

# List of Figures

# List of Tables

# Chapter 1: Introduction

Physicists have been looking at the solar spectrum since Isaac Newton first used a simple prism to observe the refractive properties of coloured light (Newton, 1705). It was in the early 1800s when Joseph Fraunhofer used his skills as a glass maker to create very pure prisms, which allowed him to observe 574 dark lines in the seemingly continuous solar spectrum (Fraunhofer, 1817). Soon after he combined telescope and prism to observe the spectrum of Venus, the Moon, Mars, and various stars such as Sirius and Betelgeuse (see Hearnshaw, 1986, pages 28-29). Since then spectroscopy has always been one of the most powerful tools available to astronomers to characterize celestial objects and thus understand their nature, becoming the foundation of the modern classification of stars, the MK system (Morgan et al., 1943).

With the recent discovery of brown dwarfs (Nakajima et al., 1995) a new, MK-like classification system for sub-stellar objects has been introduced (Kirkpatrick, 2005). Spectroscopy is again at the heart of it, providing the key observational features that allow for the distinction between different classes of objects.

In this thesis I will use spectroscopy to characterize a large sample of brown dwarfs, to try to contribute in answering some of the open questions regarding these types of celestial objects. In particular I will try to understand the influence of atmospheric parameters (effective temperature, surface gravity, and metallicity) in the transition between the types L and T.

In this first chapter I will briefly introduce the fundamental background information on the physics of brown dwarfs, focusing in particular on the aspects more relevant to this thesis. I will then present, in Chapter 2, the results obtained by a large astrometric program, the Parallaxes of Southern Extremely Cool objects (PARSEC). In Chapter 3 I will present the results of the analysis on a large collection of brown dwarfs' optical and infrared spectra, to try to identify binaries and peculiar objects that serve as powerful benchmark objects to test formation and evolution models. Chapter 4 shows the attempt to constrain the formation rate of brown dwarfs. In Chapter 5 I will present the discovery of a very peculiar brown dwarfs, and the constraint I obtained on the dust properties in its atmosphere. Finally, in Chapter 6 I will summarize the results obtained, and discuss the possible future developments of my work.

## 1.1 Theoretical prediction of brown dwarfs and first developments

The existence of brown dwarfs was first predicted theoretically by Kumar (1963) and Hayashi & Nakano (1963). In those two contemporary works, the authors demonstrated that during the initial contraction, in objects less massive than $\sim 0.08-0.09\ M_{\odot}$ the core reaches electron degeneracy *before* the thermonuclear power generated by the fusion of hydrogen into helium achieves a value sufficient to balance surface losses. It is therefore the degeneracy pressure that supports the structure of the object and prevents its further collapse. Since they lack a stable internal source of energy, these objects do not follow the standard stellar evolution (i.e. they do not form a main sequence), instead they slowly cool down and keep on contracting over time.

More refined calculations have progressively improved the mass limit between hydrogen burning stars and brown dwarfs (e.g. Grossman, 1970; Grossman et al., 1970;

Straka, 1971; Rappaport & Joss, 1984) and the current estimate sets it at $\sim 0.07\ M_\odot$ (Chabrier & Baraffe, 2000). This limit however is sensitive to the metal content of the object, and can vary from $0.072\ M_\odot$ for solar metallicity (Chabrier & Baraffe, 2000) up to $0.094-0.098\ M_\odot$ for zero metallicity (Burrows et al., 1993, 2001).

## 1.2 Internal structure

The main source of heat in a brown dwarf is the slow release of the gravitational energy. In the very first stages of their evolution, brown dwarfs more massive than $\sim 0.012\ M_\odot$ have an additional source of energy in the deuterium fusion in their centre. This phase however is very short, generally shorter than $\sim 20$ Myr (Chabrier & Baraffe, 2000).

The energy is transported form the interior of the dwarf to its surface mainly via convection, while the radiative transport is negligible (because the interior of a brown dwarf is dense and optically thick). The internal structure and thermal profile is therefore defined by the equation of state (hereafter EOS) of its chemical constituents, which are mostly hydrogen and helium. The most used EOS to describe brown dwarfs' interiors is the Saumon et al. (1995) EOS for H/He mixtures (e.g. Fortney et al., 2011).

## 1.3 Evolution

The lack of a stable internal source of energy results in brown dwarfs slowly cooling and fading over time. Their evolution is described clearly in Figure 1.1 (which is a collage of Figures 1, 3, and 8 from Burrows et al., 2001). The three panels show, from top to bottom, the evolution of bolometric luminosity, radius, and effective temperature (hereafter $T_{\rm eff}$). Different lines represent the tracks for objects of different masses, with the mass decreasing, in each panel, from top to bottom. Blue tracks are low-mass hydrogen burning stars (i.e. objects more massive than $\sim 73\ M_{\rm Jup}$), green tracks are high-mass brown dwarfs (i.e. objects above the deuterium burning limit, $\sim 13\ M_{\rm Jup}$), and red tracks are low-mass brown dwarfs and planets (i.e. objects below the deuterium burning limit). In the top and bottom panel the yellow and purple dots mark the evolution point where 50% of the initial deuterium and lithium have been burned, respectively. In the central panel the dashed line indicates the radius of Jupiter. In the bottom panel the dashed lines represent the approximate temperature limits between the spectral classes M, L, T, and Y.

In low-mass stars the luminosity decreases in the first stages of the evolution, as the pre-stellar object keeps contracting fast. When the object reaches $\sim 200$ Myr, the energy output from the hydrogen fusion stabilizes the star, that settles onto the main sequence. Luminosity, radius, and $T_{\rm eff}$ remain essentially constant for the rest of the evolution. The least massive stars can reach quite compact states ($R_* \sim R_{\rm Jup}$) and cool down into the L dwarfs regime (see Section 1.5).

High-mass brown dwarfs (as well as low-mass stars) experience a quick deuterium burning phase in their early evolution. This can be seen in Figure 1.1 as a plateau in the luminosity, radius and $T_{\rm eff}$ evolution. The duration of this phase depends on the mass of the dwarf, but it is believed not to last longer than $\sim 20$ Myr (Chabrier & Baraffe, 2000). After that, the dwarf resumes its slow but steady cooling and contraction, leading it to evolve in spectral type from M to L, T, and for the least massive eventually into Y type, and very compact states ($R_* < R_{\rm Jup}$).

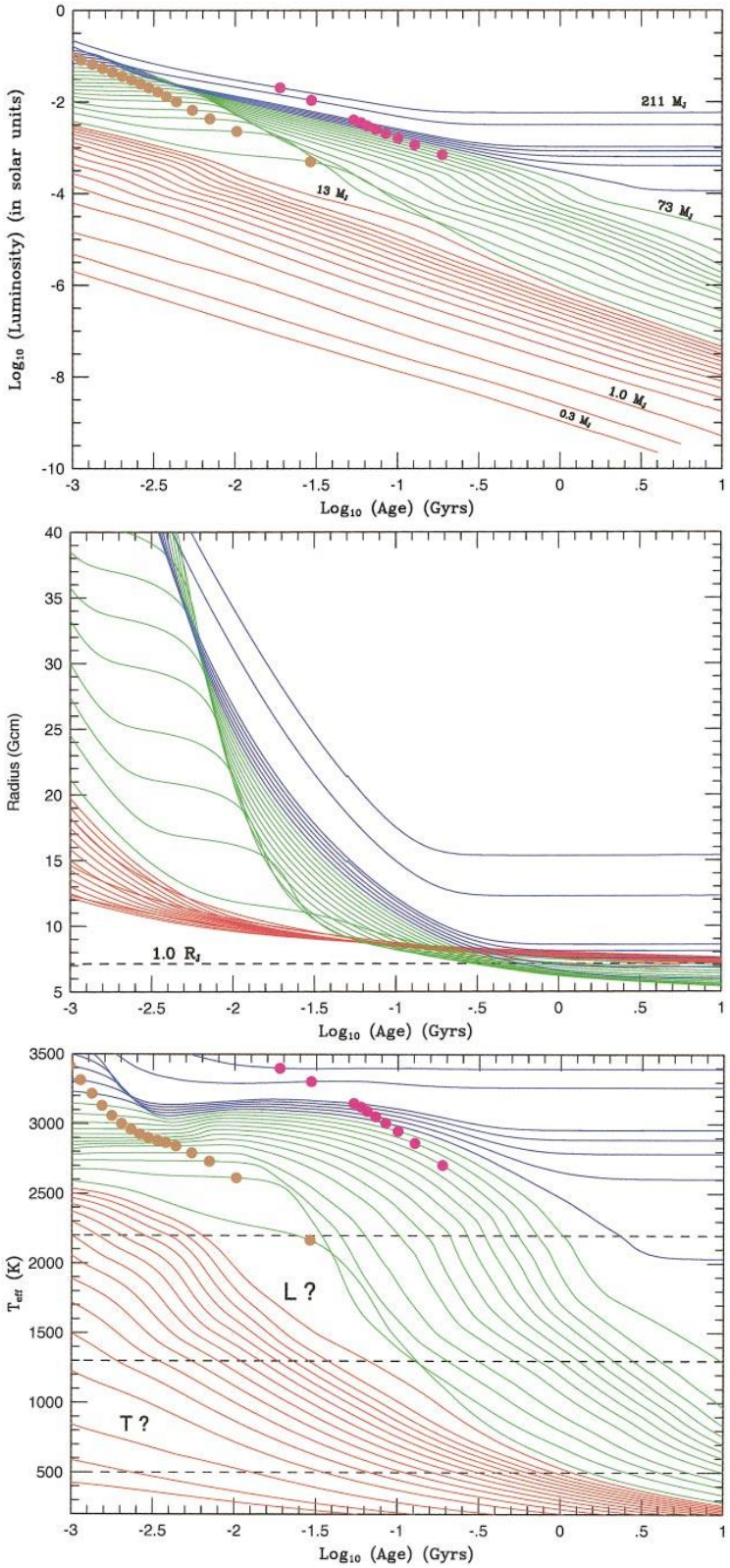


Fig. 1.1: The evolution of low-mass stars and brown dwarfs over time (from Burrows et al., 2001). The three panels show, from top to bottom, the evolution of bolometric luminosity, radius, and effective temperature. Different lines represent the tracks for objects of different masses. Blue tracks are low-mass stars, green tracks are high-mass brown dwarfs, and red tracks are low-mass brown dwarfs and planets. In the top and bottom panel the yellow and purple dots mark the evolution point where 50% of the initial deuterium and lithium have been burned, respectively. In the central panel the dashed line indicates the radius of Jupiter. In the bottom panel the dashed lines represent the approximate temperature limits between the spectral classes M, L, T, and Y.

Low-mass brown dwarfs and planets never develop the conditions for deuterium burning in their cores. As a result, there is no initial plateau in the evolution of their physical parameters. Interestingly, they never reach the extremely compact states typical of more massive brown dwarfs (i.e. their radii stabilize at $R_* \sim R_{\rm Jup}$). While at young ages the radius of an object is roughly a linear function of its mass, after $\sim 100$ Myr the situation for sub-stellar object inverts, with the more massive objects having the smaller radii (the peak radius is at a mass of $\sim 4M_{\rm Jup}$, see Zapolsky & Salpeter, 1969; Hubbard, 1977). This is a direct consequence of their internal structure being governed by electron degeneracy pressure, and this depends solely on the electrons density. To balance their higher self-gravity, more massive brown dwarfs need to reach denser states.

It must be noted at this point that the models of Burrows et al. (2011) suggest that the radius of a sub-stellar object also depends on its metallicity and its helium mass fraction. A higher metallicity in fact alters the temperature-pressure profile, leading to lower a pressure for a given temperature compared to solar metallicity objects. A higher helium mass fraction enhances the nuclear luminosity, leading to significant core burning even at masses as low as 0.05 $M_\odot$ (see Figure 6 from Burrows et al., 2011).

The constant cooling over time, and the mass-radius relation inversion, pose a series of challenges in the understanding of brown dwarfs, and create a number of observable effects in their spectra, that we will discuss in more details in the following Sections.

## 1.4 Formation mechanisms

Understanding what is the dominant formation process for brown dwarfs is one of the open challenges in modern sub-stellar astrophysics. As the formation mechanisms could be different for sub-stellar objects compared to stars, it is important to determine the mass function and formation history in the very low mass regime if we wish to fully understand their contribution to the Galactic population. This can have implications also in distinguishing between brown dwarfs and giant planets. The current IAU distinction between the two category of objects is based on the minimum mass for deuterium burning, but there is growing consensus on the need for a definition based on the formation mechanism instead (e.g Chabrier et al., 2014).

The main formation scenarios proposed are circumstellar disk fragmentation, ejection of pre-stellar embryos from multiple systems, photo-erosion of pre-stellar cores, and gravoturbulent fragmentation of molecular clouds. I will briefly discuss them in the following subsections.

### 1.4.1 Disk fragmentation

Disk fragmentation has been proposed as a formation mechanism for both brown dwarfs and giant planets (Boffin et al., 1998; Bate et al., 2003; Whitworth & Stamatellos, 2006). Massive circumstellar discs form around massive stars during the cloud collapse phase. Pure hydrodynamical simulations have shown that the disk can become gravitationally unstable if it is massive and extended enough (typically $M_d \gtrsim 0.3M_*$ and $R_d \gtrsim 100(M_*/M_\odot)^{1/3}$ AU, see e.g. Stamatellos & Whitworth, 2009). More recent simulations including non-ideal magnetohydrodynamics effects (Masson et al., 2012) have argued against this scenario, showing that the discs cannot become massive and extended enough to lead to fragmentation. Moreover, observations of early class 0 ob-

jects have shown compact discs, while massive discs seem to be rare (Rodríguez et al., 2005).

On the other hand, Stamatellos (2013) points out that this scenario is the only one to successfully explain the so called "brown dwarf desert", i.e. the lack of brown dwarfs as close companions to main sequence stars, in contrast to planetary mass and hydrogen burning star companions (Marcy & Butler, 2000; Grether & Lineweaver, 2006; Sahlmann et al., 2011; Ma & Ge, 2014).

The "brown dwarf desert" was first noticed by Marcy & Butler (2000) analysing the statistical properties of sub-stellar companions to FGKM stars detected in radial velocity surveys. They found that only 0.5% of stars harbour a brown dwarf companion at separations <3 AU, compared to a 5% occurrence rate of planetary-mass companions. More thorough analysis of potential biases (Grether & Lineweaver, 2006), and an increased sample size from the CORALIE (Queloz et al., 2000) and HARPS (High-Accuracy Radial velocity Planet Searcher, Mayor et al., 2003) radial velocity surveys have confirmed the presence of the "desert", placing a stronger upper limit to the rate of brown dwarf companions in close orbits to 0.6% (Sahlmann et al., 2011). The recent statistical analysis of Ma & Ge (2014) have stressed further the lack of brown dwarf companions with masses between 30 and 55 $M_{\rm Jup}$ with orbital periods shorter than 100 days (see their Figure 2 and 3), claiming that is the evidence for the presence of two separate populations of sub-stellar companions to main sequence stars. Objects below $\sim 42.5 M_{\rm Jup}$ form predominantly like planets, while objects above that mass form predominantly like stars. It is worth noticing at this point that the brown dwarf desert is *not* and observational effect. Radial velocity surveys are in fact sensitive to masses well below the lower limit of the "brown dwarf desert" (see for instance Figure 2 in Ma & Ge, 2014).

In the disk fragmentation scenario the "brown dwarf desert" is explained because all the fragments start with roughly the same mass ($\sim 1\ M_{\rm Jup}$, Stamatellos & Whitworth, 2009), and then grow in mass accreting material from the disk. Objects that form first migrate inwards and accrete more mass, becoming stars, while those that remain in the outer regions of the disk can only become brown dwarfs. If brown dwarfs from the outer region migrate inward they are dynamically "bounced back", and could even be ejected by the system. Planetary mass objects form in the inner region via core accretion at a later stage. According to this scenario, brown dwarfs therefore can only be found either in isolation (i.e. after they have been ejected by the system) or as wide companions. Such wide companions have been indeed observed (e.g. Gomes et al., 2013; Pinfield et al., 2012; Day-Jones et al., 2011; Faherty et al., 2010; Zhang et al., 2010).

### 1.4.2 Ejection of pre-stellar embryos

In this scenario, brown dwarfs are formed by small ($\sim 1 M_{\rm Jup}$) accreting pre-stellar cores, formed via cloud fragmentation, that subsequently get ejected by the surrounding environment via dynamical interaction (Reipurth & Clarke, 2001; Delgado-Donate et al., 2003; Bate et al., 2002; Sterzik & Durisen, 2003). Simulations investigating this scenario were conducted by Bate (2012). Although these simulations reproduce quite well the Chabrier (2005) IMF, their initial conditions correspond to extreme clouds, much denser and more turbulent than the typical observed ones (e.g. Heyer et al., 2009). Arguments against this scenario come from the observations of significant populations of brown dwarfs in low density environments like the Taurus cloud (e.g. Luhman, 2012),

where the dynamical interactions required by this formation scenario are strongly hampered.

### 1.4.3 Photo-erosion of pre-stellar cores

If a pre-stellar core forms near a massive OB star embedded in an H II region, its outer layers can be photo-eroded by the bright nearby star, preventing it to accrete enough mass to become a star (e.g. Whitworth & Zinnecker, 2004). However, brown dwarfs have been observed in isolation, and not all of the star forming regions contain enough massive OB stars to make this mechanism efficient.

### 1.4.4 Gravoturbulent fragmentation

In this model, brown dwarfs are the result of the fragmentation and subsequent collapse of giant molecular clouds. The turbulence in the cloud generates a wide spectrum of core masses, originating from the different scales of turbulence. The smaller cores form brown dwarfs and giant planets. Simulations from Padoan & Nordlund (2004, 2002) suggest that the IMF is the consequence of supersonic turbulence in molecular clouds. An issue raised against this theory is that it would be unable to explain the final IMF if the cores would fragment further during their collapse. However numerical simulations (e.g. Seifried et al., 2013) show that radiative feedback and magnetic field reduce the fragmentation process. The observation of the pre-brown dwarf core Oph B-11 (André et al., 2012) lends support to this formation scenario, but the number of such systems observed is still too small to be conclusive.

Being essentially an extension of the star formation process to low masses, the gravoturbulent fragmentation scenario should lead to a stellar-like initial mass function (i.e. a power law + lognormal form, see Chabrier, 2005). If written as $dN/dM \propto M^{-\alpha}$, the Chabrier (2005) initial mass function would correspond to a negative $\alpha$ value. On the other hand the planetary initial mass function corresponds to a positive $\alpha$ value, i.e. the number of objects increases with decreasing mass (e.g. Howard et al., 2010). This would be the expected scenario if brown dwarfs form in a planet-like way, as suggested by the disk fragmentation scenario. Constraining $\alpha$ in the sub-stellar regime, like I will try to do in Chapter 4, is therefore one of the key observational results required to distinguish between the formation scenarios proposed.

## 1.5 The spectral classification

Over the past century, astronomers have developed a system of spectral classification for stars, represented by the sequence OBAFGKM where O indicates the most massive and hot stars and M the smallest and coldest ones. This system was sufficient for almost a century until the late '80s, when the first observations of brown dwarfs (Becklin & Zuckerman, 1988) triggered the introduction of three new spectral classes: L, T, and Y.

The absence of hydrogen fusion makes brown dwarfs intrinsically faint, so that the first one was observed only in 1988 when, during observations in the near infrared, Becklin & Zuckerman (1988) found a faint object orbiting the white dwarf GD165. The analysis of its spectrum (Kirkpatrick et al., 1993) highlighted the lack of TiO absorption bands, which is the most common feature in M dwarfs, and no bands of

$CH_4$ and $NH_3$, which are typical in Jupiter and Saturn. It was the first hint that GD165B was an "intermediate" object, straddling the transition between stars and giant planets. This initial discovery was followed a few years later by the discovery of Gl229B (Nakajima et al., 1995) whose spectrum shows absorption bands of $CH_4$ and a general resemblance with the spectrum of Jupiter (Oppenheimer et al., 1998), making it the first unambiguous brown dwarfs observed. More or less at the same time PPl 15 ans Teide 1 were identified as brown dwarf candidates in the Pleiades (Stauffer et al., 1994; Rebolo et al., 1995) and later confirmed as sub-stellar objects by the detection of lithium in their spectra (Basri et al., 1996; Rebolo et al., 1996).

In the following years many more discoveries add up to these, gradually forming a tail to the main sequence. Thus, the need to extend the spectral classification became indisputable. The spectra of GD165B-like objects were clearly distinct from that of M-type stars and the spectra of Gl229B-like objects were different from both the previous. Astronomers agreed then with the introduction of two new spectral types: objects like GD165B formed class L, while objects like Gl229B were named as class T (for a more detailed history of the introduction of these new spectral types, please see Kirkpatrick, 2005).

The discovery of colder and colder objects has progressively pushed the boundary of the classification towards later and later types (e.g. Delorme et al., 2008a; Lucas et al., 2010; Liu et al., 2011). But only recently, the NASA infrared satellite *WISE* identified objects that are even colder (and fainter) than L and T dwarfs (Kirkpatrick et al., 2011; Cushing et al., 2011). In these objects the alkali lines disappear, because the main alkali metals (Na and K) condense into molecules and are therefore removed from the photosphere, and the optical and near infrared flux collapses as the flux distribution shifts towards longer wavelengths. These new objects have been classified as Y dwarfs, but a definitive classification scheme has not been established yet.

The spectroscopic characteristics that distinguish these classes, and their classification schemes are discussed in the following sections.

### 1.5.1 L dwarfs

Early-L type objects present a mix of atomic and molecular bands, the most prominent of which are caused by alkali metals (e.g. Na I, K I, Rb I, Cs I), oxides (mainly TiO and VO), and hydrides (the most prominent being CrH and FeH). Starting from mid-L objects, Na I and K I lines grow in strength, while TiO and VO bands have almost disappeared. In late-Ls the strength of the $H_2O$ bands keeps on increasing, while the bands of hydrides weaken. The red end of the spectra (i.e. $\lambda \sim$ 2-2.3 $\mu$m) is characterized by strong lines of Ca and the prominent band of CO at $\sim$ 2.3 $\mu$m.

Another important source of opacity is $H_2$, which plays a vital but indirect role in the formation of the observed spectra. Its absorption is caused by the dipole momentum induced by transient interactions between molecules, generally referred to as collision-induced absorption (hereafter CIA). At the temperatures of L and T dwarfs molecular hydrogen is abundant and, given that the density is high, close-range interactions (generally called collisions) are frequent. These cause shifts in the electron density distribution of the molecules, generating dipole moments. The result is an almost continuous absorption throughout the infrared spectrum (because of the overlap of several broad lines), particularly in the K-band ($\sim$ 2.2 $\mu$m, Saumon et al., 2012). For further details on the treatment of this complex phenomenon we refer the reader to the literature on the subject, with particular reference to Linsky (1969), Frommhold

(2006), Li et al. (2012), and Abel & Frommhold (2013).

Following the evolution of the features mentioned above, the classification of L dwarfs was systematized by Kirkpatrick et al. (1999) for the optical spectra, and Geballe et al. (2002) for the NIR spectra.

The atmospheres of L type objects are also characterized by the presence of great amounts of dust, which plays a fundamental role in shaping the emergent spectral energy distribution. We will discuss in more details the role played by dust in Section 1.6.1.

### 1.5.2 T dwarfs

T dwarfs are also known as "methane dwarfs" as their spectra show prominent $CH_4$ absorption bands. The strength of the $H_2O$ keeps on increasing while the bands of hydrides disappear. In the mid- and late-Ts water has become the main absorber and the Na I and K I lines in the optical range are so deep and wide that they almost merge. Late-T spectra are essentially characterized by four "peaks" (1.08, 1.27, 1.59 and 2.08 $\mu$m) separated by the absorption bands of methane and water. The peak at $\sim$ 2.08 $\mu$m is further dampened by the CIA of $H_2$.

T dwarfs classification scheme is defined by Burgasser et al. (2003b) for the optical spectra, and Burgasser et al. (2006a, for early-to-mid T dwarfs) and Burningham et al. (2008, for late-Ts) for the NIR spectra.

The evolution of spectral features from late-M dwarfs to late-T dwarfs is shown in Figure 1.2 in the optical range, and Figure 1.3 and 1.4 in the NIR range (all are taken from Kirkpatrick, 2005).

It must be noted at this point that it is not obvious *a priori* that an object falls into the same subclass in both the optical and the infrared system, since the two bands are influenced by different atmospheric phenomena. However, many studies (Reid et al., 2001b; Testi et al., 2001; McLean et al., 2003) showed that the optical sequence of L dwarfs is usually reflected in the infrared. There are of course exceptions. As it is possible to see in Figure 1.3, the sequence of infrared spectra does not show the linear evolution that is evident in the optical sequence (Figure 1.2). For example, the shape of the peak at 1.59 $\mu$m does not change continuously between types L2 and L8. We will return in Section 1.6 to the reasons for this discrepancy.

### 1.5.3 Y dwarfs

The first Y dwarfs were observed only recently (Cushing et al., 2011; Kirkpatrick et al., 2011), and the census of this type of objects amounts to a total of only 15 (at the time of writing). With such a small sample, a proper classification scheme has not yet been defined. However, some peculiar characteristics that distinguish Y dwarfs from T dwarfs have been noticed in the spectra obtained (Kirkpatrick et al., 2012).

The peak at $\sim$ 1.27 $\mu$m is narrower than in T dwarfs, and it is about the same intensity as the peak at $\sim$ 1.08 $\mu$m. This is due to the disappearance of the resonance lines of Na I and K I, as K I condenses into KCl. Ammonia, which was indicated in early atmospheric models (e.g. Burrows et al., 2003) as the possible "trademark" for Y dwarfs, has not been unequivocally detected yet, chiefly because its bands blend with those of water and methane. At the latest types ($\geq$ Y2) the peaks at $\sim$ 1.27 and at $\sim$ 1.59 $\mu$m are about the same intensity, probably indicating the collapse of the flux in the red optical and near infrared (these objects are expected to be colder than 300 K). A

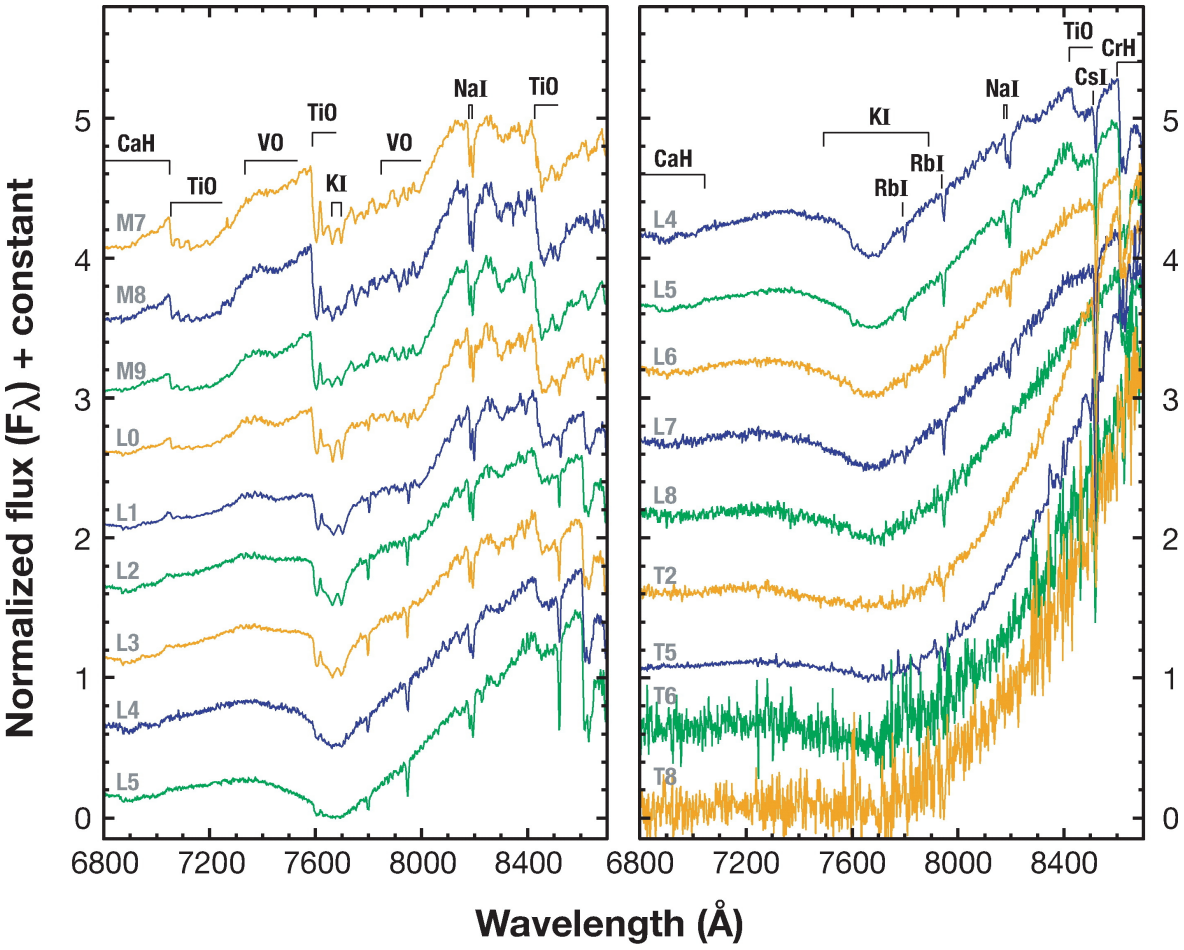


Fig. 1.2: The optical spectral sequence of L and T dwarfs from Kirkpatrick (2005). The objects plotted are taken from Kirkpatrick et al. (1999) and Burgasser et al. (2003b). Each spectrum is normalized to one at 1.27 $\mu$m and offset vertically by 0.5 flux units.

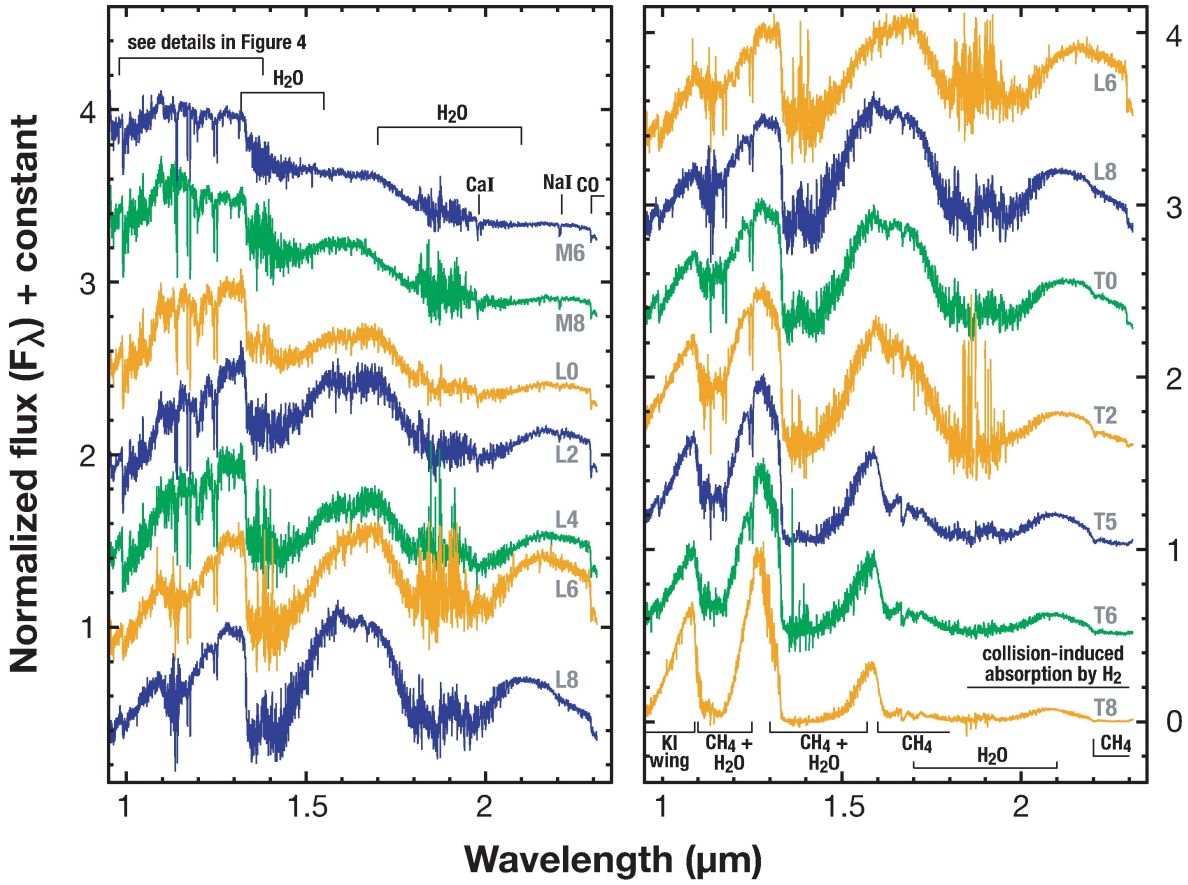


Fig. 1.3: The infrared spectral sequence of L and T dwarfs from Kirkpatrick (2005). Details of the J band are shown in Figure 1.4. Each spectrum is normalized to one at 1.27 $\mu$m and offset vertically by 0.5 flux units. The objects plotted are taken from McLean et al. (2003).

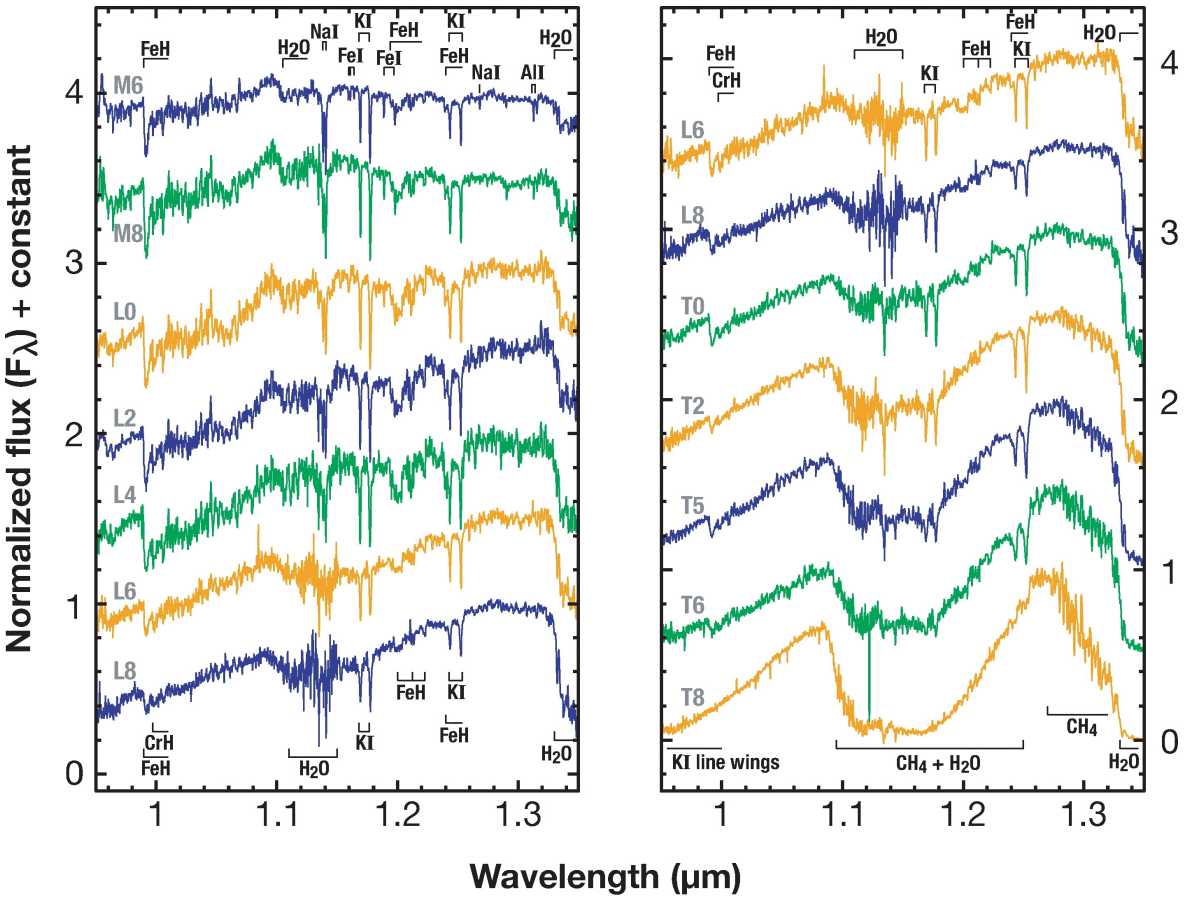


Fig. 1.4: Details of the J band infrared spectra shown in Figure 1.3.

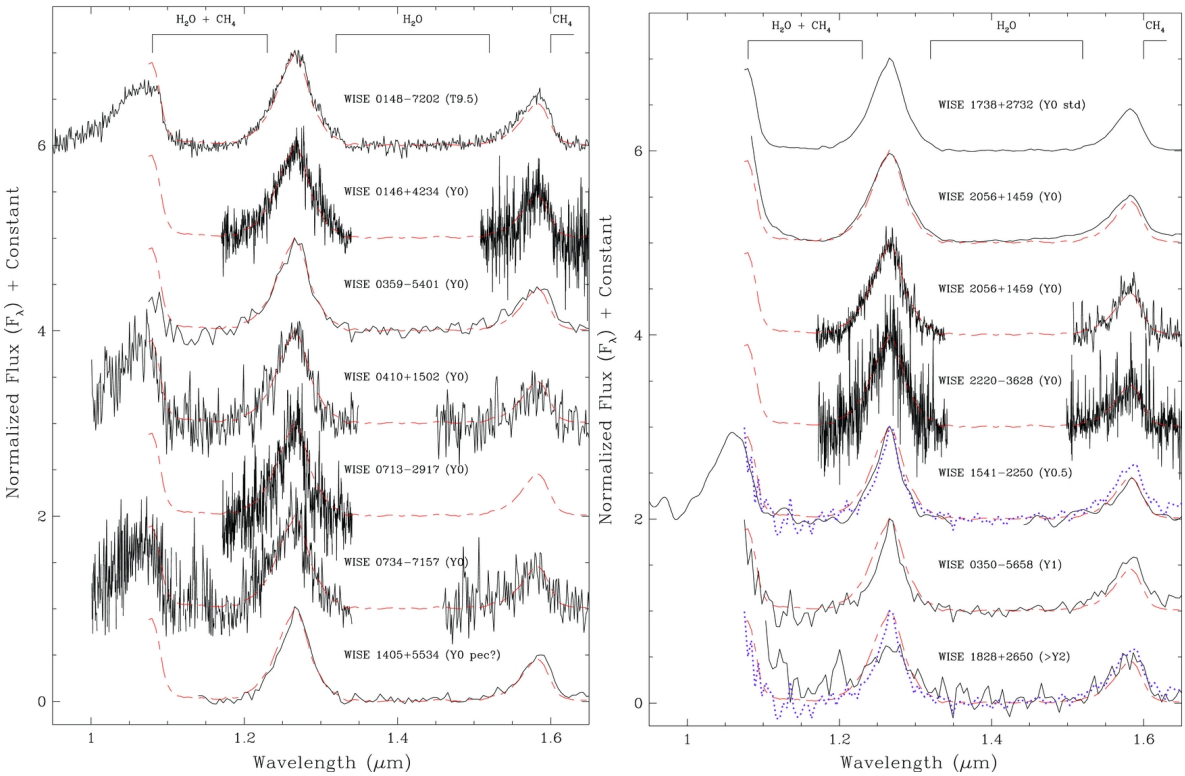


Fig. 1.5: The spectral sequence of Y dwarfs from Kirkpatrick et al. (2012). Overplotted in red and purple for comparison are the proposed Y0 and Y1 standards, WISE 1738+2732 and WISE 0350-5658. Each spectrum is normalized to one at 1.28 $\mu$m and offset vertically by one flux unit.

preliminary classification scheme, and some tentative standards, have been defined in Kirkpatrick et al. (2012), from which we reproduce in Figure 1.5 the proposed spectral sequence.

## 1.6 Physics and chemistry of the atmosphere

Once the empirical classification of L, T, and Y dwarfs is defined, one needs to find out what physical and chemical mechanisms determine the formation of the spectra. For main sequence stars the leading parameter is temperature. It is reasonable to assume that this also extends to the new spectral types.

An example of a trend of $T_{\rm eff}$ as a function of spectral type is shown in Figure 1.6, compiled with data from Vrba et al. (2004), Marocco et al. (2010) and Marocco et al. (2013). It is evident that the correlation between temperature and spectral type is clearer in the case of optical spectra than for the near-infrared ones, where the proportionality exists only in the L0-L6 range and from type T6 onwards. This is because, as mentioned before, the two spectra are the product of different physical phenomena within the photosphere.

In particular, Stephens (2003) hypothesized that while the optical spectral types are mainly correlated with temperature, the infrared ones are influenced by the presence of dust clouds in the photosphere and by surface gravity and metallicity. The role of these parameters will be discussed in the following sections.

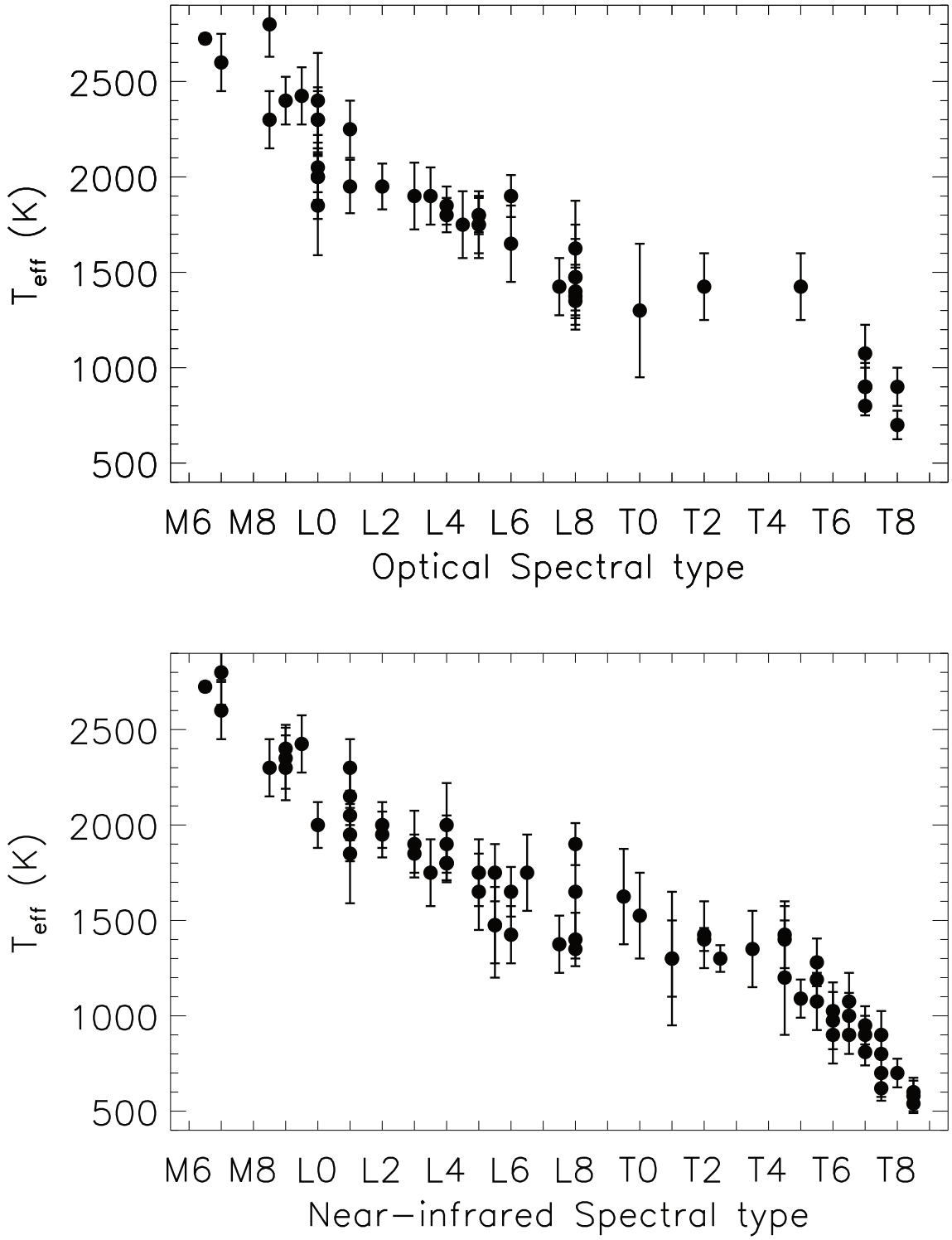


Fig. 1.6: Effective temperature as a function of optical spectral type (top panel) and infrared spectral type (bottom panel). The data are taken from Vrba et al. (2004), Marocco et al. (2010) and Marocco et al. (2013).

### 1.6.1 Dust clouds

As mentioned above, L dwarfs were identified because of the absence of TiO and VO bands in their spectra. Studies of the chemical equilibrium in stellar atmospheres (Lodders, 1999; Burrows & Sharp, 1999; Allard et al., 2001) have shown that their disappearance is due to the transformation of TiO into $TiO_2$ and of VO into $VO_2$, and their subsequent condensation in complex molecules and then dust grains, that "sink" below the photosphere.

As the oxides condense, their bands weaken and the contrast increases between the continuum and the lines of Na I and K I, whose wings extend for thousands of Å. A study by Burrows & Volobuyev (2003) showed how the formation of condensates cleans the atmosphere of most metals, therefore between 4000 and 10000 Å the main source of opacity are alkali metals (in particular Na and K). The energy levels of Na and K are perturbed by the dipole momentum induced by the collisions with $H_2$, the main component of the gas at these temperatures (1000-2500 K), so the red wing of the K I doublet (7665, 7699 Å) extends up to 9500-10000 Å and that of the Na I doublet (5890, 5896 Å) up to about 8000 Å.

The fundamental band of methane (3.3 $\mu$m) is observed for the first time in the mid-L, indicating the onset of the conversion process of carbon monoxide, $CO + 3H_2 \rightarrow CH_4 + H_2O$ (Noll et al., 2000; Cushing et al., 2005). This process also leads to the strengthening of the $H_2O$ bands. Other bands of methane (1.6, 2.2, 7.8 $\mu$m) are rarely seen in late-L, but are clearly distinguishable in T-dwarfs, where they represent the main absorption feature (Roellig et al., 2004).

The condensates mentioned above have even more important effects in the L-T transition range, where their vertical distribution, numerical density and size play an important role in the formation of the emission spectra (Burrows et al., 2001). Theoretical models (model B by Tsuji 2000, AMES-dusty models by Allard et al. 2001) have shown that the only way to explain the strong shift of the early-to-mid L-dwarfs colours towards red (J−K ≈ 2) is by invoking the presence of these dust condensates. The same models are not able to explain the colours of T-dwarfs though. Other models (model C by Tsuji 2000, AMES-cond models by Allard et al. 2001), which take into account the disappearance of condensates (because of their settling into the internal layers), effectively predict the colours (J−K ≈ 0) of mid-to-late Ts, but not those of the early-Ts. It is therefore plausible to assume that the L-T transition phase is where the sedimentation of condensates takes place.

Tsuji (2002) analysed the temperature range between the beginning of the condensation of dust clouds and the beginning of their sedimentation in the deeper layers. In this model, the dust clouds are confined in the region defined by the temperature at which the dust grains begin to form ($T_{\rm cond}$) and the temperature at which they have grown so large that they precipitate below the photosphere ($T_{\rm cr}$). This region is located in the optically thin layers of the photosphere for $T_{\rm eff} \sim 1800$ K and the effect of the clouds is to veil the molecular bands considerably. In the 1700-1500 K range the clouds thicken but also start to "move" towards the optically thick layers, where their contribution to total opacity is less important, creating an effect of mutual compensation of the two phenomena. As temperature drops below 1400 K the clouds are confined into even deeper layers, the upper atmosphere cools quickly and therefore triggers the already mentioned process of formation of $CH_4$, with a reversal of the infrared colours. However, according to this model, the process that leads J−K from ∼2 to ∼0 should occur in a temperature span of 600 K, while in reality, as one can see in Figure 1.7, it

occurs in a smaller range (possibly as little as 200-300 K).

Different models were developed by Marley et al. (2002), in which the evolution of dust clouds is governed by a parameter called $f_{\rm sed}$, which represents the ratio of the efficiency of sedimentation to convective mixing. Homogeneous atmospheres, full of dust, where the convection cancels completely the effects of sedimentation, will have $f_{\rm sed} = 0$. A bigger value indicates instead that the sedimentation becomes dominant eliminating the clouds. For late-L dwarfs $f_{\rm sed} < 3$, for early-Ts is $f_{\rm sed} > 3$, and finally for mid and late-Ts the atmosphere is assumed to be completely free of clouds ($f_{\rm sed} \to \infty$). The results are in agreement with those of Tsuji, though this model can not justify the rapidity of the reversal of colours, nor the reason why the $f_{\rm sed}$ should change.

A possible solution to this problem has been proposed by Burgasser et al. (2002) from an initial idea of Ackerman & Marley (2001). The above models assume a uniform distribution of the condensates in the atmosphere, but observations of Jupiter and Saturn have instead highlighted "stripes" and "spots" of varying thickness and even "holes". Assuming that those inhomogeneities are also in the atmospheres of L and T dwarfs, the position of transition objects in Figure 1.7 depends on the percentage of cloud coverage. Having equal temperature, an object with a cleaner atmosphere looks brighter and bluer than a more "cloudy" one. Burgasser et al. (2002) present the curious behaviour of the Wing-Ford band (9896 Å) of FeH as evidence in favour of this scenario: the line weakens strongly from late-L and then regains intensity from early-T, until it weakens and disappears again from mid-T. This happens because in the cold layers above the clouds most of the iron is condensed, so FeH is rare. From early-Ts clouds disruption lets through light from the hot lower layers where the iron has not yet condensed and FeH is still abundant. In late-Ts the temperature finally drops to the point that none of the visible layers contains appreciable quantities of FeH.

A different solution was proposed by Tsuji & Nakajima (2003). According to these authors the sequence in Figure 1.7 can not be interpreted as a single sequence, but as a superposition of several evolutionary tracks, dictated by the different mass of the objects. In this case the previous model of Tsuji (2002) would be correct, while the interpretation of experimental data would be wrong. Basically, an object of high mass loses its layer of clouds at a lower temperature (thus a fainter magnitude) than one of smaller mass, which causes a shift in the reversal point of the colours (1.5 magnitudes in the range of 70 to 10 $M_{\rm Jup}$).

A third scenario is proposed by Knapp et al. (2004), where the L-T transition is interpreted as the region of rapid sedimentation of condensates (a real "rain") which ends in mid-T. From this point onward the spectral sequence becomes a function of temperature only.

A clear answer to the problem has not been found yet. The most recent models deal with the transition between L and T dwarfs by invoking a change in particle size of dust (Burrows et al., 2006), which settle quicker as they become larger, or assuming rapid changes in the $f_{\rm sed}$ parameter (Saumon & Marley, 2008) from values of 1-2 to 3-4. In both cases, however, it is not clear what physical process would cause these rapid changes.

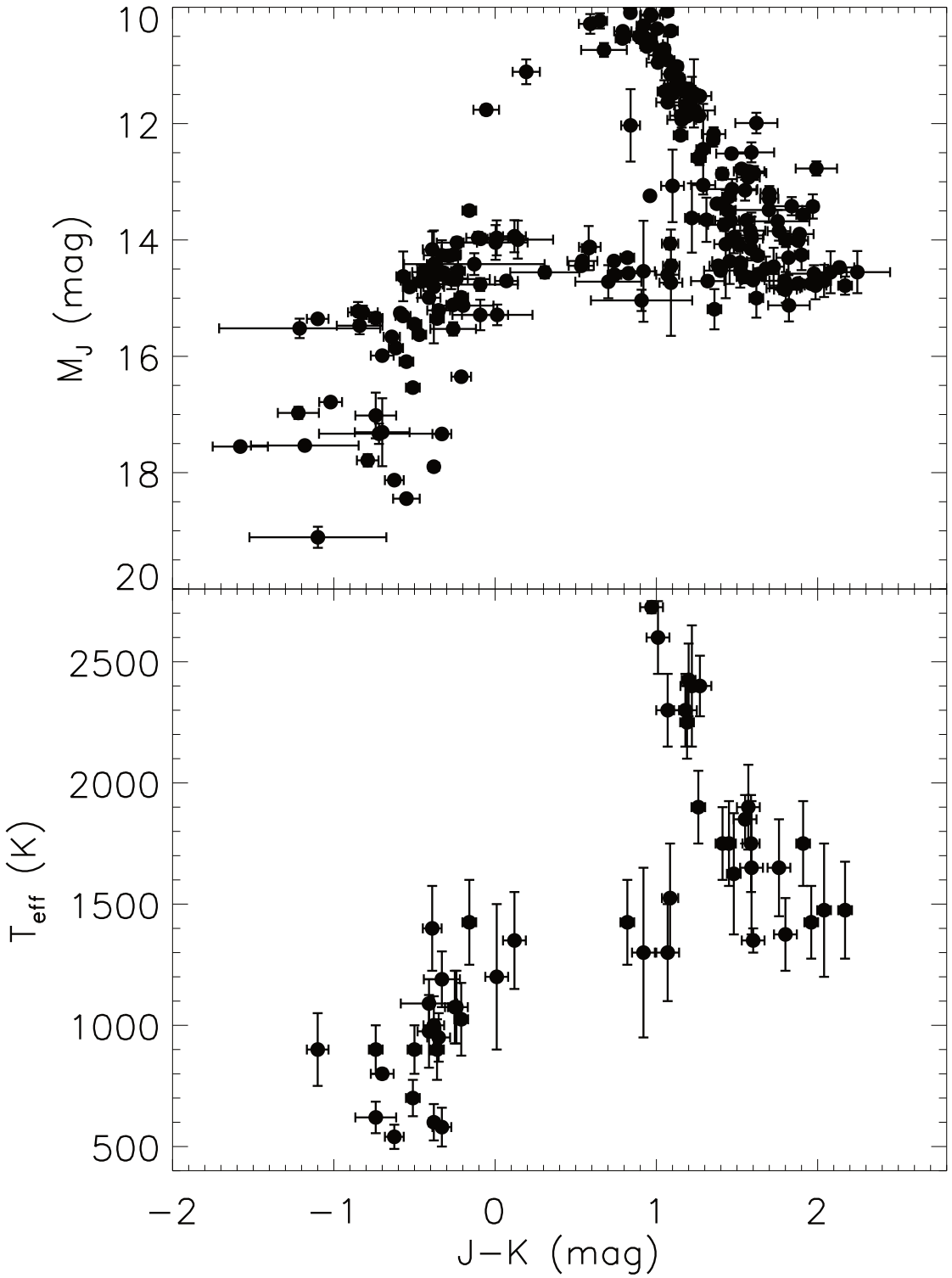


Fig. 1.7: Absolute J magnitude (top panel) and effective temperature (bottom panel) as a function of J−K. The data are taken from Dupuy & Liu (2012), Vrba et al. (2004), Marocco et al. (2010) and Marocco et al. (2013).

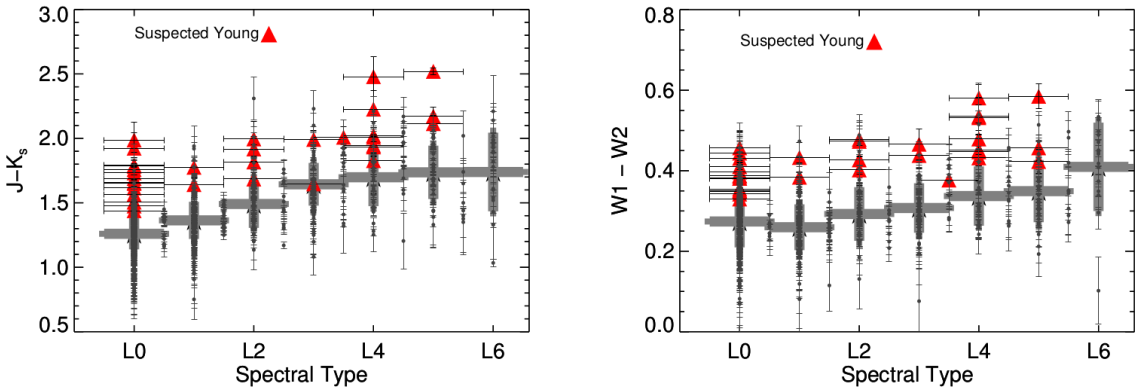


Fig. 1.8: The NIR (left) and MIR (right) colour sequence from Faherty et al. (2013a). The average colour for each type is marked by a black point, and their $1\sigma$ deviation are highlighted by a grey box. Suspected young low-gravity sources are shown as red triangles.

### 1.6.2 Surface gravity

Any given spectral subclass may includes objects with very different properties. Looking at Figure 1.1 one can see that dwarfs at a given $T_{\rm eff}$ (for example 2200 K, corresponding to $\approx$ L0) can be a mixture of different objects, from very old low-mass stars (M $\approx 0.085\ M_{\odot}$, age $> 3$ Gyr) to intermediate age high-mass brown dwarfs (M $\approx 0.065\ M_{\odot}$, age $> 200$ Myr) to very young planetary-mass objects (M $\approx 0.020\ M_{\odot}$, age $< 20$ Myr). Moreover, young low-mass brown dwarfs have not yet had time to contract to their final radii, so they are larger than their counterparts of greater mass (Burrows et al., 2001; Baraffe et al., 2003). This enhances the differences in surface gravity between objects of the same spectral type and has an influence on the formation of their spectra.

The effect of surface gravity can be seen clearly in Figure 1.8 (from Faherty et al., 2013a), showing the scatter in near-infrared and mid-infrared colours for early to mid-Ls. For each type, the black point indicates the average colour and the grey bar the $1\sigma$ scatter. Red triangles indicate suspected young low-gravity dwarfs. The scatter around the mean colour is very large, spanning $\sim 2$ magnitudes in 2MASS J$-$K$_s$ and $\sim 0.5$ magnitudes in WISE W1$-$W2 (centred at 3.4 and 4.6 $\mu$m respectively). Interestingly, young objects are redder than the average, while old high-gravity objects are bluer.

The same effect can be seen in the spectra. This is well illustrated by Figure 1.9 (from Zhang et al., 2013a), where one can see seven objects classified as L7 using their optical spectra alone. Their infrared spectra (all normalized at 1.08 $\mu$m) show extreme variations, going from the very blue subdwarfs and extreme subdwarfs (J0216 and J0532) to the very red, probably very young J0047 and J0103. The most apparent difference is certainly the overall slope of the spectra, which is falling towards longer wavelength for the old high-gravity subdwarfs, and rising in the young low-gravity objects. This is the result of an enhanced/suppressed CIA of $H_2$, respectively. Being an effect of collisional interactions between hydrogen molecules, CIA is strongly dependent on the surface gravity. An increase in gravity favours it, because it causes an increase in atmospheric pressure, thus in the frequency of collisions, while low gravity hampers it. The observable result is an almost continuous absorption, stronger as it gets to longer wavelengths.

It must be noted at this point that a similar effect can be caused by a scarcity/excess of dust in the photosphere of the dwarf (e.g. Marocco et al., 2014). The cause of

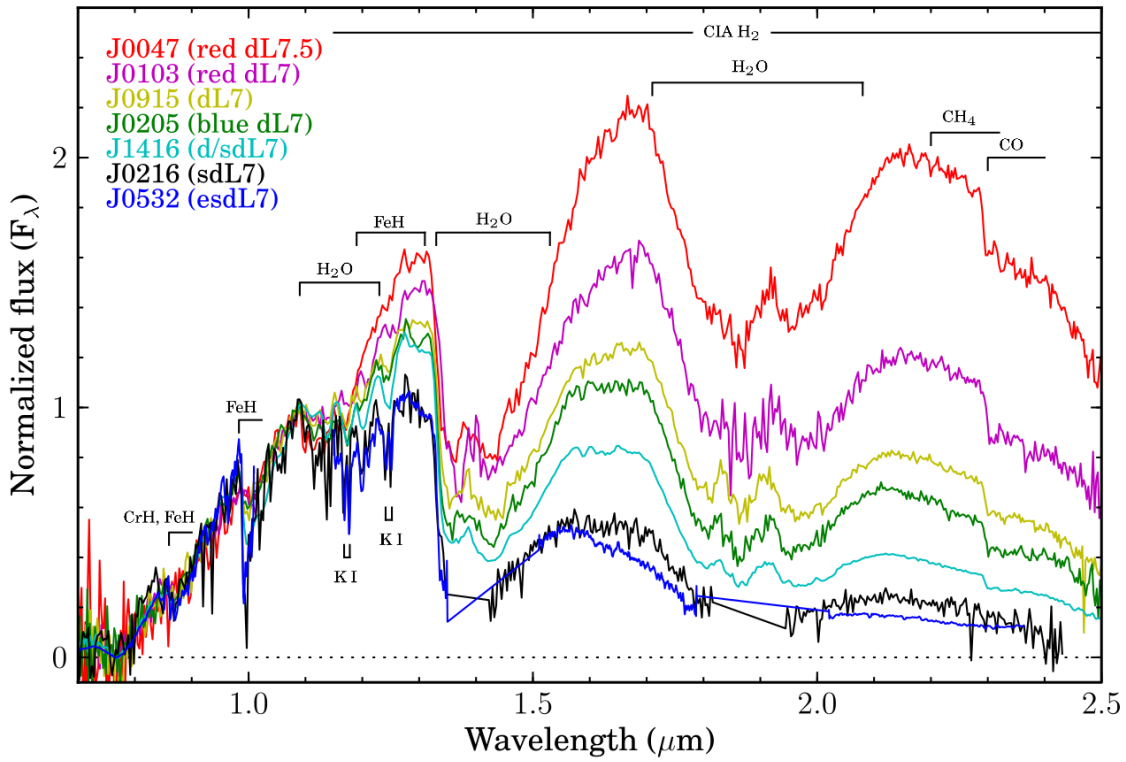


Fig. 1.9: The sequence of L7 dwarfs from Zhang et al. (2013a). All the spectra are normalized at 1.08 $\mu$m. Moving from the spectrum of J0047 down towards the spectrum of J0532 corresponds essentially to moving from young low-mass dwarfs towards old high-mass dwarfs.

differences in the dust content of ultracool atmospheres are not well understood, and could be attributed to differences in surface gravity, but also in differences in metallicity. more details about the influence of this parameter on the spectra of brown dwarfs are given in the following section.

The first attempts to quantify the effect of surface gravity on the spectra of brown dwarfs were conducted by Kirkpatrick et al. (2000) and Gorlova et al. (2003). They showed that the absorption lines of K I at 1.25 $\mu$m and of Na I at 1.21 $\mu$m are very sensitive to gravity, while the bands of $H_2O$ and CO at 1.35 $\mu$m and 2.30 $\mu$m are almost insensitive. At the same time Lucas et al. (2001) found that young objects tend to have "triangular-shaped' H band peaks, as opposed to the "trapezoidal-shaped" peaks of field dwarfs.

A few years later Cruz et al. (2009) defined a gravity based classification scheme for early L dwarfs. A detailed study of the optical spectra of 23 young L dwarfs showed that low-gravity L dwarfs display weak Na I, Cs I, Rb I lines. The prominent K I doublet at 7665,7699 Å has both weak line cores and weak pressure-broadened wings. The molecular bands of FeH and TiO are also weaker than in field L dwarfs while, at early types, VO is stronger. Using a set of 12 indices measuring the strength of the features described above, Cruz et al. (2009) defined three gravity classes, labeled using Greek suffix notations. An $\alpha$ suffix denotes normal-gravity objects, $\beta$ indicates moderately low gravity, while $\gamma$ is used for very low-gravity objects.

More recently Allers & Liu (2013) proposed an alternative classification using near-infrared spectra. In this fundamental work the authors analysed a sample of 73 M and L dwarfs, comparing in particular "old" field dwarfs with members of young mov-

ing group of different ages. By measuring the strength of the prominent absorption features in the near-infrared, using both spectral indices and direct equivalent width measurements, the authors confirmed that the $H_2O$ bands are gravity-insensitive, and therefore used the "water-based" indices to define the spectral typing scheme. The gravity classification scheme is instead based on the spectral indices and the equivalent widths of the gravity-sensitive features, specifically the K I and Na I lines (weaker in low-gravity objects), the FeH (weaker) and VO bands (stronger), and the "peakiness" of the H band (i.e. quantifying the effect first seen by Lucas et al. 2001). Based on the combination of these indicators, M and L dwarfs are divided in three categories: FLD-G indicates normal field dwarfs (corresponding to $\alpha$ from Cruz et al. 2009), INT-G labels intermediate gravity (like $\beta$ in Cruz et al. 2009), while VL-G stands for low gravity (analogue to $\gamma$ in Cruz et al. 2009). Allers & Liu (2013) attempted to establish a rough correspondence between their classification and the ages of the dwarfs studied, indicating that INT-G objects appear to be ∼50-200 Myr old, while VL-G objects should be ∼10-30 Myr old.

### 1.6.3 Metallicity

Objects formed in the early stages of our galaxy will have reduced abundances. Although the theory is of great help, it is necessary to observe reference objects to determine how the metallicity affects the spectral characteristics. Since they must have formed early in life in the Galaxy, these objects will be members of the halo or thick disk and will, in general, have higher proper motions than solar metallicity objects. The most effective way to discover them is therefore through the kinematic study of large portions of sky. In Zhang et al. (2013b) the authors used the SDSS DR8, scanning 9274 $deg^2$ of sky. By studying the large sample of late-M and early-L sub-dwarfs found, they conclude that sub-stellar sub-dwarfs tend to be brighter than their solar-metallicity counterparts of similar spectral type, especially in the optical bands.

Kirkpatrick et al. (2010) used multi-epoch 2MASS data covering 4030 $deg^2$ to look for high proper motion candidates. Among the various findings, they identified 15 late-M and L sub-dwarfs. All of these ultra-cool sub-dwarfs show stronger hydride bands (CaH, FeH, and CrH) compared to solar-metallicity objects, a result of the reduced opacity from oxides (e.g. VO and TiO). Counterintuitively, metal-poor dwarfs show stronger alkali (Na I, K I, Cs I, and Rb I) and metal lines (in particular Ti I and Ca I), a consequence of a reduced condensate formation in those metal-deficient atmospheres. Another clear distinction is in the strength of the CIA of $H_2$. This particular phenomenon is very sensitive to metallicity, and is particularly strong in metal-poor dwarfs, where the reduced dust opacity allows to look deeper into the photosphere where the pressure is higher, and therefore the collisions more frequent. A stronger CIA results in bluer colour and spectra for the sub-dwarfs compared to normal dwarfs. However, as described in the previous section, CIA is also very sensitive to surface gravity, and older objects are more compact than field objects (see Section 1.3).

One way to disentangle the effects of surface gravity and metallicity is by studying binaries (e.g. Day-Jones et al., 2008, 2011; Burningham et al., 2009; Faherty et al., 2010; Zhang et al., 2010). When a brown dwarf is found in a binary system with a brighter star, the study of the primary can provide valuable information. Depending on the type of the primary, one can put precise limits on age and metallicity of the system, thus identify the spectral signatures of these quantities in the spectrum of the dwarf.

One of the most famous binaries is probably the T7.5 HD 3651B, companion of a K0 star, discovered by Liu et al. (2007). What is particularly interesting is the comparison between HD 3651B and Gl 570D, a T7.5 which is part of another binary system (Burgasser et al., 2000). The two dwarfs have very similar temperatures ($\sim$ 800 K), but quite different ages: Gl 570D is relatively young ($\sim$ 2 Gyr) while HD 3651B is pretty old ($\sim$ 6 Gyr). In addition, an estimate of the mass of the two (based on the theoretical models of Burrows et al., 1997) lead to the conclusion that HD 3651B is more massive. From all these considerations it follows that the first has a surface gravity greater than the second ($\log[g] = 5.35$ against 5.0). As mentioned above, a lower strength of the peak at 2.18$\mu$m was expected in HD 3651B. Liu et al. (2007) observed instead the opposite effect. What acts against gravity is metallicity. HD 3651B has a higher metallicity ([Fe/H] = 0.13 against 0.06) and this causes a decrease in the photospheric pressure (Burrows et al., 2006) and suppress the CIA.

These first observations were followed by others (Pinfield et al., 2008; Leggett et al., 2009) which essentially confirmed the strong dependence of CIA on metallicity, and indicate that also the absorption of CO at 4.5$\mu$m is influenced, but in an opposite way.

Metallicity and gravity, therefore, have an opposing effect on the infrared spectra of brown dwarfs and thus tend to "hide" each other. This makes the study of these parameters in isolated objects extremely complex.

## 1.7 Initial mass function and formation history

The distribution of star formation with mass and time are key pieces of observational evidence for understanding star formation in the galaxy. The former is described by the initial mass function (IMF, Salpeter, 1955), which can be described as a power law of the form $\Psi(M) \propto M^{-\alpha}$, with $\alpha = 2.35$, and has been determined across the stellar mass regime by measuring the luminosity function for a population of stars, and applying a mass−luminosity relation, which should account for metallicity variations. Since brown dwarfs never reach the main sequence, this determination is complicated by the lack of a unique mass−luminosity relationship. Instead, the $T_{\rm eff}$ and luminosity are dependent on mass and age (Allard et al., 1997). This means that the luminosity function and $T_{\rm eff}$ distributions of field brown dwarfs depend not only on the mass function, but also on their formation history (Chabrier, 2002).

Using the relation between absolute magnitude and spectral type shown in Figure 1.6, the rate of discovery of L and T-dwarfs within large surveys (2MASS, DENIS, UKDISS, WISE, etc.) can be converted into space density. For L dwarfs Burgasser (2001) estimated a value of $10\pm2\times10^{-3}$/pc$^3$, while in the range L0 - L4.5 Gizis et al. (2000) estimated a value of $2.11\pm0.92\times10^{-3}$/pc$^3$. For T dwarfs, Burgasser (2001) estimated a value of $\sim 21\times10^{-3}$/pc$^3$ which means, simplifying, that in a random field of our galaxy there is about twice as many T-dwarfs than L-dwarfs. These values take on greater significance when compared to the density of stars of type M to type O, which is $93\pm8\times10^{-3}$/pc$^3$, 70% of which is represented by objects of type M.

We can use these numbers to determine the mass function of brown dwarfs. The first attempt was done by Reid et al. (1999). To break the mass−luminosity degeneracy it is necessary to know the age of these objects, but it is difficult to determine the age of isolated field objects. The solution adopted by Reid et al. (1999) was to assume a constant formation rate, which is supported by the work of Miller & Scalo (1979), who suggest that the birth rate does not depend strongly on the gas density, and is

approximately consistent across the Galactic disc. The mass function was supposed to be in the form $\Psi(M) \propto M^{-\alpha}$. Finally they used the models of Burrows et al. (1997) to describe the subsequent evolution of the objects. With these assumptions, synthetic sub-stellar populations were generated for different values of $\alpha$. After that, applying to the generated sample the selection criteria of 2MASS, they created pseudo-observational samples, which were then compared with the real observations. It was thus found that the value of $\alpha$ that better reproduces the observational data is 1.3.

Based on model data and direct comparisons with DENIS and 2MASS observations, Chabrier (2002) made simulations using two different IMFs and birth rates. One scenario considers a flat or constant birth rate, as in the work from Reid et al. (1999). The other scenario considers an exponential form where the formation decreases with time. These are coupled with IMFs of a power-law form derived by Chabrier (2001), and a log-normal and an exponential form which essentially give the same result when considering the effects from the birth rate. The comparison with DENIS and 2MASS observed luminosity function pointed towards $\alpha < 1$, but the authors noticed the degeneracy between IMF and formation history. A steeper IMF combined with a time decreasing formation rate leads to a similar luminosity function as a shallower IMF combined with a constant formation rate.

Burgasser (2004) considers a wider range of birth rates in his Monte Carlo simulations. In addition to flat and exponential forms, the author considered an "empirical" birth rate, which is the same as that measured for stars by Rocha-Pinto et al. (2000a,b), which represents "bursts" of formation at peak intervals of 0-1, 2-5 and 7-9 Gyr. This formation history scenario is also supported by the more recent work of the stellar formation history by Cignoni et al. (2006). Another scenario considered by Burgasser (2004) is the "cluster" birth rate which assumes a flat, but stochastic (i.e. in a number of clusters) formation, which produces a similar result to a flat formation scenario. Finally, he considers a "halo" type birth rate, that includes formation within a 1 Gyr burst, 9 Gyr in the past, in an attempt to explain a number of sub-dwarf brown dwarfs that have been identified (e.g. Burgasser et al. 2003a, and more recently Kirkpatrick et al. 2014 and Burningham et al. 2014). This scenario gives a radically different $T_{\rm eff}$ distribution for L and T dwarfs compared to the other scenarios, and seems unlikely since we are now seeing a larger number of L dwarfs identified in very young clusters (e.g. Taurus, Luhman et al. 2009, Quanz et al. 2010; Chameleon, Luhman 2007; Serpens, Lodieu et al. 2002a; TWA Hydra, Chauvin et al. 2004; Upper Sco, Lodieu et al. 2013; Lodieu 2013).

More recent simulations performed by Deacon & Hambly (2006) looked more specifically at L and T dwarfs from the United Kingdom Deep Infrared Sky Survey (UKIDSS) Large Area Survey (ULAS). They produced simulations that take into account several IMFs including a flat, log-normal and different power laws ($\alpha$ = +1.0, 0.0 and -1.0), combined with different exponential forms of the birth rate, similarly to those described above. These simulations also included the effect of Galactic disc heating, which had not been included in previous simulations of the birth rate. A histogram of these simulations (a log-normal form of the IMF with different birth rates) is shown in Figure 1.10. These simulations are similar to those of Allen et al. (2005, see their Figure 2), with the main differences arising from the differences in the normalization of the space density. Allen et al. (2005) use 0.35 stars pc$^{-3}$ according to Reid & Gizis (1997), whereas the simulations based on those of Deacon & Hambly (2006) use 0.0024 stars pc$^{-3}$ according to Deacon et al. (2008). In addition, changes also arise from the different values used for their birth rates, and as such are similar and show the same trends but are not

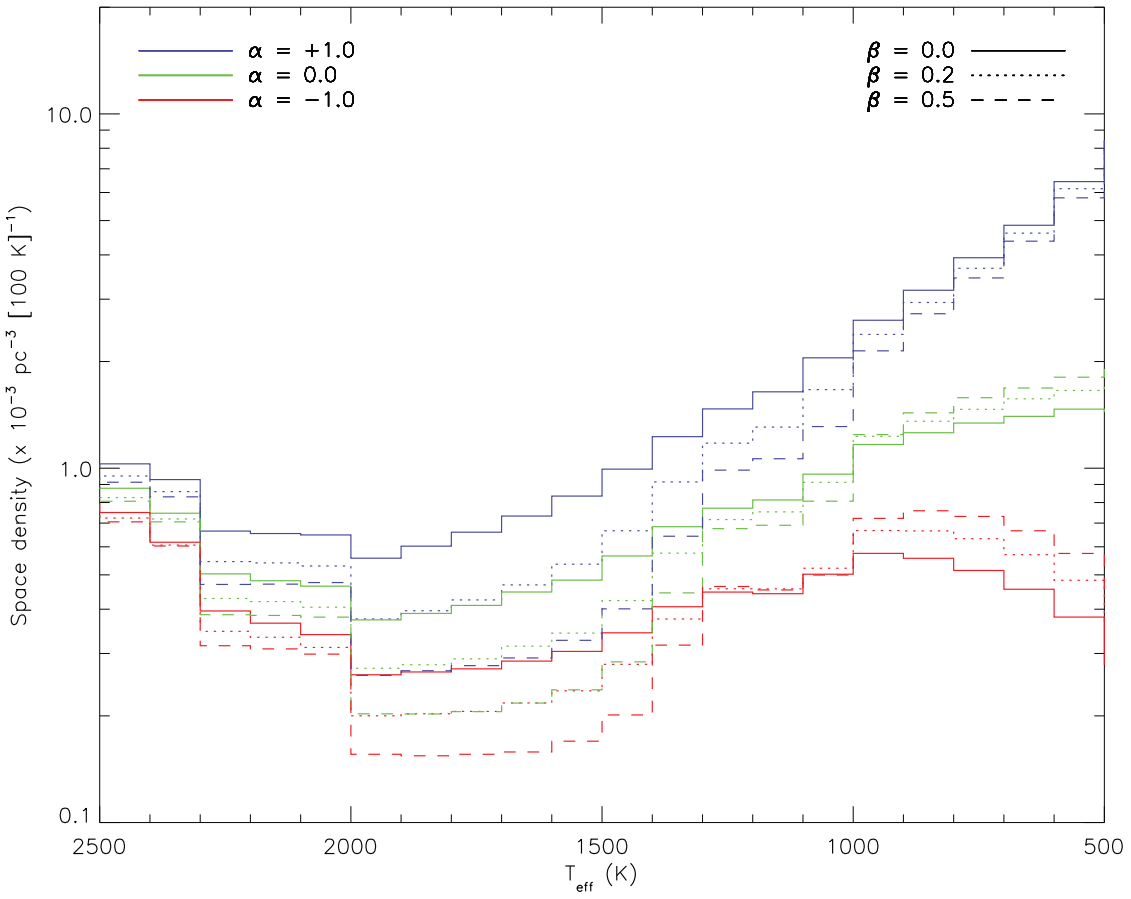


Fig. 1.10: The expected space density of brown dwarfs from the simulations performed by Deacon & Hambly (2006). The plot shows the expected space density for an IMF in the form $\Psi(M) \propto M^{-\alpha}$ for values of $\alpha$ = +1.0, 0.0, -1.0, and a birthrate in the form $b(t) \propto e^{-\beta t}$ for values of $\beta$ = 0.0, 0.2, 0.5.

directly comparable. It can be clearly seen in the Deacon & Hambly (2006) simulations that the sub-1000 K region is extremely sensitive to the IMF, but relatively insensitive to the birth rate, while the 1100-1500 K corresponding to the mid-L to mid-T spectral range is most sensitive to differing birth rates. The results of this simulations have been compared to observed space densities reported in the literature, most recently by Burningham et al. (2013) and Kirkpatrick et al. (2012), who used UKIDSS and WISE respectively to derive the space density of late T dwarfs (> T6) and found that the observed data are consistent with -1.0 < $\alpha$ < -0.5. This value is discrepant with the findings for young clusters, where $\alpha$ is found to be $\approx$ +0.6. Burningham et al. (2013) argue that this discrepancy can hint to the possibility that either the formation of brown dwarfs is favoured in low density environment, and therefore the resulting field IMF is different from the IMF in higher density environments like the aforementioned clusters, or the cooling time assumed to transform the IMF into field-like luminosity function is affected by systematic errors.

Other very interesting findings were presented in van Dokkum & Conroy (2010). Investigating the stellar mass function in luminous elliptical galaxies by measuring the strength of the Na I doublet (8183,8195 Å) and the Wing-Ford band of FeH in their spectra, van Dokkum & Conroy (2010) found that the mass function is steeper than the Salpeter one (Salpeter, 1955), leading to a greater contribution of low-mass objects in terms of total number of objects (> 80% of the total) and of total mass (> 60%) of

the galaxy. In a recent paper, La Barbera et al. (2013) states that this is related to the central velocity dispersion in massive early type galaxies, while is mostly independent from differences in metallicity. Similarly, the results of recent radiation hydrodynamical simulations from Bate (2014) suggest that the IMF is essentially insensitive to metallicity over a large range of values from 1/100 to 3 times solar. Another contribution came from Sumi et al. (2011). Conducting a micro-lensing survey of objects towards the galactic centre, they found a significant population of unbound or wide separated Jupiter-mass planets. According to Sumi et al. (2011) these planets are almost twice as numerous as main sequence stars (1.8 to 1.9 depending on the mass function considered). While some examples of free floating planetary mass objects have been observed (e.g. Delorme et al., 2012a; Liu et al., 2013), they appear to be rare. Choi et al. (2012) and Park et al. (2014) have pointed out how ambiguity in planetary detection via microlensing surveys due to incomplete coverage of planetary signal, or degeneracy between a "planet solution" and a "binary solution", could bias the results of Sumi et al. (2011), and would potentially reconcile the findings of microlensing surveys with those of direct imaging surveys. These contributions put even more emphasis on the need to determine precisely the initial mass function and the birthrate of brown dwarfs, as this will be fundamental to also understand their formation mechanism.

### 1.7.1 Binary fraction

An additional complication in accurately determining the luminosity function of sub-stellar objects comes from the presence of unresolved binary (or multiple) systems. Unfortunately, the binary fraction among low mass stars and brown dwarfs is poorly constrained, chiefly because of the intrinsic difficulty of studying close and faint pairs. Much effort has been devoted to determine the sub-stellar binary fraction, and I will try to give a quick summary of the current knowledge of this important observable.

The search for very low mass binaries has been conducted predominantly via high-resolution imaging (e.g. Reid et al., 2001b, 2008a; Bouy et al., 2003, 2008; Burgasser et al., 2003c; Beuzit et al., 2004; Delorme et al., 2012b; Gizis et al., 2003; Ahmic et al., 2007) and high resolution spectroscopy surveys (e.g. Delfosse et al., 1999a; Basri & Reiners, 2006; Joergens & Guenther, 2001; Joergens, 2006, 2008; Reid et al., 2002b). While high-resolution imaging is more sensitive to typical separations $\gtrsim 2-3$ AU (at the typical distances of observed brown dwarfs), high-resolution spectroscopy is more sensitive to tightly bound systems, making these techniques complementary.

Magnitude-limited high-resolution imaging surveys tend to suggest a binary fraction of $7-15\%$ ($9^{+11}_{-4}\%$, Burgasser et al. 2003c; $7.6^{+5.9}_{-1.7}\%$, Bouy et al. 2003; $13-15\%$, Martín et al. 2000), but as already mentioned they are biased against tight binaries (i.e. with separations shorter than $\sim 2-3$ AU).

Using high-resolution spectroscopy Reid et al. (2002b) have estimated $6^{+7}_{-2}\%$ for a sample of late-M dwarfs; Guenther & Wuchterl (2003) estimated $12^{+10}_{-4}\%$ from a sample of 25 late-M and early L dwarfs; more recently Joergens (2008) derived $10^{+18}_{-8}\%$ at separations $< 3$ AU and $7^{+5}_{-3}\%$ at separations $\leq 0.3$ AU via radial velocity monitoring of low mass stars and brown dwarfs in Chamaeleon I, claiming a decline in the binary fraction at separations $< 1$ AU. This is in agreement with what was found by Maxted et al. (2008) in $\sigma$ and $\lambda$ Orionis (the estimated binary fraction is $< 7.5\%$ at separations $< 0.28$ AU), but contrasts with the findings of Kurosawa et al. (2006) who obtained $24^{+16}_{-13}\%$ at separations $< 0.1$ AU in Upper Scorpius.

A much higher ratio of tight binaries is derived by Maxted & Jeffries (2005), who

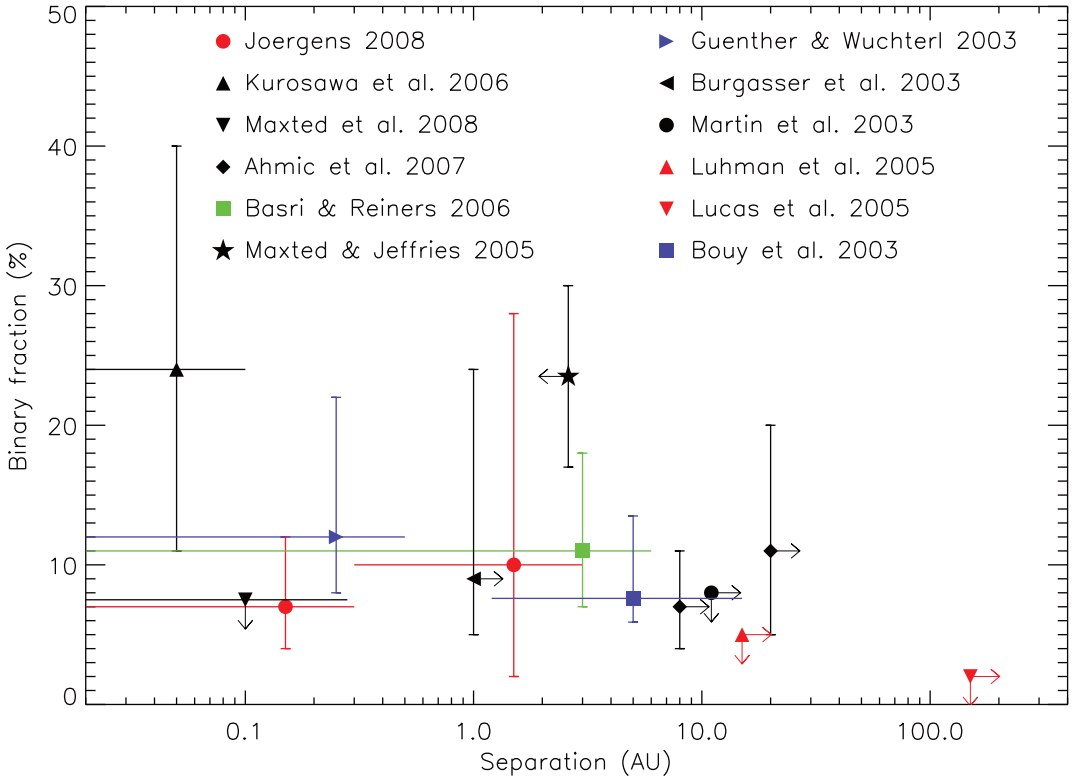


Fig. 1.11: The binary fraction as a function of separation. Please refer to the text for details on how the different values were obtained

analysed all the possible sources of incompleteness and biases in the aforementioned surveys. They conclude that the binary fraction among very low mass stars and brown dwarfs could be $17-30\%$ for separations $< 2.6$ AU, leading to a total binary fraction of $32-45\%$ (assuming a binary fraction of 15 % for separation $> 2.6$ AU). This result is in agreement with the work of Pinfield et al. (2003), who derived a binary fraction of $50^{+11}_{-10}\%$ in the Pleiades and Praesepe clusters.

On the other hand, wide very low mass binaries appear to be rare, and the binary fraction seems to decline with separation, from an upper limit of 8% for separation $>$ 11 AU in $\alpha$ Perseus (Martín et al., 2003) to an upper limit of 5% for separation $> 15$ AU in IC 348 (Luhman et al., 2005), down to an upper limit of 2% for separation $>$ 150 AU in trapezium (Lucas et al., 2005). This decline is not an observational bias, as the limitation imposed on high-resolution imaging by the field of view (typically 10-20"), this only excludes systems with separation $\gtrsim$ 150 AU at 30 pc, or at even wider separations ($\gtrsim 200-1000$ AU) in young nearby clusters.

The results presented above are summarized in Figure 1.11, as a function of separation.

The binary fraction also depends strongly on the mass ratio $q$ between the components, defined as $q = M_{\rm secondary}/M_{\rm primary}$. The very low mass binaries known to date show a peaked distribution at $q \sim 1$, as can be seen in Figure 1.12, taken from Burgasser et al. (2007). These ratios were derived by a variety of methods, including comparison of component fluxes to evolutionary models (e.g. Chabrier et al., 2000), analytic relations (e.g. Burrows et al., 2001) and direct estimates from orbital motion measurements, and are therefore prone to different systematics.

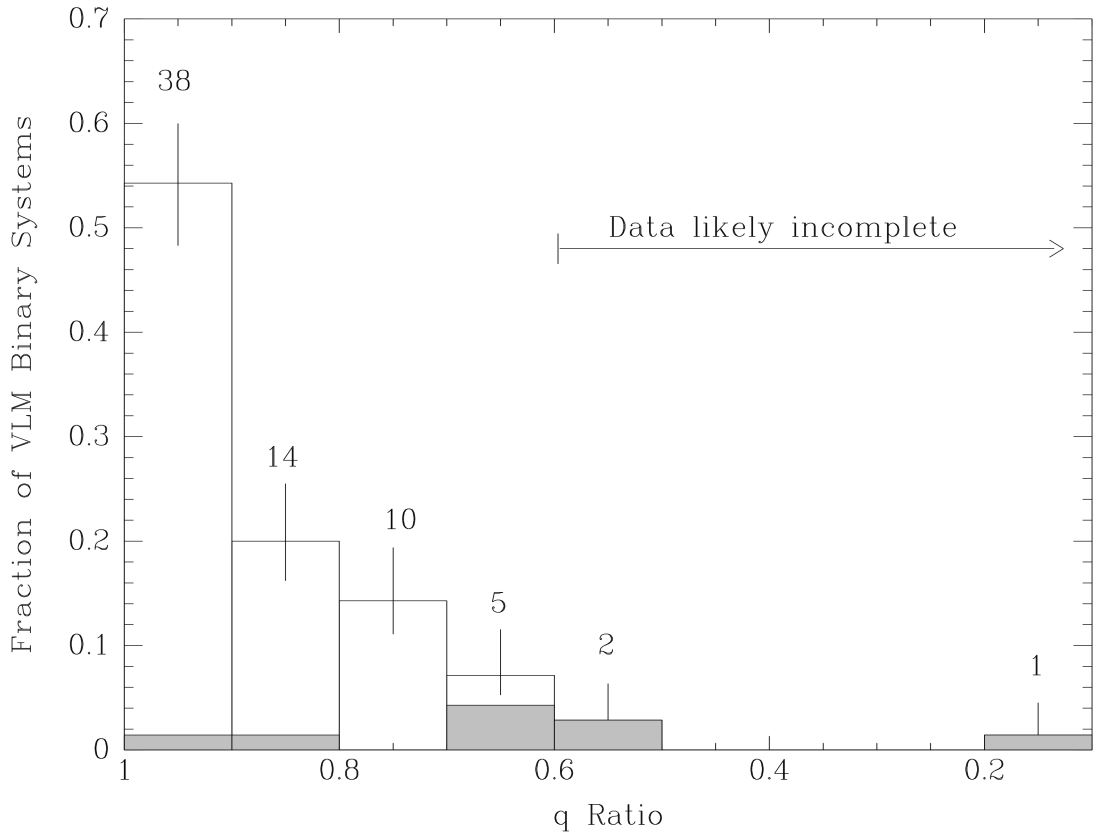


Fig. 1.12: Mass ratio distribution of known very low mass binaries (spectral type later than M6) from Burgasser et al. (2007). The number of binaries in each bin is labelled. The shaded bins represent the systems with age $< 10$ Myr.

As with the separation distribution, it is important to consider selection biases in the observed mass ratios. In particular, secondaries in low $q$ binaries may be too faint for direct imaging or of insufficient mass to induce a measurable radial velocity variation on the primary. However, most imaging and spectroscopic surveys to date are sensitive down to $q \gtrsim 0.5$, while the drop-off is clearly visible at the highest mass ratios (more than half of the know, very low mass binaries have $q > 0.9$). Therefore the peak at $q \sim 1$ is not the result of this bias, while the number of low mass ratio systems may indeed be underestimated.

# Chapter 2: Parallaxes of Southern Extremely Cool objects (PARSEC): Spectroscopic Follow-up and Parallaxes of 52 Targets

This chapter is a version of: "Parallaxes of Southern Extremely Cool objects (PARSEC). II. Spectroscopic Follow-up and Parallaxes of 52 Targets", F. Marocco, A. H. Andrei, R. L. Smart, H. R. A. Jones, D. J. Pinfield, A. C. Day-Jones, J. R. A. Clarke, A. Sozzetti, P. W. Lucas, B. Bucciarelli, and J. L. Penna, The Astronomical Journal, Volume 146, Issue 6, article id. 161, , 19 pp. (2013), and is reproduced by permission of the AAS.

The co-authors of the paper contributed entirely to Section 2.2 and partly to Section 2.4. Everything else is my own original work.

## 2.1 Introduction

As discussed in Chapter 1 the depletion of photospheric condensate clouds at the transition between the spectral classes L and T is one of the outstanding problems in brown dwarfs physics. In particular, current models are unable to explain the extremely narrow range of effective temperatures and luminosities in which this transition takes place (e.g. Burrows et al., 2006; Marley et al., 2007). Also, our understanding of the effects of gravity and metallicity on the spectra of the cool dwarfs is still incomplete (e.g. Murray et al., 2011; Leggett et al., 2012; Pinfield et al., 2012).

In order to examine the role of binarity, metallicity and gravity in the L-T transition region of the H.-R. diagram, it is necessary to combine spectroscopy, photometry and astrometry of a large sample of objects. For instance, binary candidates can be identified using spectral indices, and the spectral type of their components can be determined by spectral fitting. In particular, for objects in the L-T transition region, we refer the reader to Burgasser et al. (2010), where the authors developed a set of selection criteria based on a combination of spectral indices and spectral types. Unresolved binaries deserve particular attention as they are extremely important "benchmark objects", which can lead to dynamical masses measurements (if their components can be spatially resolved, e.g. Dupuy & Liu, 2011, and references therein) or to radii measurements (if they form an eclipsing pair, e.g. Stassun et al., 2006). Both quantities are required to put observational constraints on structure models and evolutionary theories of low-mass objects (Baraffe et al., 1998; Burrows et al., 2011). Metallicity and gravity can be estimated similarly by using spectral indices or via spectral fitting with benchmark objects (Pinfield et al., 2006; Rojas-Ayala et al., 2010). Finally, a better sampling of the L and T spectral sequence is necessary to improve our understanding of the luminosity function and the substellar mass function, both still not well constrained (e.g. Burningham et al., 2010b).

The PARallaxes of Southern Extremely Cool objects (PARSEC[1]) program has been observing with the ESO2.2 Wide Field Imager (WFI) over 140 known L and T dwarfs to obtain their parallaxes and proper motions at a high S/N level. The observing campaign is complete and the project has already produced a proper motion catalogue of 220,000 objects and 10 parallaxes with 2 mas precision for the best cases (Andrei et al., 2011, hereafter AHA11). A significant fraction of PARSEC targets do not have infrared spectroscopy, a lack that limits the depth of the analysis on the targets. We therefore started a spectroscopic campaign in parallel to the PARSEC program to follow-up those targets missing near-infrared (NIR) spectra.

In this contribution we present the first 52 spectra we obtained for PARSEC targets and new parallaxes and proper motions for 21 of them. The parameters of the sample can be found in Table 2.1, where we present objects' names, coordinates and infrared magnitudes.

[1]http://parsec.oato.inaf.it

| Object name | Object short name | $\alpha$ hh:mm:ss.ss | $\delta$ dd:mm:ss.s | 2MASS J | 2MASS H | 2MASS $K_s$ | WISE W1 | WISE W2 | WISE W3 | WISE W4 | Ref. |
|---|---|---|---|---|---|---|---|---|---|---|---|
| 2MASS J00145575−4844171 | 0014-4844 | 00:14:55.75 | -48:44:17.1 | 14.050 | 13.107 | 12.723 | 12.244 | 11.994 | 11.445 | 8.682 | 7 |
| EROS-MP J0032−4405 | 0032-4405 | 00:32:55.84 | -44:05:05.8 | 14.776 | 13.857 | 13.269 | 12.820 | 12.490 | 11.726 | 9.289 | 1 |
| 2MASS J00531899−3631102 | 0053-3631 | 00:53:18.99 | -36:31:10.2 | 14.445 | 13.480 | 12.937 | 12.312 | 12.029 | 11.520 | 9.123 | 7 |
| 2MASSW J0058425−065123 | 0058-0651 | 00:58:42.53 | -06:51:23.9 | 14.311 | 13.444 | 12.904 | 12.562 | 12.248 | 11.692 | 8.739 | 2 |
| SSSPM J0109−5100 | 0109-5100 | 01:09:01.50 | -51:00:49.4 | 12.228 | 11.538 | 11.092 | 10.833 | 10.573 | 10.373 | 9.309 | 3 |
| 2MASS J01282664−5545343 | 0128-5545 | 01:28:26.64 | -55:45:34.3 | 13.775 | 12.916 | 12.336 | 11.944 | 11.690 | 11.300 | 9.482 | 4 |
| 2MASS J01443536−0716142 | 0144-0716 | 01:44:35.36 | -07:16:14.2 | 14.191 | 13.008 | 12.268 | 11.603 | 11.361 | 10.948 | 8.928 | 18 |
| 2MASS J01473282−4954478 | 0147-4954 | 01:47:32.82 | -49:54:47.8 | 13.058 | 12.366 | 11.916 | 11.699 | 11.487 | 11.220 | 8.615 | 5 |
| 2MASSI J0218291−313322 | 0218-3133 | 02:18:29.13 | -31:33:23.0 | 14.728 | 13.808 | 13.154 | 12.599 | 12.287 | 11.926 | 9.415 | 6 |
| SSSPM J0219−1939 | 0219-1939 | 02:19:28.07 | -19:38:41.6 | 14.110 | 13.339 | 12.910 | 12.546 | 12.307 | 12.868 | 9.176 | 3 |
| 2MASS J02271036−1624479 | 0227-1624 | 02:27:10.36 | -16:24:47.9 | 13.573 | 12.630 | 12.143 | 11.772 | 11.557 | 11.210 | 9.322 | 11 |
| 2MASS J02304498−0953050 | 0230-0953 | 02:30:44.98 | -09:53:05.0 | 14.818 | 13.912 | 13.403 | 12.943 | 12.700 | 11.901 | 9.481 | 5 |
| 2MASSI J0239424−173547 | 0239-1735 | 02:39:42.45 | -17:35:47.1 | 14.291 | 13.525 | 13.039 | 12.710 | 12.425 | 11.833 | 9.353 | 6 |
| 2MASS J02572581−3105523 | 0257-3105 | 02:57:25.81 | -31:05:52.3 | 14.672 | 13.518 | 12.876 | 12.018 | 11.591 | 10.596 | 8.952 | 7 |
| DENIS-P J035726.9−441730 | 0357-4417 | 03:57:26.95 | -44:17:30.5 | 14.367 | 13.531 | 12.907 | 12.475 | 12.086 | 11.600 | 9.318 | 8 |
| SDSSp J053951.99−005902.0 | 0539-0059 | 05:39:52.00 | -00:59:01.9 | 14.033 | 13.104 | 12.527 | 11.869 | 11.578 | 11.411 | 8.419 | 9 |
| SIPS0614−2019 | 0614-2019 | 06:14:11.96 | -20:19:18.1 | 14.783 | 13.901 | 13.375 | 13.044 | 12.789 | 12.563 | 9.344 | 10 |
| 2MASS J06244595−4521548 | 0624-4521 | 06:24:45.95 | -45:21:54.8 | 14.480 | 13.335 | 12.595 | 11.830 | 11.478 | 10.866 | 9.526 | 11 |
| 2MASS J07193535−5050523 | 0719-5050 | 07:19:35.35 | -50:50:52.4 | 10.327 | 9.735 | 9.482 | 9.270 | 9.122 | 9.012 | 8.609 | 12 |
| 2MASS J07193188−5051410 | 0719-5051 | 07:19:31.88 | -50:51:41.0 | 14.094 | 13.282 | 12.773 | 12.443 | 12.220 | 11.540 | 8.988 | 11 |
| SSSPM J0829−1309 | 0829-1309 | 08:28:34.19 | -13:09:19.8 | 12.803 | 11.851 | 11.297 | 10.916 | 10.667 | 10.132 | 8.823 | 13 |
| 2MASSW J0832045−012835 | 0832-0128 | 08:32:04.15 | -01:28:35.8 | 14.128 | 13.318 | 12.712 | 12.411 | 12.173 | 11.809 | 9.141 | 2 |
| 2MASSI J0835425−081923 | 0835-0819 | 08:35:42.56 | -08:19:23.7 | 13.169 | 11.938 | 11.136 | 10.392 | 10.035 | 9.472 | 8.489 | 6 |
| DENIS-P J0909−0658 | 0909-0658 | 09:09:57.49 | -06:58:18.6 | 13.890 | 13.090 | 12.539 | 12.207 | 11.957 | 11.300 | 8.572 | 19 |
| 2MASSW J0928397−160312 | 0928-1603 | 09:28:39.72 | -16:03:12.8 | 15.322 | 14.292 | 13.615 | 13.047 | 12.747 | 12.367 | 8.722 | 2 |
| 2MASS J09532126−1014205 | 0953-1014 | 09:53:21.26 | -10:14:20.5 | 13.469 | 12.644 | 12.142 | 11.757 | 11.404 | 10.761 | 8.719 | 14 |
| 2MASS J10044030−1318186 | 1004-1318 | 10:04:40.30 | -13:18:18.6 | 14.685 | 13.883 | 13.357 | 12.774 | 12.482 | 12.206 | 9.167 | 21 |

Continued on next page.

Continued from previous page.

| Object name | Object short name | $\alpha$ hh:mm:ss.ss | $\delta$ dd:mm:ss.s | 2MASS J | 2MASS H | 2MASS $K_s$ | WISE W1 | WISE W2 | WISE W3 | WISE W4 | Ref. |
|---|---|---|---|---|---|---|---|---|---|---|---|
| 2MASSW J1004392−333518 | 1004-3335 | 10:04:39.29 | -33:35:18.9 | 14.480 | 13.490 | 12.924 | 12.285 | 11.998 | 12.667 | 9.223 | 15 |
| LHS 5166 | LHS 5166 | 10:04:38.70 | -33:35:09.3 | 9.849 | 9.303 | 9.026 | 8.838 | 8.643 | 8.522 | 8.297 | 20 |
| 2MASSI J1045240−014957 | 1045-0149 | 10:45:24.00 | -01:49:57.6 | 13.160 | 12.352 | 11.780 | 11.452 | 11.227 | 10.762 | 8.957 | 15 |
| 2MASSI J1059513−211308 | 1059-2113 | 10:59:51.38 | -21:13:08.2 | 14.556 | 13.754 | 13.210 | 12.940 | 12.634 | 12.287 | 9.254 | 6 |
| 2MASS J11544223−3400390 | 1154-3400 | 11:54:42.23 | -34:00:39.0 | 14.195 | 13.331 | 12.851 | 12.350 | 12.037 | 11.369 | 9.548 | 8 |
| 2MASS J12462965−3139280 | 1246-3139 | 12:46:29.65 | -31:39:28.0 | 15.024 | 14.186 | 13.974 | 13.325 | 12.383 | 11.407 | 8.831 | 5 |
| SDSS J133148.92−011651.4 | 1331-0116 | 13:31:48.94 | -01:16:50.0 | 15.459 | 14.475 | 14.073 | 13.412 | 13.123 | 12.262 | 9.481 | 16 |
| 2MASS J14044941−3159329 | 1404-3159 | 14:04:49.48 | -31:59:33.0 | 15.577 | 14.955 | 14.538 | 13.806 | 12.869 | 11.743 | 8.953 | 17 |
| 2MASSW J1438549−1309103 | 1438-1309 | 14:38:54.98 | -13:09:10.3 | 15.490 | 14.504 | 13.863 | 13.288 | 12.973 | 11.813 | 8.555 | 2 |
| SIPS1753−6559 | 1753-6559 | 17:53:45.18 | -65:59:55.9 | 14.095 | 13.108 | 12.424 | 11.837 | 11.519 | 11.127 | 9.383 | 10 |
| 2MASS J19285196−4356256 | 1928-4356 | 19:28:51.96 | -43:56:25.6 | 15.199 | 14.127 | 13.457 | 12.824 | 12.558 | 12.369 | 9.222 | 11 |
| 2MASS J19360187−5502322 | 1936-5502 | 19:36:01.87 | -55:02:32.2 | 14.486 | 13.628 | 13.046 | 12.278 | 11.998 | 11.646 | 8.146 | 11 |
| 2MASS J20025073−0521524 | 2002-0521 | 20:02:50.73 | -05:21:52.4 | 15.316 | 14.278 | 13.417 | 12.532 | 12.090 | 11.441 | 8.818 | 14 |
| 2MASS J20115649−6201127 | 2011-6201 | 20:11:56.49 | -62:01:12.7 | 15.566 | 15.099 | 14.572 | 14.431 | 14.117 | 12.371 | 9.196 | 5 |
| 2MASS J20232858−5946519 | 2023-5946 | 20:23:28.58 | -59:46:51.9 | 15.530 | 14.965 | 14.485 | 14.127 | 13.959 | 12.905 | 9.288 | 5 |
| SIPS2045−6332 | 2045-6332 | 20:45:02.38 | -63:32:06.6 | 12.619 | 11.807 | 11.207 | 10.738 | 10.358 | 9.860 | 8.682 | 10 |
| 2MASS J21015233−2944050 | 2101-2944 | 21:01:52.33 | -29:44:05.0 | 15.604 | 14.845 | 14.554 | 14.064 | 13.786 | 12.784 | 9.105 | 5 |
| 2MASS J21324898−1452544 | 2132-1452 | 21:32:48.98 | -14:52:54.4 | 15.714 | 15.382 | 15.268 | 14.955 | 13.635 | 12.014 | 8.733 | 5 |
| 2MASS J21481326−6323265 | 2148-6323 | 21:48:13.26 | -63:23:26.5 | 15.330 | 14.338 | 13.768 | 13.484 | 13.312 | 12.283 | 8.952 | 5 |
| 2MASS J21580457−1550098 | 2158-1550 | 21:58:04.57 | -15:50:09.8 | 15.040 | 13.867 | 13.185 | 12.571 | 12.226 | 11.656 | 8.472 | 7 |
| 2MASS J22092183−2711329 | 2209-2711 | 22:09:21.83 | -27:11:32.9 | 15.786 | 15.138 | 15.097 | 14.623 | 13.513 | 12.351 | 9.077 | 5 |
| 2MASS J22134491−2136079 | 2213-2136 | 22:13:44.91 | -21:36:07.9 | 15.376 | 14.404 | 13.756 | 13.229 | 12.832 | 11.552 | 9.070 | 14 |
| SSSPM J2310−1759 | 2310-1759 | 23:10:18.46 | -17:59:09.0 | 14.376 | 13.578 | 12.969 | 12.593 | 12.285 | 12.106 | 8.693 | 3 |
| 2MASS J23185497−1301106 | 2318-1301 | 23:18:54.97 | -13:01:10.6 | 15.553 | 15.237 | 15.024 | 15.080 | 13.675 | 12.649 | 9.014 | 5 |
| SIPS2346−5928 | 2346-5928 | 23:46:26.56 | -59:28:42.6 | 14.515 | 13.905 | 13.500 | 13.252 | 12.925 | 12.279 | 9.182 | 10 |

Table 2.1: List of the objects observed.

JHK magnitudes are from the 2MASS Point Source Catalogue. Refs: (1) EROS Collaboration et al. (1999); (2) Kirkpatrick et al. (2000); (3) Lodieu et al. (2002b); (4) Kendall et al. (2007); (5) This paper; (6) Cruz et al. (2003); (7) Kirkpatrick et al. (2008); (8) Bouy et al. (2003); (9) Fan et al. (2000); (10) Deacon & Hambly (2007); (11) Reid et al. (2008b); (12) Finch et al. (2007); (13) Scholz & Meusinger (2002); (14) Cruz et al. (2007); (15) Gizis (2002); (16) Hawley et al. (2002); (17) Looper et al. (2007); (18) Liebert et al. (2003); (19) Delfosse et al. (1999b); (20) Bakos et al. (2002); (21) Martín et al. (2010).

Ten of these targets were previously un-identified brown dwarfs (indicated as Ref. 5 in Table 2.1). They were selected as late-L and early-T candidates using 2MASS to provide near infrared colours, and combining this with Schmidt plate constraints from both USNO-B and the SuperCOSMOS Science Archive. We used the General Catalogue Query engine at the NASA/IPAC Infrared Science Archive to search the 2MASS database. Our 2MASS photometric constraints were designed to select ultracool objects over the range L8/9 to ∼T4. In general we selected 2MASS sources where J⩽16.0 (which is the signal-to-noise ratio > 10 in 2MASS), 0.3<J-H<1.0, 0.0<H-K<0.9, 0.0<J-K<1.6, because these are the typical colours of L-T transition dwarfs. For sources with the reddest J-H>0.8, we instead imposed a limit of J<15.5. To minimize the contamination from reddened background stars we required either non-detection in USNO-B or an R-band detection leading to a colour of R-K>8, with these constraints being implemented as part of our initial database search. In addition we excluded declinations of <-86 deg (since optical cross-matching in the database is incomplete in this range), and avoided the Galactic plane by examining outside galactic latitudes between -15 and +15 deg (to minimize contamination from reddened sources and blending issues). We also required no other 2MASS source within 6 arcseconds, no database evidence of contamination and confusion (cc_flag="000"), and no minor planet association (mp_flg="0"). This resulted in a large selection of candidates, dominated by contamination because our near-infrared colours constraints overlap greatly with stellar colours. The contamination took a variety of forms, including in the main part sources affected by bright star diffraction spikes, blended sources, and sources with faint (un-matched in the database) optical counterparts. To identify this contamination we visually inspected our full initial sample using the SuperCOSMOS Science Archive facility, and selected only candidates that were genuine non-detections in all bands, or if detected in the I-band, had colours consistent with late L or T dwarfs (I−J>3.5). Ten objects from this final selection form part of the sample investigated in this paper.

## 2.2 Astrometry

The observing strategy adopted in PARSEC is described and discussed extensively in AHA11, and the reader is referred to that contribution for details.

The parallax solution also delivers the two components of the proper motion ($\mu_\alpha$ and $\mu_\delta$), based solely on the observations used for the parallax solution, thus reasonably independent from the previous result obtained by combining an early subset of these observations against the 2MASS position (AHA11).

The objects in each image were centroided using the Cambridge Astronomy Survey Units *imcore* maximum likelihood baricenter (CASUTOOLS, v 1.0.21).The ensuing astrometry is done in relative mode, that is selecting a reference frame and referring all others to this frame using the standard coordinates calculated from the measured centroids. In fact, we unbias the outcome from a priori choices by selecting every frame in turn as the reference frame, thus producing as many parallax solutions as frames. The parallax and proper motion are calculated using the methods adopted in the Torino Observatory Parallax Program (Smart et al., 2003, 2007) and identical to those in AHA11.

Differential colour refraction (DCR, Monet et al., 1992) is not an issue for our astrometric accuracy. DCR is the small varying displacement of objects with different

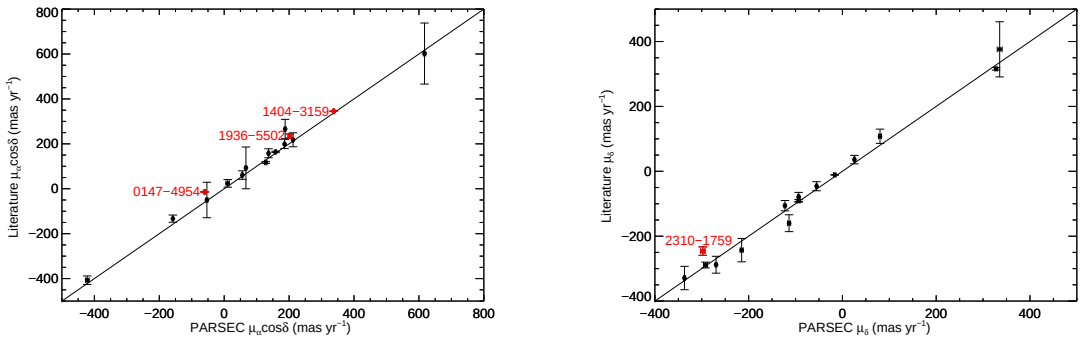


Fig. 2.1: Comparison of proper motions obtained here with those published in the literature. The solid line in each panel is the line of unity. The agreement is good, with only three targets (1404-3159, 1936-5502 and 0147-4954) showing a $3\sigma$ inconsistence in $\mu_\alpha \cos\delta$ and one (2310-1759) with a $3\sigma$ inconsistence in $\mu_\delta$. All the literature values are estimated from shorter baselines than those covered in this paper.

colors in a field that results from the variation of the atmosphere refractive index with wavelength. The targets in this parallax program are redder than the anonymous reference objects so this displacement is systematically different from the average of those reference objects. The effect is wavelength, weather, and zenith-distance dependent. However Stone (2002) has demonstrated that DCR is strongest in the blue bands and gradually decreases with wavelength. In particular that contribution demonstrates that by maintaining small zenith distances, DCR effects in $I$ and longer wavelengths (such as $z$) are typically <1 mas. The low-mass star optical parallax program of Jao et al. (2005) and Smart et al. (2003) and the brown dwarf optical parallax program of Dahn et al. (2002) also found negligible $z$-band DCR corrections ($\sim$0.3 mas) as did the infrared T dwarf parallax program of Tinney et al. (2003). To further minimize the variation in airmass, and hence DCR, all our targets are observed within 30 minutes of their meridian crossing. Therefore, DCR corrections are not applied to the positions in our pipeline.

We compared the proper motions to literature values as reproduced in Figure 2.1. Three targets, 1404-3159, 1936-5502 and 0147-4954, have differences in right ascension proper motion greater than 3 times the mean error and one target, 2310-1759, in declination proper motion. However, all the estimates are from short baselines of a few years and only one, 0147-4954, is outside 4 times the mean error so we believe this is reasonable consistency.

We also found 5 objects with published parallaxes, all with short baseline programs. Of these only one, 1936-5502, differs by more than 3 times the mean error. The Faherty et al. (2012) value is from only 1.31 years coverage which is the limit for disentangling proper motion and parallaxes and our experience is that often increased epoch coverage changes the value beyond the formal errors. We await the Faherty et al. (2012) updated value before we consider this a significant difference.

The two panels of Figure 2.2 compare respectively the right ascension and declination proper motions obtained here against the values obtained in the PARSEC proper motion catalogue, which uses the subsample of the first 1.5 yr of PARSEC observations and the 2MASS positions, to a total time span of about 10 yr. It is clear that the agreement is good, with a Pearson correlation coefficient (Pearson, 1895) larger than 0.8.

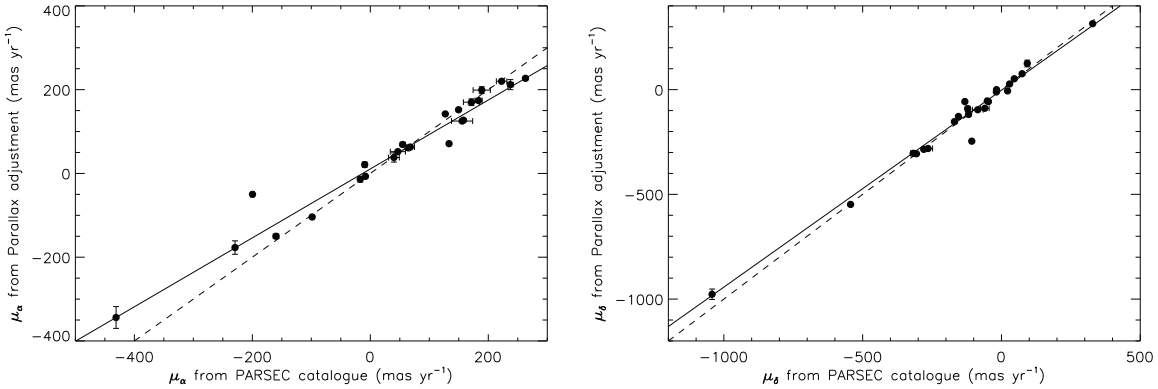


Fig. 2.2: Comparison of the proper motions from the PARSEC published catalogue (AHA11) against the proper motions obtained in the parallax determination. Overplotted for reference are the bisector of the plot (dashed line) and a linear fit to the data (solid line). The angular coefficients of the linear fit are larger than 0.8 in both cases.

The significance of the Pearson correlation goes as $r * (\sqrt{N-2}/\sqrt{1-r^2})$ that is, for a given correlation coefficient $r$ the larger the number of $N$ pairs the more significant is $r$. In our case with $N = 23$, $r = 0.8$ is significant to the 99.5% level. This lends support to the methods and significance to the assigned errors. Notice also that for 6 targets there was no corresponding proper motion in the PARSEC catalogue, meaning that they were either not found or not uniquely found in the 2MASS comparison.

Proper motions and parallaxes of the targets are listed in Table 2.2. For each target we present short name, the absolute parallax ($\pi_{abs}$), the two components of the proper motion ($\mu_\alpha \cos\delta$ and $\mu_\delta$), the time span covered by the observations, and the number of observations available for each target ($N_{obs}$).

| Object short name | $\pi_{abs}$ (mas) | $\mu_\alpha \cos\delta$ (mas yr$^{-1}$) | $\mu_\delta$ (mas yr$^{-1}$) | $V_{\tan}$ km s$^{-1}$ | Time span (yr) | $N_{obs}$ |
|---|---|---|---|---|---|---|
| 0032-4405 | 21.6 ± 7.2 | 128.3 ± 3.4 | -93.4 ± 3.0 | 34.8 ± 11.6 | 3.88 | 23 |
| 0058-0651 | 33.8 ± 4.0 | 136.7 ± 2.0 | -122.6 ± 1.8 | 25.8 ± 3.0 | 3.88 | 24 |
| 0109-5100 | 57.8 ± 3.5 | 212.0 ± 1.7 | 80.2 ± 3.2 | 18.6 ± 1.1 | 3.88 | 25 |
| 0147-4954 | 26.6 ± 3.1 | -60.1 ± 1.9 | -269.5 ± 1.8 | 49.2 ± 5.8 | 3.20 | 16 |
| 0219-1939 | 37.2 ± 4.1 | 187.8 ± 2.5 | -113.8 ± 3.3 | 27.9 ± 3.0 | 2.62 | 16 |
| 0230-0953 | 32.4 ± 3.7 | 148.2 ± 1.9 | -39.1 ± 2.7 | 22.4 ± 2.6 | 3.30 | 21 |
| 0239-1735 | 32.1 ± 4.7 | 55.8 ± 2.2 | -93.4 ± 2.2 | 16.1 ± 2.4 | 3.31 | 22 |
| 0257-3105 | 99.7 ± 6.7 | 617.3 ± 3.6 | 335.5 ± 5.3 | 33.4 ± 2.2 | 3.09 | 13 |
| 0539-0059 | 79.1 ± 2.4 | 158.3 ± 1.6 | 327.8 ± 2.4 | 21.8 ± 0.7 | 3.46 | 23 |
| 0614-2019 | 34.3 ± 3.0 | 138.8 ± 2.0 | -294.4 ± 2.9 | 45.0 ± 4.0 | 3.46 | 35 |
| 0719-5051 | 34.6 ± 2.2 | 186.0 ± 1.2 | -55.1 ± 1.7 | 26.6 ± 1.7 | 3.95 | 46 |
| 0928-1603 | 34.4 ± 3.9 | -158.1 ± 2.1 | 25.6 ± 1.8 | 22.0 ± 2.5 | 3.94 | 23 |
| 1246-3139 | 87.3 ± 3.2 | -5.3 ± 1.7 | -562.5 ± 2.6 | 30.5 ± 1.1 | 3.06 | 21 |
| 1331-0116 | 67.3 ± 12.6 | -421.9 ± 5.7 | -1039.0 ± 5.2 | 79.0 ± 14.8 | 3.39 | 17 |
| 1404-3159 | 49.2 ± 3.4 | 337.6 ± 1.9 | -16.3 ± 2.4 | 32.5 ± 2.2 | 3.39 | 24 |
| 1753-6559 | 58.0 ± 4.9 | -53.3 ± 3.0 | -336.9 ± 2.2 | 27.9 ± 2.4 | 4.28 | 55 |
| 1936-5502 | 43.3 ± 4.5 | 202.0 ± 2.9 | -292.0 ± 4.3 | 38.9 ± 4.1 | 3.88 | 40 |
| 2045-6332 | 40.0 ± 3.7 | 67.0 ± 2.4 | -214.9 ± 3.2 | 26.6 ± 2.5 | 3.87 | 25 |
| 2209-2711 | 47.9 ± 12.5 | -5.9 ± 8.1 | -133.6 ± 9.9 | 13.2 ± 3.6 | 2.96 | 15 |
| 2310-1759 | 36.4 ± 6.9 | 10.7 ± 5.4 | -297.9 ± 4.7 | 38.8 ± 7.4 | 2.06 | 8 |
| 2346-5928 | 14.3 ± 3.4 | 245.1 ± 1.7 | 57.6 ± 1.9 | 83.5 ± 19.7 | 3.88 | 24 |

Table 2.2: Summary of astrometric results. For each target we present short name, the absolute parallax ($\pi_{abs}$), the two components of the proper motion ($\mu_\alpha \cos\delta$ and $\mu_\delta$), the corresponding tangential velocity ($V_{\tan}$), the time span covered by the observations, and the number of observations available for each target ($N_{obs}$).

## 2.3 Spectroscopy

### 2.3.1 Observations and Reduction Procedures

Forty-five of the spectra were obtained using the OSIRIS spectrograph on the SOAR telescope in low-resolution (R = 1200) cross-dispersed mode, covering the wavelength range 1.2-2.3 $\mu$m. The data were reduced following standard procedures. The spectra were flat-fielded using dome flats, dark subtracted, and pair-wise subtracted to remove sky lines. The extraction was performed using IRAF standard routines and the wavelength calibration was done with He-Ar arc lamps. In order to correct the measured spectra for the telluric absorption, standard stars were observed immediately before or after each target, close on the sky and at a similar airmass. The spectra were corrected dividing each of them by the spectrum of the associated standard and then multiplying the result by the theoretical SED from Kurucz 1993 (for the appropriate temperature and surface gravity). The different orders of the telluric corrected spectra (roughly coincident with J, H and K band) were then merged, using the overlapping regions to adjust the relative flux levels, and finally turned into an absolute flux scale using the measured magnitudes (2MASS H and $K_s$). To do that, we convolved the spectra with 2MASS filters' profiles and integrated over the passbands to obtain synthetic magnitudes. Given that the difference between two magnitudes is, by definition, $m_1$-$m_2$=-2.5$\times \log_{10}(f_1/f_2)$, where $m_1$ and $m_2$ are the apparent magnitudes and $f_1$ and $f_2$ the corresponding fluxes, the scaling factors ($sf_{\rm i}$) are given by the equation:

$$sf_{\rm i} = 10^{0.4\times\left(m_{i,synt}-m_{i,obs}\right)} \tag{2.1}$$

where $m_{i,obs}$ is the measured 2MASS magnitude in the $ith$ band (H or $K_s$) and $m_{i,synt}$ is the corresponding synthetic one. We use H and $K_s$ band only, as the spectral coverage of OSIRIS is insufficient to compute a synthetic J magnitude. Finally, after checking that the two values were consistent, we took their weighted average as our scaling factor. To check the accuracy of our flux calibration, we tried to use different telluric stars taken during the same night (if possible) for each target. We noticed that there are no significant differences on the flux level outside of the telluric absorption bands. However, using a different telluric star significantly affects the quality of the telluric corrections, resulting in noisy telluric bands and significant variations in their flux level (up to a factor of 2).

Two other spectra were obtained with SOFI, on NTT, using a blue grism at low resolution (R = 1000) covering the wavelength range 0.95-1.64$\mu$m. The spectra reduction follows the same steps as for the OSIRIS ones, but the wavelength calibration was done using Xe arc lamps, and the flux calibration used the J magnitude only.

Finally five spectra were obtained with Xshooter, the echelle spectrograph mounted on the UT2 at VLT. This instrument covers a wide wavelength range (0.3-2.48 $\mu$m) with a resolution of 8100 in the VIS arm and 5500 in the NIR arm. To reduce these targets we used the Xshooter pipeline (version 1.3.7). The details of the Xshooter data reduction can be found in Day-Jones et al. (2013), and here we briefly summarize the main steps. The pipeline performs all the standard reduction steps (flat fielding, dark subtraction, wavelength calibration and flux calibration) and produces a 2D image containing the reduced spectrum. We extracted the spectra using standard IRAF routines and we corrected them for telluric absorption using standard telluric stars observed during the night, following the procedure described above. The telluric stars were also processed using the Xshooter pipeline. We tested the accuracy of the telluric correction by using

different telluric stars observed during the same night. As for the OSIRIS spectra, the use of different standards does not affect the global flux calibration, but results in some cases in slightly different flux levels in the telluric bands.

The spectra obtained are presented in Figures 2.3 - 2.5. All the spectra are normalized to 1 at 1.28 $\mu$m and shifted vertically by increments of one flux unit. The spectra have been normalized at 1.28 $\mu$m as this represents the peak of the J band and it is a reasonably flat region of the spectrum, not affected by major absorption lines.

### 2.3.2 Spectral Classification

To determine the spectral types of the objects, all the spectra were fitted to standard template spectra taken from the SpeX-Prism spectral library[2] using a $\chi^2$ fitting technique, excluding the telluric absorption bands when computing the statistic. The best-fit template was visually inspected to check it was a good fit to the spectrum of the object, and to spot possible peculiarities. If the best-fit template matches the real spectrum, the fit was accepted and the uncertainty on the spectral type of the target was assigned based on a parabolic fit to the $\chi^2$ distribution, rounding it to multiples of 0.5.

If the best-fit does not reproduce the spectrum well, we assigned a spectral type to the object based on a "by-eye" matching, selecting the template that gives the best match to the J band, and labeling the object as "peculiar". The properties of the peculiar objects, their spectral peculiarities, and the assigned spectral types are discussed further in Section 2.6.

Figure 2.8 shows an example of a good fit and of a bad fit. On the top panel we present the spectrum of 0257-3105. The best-fit template, the L8.0 standard 2MASSW J1632291+190441 is overplotted in red for comparison. The standard reproduces well the spectrum of the target, matching the flux level on the J, H, and K band, as well as the strength of the main absorption features (i.e. the CO band at 2.3 $\mu$m and the K I doublet at 1.25$\mu$m). This object is therefore classified L8.0. The bottom panel of Figure 2.8 shows instead an example of a poor fit. The target is 1331-0116 and overplotted in red we show the best-fit template, the T1.0 standard SDSS J015141.69+124429.6. While the standard reproduces quite well the depth of the $H_2O$ absorption bands, the target does not show any sign of $CH_4$ absorption in the H and K band, and the K I doublet at 1.25$\mu$m is much stronger than in the standard. 1331-0116 therefore cannot be classified as a T dwarf, and its spectral type has to be determined via "by-eye" matching. More details on this peculiar object can be found in Section 2.6.6.

A summary of the observations and the results obtained is given in Table 2.3. For each object we list the short name, the instrument used to obtain its spectrum, the night when it was observed, the associated standard and its spectral type, the object's previous optical and NIR classification (if available) and our new NIR spectroscopic classification.

[2]http://pono.ucsd.edu/~adam/browndwarfs/spexprism

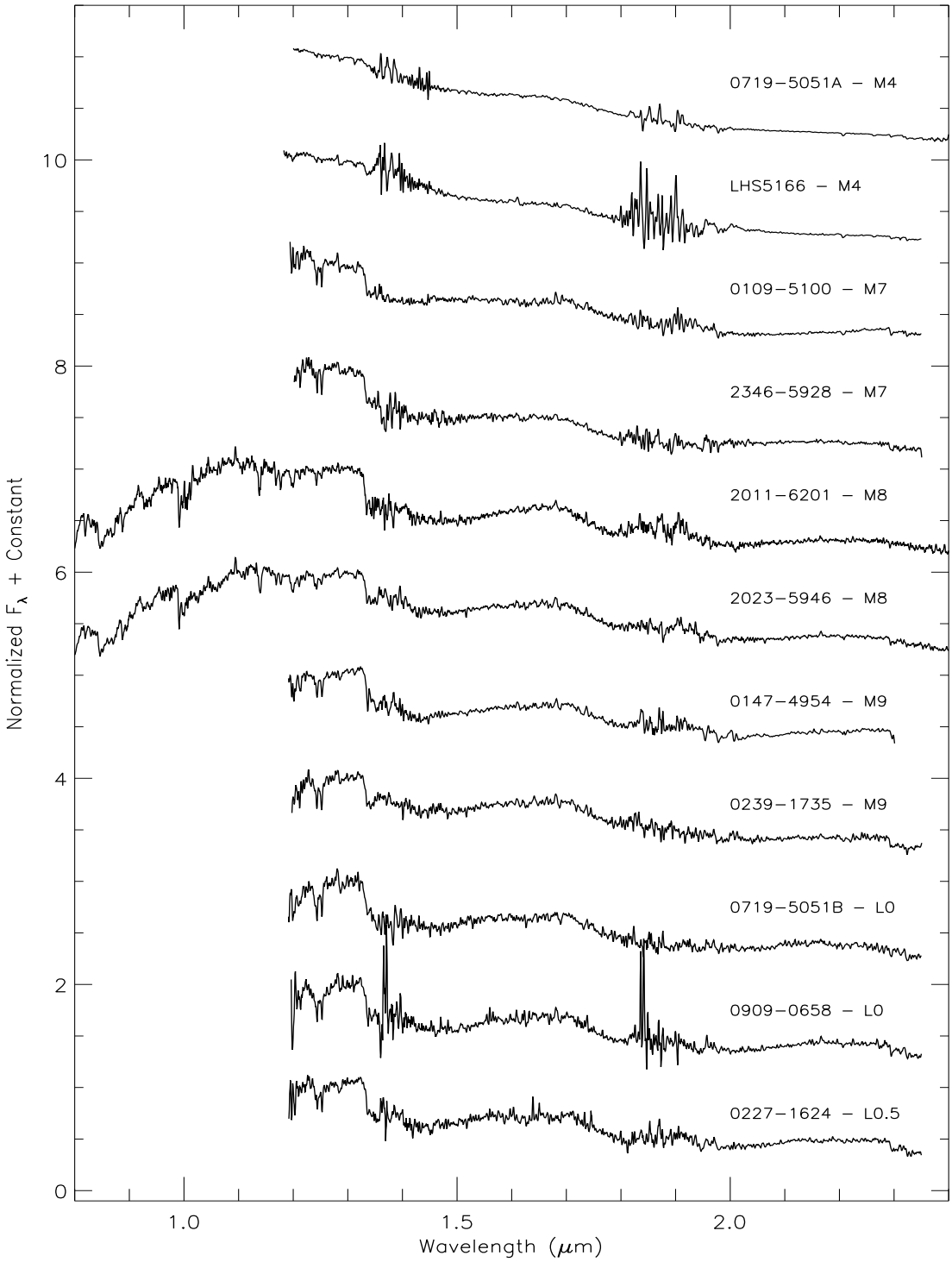


Fig. 2.3: The spectra obtained for our targets, sorted from earlier to later spectral type. The spectra showed here are in the M4-L0.5 range. They have all been normalized to 1 at 1.28$\mu$m, smoothed to a resolution of $\sim$10 Å per pixel, and displaced vertically by increments of one flux unit.

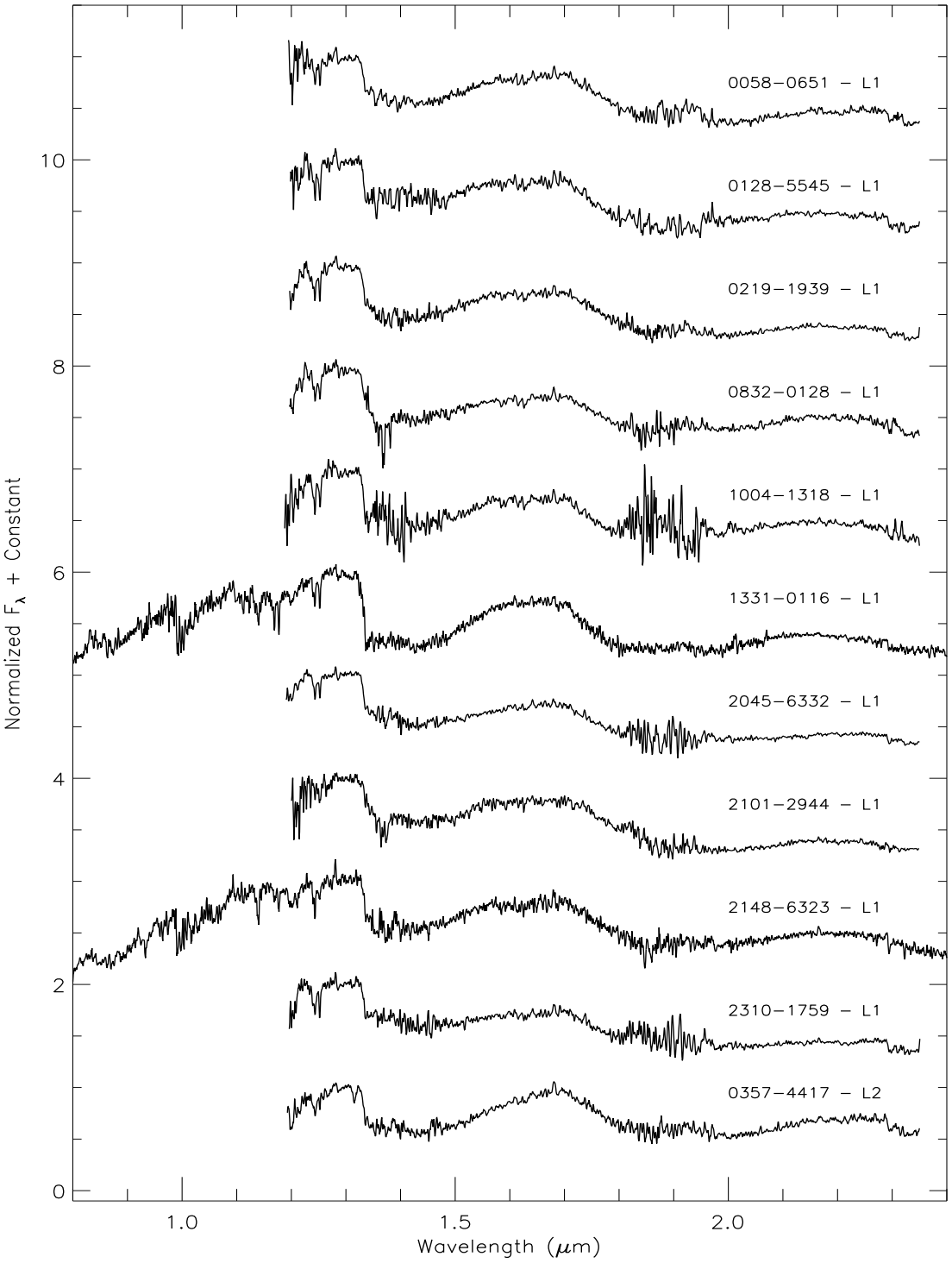


Fig. 2.4: Same as Figure 2.3, but for objects in the range L1-L2.

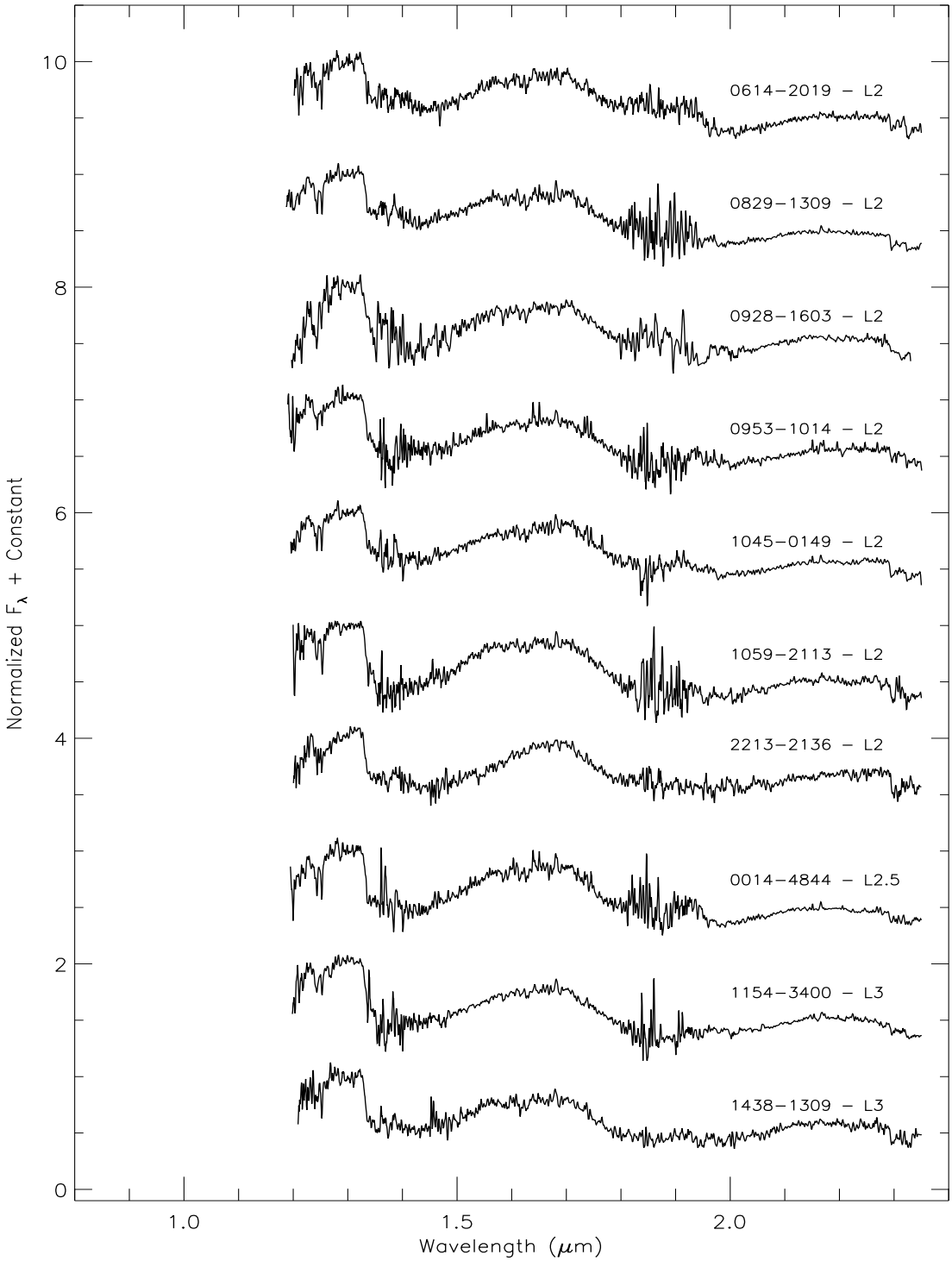


Fig. 2.5: Same as Figure 2.3, but in the range L2-L3.

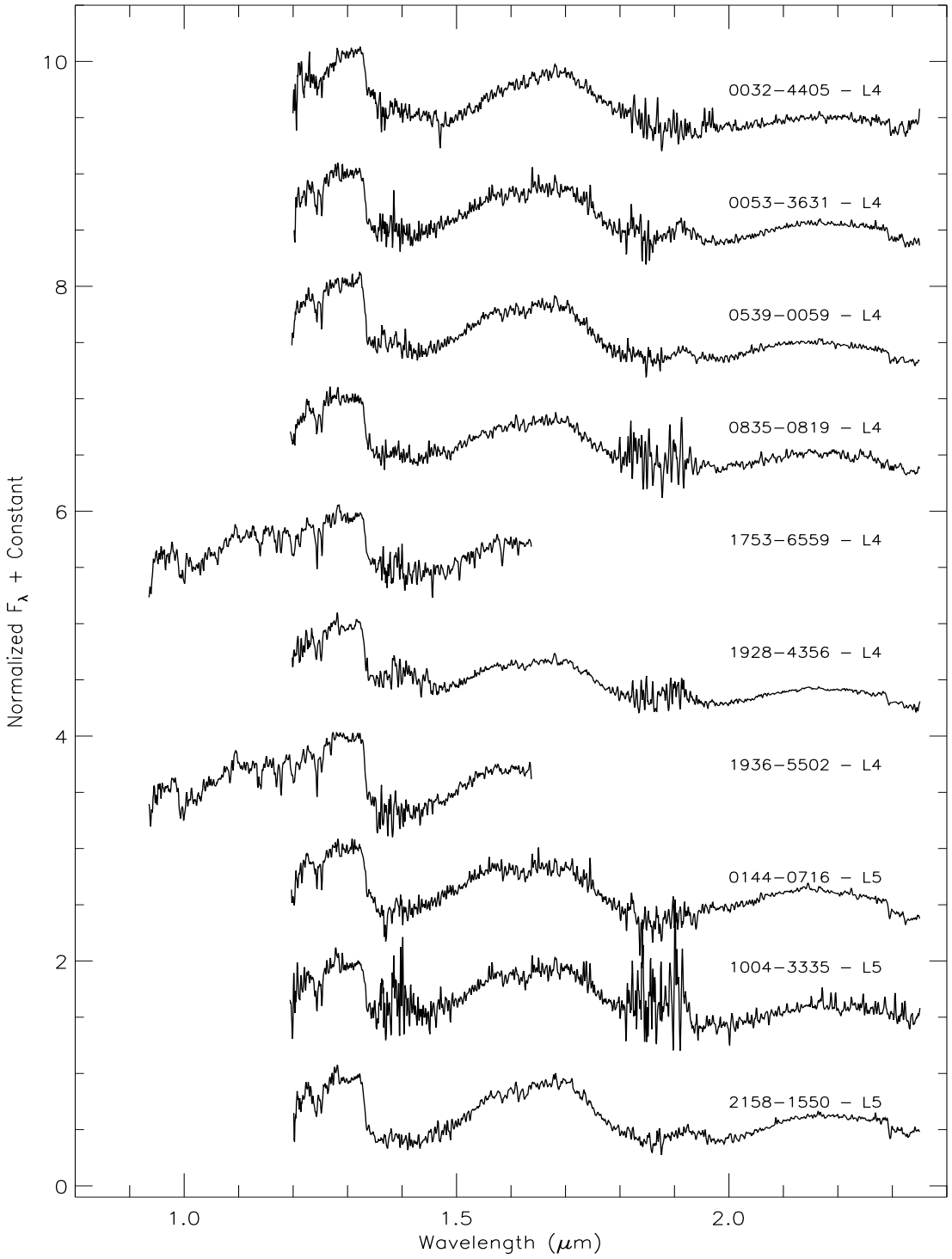


Fig. 2.6: Same as Figure 2.3, but in the range L4-L5.

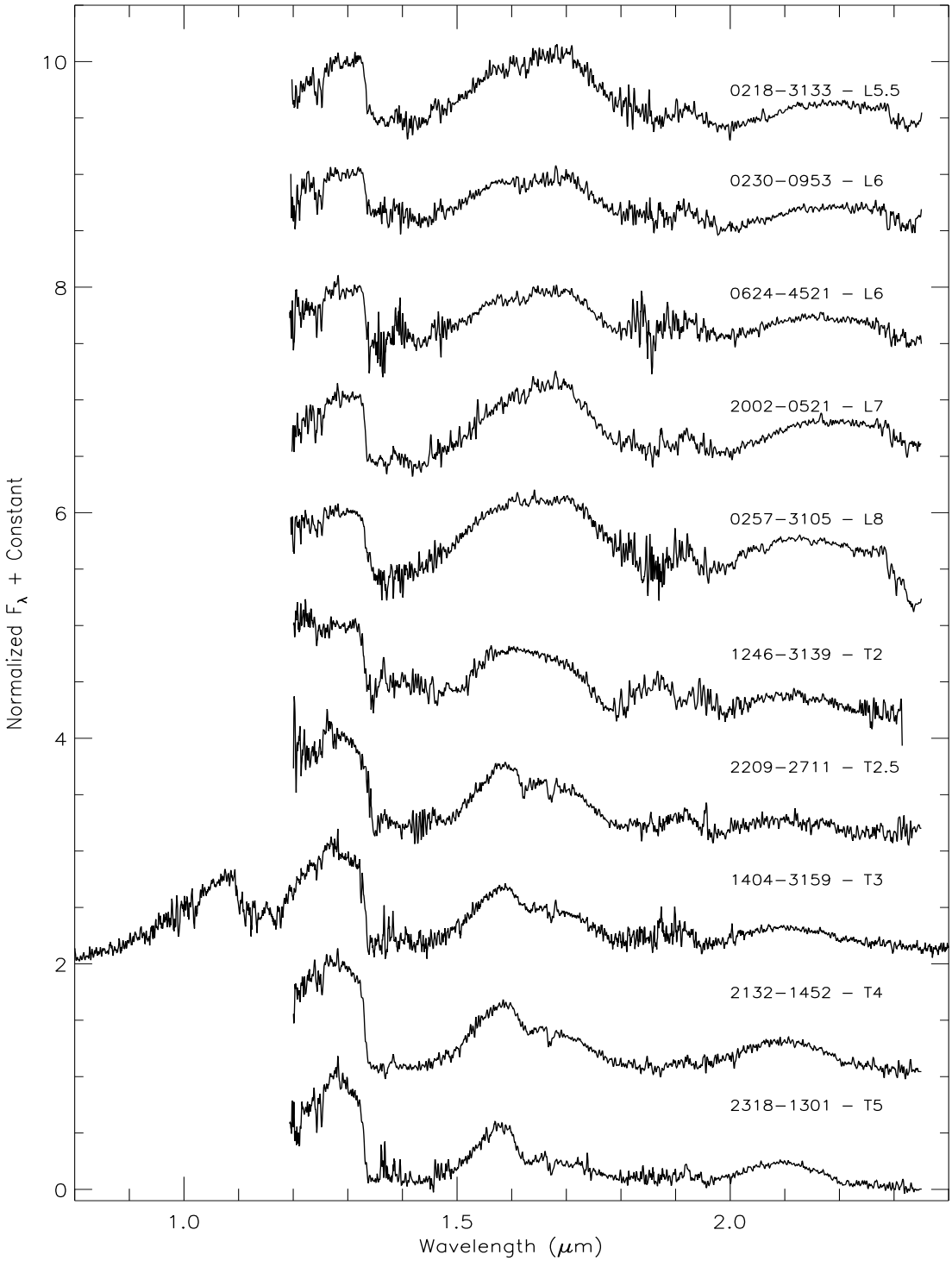


Fig. 2.7: Same as Figure 2.3, but in the range L5.5-T5.

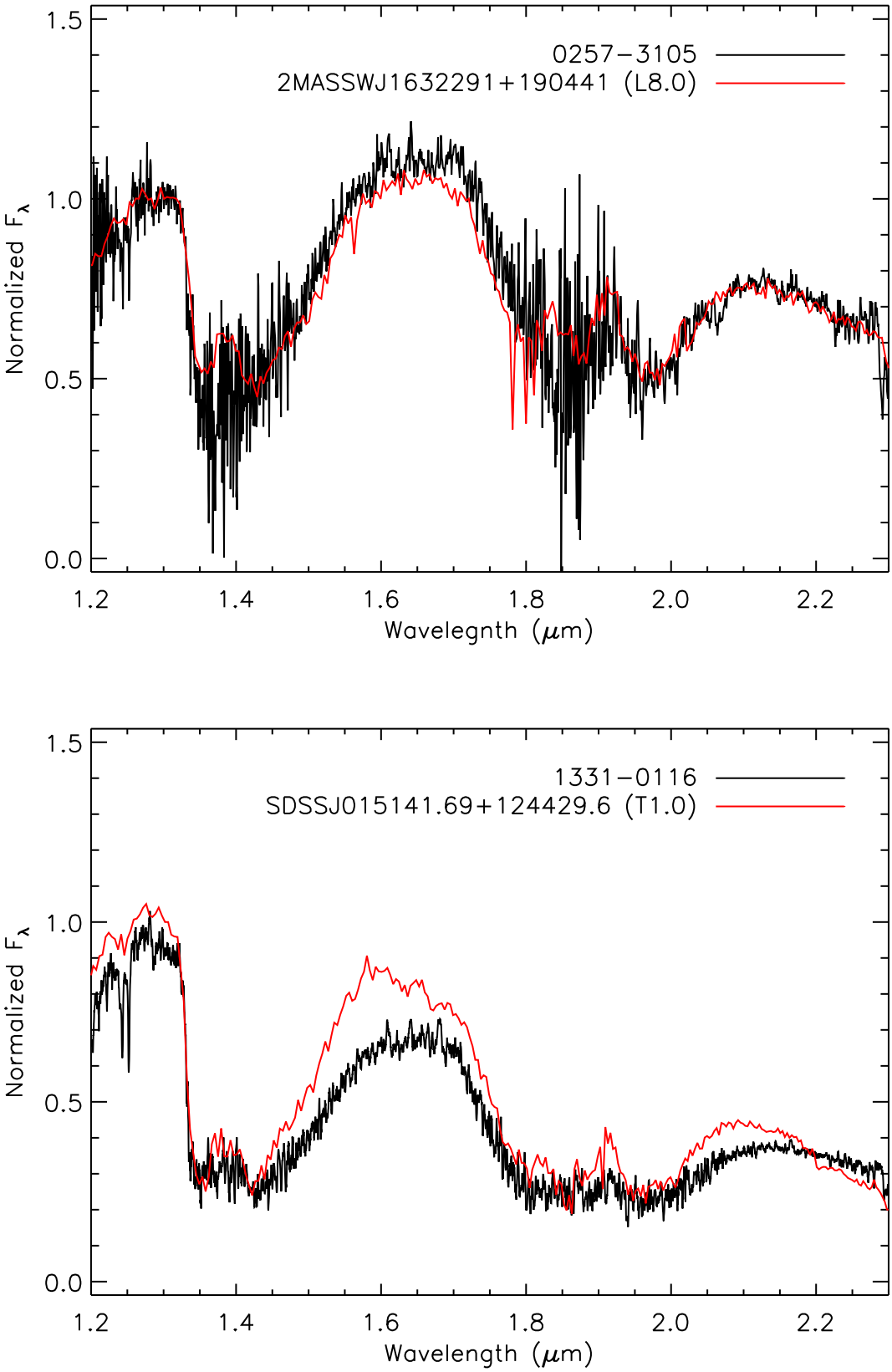


Fig. 2.8: Two examples of spectral fitting. *Top*: 0257-3105, with the best-fit standard template overplotted in red for comparison (the L8.0 2MASSW J1632291+190441). The standard reproduces very well all the spectral features of the target. *Bottom:* 1331-0116, with the best-fit standard template overplotted in red for comparison (the T1.0 SDSS J015141.69+124429.6). Despite being the best-fit template, the T1.0 does not match the specctrum of the target, which does not show any sign of methane absorption. For more details on the classification of this peculiar object see Section 2.6.6.

| Object short name | Instrument | Date of observation (DD-MM-YYYY) | Standard name | Standard type | Previous optical type | Previous NIR type | New NIR type | Ref. O,I |
|---|---|---|---|---|---|---|---|---|
| 0014-4844 | OSIRIS | 2012-09-08 | HIP3471 | A1V | L2.5pec | ... | L2.5±1 | 7,- |
| 0032-4405 | OSIRIS | 2011-08-30 | HD2811 | A3V | L0$\gamma$ | ... | L4 pec | 1,- |
| 0053-3631 | OSIRIS | 2012-09-08 | HIP6257 | A1V | L3.5 | ... | L4±1 | 7,- |
| 0058-0651 | OSIRIS | 2011-09-09 | HIP5164 | A1V | L0 | ... | L1 | 2,- |
| 0109-5100 | OSIRIS | 2011-09-08 | HIP8241 | A1V | M8.5 | L2 | M7 | 3,3 |
| 0128-5545 | OSIRIS | 2011-09-08 | HIP8241 | A1V | L2 | L1 | L1 | 4,5 |
| 0144-4844 | OSIRIS | 2012-09-08 | HIP10512 | A0V | L5 | ... | L5 | 16,- |
| 0147-4954 | OSIRIS | 2011-10-06 | HIP8241 | A1V | ... | ... | M9±1 | |
| 0218-3133 | OSIRIS | 2012-09-10 | HIP12786 | A1V | L3 | ... | L5.5 | 6,- |
| 0219-1939 | OSIRIS | 2011-09-10 | HD17224 | A0V | L1 | L2.5 | L1±1 | 3,3 |
| 0227-1624 | OSIRIS | 2012-11-02 | HIP14627 | A0V | L1 | ... | L0.5∓1 | 4,- |
| 0230-0953 | OSIRIS | 2011-10-06 | HIP10512 | A0V | ... | ... | L6 | |
| 0239-1735 | OSIRIS | 2011-09-10 | HD17224 | A0V | L0 | ... | M9 | 6,- |
| 0257-3105 | OSIRIS | 2011-10-06 | HR903 | A0V | L8 | ... | L8±1 | 7,- |
| 0357-4417 | OSIRIS | 2011-09-10 | HD28813 | A0V | L0$\beta^a$ | ... | L2 pec$^a$ | 1,- |
| 0539-0059 | OSIRIS | 2011-12-12 | HIP28449 | A0V | L5 | ... | L4±1 | 8,- |
| 0614-2019 | OSIRIS | 2011-10-07 | HIP31094 | A0V | ... | ... | L2 | |
| 0624-4521 | OSIRIS | 2012-03-03 | HD47925 | A0V | L5±1 | ... | L6 | 4,- |
| 0719-5050 | OSIRIS | 2009-02-14 | HD56980 | A0V | ... | ... | M4 | |
| 0719-5051 | OSIRIS | 2011-12-10 | HD60130 | A0V | L0 | ... | L0±1 | 4,- |
| 0829-1309 | OSIRIS | 2011-12-12 | HD73687 | A0V | L2 | ... | L2±1 | 3,- |
| 0832-0128 | OSIRIS | 2012-03-04 | HR3383 | A1V | L1.5 | ... | L1±1 | 2,- |
| 0835-0819 | OSIRIS | 2012-03-04 | HR3383 | A1V | L5 | ... | L4 | 6,- |
| 0909-0658 | OSIRIS | 2013-01-05 | HIP47249 | A1V | L0 | ... | L0±1 | 7,- |
| 0928-1603 | OSIRIS | 2009-02-14 | HIP45800 | A0V | L2 | ... | L2±1 | 2,- |
| 0953-1014 | OSIRIS | 2012-03-08 | HD86593 | A0V | L0 | ... | L2 | 13,- |
| 1004-1318 | OSIRIS | 2012-03-08 | HD86593 | A0V | L0 | ... | L1±1 | 14,- |

Continued on next page.

Continued from previous page.

| Object short name | Instrument | Date of observation (DD-MM-YYYY) | Standard name | Standard type | Previous optical type | Previous NIR type | New NIR type | Ref. O,I |
|---|---|---|---|---|---|---|---|---|
| 1004-3335 | OSIRIS | 2012-03-09 | HD89213 | A0V | L4 | ... | L5±1 | 15,- |
| LHS 5166 | OSIRIS | 2012-03-09 | HD89213 | A0V | ... | ... | M4 | |
| 1045-0149 | OSIRIS | 2013-01-05 | HIP54849 | A0V | L1 | ... | L2 | 15,- |
| 1059-2113 | OSIRIS | 2013-03-17 | HIP55830 | A0V | L1 | ... | L2 | 6,- |
| 1154-3400 | OSIRIS | 2013-03-07 | HIP61211 | A0V | L0 | ... | L3 | 7,- |
| 1246-3139 | OSIRIS | 2011-02-25 | HIP60819 | A0V | ... | ... | T2 | |
| 1331-0116 | XSHOOTER | 2011-06-07 | HIP68713 | A0V | L6 | L8±2.5 | L1 pec | 9,10 |
| 1404-3159 | XSHOOTER | 2011-06-05 | HIP065688 | B8V | T0[a] | T2.5[a] | T3[a] | 11,12 |
| 1438-1309 | OSIRIS | 2012-06-04 | HD132072 | A0V | L3±1 | ... | L3±1 | 2,- |
| 1753-6559 | SOFI | 2011-04-21 | HD168741 | A0V | L4±2 | ... | L4±1 | 4,- |
| 1928-4356 | OSIRIS | 2009-06-08 | HIP95464 | A0V | L4 | ... | L4 pec | 4,- |
| 1936-5502 | SOFI | 2011-04-21 | HD168741 | A0V | L5±1 | ... | L4 | 4,- |
| 2002-0521 | OSIRIS | 2012-06-04 | HIP98953 | A0V | L6 | ... | L7 | 13,- |
| 2011-6201 | XSHOOTER | 2011-06-05 | HD192510 | A0V | ... | ... | d/sdM8 | |
| 2023-5946 | XSHOOTER | 2011-06-05 | HD192510 | A0V | ... | ... | M8 | |
| 2045-6332 | OSIRIS | 2011-09-10 | HD197165 | A3V | ... | ... | L1±1 | |
| 2101-2944 | OSIRIS | 2011-04-29 | HIP103315 | A0V | ... | ... | L1 | |
| 2132-1452 | OSIRIS | 2011-08-30 | HD206703 | A3V | ... | ... | T4 | |
| 2148-6323 | XSHOOTER | 2011-06-06 | HIP097611 | B5V | ... | ... | L1 | |
| 2158-1550 | OSIRIS | 2012-06-04 | HD211278 | A0V | L4±1 | ... | L5 | 7,- |
| 2209-2711 | OSIRIS | 2011-06-11 | HD211278 | A0V | ... | ... | T2.5 | |
| 2213-2136 | OSIRIS | 2011-08-30 | HR8542 | A0V | L0$\gamma$ | ... | L2 pec | 1,- |
| 2310-1759 | OSIRIS | 2011-09-08 | HD219179 | A3V | L0±1 | L1 | L1±1 | 13,3 |
| 2318-1301 | OSIRIS | 2012-09-16 | HIP117734 | A1V | ... | ... | T5 | |
| 2346-5928 | OSIRIS | 2011-09-08 | HD224377 | A0V | ... | ... | M7 pec | |

Table 2.3: Summary of the observations. For each object we present the instrument used to obtain its spectrum, the date of observation, the telluric standard used and its spectral type, the previous optical and NIR classification of the target, our new NIR spectral classification, and the references to the previous types (optical and NIR). If not specified, the uncertainty on the new NIR type is 0.5. (*a*) Known unresolved binary, the reported type is the unresolved classification. The spectral types of the components are determined and discussed further in Section 2.3.3. Refs: (1) Cruz et al. (2009); (2) Kirkpatrick et al. (2000); (3) Lodieu et al. (2005); (4) Reid et al. (2008b); (5) Kendall et al. (2007); (6) Cruz et al. (2003); (7) Kirkpatrick et al. (2008); (8) Fan et al. (2000); (9) Hawley et al. (2002); (10) Knapp et al. (2004); (11) Looper et al. (2008a); (12) Looper et al. (2007); (13) Cruz et al. (2007); (14) Martín et al. (2010); (15) Gizis (2002); (16) Liebert et al. (2003).

In Figure 2.9 we plot the absolute 2MASS JHK$_s$ magnitudes as a function of spectral type. The targets presented here are plotted as red dots, while diamonds represent objects taken from the literature (see Dupuy & Liu, 2012, Table 9, for a complete census of ultracool dwarfs with measured parallaxes). For the literature sample, we use the NIR spectral type when available, otherwise we plot the optical spectral type. Our sample represents a significant increase in the number of objects with measured parallaxes and NIR spectral types at early types (L0-L4). Most of the previous parallax programs have indeed focused on the cooler, later-type targets.

We notice that the scatter in absolute magnitudes across the sequence is ∼1 mag on average but goes up to ∼2 mag between late-M and mid-L. The number of objects per spectral type, especially at early types, is high enough to allow us to identify the outliers (which are marked in Figure 2.9), and therefore the remaining scatter is most likely intrinsic to the sequence. The cause of such a spread can probably be found in the known mass-age degeneracy, typical of brown dwarfs. Objects of the same spectral type can have very different mass and age, and this would result in peculiar colours, but also in differences in the absolute magnitude of the dwarfs (e.g. Kirkpatrick, 2005, and references therein).

There are six outliers to the sequence, and they are marked in Figure 2.9. Two are the components of the brown dwarf + planet system 2MASSW J1207334−393254. This system is part of the TW Hydrae Association, with an age of $8^{+4}_{-3}$ Myr (Chauvin et al., 2004, and references therein). The primary is a M8.5 dwarf (Gizis, 2002), while for the planetary companion Patience et al. (2010) derived a spectral type in the range M8.5−L4. The primary is ∼1 mag overluminous compared to objects of similar spectral type, as expected for an object that has not contracted to its final radius (e.g. Burrows et al., 1997). On the other hand, the companion is more than 1 mag underluminous compared to objects of similar spectral type (i.e. in the M8.5−L4 range) and ∼2.5 mag underluminous when compared to standard models of giant planet evolution (Barman et al., 2011; Skemer et al., 2011). Faherty et al. (2012) have found similar results for other young, very red L dwarfs, and have speculated that the underluminosity can be due to a combination of two factors. One is the possibility that the low-gravity spectral classification has a different temperature relation compared to the standard classification scheme (Kirkpatrick et al., 1999; Burgasser et al., 2006a). The other factor is the possibility that young L dwarfs have dustier photospheres, that make them appear fainter and redder in the NIR compared to other field L dwarfs. SSSPM J1102−3431 is also ∼1 mag overluminous respect to the other M8.5 object plotted. This object is another young M dwarfs, known to be part of the TW Hydrae Association (Scholz et al., 2005; Teixeira et al., 2008). Another outlier is the peculiar red L9 dwarf WISEPA J164715.59+563208.2 (Kirkpatrick et al., 2011). This object pertains to the class of peculiar red, non-low-gravity L dwarfs, whose nature is not yet fully understood (e.g. Kirkpatrick et al., 2010). Finally, the last two outliers are our targets 1331-0116 and 2045-6332. The first one, 1331-0116, is a peculiar blue L1 dwarf, while 2045-6332 is overluminous and very red (J-K$_s$ = 1.41). We discuss further their properties in Section 2.6.6 and 2.6.10.

To better understand the properties of the objects in our sample, in Figure 2.10 we plot the absolute 2MASS JHK$_s$ magnitudes as a function of J-K$_s$. Colours and symbols follow the same convention as in Figure 2.9.

The objects follow the expected trend, moving towards redder colours as they become fainter because of thickening of the cloud decks in their atmospheres. Brown dwarfs then rapidly turn towards blue colours at the L-T transition, because of the

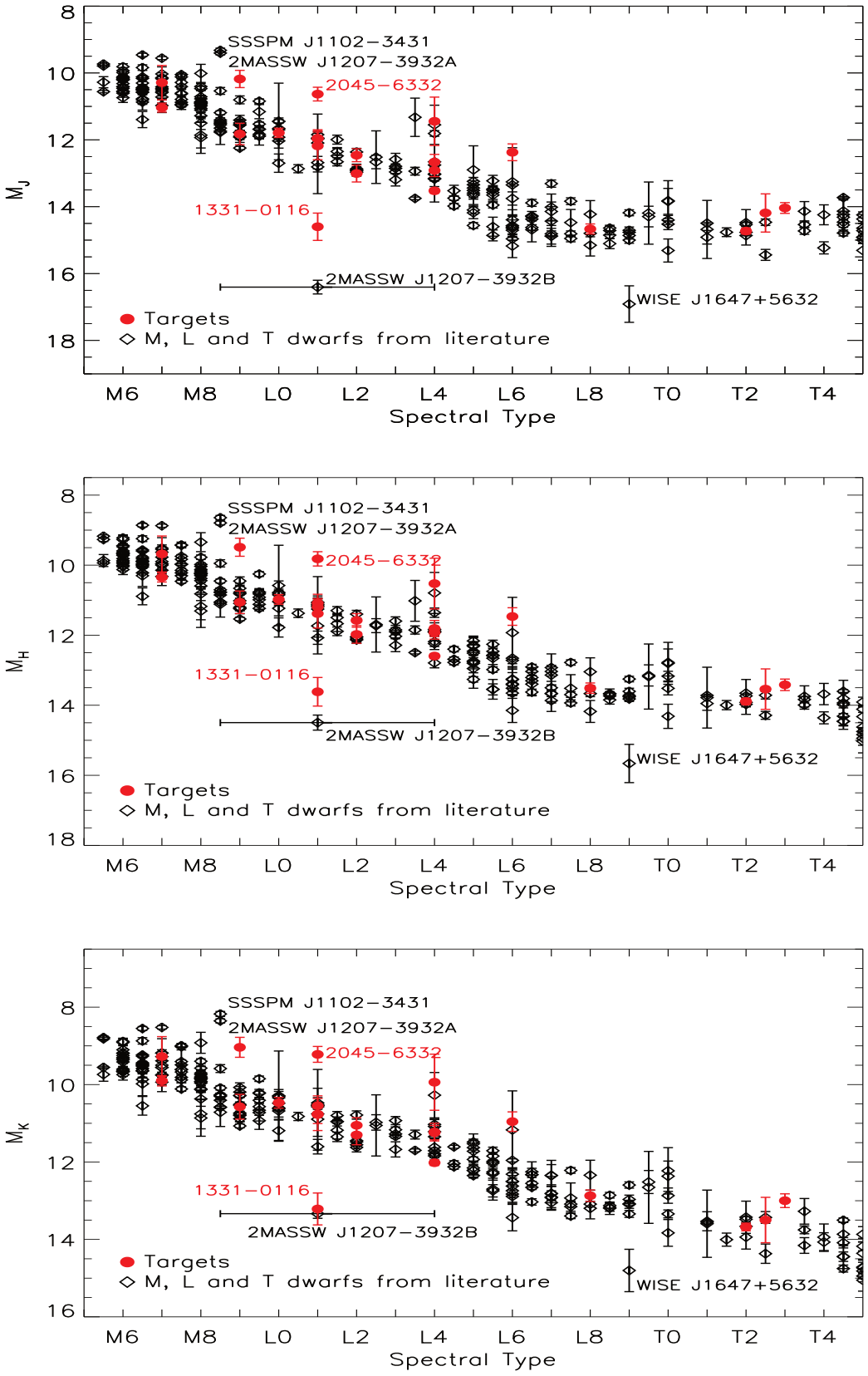


Fig. 2.9: Absolute 2MASS JHK magnitudes as a function of spectral type. The objects presented in this paper are plotted as red circles. Other objects are plotted as black diamonds. Magnitudes and parallaxes for the ultracool dwarfs are taken from Dupuy & Liu (2012). For literature objects, we plot the NIR spectral type when available, otherwise we use the optical spectral type. The outliers are marked, and more details about them can be found in the text (Section 2.3.2).

dust settling and the onset of the $CH_4$ and CIA absorption. The colour turnaround is sharper in the top panel of Figure 2.10 ($M_J$ vs. J-K) but also shows a larger scatter in absolute magnitude (almost 2 mag) compared to the bottom panel ($M_K$ vs. J-K) where the transition is shallower but the scatter is only ∼1 mag.

The outliers are labelled. Two are the already mentioned 2MASSW J1207334−393254B and WISEPA J164715.59+563208.2. Another outlier is the very red HD 1160B, a L dwarf companion to the young star HD 1160A (Nielsen et al., 2012). As stated above, the unusual red colours of these objects can be explained assuming an enhanced dust content in their atmospheres (e.g. Faherty et al., 2012). Another two outliers are the unusually blue SSSPM J1013−1356 and 2MASS J16262034+3925190, both known to be subdwarfs (sdM9.5 and sdL4 respectively, Faherty et al., 2009). Their blue colour are most probably due to the reduced cloud opacity (which affects especially the J-band) due to their low metallicity (e.g. Faherty et al., 2012). Finally, the last outlier is our target 2045-6332, which is the most luminous L1. Its very red J-$K_s$ could be an indication of low surface gravity, therefore of youth. We discuss further the nature of this object in Section 2.6.10.

In Table 2.4 we present the spectral indices calculated for our targets. The indices are those defined in Burgasser et al. (2006a) and Burgasser et al. (2010). The indices are plotted also in Figure 2.11, where we show $H_2O$-H and $H_2O$-K as a function of spectral type (top two panels) and $CH_4$-H and $CH_4$-K as a function of spectral type. Our targets are plotted as filled circles, while literature objects are overplotted as open circles for comparison. The literature objects are taken from the SpeX-Prism library. We can see that the $H_2O$-H and $H_2O$-K correlate very well with the fit-based spectral type, with only one outstanding outlier to the sequence, which is once again 1331-0116. Its indices have values that are typical of much later type objects (L8-T0) because of the unusually strong $H_2O$ absorption bands showed by its spectrum. The $CH_4$-H and $CH_4$-K indices correlates with the spectral type only for the late-L and T dwarfs (i.e. from L8 onward). We also note that the scatter is larger compared to the $H_2O$ indices. The only outlier to the sequence is 1404-3159, whose unusual position in the bottom right plot of Figure 2.11 is due to its binarity. In the $K$-band, the early type component of the binary dominates, and its methane absorption is less prominent than in the late type component, and also weaker than it would be in a single object of type T3. The discrepancy is not present in the $CH_4$-H plot because in the $H$-band the contribution to the total flux coming from the two components is almost equal (similarly for the $H_2O$-H and $H_2O$-K plots).

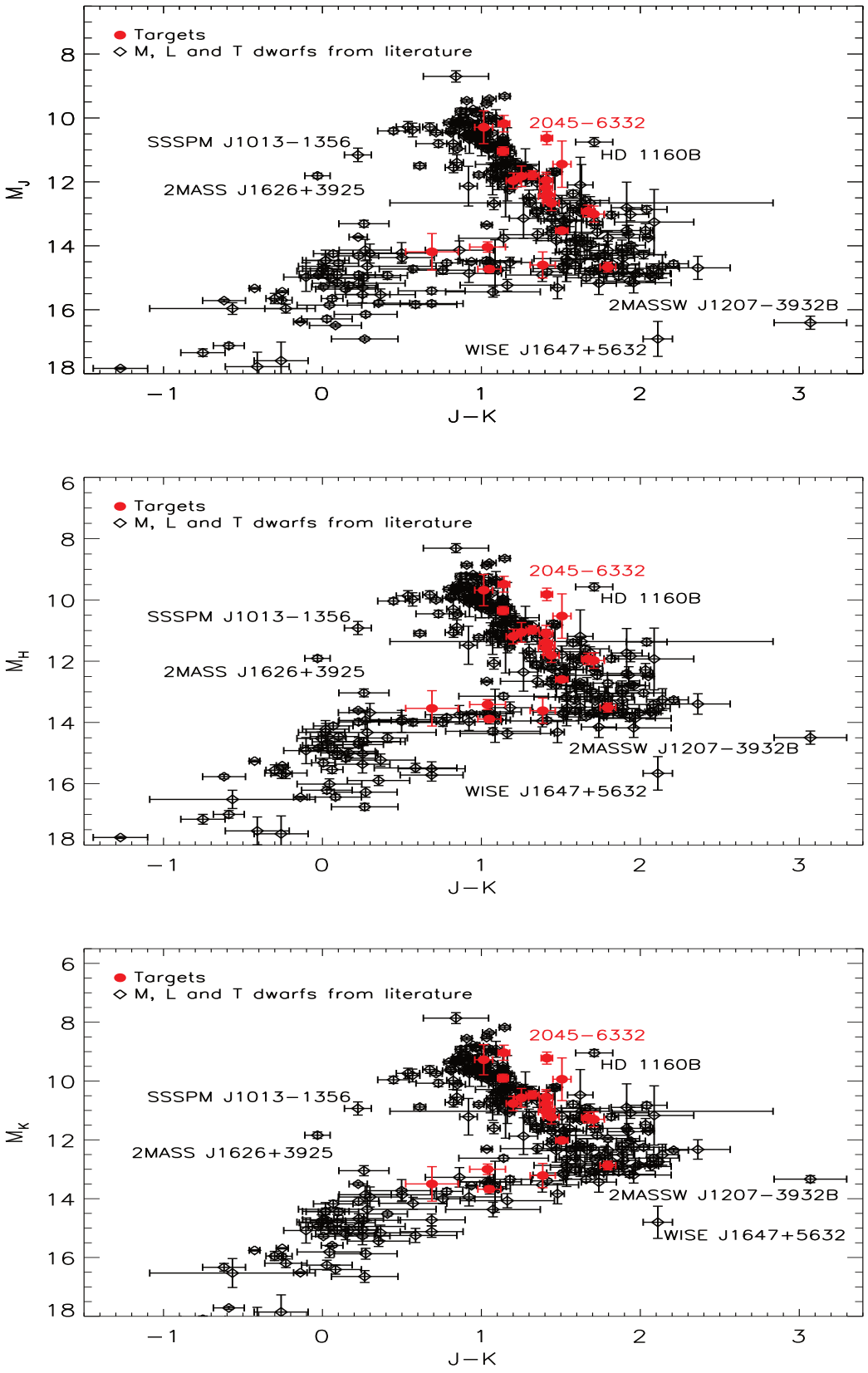


Fig. 2.10: Absolute 2MASS JHK magnitudes as a function of J-K. Colours and symbols follow the same convention as in Figure 2.9. Magnitudes and parallaxes for the ultracool dwarfs are taken from Dupuy & Liu (2012). The outliers are marked, and more details about them can be found in the text (Section 2.3.2).

| Object short name | $H_2O$-J | $H_2O$-H | $H_2O$-K | $CH_4$-J | $CH_4$-H | $CH_4$-K | K/J | H-dip |
|---|---|---|---|---|---|---|---|---|
| 0014-4844 | ... | 0.772 ± 0.009 | 0.944 ± 0.011 | 0.862 ± 0.016 | 1.078 ± 0.014 | 1.004 ± 0.005 | 0.461 ± 0.005 | 0.491 ± 0.006 |
| 0032-4405 | ... | 0.678 ± 0.010 | 1.082 ± 0.029 | 0.998 ± 0.015 | 1.182 ± 0.011 | 1.026 ± 0.014 | 0.486 ± 0.006 | 0.502 ± 0.005 |
| 0053-3631 | ... | 0.747 ± 0.009 | 0.935 ± 0.012 | 0.860 ± 0.015 | 1.091 ± 0.016 | 1.033 ± 0.007 | 0.526 ± 0.006 | 0.495 ± 0.007 |
| 0058-0651 | ... | 0.825 ± 0.007 | 1.062 ± 0.023 | 0.876 ± 0.011 | 1.053 ± 0.007 | 1.129 ± 0.011 | 0.434 ± 0.005 | 0.486 ± 0.004 |
| 0109-5100 | ... | 1.013 ± 0.006 | 1.239 ± 0.020 | 0.872 ± 0.010 | 0.982 ± 0.006 | 1.113 ± 0.005 | 0.311 ± 0.002 | 0.481 ± 0.004 |
| 0128-5545 | ... | 0.842 ± 0.008 | 1.063 ± 0.026 | 0.875 ± 0.015 | 1.017 ± 0.008 | 0.971 ± 0.008 | 0.473 ± 0.005 | 0.486 ± 0.005 |
| 0144-0716 | ... | 0.778 ± 0.011 | 0.966 ± 0.010 | 0.870 ± 0.014 | 1.025 ± 0.016 | 0.967 ± 0.006 | 0.623 ± 0.006 | 0.477 ± 0.007 |
| 0147-4954 | ... | 0.915 ± 0.004 | 1.165 ± 0.017 | 0.963 ± 0.013 | 1.028 ± 0.005 | 1.087 ± 0.005 | 0.424 ± 0.002 | 0.497 ± 0.003 |
| 0218-3133 | ... | 0.701 ± 0.009 | 0.930 ± 0.018 | 0.887 ± 0.017 | 1.124 ± 0.014 | 1.061 ± 0.010 | 0.565 ± 0.007 | 0.487 ± 0.006 |
| 0219-1939 | ... | 0.817 ± 0.008 | 1.027 ± 0.018 | 0.846 ± 0.012 | 1.022 ± 0.007 | 1.036 ± 0.008 | 0.370 ± 0.004 | 0.484 ± 0.004 |
| 0227-1624 | ... | 0.907 ± 0.010 | 1.108 ± 0.013 | 0.968 ± 0.012 | 1.009 ± 0.016 | 1.033 ± 0.006 | 0.458 ± 0.004 | 0.491 ± 0.007 |
| 0230-0953 | ... | 0.775 ± 0.006 | 0.982 ± 0.010 | 0.924 ± 0.014 | 1.049 ± 0.009 | 1.071 ± 0.006 | 0.648 ± 0.006 | 0.486 ± 0.005 |
| 0239-1735 | ... | 0.902 ± 0.006 | 1.194 ± 0.020 | 0.924 ± 0.011 | 1.032 ± 0.006 | 1.021 ± 0.010 | 0.421 ± 0.004 | 0.495 ± 0.003 |
| 0257-3105 | ... | 0.707 ± 0.006 | 0.833 ± 0.010 | 0.835 ± 0.014 | 1.058 ± 0.006 | 0.870 ± 0.005 | 0.731 ± 0.006 | 0.515 ± 0.003 |
| 0357-4417 | ... | 0.780 ± 0.006 | 1.090 ± 0.016 | 0.884 ± 0.013 | 1.153 ± 0.006 | 1.134 ± 0.010 | 0.616 ± 0.005 | 0.498 ± 0.003 |
| 0539-0059 | ... | 0.714 ± 0.007 | 0.905 ± 0.013 | 0.867 ± 0.018 | 1.081 ± 0.010 | 0.952 ± 0.007 | 0.485 ± 0.005 | 0.490 ± 0.005 |
| 0614-2019 | ... | 0.802 ± 0.010 | 1.022 ± 0.019 | 0.941 ± 0.018 | 1.070 ± 0.011 | 1.096 ± 0.010 | 0.468 ± 0.006 | 0.487 ± 0.006 |
| 0624-4521 | ... | 0.763 ± 0.008 | 0.996 ± 0.012 | 0.830 ± 0.021 | 1.089 ± 0.007 | 1.005 ± 0.007 | 0.721 ± 0.008 | 0.491 ± 0.003 |
| 0719-5051A | ... | 1.057 ± 0.003 | 1.282 ± 0.014 | 0.944 ± 0.003 | 0.968 ± 0.002 | 0.910 ± 0.002 | 0.282 ± 0.001 | 0.503 ± 0.001 |
| 0719-5051B | ... | 0.902 ± 0.009 | 1.115 ± 0.024 | 0.881 ± 0.015 | 1.004 ± 0.009 | 0.971 ± 0.011 | 0.381 ± 0.005 | 0.482 ± 0.005 |
| 0829-1309 | ... | 0.837 ± 0.007 | 1.013 ± 0.013 | 0.918 ± 0.014 | 1.032 ± 0.011 | 1.028 ± 0.006 | 0.465 ± 0.004 | 0.482 ± 0.006 |
| 0832-0128 | ... | 0.847 ± 0.009 | 1.061 ± 0.014 | 0.854 ± 0.015 | 1.057 ± 0.007 | 1.045 ± 0.012 | 0.468 ± 0.005 | 0.485 ± 0.004 |
| 0835-0819 | ... | 0.753 ± 0.008 | 0.964 ± 0.018 | 0.843 ± 0.016 | 1.092 ± 0.008 | 0.988 ± 0.013 | 0.476 ± 0.006 | 0.498 ± 0.005 |
| 0909-0658 | ... | 0.860 ± 0.011 | 1.129 ± 0.017 | 0.929 ± 0.016 | 1.037 ± 0.012 | 1.060 ± 0.008 | 0.413 ± 0.004 | 0.494 ± 0.008 |
| 0928-1603 | ... | 0.774 ± 0.013 | 1.077 ± 0.020 | 0.935 ± 0.024 | 1.055 ± 0.010 | 1.062 ± 0.008 | 0.527 ± 0.009 | 0.484 ± 0.005 |
| 0953-1014 | ... | 0.807 ± 0.012 | 1.112 ± 0.023 | 0.911 ± 0.014 | 1.088 ± 0.015 | 1.134 ± 0.010 | 0.503 ± 0.005 | 0.502 ± 0.006 |
| 1004-1318 | ... | 0.792 ± 0.010 | 0.999 ± 0.022 | 0.820 ± 0.022 | 1.026 ± 0.009 | 0.998 ± 0.009 | 0.474 ± 0.005 | 0.483 ± 0.005 |

Continued on next page.

Continued from previous page.

| Object short name | $H_2O$-J | $H_2O$-H | $H_2O$-K | $CH_4$-J | $CH_4$-H | $CH_4$-K | K/J | H-dip |
|---|---|---|---|---|---|---|---|---|
| 1004-3335 | ... | 0.740 ± 0.012 | 0.965 ± 0.031 | 0.851 ± 0.017 | 1.064 ± 0.015 | 1.088 ± 0.019 | 0.561 ± 0.009 | 0.478 ± 0.007 |
| LHS5166 | ... | 1.075 ± 0.004 | 1.334 ± 0.019 | 0.925 ± 0.005 | 0.954 ± 0.003 | 0.919 ± 0.003 | 0.299 ± 0.001 | 0.500 ± 0.002 |
| 1045-0149 | ... | 0.835 ± 0.006 | 1.048 ± 0.011 | 0.930 ± 0.012 | 1.072 ± 0.010 | 1.081 ± 0.006 | 0.529 ± 0.005 | 0.485 ± 0.005 |
| 1059-2113 | ... | 0.760 ± 0.009 | 0.965 ± 0.017 | 0.872 ± 0.016 | 1.036 ± 0.007 | 1.040 ± 0.010 | 0.487 ± 0.006 | 0.489 ± 0.004 |
| 1154-3400 | ... | 0.800 ± 0.006 | 1.075 ± 0.013 | 0.920 ± 0.023 | 1.080 ± 0.007 | 1.089 ± 0.007 | 0.473 ± 0.004 | 0.498 ± 0.004 |
| 1246-3139 | ... | 0.578 ± 0.009 | 0.767 ± 0.046 | 0.747 ± 0.021 | 0.960 ± 0.008 | 0.682 ± 0.030 | 0.376 ± 0.005 | 0.529 ± 0.003 |
| 1331-0116 | 0.721 ± 0.010 | 0.645 ± 0.007 | 0.800 ± 0.015 | 0.713 ± 0.010 | 1.079 ± 0.006 | 0.928 ± 0.006 | 0.375 ± 0.004 | 0.512 ± 0.003 |
| 1404-3159 | 0.444 ± 0.006 | 0.509 ± 0.006 | 0.772 ± 0.010 | 0.554 ± 0.006 | 0.729 ± 0.003 | 0.651 ± 0.005 | 0.311 ± 0.002 | 0.453 ± 0.002 |
| 1438-1309 | ... | 0.803 ± 0.014 | 0.977 ± 0.022 | 0.868 ± 0.017 | 1.038 ± 0.010 | 1.022 ± 0.012 | 0.538 ± 0.008 | 0.480 ± 0.006 |
| 1753-6559 | 0.843 ± 0.015 | 0.741 ± 0.014 | ... | 0.888 ± 0.019 | ... | ... | ... | ... |
| 1928-4356 | ... | 0.735 ± 0.007 | 0.911 ± 0.011 | 0.858 ± 0.020 | 1.066 ± 0.005 | 1.018 ± 0.006 | 0.400 ± 0.004 | 0.484 ± 0.003 |
| 1936-5502 | 0.757 ± 0.015 | 0.732 ± 0.009 | ... | 0.845 ± 0.024 | ... | ... | ... | ... |
| 2002-0521 | ... | 0.660 ± 0.011 | 0.908 ± 0.013 | 0.815 ± 0.018 | 1.182 ± 0.011 | 1.066 ± 0.007 | 0.720 ± 0.008 | 0.504 ± 0.005 |
| 2011-6201 | 0.993 ± 0.004 | 0.860 ± 0.003 | 1.142 ± 0.008 | 0.840 ± 0.005 | 1.091 ± 0.003 | 1.065 ± 0.004 | 0.281 ± 0.001 | 0.504 ± 0.001 |
| 2023-5946 | 1.016 ± 0.002 | 0.913 ± 0.002 | 1.158 ± 0.004 | 0.913 ± 0.002 | 1.037 ± 0.001 | 1.049 ± 0.002 | 0.360 ± 0.001 | 0.498 ± 0.001 |
| 2045-6332 | ... | 0.863 ± 0.006 | 1.189 ± 0.016 | 0.895 ± 0.011 | 1.087 ± 0.006 | 1.089 ± 0.007 | 0.394 ± 0.003 | 0.499 ± 0.003 |
| 2101-2944 | ... | 0.817 ± 0.010 | 1.069 ± 0.022 | 0.957 ± 0.017 | 1.033 ± 0.010 | 1.077 ± 0.012 | 0.360 ± 0.005 | 0.501 ± 0.005 |
| 2132-1452 | ... | 0.395 ± 0.011 | 0.640 ± 0.031 | 0.550 ± 0.019 | 0.627 ± 0.010 | 0.358 ± 0.017 | 0.312 ± 0.005 | 0.441 ± 0.007 |
| 2148-6323 | 0.895 ± 0.007 | 0.827 ± 0.004 | 1.013 ± 0.008 | 0.890 ± 0.006 | 1.018 ± 0.005 | 1.034 ± 0.005 | 0.446 ± 0.002 | 0.479 ± 0.003 |
| 2158-1550 | ... | 0.683 ± 0.010 | 0.877 ± 0.013 | 0.827 ± 0.016 | 1.115 ± 0.007 | 1.041 ± 0.007 | 0.587 ± 0.006 | 0.486 ± 0.005 |
| 2209-2711 | ... | 0.463 ± 0.009 | 0.699 ± 0.047 | 0.704 ± 0.019 | 0.773 ± 0.010 | 0.579 ± 0.031 | 0.261 ± 0.007 | 0.448 ± 0.009 |
| 2213-2136 | ... | 0.805 ± 0.012 | 1.183 ± 0.025 | 0.973 ± 0.015 | 1.201 ± 0.009 | 1.086 ± 0.012 | 0.637 ± 0.007 | 0.519 ± 0.004 |
| 2310-1759 | ... | 0.886 ± 0.008 | 1.140 ± 0.017 | 0.899 ± 0.013 | 1.026 ± 0.007 | 1.031 ± 0.008 | 0.423 ± 0.004 | 0.490 ± 0.004 |
| 2318-1301 | ... | 0.386 ± 0.015 | 0.551 ± 0.025 | 0.484 ± 0.019 | 0.457 ± 0.013 | 0.212 ± 0.017 | 0.243 ± 0.004 | 0.348 ± 0.009 |
| 2346-5928 | ... | 0.945 ± 0.012 | 1.149 ± 0.030 | 0.843 ± 0.011 | 0.990 ± 0.008 | 0.951 ± 0.008 | 0.265 ± 0.002 | 0.493 ± 0.004 |

Table 2.4: Spectral indices for the objects in the sample. The indices presented here are defined in Burgasser et al. (2006a) and Burgasser et al. (2010).

### 2.3.3 Unresolved Binaries

We also performed a search for unresolved binaries within our sample, using the spectral indices and the criteria defined by Burgasser et al. (2010, see Section 3.4.2 of this manuscript for more details). Two of the objects in the sample are known unresolved binaries: 1404-3159 (Looper et al., 2008a) is indeed identified as a strong candidate by the selection criteria; 0357-4417 (Bouy et al., 2003) is not selected as a candidate, a result which is not surprising, as this is an early-L pair, and the technique used is sensitive mostly to L-T transition systems. None of the other objects in our sample match the criteria defined.

We estimated the spectral types of the components of these two systems by fitting their spectra with a set of synthetic unresolved templates. We created the synthetic binaries by combining the spectra taken from the already mentioned SpeX-Prism library. The spectra were normalized to one at 1.28$\mu$m, and then scaled to the appropriate flux level using the $M_J$−Spectral type relation presented in Marocco et al. (2010). The results of this fitting are presented in Figure 2.12. For each target we plot the observed spectrum (in black), the best fit standard template (green), the best fit combined template (red) and its two components (blue and yellow). For 1404-3159 we obtain a best fit with a L9+T5 ($\pm$1) template, which is in good agreement with the previous results obtained by Looper et al. 2008a (T1+T5), Burgasser et al. 2010 (T0+T5), and Dupuy & Liu 2012 (L9+T5). For 0357-4417, our deconvolution gives a best fit of L4.5+L5 ($\pm$1). Resolved optical spectroscopy obtained by Martín et al. (2006) indicates that the system is likely to be composed of a M9 and an L1. We note however that this object was also identified as a probable young object (Reid et al., 2008b). Its NIR spectrum indeed shows peculiarities associated with young ages, especially a triangular shaped H band and an enhancement of the flux in the K band. We therefore conclude that this is a young binary system, and we note that our best fit binary template does not reproduce very well the shape of the H band peak. This is because the spectra we used to create our synthetic binaries are mostly field-aged objects.

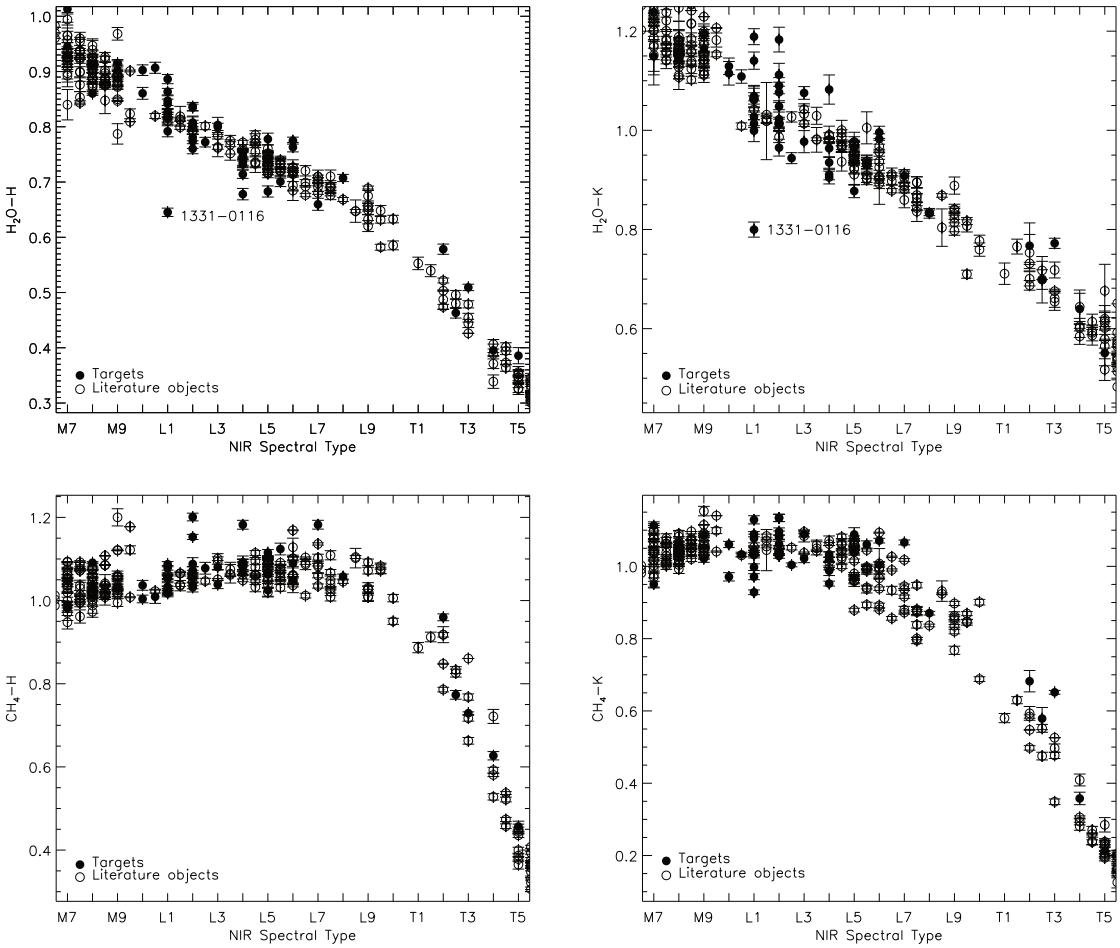


Fig. 2.11: The spectral indices derived for our targets as a function of their spectral type. The indices presented here are defined in Burgasser et al. (2006a) and Burgasser et al. (2010).

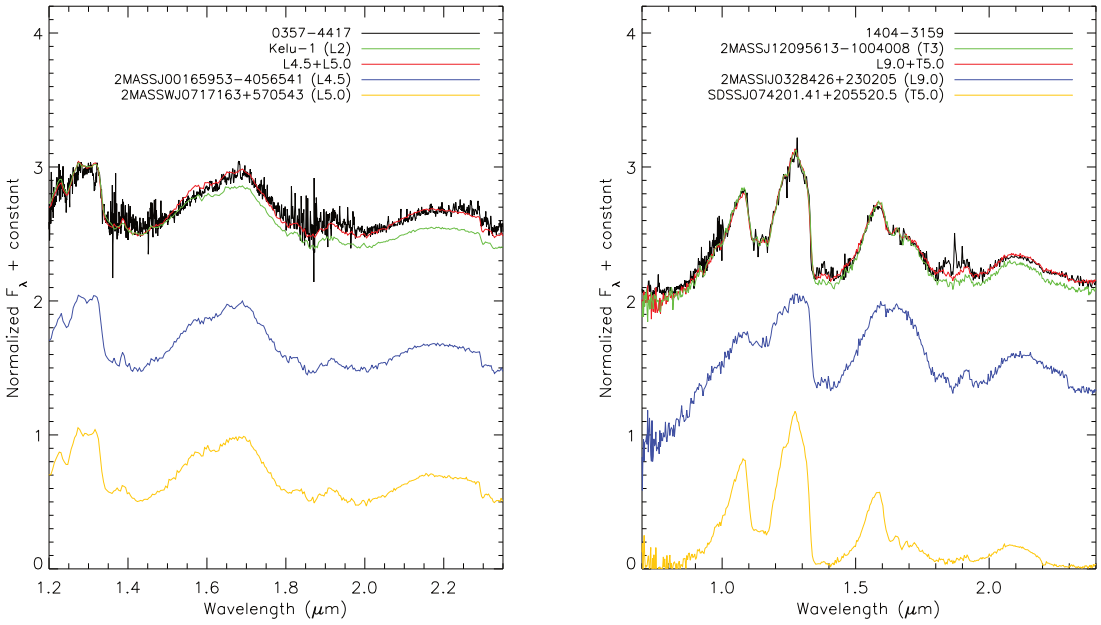


Fig. 2.12: The spectral deconvolution of the unresolved binaries 0357-4417 (left panel) and 1404-3159 (right panel). On each panel we plot the observed spectrum (in black), the best fit standard template (green), the best fit combined template (red) and its two components (blue and yellow).

## 2.4 Kinematics

The analysis of the kinematics properties of stars can provide useful insights on their nature. It is well known that different populations of stars (i.e. thin disk, thick disk, and halo members) have different velocity distributions in the U,V,W parameter space. Determining the three components of the Galactic velocity of our targets can therefore lead to the determination of their membership. To do this we follow the approach of Bensby et al. (2003). In this contribution the authors find that the distribution of the three different stellar populations in the solar neighborhood are defined by a three-dimensional gaussian:

$$f(U,V,W) = k \cdot exp\left(-\frac{U^2}{2\sigma_U^2} - \frac{(V-V_{asym})^2}{2\sigma_V^2} - \frac{W^2}{2\sigma_W^2}\right) \tag{2.2}$$

where

$$k = \frac{1}{(2\pi)^{3/2}\sigma_U\sigma_V\sigma_W} \tag{2.3}$$

and $(\sigma_U, \sigma_V, \sigma_W)$ are the characteristic velocity dispersions, $V_{\rm asym}$ is the velocity lag for each component behind the galactic rotation.

So if we determine U, V and W for each target, the probability to belong to one of the components (e.g. the thin disk) is given by:

$$P_{Tn} = \frac{X_{Tn}f_{Tn}}{X_{Tn}f_{Tn} + X_{Tk}f_{Tk} + X_H f_H} \tag{2.4}$$

where $f_{Tn}$, $f_{Tk}$, $f_H$ are the velocity distribution $f(U,V,W)$ for thin disk, thick disk, and halo respectively, and $\mathrm{X}_{Tn}$, $\mathrm{X}_{Tk}$, $\mathrm{X}_H$ are the observed fraction of objects of each component. The values adopted for $X, \sigma_U, \sigma_V, \sigma_W$ and $V_{\rm asym}$ for each component are those listed in Bensby et al. (2003).

However, to determine the components of the galactic velocity of our objects, we need the radial velocity of the dwarfs. Given that none of our targets has radial velocity measurements, to compute the membership probabilities we follow this approach: first we assume that our objects follow the radial velocity distribution of brown dwarf in the solar neighborhood, which is a gaussian profile centered on 0 km s$^{-1}$ with a sigma of 34 km s$^{-1}$ (e.g. Schmidt et al., 2010b). Then for each target we assume 10000 radial velocity values randomly taken from the gaussian distribution, and for each of these values we calculate a value for $P_{Tn}$, $P_{Tk}$, and $P_H$. The uncertainties on the parallax and proper motion are treated the same way, so drawing 10000 values from a gaussian distribution centered on the values given in Table 2.2, and with the associated sigma. Finally, we assume the average value as the membership probability of each target.

The probabilities obtained are listed in Table 2.5. As we can see, all of our targets are disk members ($P_{Tn} + P_{Tk} > 99\%$).

We note that the sample of brown dwarfs studied in Schmidt et al. (2010b) is formed mostly of thin disk objects (90%). The sigma of the distribution derived in that paper is therefore dictated by the thin disk dwarfs, and it can introduce a bias in the results presented in our Table 2.5. So we tested the membership assigned with our simulation using other two purely kinematic methods.

One is the classical Toomre diagram as used by Nissen (2004) to discriminate between thin disk, thick disk and halo stars. For each of our targets we used the parallaxes and proper motions presented here and we calculated a range for their $UVW$ velocities,

| Object | $P_{\rm Tn}$ | $P_{\rm Tk}$ | $P_{\rm H}$ |
|---|---|---|---|
| 0032-4405 | 85 | 15 | 0 |
| 0058-0651 | 90 | 10 | 0 |
| 0109-5100 | 90 | 10 | 0 |
| 0147-4954 | 77 | 23 | 0 |
| 0219-1939 | 89 | 11 | 0 |
| 0230-0953 | 90 | 10 | 0 |
| 0239-1735 | 89 | 11 | 0 |
| 0257-3105 | 88 | 12 | 0 |
| 0539-0059 | 86 | 14 | 0 |
| 0614-2019 | 85 | 15 | 0 |
| 0719-5051B | 90 | 10 | 0 |
| 0928-1603 | 84 | 16 | 0 |
| 1246-3139 | 87 | 13 | 0 |
| 1331-0116 | 62 | 38 | 0 |
| 1404-3159 | 88 | 12 | 0 |
| 1753-6559 | 85 | 15 | 0 |
| 1936-5502 | 83 | 17 | 0 |
| 2045-6332 | 86 | 14 | 0 |
| 2209-2711 | 88 | 12 | 0 |
| 2310-1759 | 86 | 13 | 0 |
| 2346-5928 | 73 | 27 | 0 |

Table 2.5: The membership probability for our targets. $P_{\rm Th}$, $P_{\rm Tk}$, and $P_{\rm H}$ are the probabilities of a brown dwarf being a thin disk, thick disk, or a halo object respectively.

assuming that their radial velocities are in a conservative range of -100/+100 km s$^{-1}$. The results are shown in the left panel of Figure 2.13. The $UVW$ ranges obtained result in an almost parabolic curve for each target. The dashed circles represent the boundaries between thin disk and thick disk stars (inner circle) and between thick disk and halo stars (outer circle). All except two of the targets fall mostly into the thin disk selection area, a result which is consistent with the high thin disk probability derived with the previous method. The two exceptions are 1331-0116 and 2346-5928 whose velocity ranges fall mostly into the thick disk selection area, consistently with their slightly higher probability of being thick disk objects ($P_{\rm Tk}$ = 38% and 27% respectively). We note, however, that 0147-4954 despite having similar $P_{\rm Tk}$ is instead among the rest of the sample, with its velocity ranges falling mostly into the thin disk selection area.

The second method we used is a direct comparison of the $UVW$ velocity ranges obtained with the velocity ellipsoids defined in Bensby et al. (2003). The results are shown in the right panel of Figure 2.13. The memberships assigned based on this criteria are consistent with those obtained by the Toomre diagram, with 2346-5928 falling mostly inside the thick disk ellipsoid, and 1331-0116 falling just outside of the thick disk ellipsoid, but being consistent with a thick disk membership when we consider the uncertainties on the proper motion and parallax.

We also used the kinematics information to check for the possible membership of our targets to one of the known young moving groups (hereafter MG). In order to do this we followed the method described in Clarke et al. (2010), that we summarize here.

We considered five MGs: the Pleiades, Castor, Hyades, Sirius (also known as Ursa

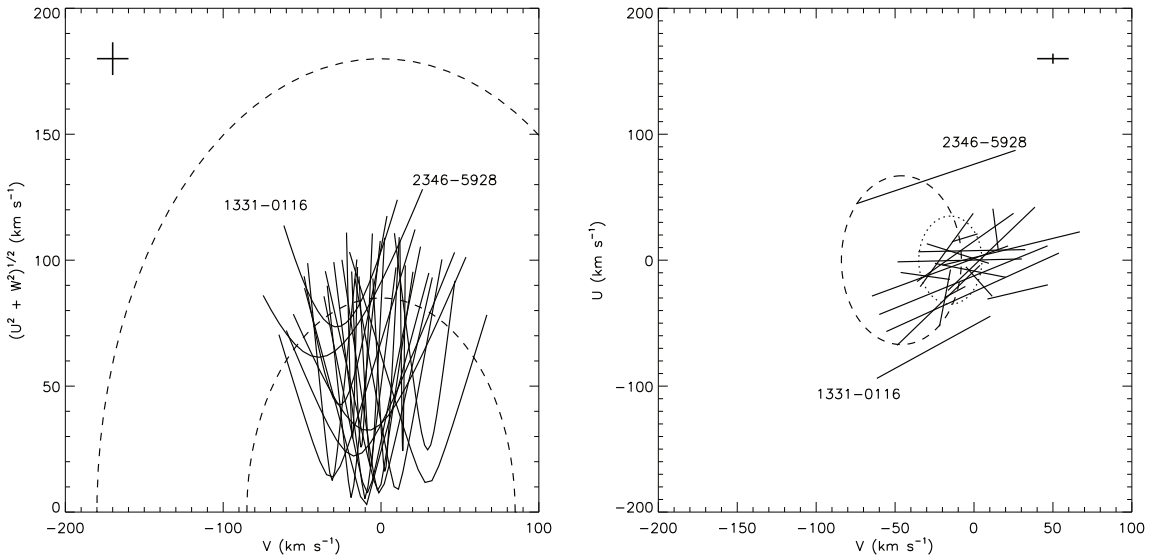


Fig. 2.13: The kinematics of the sample. *Left panel*: Toomre diagram. The solid lines represent the velocity ranges of each brown dwarf, obtained assuming a radial velocity range of -100/+100 km s$^{-1}$. The dashed circles are the boundary between thin disk and thick disk stars (inner circle) and between thick disk and halo stars (outer circle), as used by Nissen (2004). *Right panel*: $U-V$ plot showing the velocity ranges obtained for our targets. Overplotted for reference are the velocity ellipsoids obtained by Bensby et al. (2003) for thin disk (dotted) and thick disk (dashed) respectively. In each plot the outliers are labelled. Typical uncertainties are shown in the top-left and top-right corner, respectively.

Major) and IC2391. For each of our targets, using the measured proper motions, we calculated the corresponding proper motion towards the convergent point of each moving group ($\mu_{\rm tcp}$) and the proper motion perpendicular to that direction ($\mu_{\rm pcp}$) using the equations derived by Reid (1992). For each MG, we allowed for a scatter in velocity of $\pm$5 km s$^{-1}$ to take into account the intrinsic scatter of the MG and the additional scatter due to gravitational interaction of the MG members with disk stars (disk heating). We converted the velocity scatter into a proper motion scatter using our measured parallaxes. Finally, an object was considered as a MG candidate member if its $\mu_{\rm pcp}$ was less than the estimated scatter or if its 1$\sigma$ interval overlapped with the scatter. Given that we do not have any radial velocity measurement for our targets, we can only classify them as candidate members.

Eleven of the objects presented here are candidate members of at least one of the MGs considered. For each of them we used the $UVW$ velocities determined above (i.e. assuming a $V_{\rm rad}$ in the -100/+100 km s$^{-1}$ range), and applied the selection criteria defined in Clarke et al. 2010 (see their Figures 5 and 6). This allowed us to further assess the membership of the candidates, and also to derive a $V_{\rm rad}$ range for which the objects would be a member of the MG. Two of our targets passed this second selection: 0032-4405 and 2209-2711. They are both candidate members of the Pleiades and they require their $V_{\rm rad}$ to be in the range 5$-$25 and 10$-$30 km s$^{-1}$ respectively to be members of the MG. We will discuss further their properties in Section 2.6.

## 2.5 Physical parameters

The knowledge of the distances to our objects allows us to further investigate their nature, determining their physical properties such as bolometric luminosity ($L_{\rm bol}$) and effective temperature ($T_{\rm eff}$).

We determined the effective temperature via model fitting of the observed spectra, using the new version of the atmospheric models presented in Allard et al. (2011, hereafter BT-Settl). We followed three different approaches.

One approach (hereafter method 1) is to scale each model to match the observed flux using the geometric scaling factor, given by the ratio of the distance over the radius of the object squared. We do not know the radii of our targets, but we can assume they all have R = 1.0±0.2 $R_{\rm Jup}$. The evolutionary models in fact show that brown dwarfs tend to contract quite quickly (∼500 Myr) and reach similar final radii, independent of their mass (e.g. Baraffe et al., 1998). We then determined the best fit model via $\chi^2$ fitting. This method makes use of the astrometric information, but relies on a strong assumption on the radius. This can introduce a bias especially for young objects, which radii can be systematically larger than the assumed one. The random error on the temperature is in most cases dominated by the uncertainty on the radius.

The second approach (hereafter method 2) does not use the parallax but scales each model using the measured infrared photometry (2MASS JHK$_s$ and *WISE* W1-W2-W3-W4) and then determines the best fit model via $\chi^2$ fitting. The used scaling factor is the median of the seven values given by the magnitudes. In this case we do not rely on any assumption regarding the radii of the targets, but the use of the photometry can introduce other biases. Mostly, in the case of unresolved binaries, the photometric scaling factor would bias the derived temperature towards higher values. The random error introduced by the uncertainty on the photometric values are negligible compared to our floor precision level, which is dictated by the model grid spacing.

The last method we adopted (hereafter method 3) is to normalize both the models and the measured spectrum to 1 at 1.28 $\mu$m and then perform the $\chi^2$ fitting. This method does not rely on any assumptions on the radii of the object, and it is not prone to any systematic introduced by the photometry. The only constraint on the final temperature is given by the shape of the object's spectrum. However with this approach gravity and metallicty of the dwarf are important parameters of the fit. Given the known degeneracy between the two (e.g. Kirkpatrick, 2005) their determination is very uncertain, and can bias the temperature we obtain especially for the peculiar objects.

We assume as our final value the weighted average of the three values, as this approach minimizes the systematic errors. We then calculate the bolometric luminosity of the targets following the Stefan-Boltzmann law:

$$L_{\rm bol} = 4\pi\sigma R^2 T_{\rm eff}^4 \tag{2.5}$$

The results are presented in Table 2.6. In the first column we indicate the target short name, in the second one its spectral type, in the third the expected temperature according to the temperature-spectral type relation given by Stephens et al. (2009), in the fourth the derived temperature and in the last column the bolometric luminosity. We note that hottest objects tend to have systematically higher uncertainties on $T_{\rm eff}$ compared to the colder ones. This is probably a consequence of the fact that at hotter temperatures the contribution of the optical part of the spectrum becomes significant,

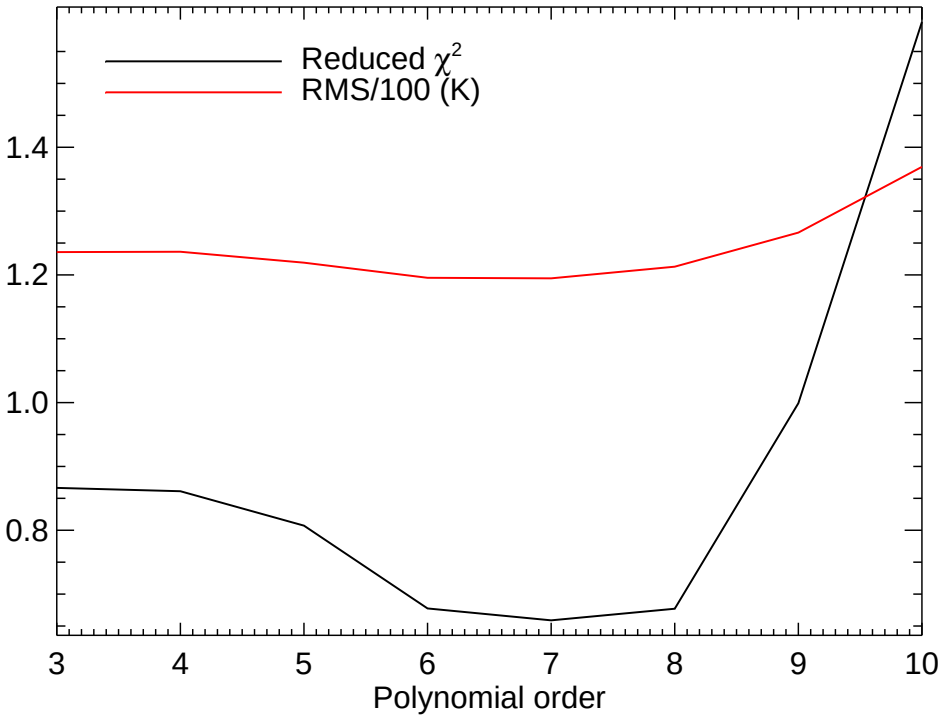


Fig. 2.14: The reduced $\chi^2$ (black line) and the RMS of the fit (red line) as a function of the order of the fitting polynomial. Both curves reach their minimum for a 7th order polynomial.

hence our fit based solely on the near-infrared portion of the spectrum becomes less and less accurate. Therefore the scatter between the three methods increases.

The results are also plotted in Figure 2.15 and 2.16. In the left panel of Figure 2.15 we show the $T_{\rm eff}$ we derived here for our targets (plotted as filled circles) as a function of the spectral type. Objects that were classified as "peculiar" are marked as asterisks. Overplotted as diamonds are objects taken from Golimowski et al. (2004) and Marocco et al. (2010). The red line is our seventh-order polynomial fit to the sequence for spectral types from M7 to T8, excluding the peculiar objects. The polynomial obtained is:

$$\begin{aligned} T_{\rm eff} = \quad & -1613.82 + 3561.47\,{\rm SpT} - 975.953\,{\rm SpT}^2 \\ & + 129.141\,{\rm SpT}^3 - 9.46896\,{\rm SpT}^4 \\ & + 0.390319\,{\rm SpT}^5 - 0.00843736\,{\rm SpT}^6 \\ & + 0.0000742110\,{\rm SpT}^7 \quad (\pm 140) \quad {\rm K} \end{aligned} \tag{2.6}$$

We have chosen a 7th order polynomial as it is the one that minimizes the reduced $\chi^2$, the uncertainties of the individual coefficients, and the root mean square (RMS) of the fit, as can be seen in Figure 2.14, where we plot the reduced $\chi^2$ and the RMS as a function of the order of the fitting polynomial.

Our new fit suggests a change in the slope of the sequence at the transition between the M and L dwarfs. This may be an effect of dust formation and its migration into the

photosphere, that causes a more rapid evolution of the spectral features as a function of $T_{\rm eff}$. The transition from M to L spectral types is indeed characterized by the formation of aluminum-, calcium- and titanium-bearing molecules such as perovskite ($CaTiO_3$), corundum ($Al_2O_3$), and grossite ($CaAl_4O_7$), which remove those elements from the atmosphere of the dwarfs. At slightly lower temperature other condensates, like forsterite ($Mg_2SiO_4$), enstatite ($MgSiO_3$), and vanadium dioxide ($VO_2$), remove the VO and Si from the atmosphere, causing the alkali metals (Na and K primarily) and the metal hydrides (in particular FeH and CrH) to be the main absorbers in the atmospheres of L dwarfs (see Kirkpatrick, 2005, and references therein for a more detailed description of the chemistry of ultracool atmospheres).

Also, in the L-T transition the sequence is almost flat. This is a known phenomenon, and it is the effect of the onset of the dust settling and of the Collision Induced Absorption (CIA) of the $H_2$ (e.g. Burrows et al., 2006; Saumon & Marley, 2008; Allard et al., 2011).

In the right panel of Figure 2.15 we present a comparison between the $T_{\rm eff}$ derived in this paper and those predicted by the polynomial relation presented by Stephens et al. (2009). The values are generally consistent with each other, but we note that our estimated temperatures are systematically slightly higher than the predicted ones. The polynomial fit by Stephens et al. (2009) is based essentially on the $T_{\rm eff}$ derived in Golimowski et al. (2004). In that contribution the authors estimated the bolometric flux using the measured NIR spectra (covering the 0.8−2.5 $\mu$m range) and applying a bolometric correction based on the $L'$ photometry only, interpolating between the K and $L'$ band and assuming a Rayleigh-Jeans tail longward of $L'$. This approximation could have led to a systematic underestimation of the bolometric flux, hence of the $T_{\rm eff}$ which would explain the discrepancy in Figure 2.15.

Figure 2.16 shows the bolometric luminosity as a function of the spectral type. Colours and symbols follow the same convention of Figure 2.15 and literature objects are the same shown in that Figure as well. The bolometric luminosity decreases smoothly from late-M type object to mid and late-L dwarfs, and from mid-T down to late-Ts. In the L/T transition the luminosity is almost constant, and despite the sparse population (only 8 objects between L7 and T1) we note a high scatter, with difference of a factor of 3-4 between objects of the same or very near spectral type. This scatter is not unexpected, as the L/T transition is known to be populated by a high fraction of unresolved binaries (Burgasser, 2013), and these objects would clearly result as overluminous compared to single dwarfs of the same spectral type.

| Object short name | Sp. Type | Exp. $T_{\rm eff}$ (K) | $T_{\rm eff}$ method 1 | $T_{\rm eff}$ method 2 | $T_{\rm eff}$ method 3 | Calc. $T_{\rm eff}$ (K) | $L_{\rm bol}$ ($L_{\odot}$) |
|---|---|---|---|---|---|---|---|
| 0032-4405 | L4 pec | 1720 | 2100±360 | 2000±100 | 2000±100 | 2000±220 | $1.49\pm0.88\times10^{-4}$ |
| 0058-0651 | L1 | 2110 | 2250±170 | 2000±110 | 2000±110 | 2050±130 | $1.65\pm0.78\times10^{-4}$ |
| 0109-5100 | M7 | 2670 | 2800±160 | 2800±170 | 2800±170 | 2800±170 | $5.7\pm2.7\times10^{-4}$ |
| 0147-4954 | M9 | 2400 | 2700±200 | 2000±120 | 2800±160 | 2350±160 | $2.8\pm1.4\times10^{-4}$ |
| 0219-1939 | L1 | 2110 | 2650±200 | 1900±90 | 1900±90 | 1950±140 | $1.35\pm0.66\times10^{-4}$ |
| 0230-0953 | L6 | 1530 | 1500±110 | 1700±170 | 1800±100 | 1650±130 | $6.9\pm3.5\times10^{-5}$ |
| 0239-1735 | M9 | 2400 | 2250±200 | 2100±120 | 2800±180 | 2300±170 | $2.6\pm1.3\times10^{-4}$ |
| 0257-3105 | L8 | 1400 | 1500±90 | 1700±210 | 1300±80 | 1400±140 | $3.6\pm2.0\times10^{-5}$ |
| 0539-0059 | L4 | 1720 | 1700±90 | 1800±90 | 2000±100 | 1800±90 | $9.8\pm4.4\times10^{-5}$ |
| 0614-2019 | L2 | 1970 | 2000±130 | 2000±120 | 2000±120 | 2000±120 | $1.49\pm0.70\times10^{-4}$ |
| 0719-5051 | L0 | 2260 | 2550±150 | 1900±100 | 1900±100 | 2000±120 | $1.49\pm0.70\times10^{-4}$ |
| 0928-1603 | L2 | 1970 | 2000±150 | 1900±110 | 2000±110 | 1950±120 | $1.35\pm0.63\times10^{-4}$ |
| 1246-3139 | T2 | 1250 | 1350±70 | 1400±60 | 1400±60 | 1400±60 | $3.6\pm1.6\times10^{-5}$ |
| 1331-0116 | L1 pec | 2110 | 1350±140 | 1900±80 | 2200±100 | 1900±110 | $1.21\pm0.56\times10^{-4}$ |
| 1753-6559 | L4 | 1720 | 1800±110 | 1800±80 | 1900±90 | 1800±90 | $9.8\pm4.4\times10^{-5}$ |
| 1936-5502 | L4 | 1720 | 1800±120 | 1900±90 | 1800±80 | 1800±100 | $9.8\pm4.5\times10^{-5}$ |
| 2045-6332 | L1 | 2110 | 3100±220 | 2200±100 | 1900±100 | 2150±150 | $1.99\pm0.97\times10^{-4}$ |
| 2209-2711 | T2.5 | 1240 | 1100±70 | 1400±70 | 1400±60 | 1300±70 | $2.7\pm1.2\times10^{-5}$ |
| 2310-1759 | L1 | 2110 | 3100±430 | 1800±80 | 1800±100 | 1850±260 | $1.09\pm0.75\times10^{-4}$ |
| 2346-5928 | M7 pec | 2670 | 3300±350 | 2700±150 | 3300±180 | 3000±240 | $7.6\pm3.9\times10^{-4}$ |

Table 2.6: Luminosity and effective temperature of the targets. For each object we list the NIR spectral type derived in this paper, the expected temperature according to Stephens et al. (2009) polynomial relation, the calculated temperature using the three methods described in the text, the final value adopted, and the bolometric luminosity. The uncertainty on the expected temperatures is ±100 K.

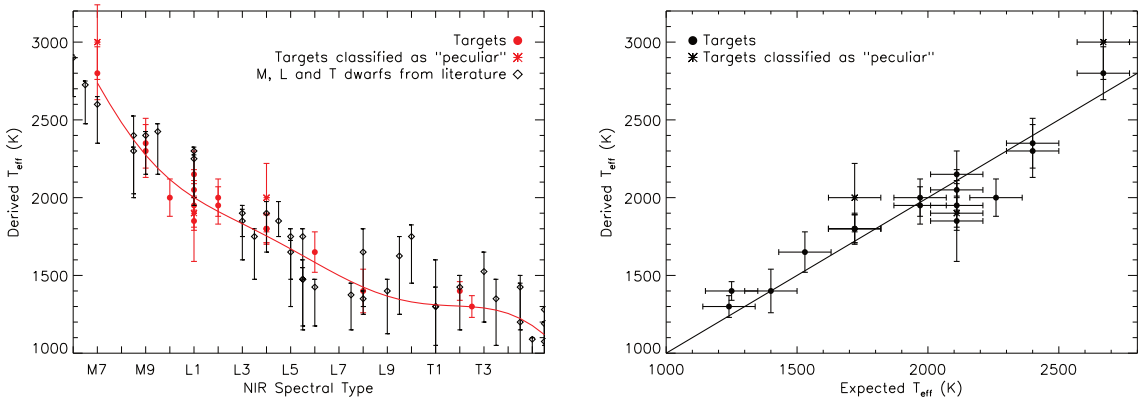


Fig. 2.15: *Left panel:* The effective temperature of our targets (filled circles) as a function of their spectral types. Peculiar objects are plotted as asterisks. Overplotted as diamonds are objects taken from Golimowski et al. (2004) and Marocco et al. (2010). The red line is our 7*th* order polynomial fit to the M7 to T8 sequence, excluding the peculiar objects. *Right panel:* A comparison between the $T_{\rm eff}$ derived in this paper and those predicted using the polynomial relation from Stephens et al. (2009). The solid line is the bisector of the plot. Although generally consistent with each other, our derived temperatures are systematically higher than the expected ones.

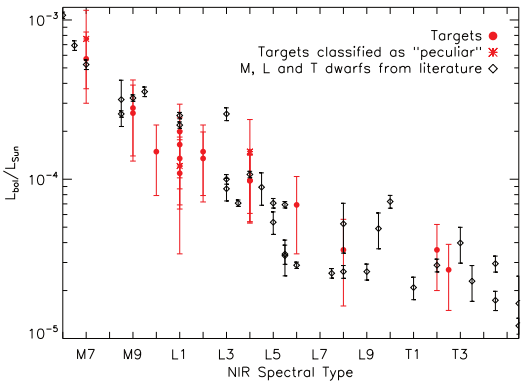


Fig. 2.16: The bolometric luminosity of our targets (filled circles) as a function of their spectral types. Peculiar objects are plotted as asterisks. Overplotted as diamonds are objects taken from Golimowski et al. (2004) and Marocco et al. (2010).

## 2.6 Comments on Individual Objects

### 2.6.1 EROS-MP J0032−4405 (0032-4405)

This object was identified as a possible young object by Reid et al. (2008b). The NIR spectrum shows indeed a slightly triangular-shaped H band, which is associated with low gravity (hence with young age, e.g. Lucas et al., 2001; Kirkpatrick et al., 2006). It is also the brightest L4 in our sample ($M_{\rm J} = 11.45, M_{\rm H} = 10.53, M_{\rm K} = 9.94$), a fact that would be consistent with a young nature, as 0032-4405 would not have fully contracted to its final radius. With a larger radius, the object would then look slightly brighter than its spectral analogue of older age. We therefore classify this object as L4 pec. We have also identified this object as a possible member of the Pleiades, a fact that would be in agreement with its young age.

### 2.6.2 SSSPM J0109−5100 (0109-5100)

Our derived NIR spectral type (M7) differs by five subtypes from the one published in Lodieu et al. 2005 (L2), while it is consistent within the uncertainties with the optical classification derived in the same paper (M8.5). No clear signs of peculiarity are present in the spectrum of 0109-5100 that could justify this discrepancy. However as noted by Lodieu et al. (2005) their NIR classification, based on the spectral indices defined in Tokunaga & Kobayashi (1999), Martìn (2000), and Reid et al. (2001a), is systematically offset towards later types when compared to their optical classification, and with a large scatter. The authors therefore assigned to the object a type of M8.5 based on the optical spectrum only. Moreover, our new NIR classification is based on a different system, which is the direct comparison of our spectra to the new standard templates defined in Kirkpatrick et al. (2010).

### 2.6.3 DENIS-P J035726.9−441730 (0357-4417)

This target is a known unresolved binary, identified by Bouy et al. (2003). As we discussed in Section 2.3.3, the spectrum of this object shows signs of low-gravity, which is associated with young ages. We assign an unresolved spectral type of L2 pec, because the L2 standard template is the one that gives the best fit in the J band. The spectral deconvolution gives spectral types for the individual components of the system of L4.5 and L5, which are much later than those derived via resolved optical spectroscopy by Martín et al. 2006 (M9+L1). The discrepancy is probably due to the fact that the templates we employed for the deconvolution are "normal" field M and L dwarfs, thus they do not reproduce well the H and K band peculiarities typical of young dwarfs.

### 2.6.4 2MASS J07193188−5051410 (0719-5051)

This object forms a common proper motion pair with 0719-5050, as already noted in AHA11. We obtained an infrared spectrum for both objects. We confirm the spectral classification of L0 for 0719-5051, as obtained by Reid et al. (2008b). For the companion, we derive a spectral type of M4, based on the spectral fitting with the templates obtained from the IRTF spectral library, which is consistent with the photometric estimate of AHA11.

Given the relatively limited time-span of our observations, it is impossible to detect hints of orbital motion for the system. The predicted average astrometric acceleration

terms along the X and Y axis (e.g. Torres, 1999), assuming masses of 0.1 $M_{\odot}$ and 0.08 $M_{\odot}$ for the two components of the system, given the projected separation and distance (and averaging over all other orbital parameters) are well below 1 $\mu$as yr$^{-1}$.

### 2.6.5 2MASSW J1004392−333518 (1004-3335)

This object is in a common proper motion system with LHS 5166 (AHA11). The infrared spectrum obtained for 1004-3335 indicates a spectral type of L5, in good agreement with the optical spectral type of L4 obtained by Gizis (2002). For the bright companion, LHS 5166, we derive a spectral type of M4, slightly later than the M3 found by AHA11, but in agreement with the dM4.5e published in Seifahrt et al. (2005). For the same reasons listed in the previous subsection, it is impossible to detect any hint of orbital motion for this system.

### 2.6.6 SDSS J133148.92−011651.4 (1331-0116)

The spectrum of this object is presented in Figure 2.17 with the spectrum of the L1 standard 2MASSW J2130446−084520 and of the sdL1 2MASS J17561080+2815238 overplotted for comparison, in red and green respectively. The overall slope of the optical spectrum of 1331-0116 is well matched by the L1 standard, the target however shows the peculiar signs of subdwarfs, i.e. stronger absorption by alkali metals, for examples the depth of the K I line at 0.78 $\mu$m and the doublets at 1.169-1.177, and 1.244-1.252 $\mu$m. In the near-infrared range, the L1 standard matches the flux level at the peak of the H band, but we can clearly see stronger $H_2$ CIA and also much deeper $H_2O$ bands. When compared the sdL1 template, 1331-0116 shows deeper $H_2O$ bands at 1.1 and 1.35 $\mu$m, but a much higher flux level in the H and K band. This object was already noted as peculiar in Knapp et al. (2004) and low-metallicity was pointed out as the possible explanation for its peculiarity. The parallax and proper motion obtained for it are $\pi_{\rm abs}$ = 67.3±12.6 mas, $\mu_{\alpha}\cos\delta$ = -421.9±5.7 mas yr$^{-1}$ and $\mu_{\delta}$ = -1039.0±5.2 mas yr$^{-1}$. The kinematics of 1331-0116 suggests that this object may pertain to a slightly older population, with a probability of 38% of being a thick disk object (see Table 2.5). We therefore conclude that this object is a slightly metal-poor L1 dwarf, and we classify it as L1 pec. We note that the previous infrared classification, based on spectral indices, was L8±2.5 (Knapp et al., 2004). This discrepancy is not surprising, as the index-based classification for peculiar L dwarfs is not well established, and the criteria used to classify normal objects can therefore lead to uncertain spectral types. The very deep $H_2O$ absorption bands are likely to be the reason of the previous late-type classification. However, the L8 and L9 standards do not match the depth of the water absorption, nor the slope and shape of the optical spectrum. Also, our new classification is consistent with the photometry of the object (J-H = 0.98, J-K = 1.39) which is typical of early-L dwarfs.

### 2.6.7 2MASS J14044941−3159329 (1404-3159)

This object is an unresolved L/T transition binary. Identified by Looper et al. (2008a) via high resolution imaging with HST, the spectral types of the two components were initially estimated to be T1+T5, then corrected to T0+T5 by Burgasser et al. (2010). More recently, Dupuy & Liu (2012) estimated L9+T5. Our spectral deconvolution also gives L9+T5.

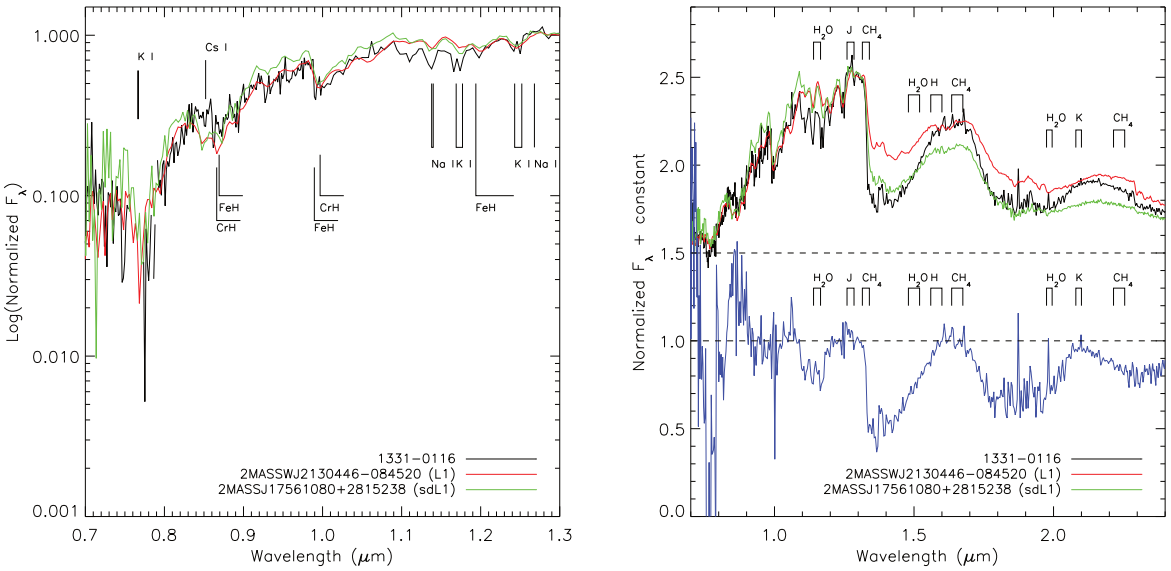


Fig. 2.17: The spectrum of 1331-0116. *Left*: a zoom to the optical and J-band spectrum; *Right*: the entire spectrum. Overplotted in both panels are the L1 standard 2MASSW J2130446−084520 (red) and the sdL1 2MASS J17561080+2815238 (green). In blue we show the flux ratio between the target and the L1 spectroscopic standard. Marked with a dashed line are the zero flux level of the normalized spectra and the 1 level of the flux ratio.

The parallax and proper motion derived here ($\pi_{\rm abs}$ = 49.2±3.4 mas, $\mu_\alpha cos\delta$ = 337.6±1.9 mas yr$^{-1}$ and $\mu_\delta$ = −16.3±2.4 mas yr$^{-1}$) are consistent with the values found by Dupuy & Liu (2012), who measured an absolute parallax of 42.1±1.1 mas and proper motion components $\mu_\alpha cos\delta$ = 344.8±1.0 mas yr$^{-1}$ and $\mu_\delta$ = −10.8±1.4 mas yr$^{-1}$, except for the $\mu_\alpha cos\delta$ component, but this difference maybe due to our derivation of the parallax which assumes single objects.

### 2.6.8 2MASS J19285196−4356256 (1928-4356)

We classified this object as L4 pec, as its spectrum appears significantly bluer than the L4 standard 2MASS J21580457−1550098. The standard reproduces well the shape and flux level of the J band spectrum, but at longer wavelengths 1928-4356 emits much less flux, which can be an indication of a stronger $H_2$ absorption due to low metallicity. We therefore conclude that 1928-4356 could be a slightly metal poor object.

### 2.6.9 2MASS J20115649−6201127 (2011-6201)

In Figure 2.18 we can see that the optical spectrum (left panel) matches quite well the spectrum of the M8 standard VB 10 (overplotted in red), while the NIR spectrum (right panel) shows signs of metal depletion. In particular, we note the flux suppression in the H and K bands and the presence of deeper water absorption bands. These features are associated with low-metallicity and are well matched by the sdM8.5 LSR 1826+3014 (overplotted in green). We calculated the metallicity index $\zeta_{\rm TiO/CaH}$ as defined by Lépine et al. (2007) and found a value of 1.01, which would yield to a classification as a normal dwarf. However, the nature of 2011-6201 is clearly intermediate between a normal dwarf and a subdwarf, and we therefore classify it as a d/sdM8.

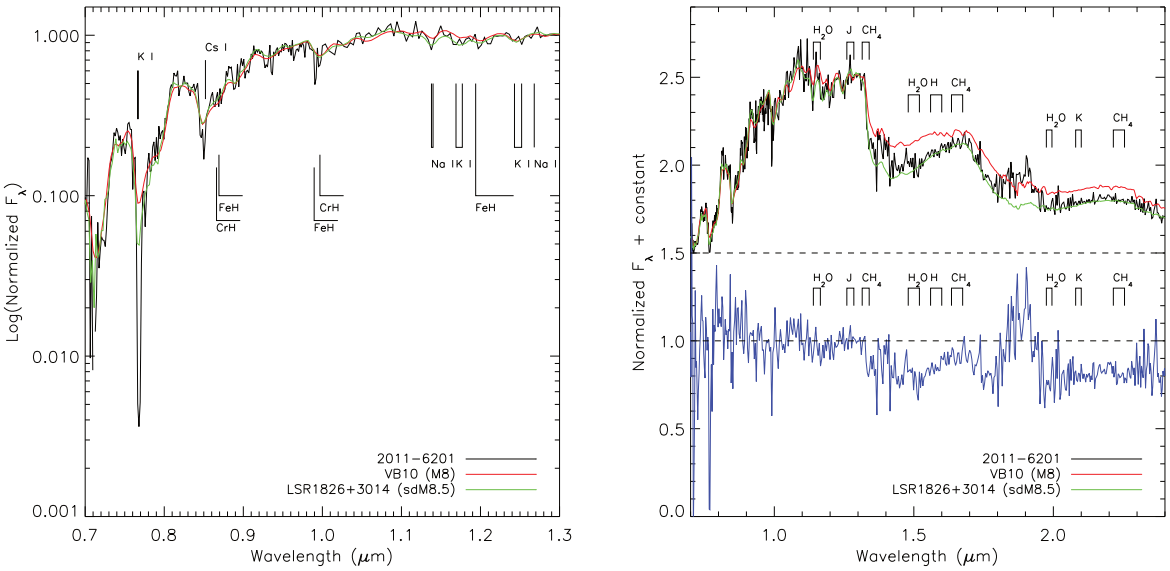


Fig. 2.18: Same as Figure 2.17, but for 2011-6201. Overplotted in red is the spectrum of the M8 standard VB 10, and in green is the spectrum of the sdM8.5 LSR 1826+3014.

### 2.6.10 SIPS2045−6332 (2045-6332)

This is the brightest L1 in our sample ($M_{\rm J} = 10.63, M_{\rm H} = 9.82, M_{\rm K} = 9.22$). The $T_{\rm eff}$ determined via model fitting is also higher than the predicted one. These can be indications of binarity. To investigate further this possibility, we fitted the spectrum of 2045-6332 with our set of unresolved templates. The two components derived by our deconvolution would be L1.0 and T6.0. To assess the significance of this deconvolution we performed an F-test. If $\eta$, which is the ratio of the $\chi^2$ of the two fits (the deconvolution and the one with standard templates) is greater than the critical value $\eta_{\rm crit}$ (which depends on the number of degrees of freedom), than the deconvolution is better than the standard fit with a 99% significance. In our case, $\eta = 1.09$, while $\eta_{\rm crit} = 1.22$. We conclude that the deconvolution is not significant. It still remains possible that the object is an equal (or nearly-equal) spectral type binary. Our deconvolution is not sensitive to these objects, but such kind of binary would clearly appear overluminous and hotter compared to other dwarfs of similar spectral type.

We note also that the H band of the spectrum of 2045-6332 appears slightly triangular, which could be a hint of youth. This can be an alternative explanation to its overluminosity, as young objects have larger radii compared to older, field-aged dwarfs of the same spectral type.

Dieterich et al. (2014) measured parallax and proper motion for this object that are consistent with our values within the formal errors. Interestingly they found that the object is highly variable at 39 mmag in the $I$ band (Johnson-Kron-Cousins system, see Bessell, 1995), which is a further indication that youth can be the explanation for its overluminosity.

Further investigation is necessary to determine the nature of this object. In particular, high-resolution imaging is required to address the possibility that this object is a binary system, while optical spectroscopy can help to investigate its young nature.

### 2.6.11 2MASS J22092183−2711329 (2209-2711)

This is a newly discovered T dwarf. We assign a spectral type of T2.5 as its spectrum shows features which are intermediate between the T2 and the T3 spectral standards (SDSSp J125453.90−012247.4 and 2MASS J12095613 −1004008 respectively). This target was also selected as a candidate member of the Pleiades. However, its spectrum does not show any sign of youth. The derived absolute magnitudes and effective temperature are in good agreement with the expected ones.

### 2.6.12 2MASS J22134491−2136079 (2213-2136)

This object was identified as a low-gravity object by Cruz et al. (2009) and classified L0$\gamma$ using its optical spectrum. The NIR spectrum confirms the low-gravity nature of this object. It shows in fact a triangular shaped H band and an enhancement of the flux in the H and K band (compared to a standard template). We classify this object as a L2 pec, as the L2 standard is the one that reproduces better the shape of the J band and the depth of the water absorption band between the J and H band.

### 2.6.13 SIPS2346−5928 (2346-5928)

This newly discovered M7 dwarf appears significantly bluer than the M7 standard VB 8. In Figure 2.19 we can see that the sdM7 2MASS J15412408+5425598 reproduces better the depth of the water absorption bands and the flux level in the K band. The H band of 2346-5928 is slightly bluer even when compared to the sdM7. The kinematics suggests that this object could be a member of the galactic thick disk, and we therefore conclude that 2346-5928 is a metal-poor M dwarf. We do not have an optical spectrum for this target, so we cannot apply the criteria defined by Lépine et al. (2007) and therefore we cannot assign a metallicty class. So we decide to classify it as M7 pec. The derived $T_{\rm eff}$ is slightly higher than the prediction, but consistent with the findings for the other M7 of the sample, 0109-5100. The big uncertainty on the $T_{\rm eff}$ is given mainly by the very high temperature (3300 K) that we derive using method 3 (i.e. normalizing the models). This could be due to the peculiarity of 2346-5928, whose blue spectrum is better fitted by a hotter model.

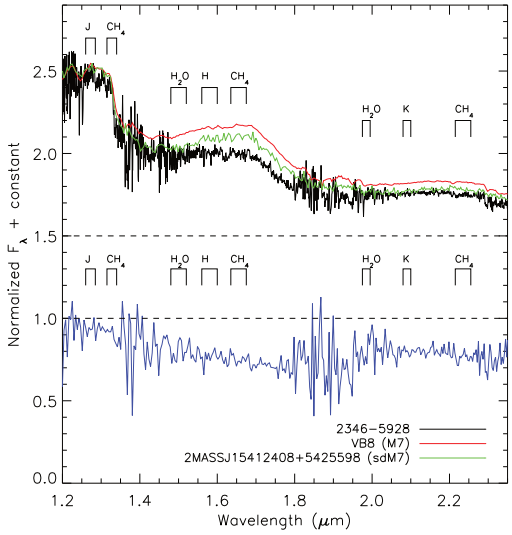


Fig. 2.19: The spectrum of 2346-5928. Overplotted in red is the spectrum of the M7 standard VB 8, and in green is the spectrum of the sdM7 2MASS J15412408+5425598.

## 2.7 Summary and Conclusions

We have presented here NIR spectra of 52 M, L and T dwarfs from the PARSEC program, and parallaxes for 21 of them. Ten of these objects are new discoveries. The new parallaxes contribute to further populate the low-mass end of the H-R diagram, especially in the L0-L4 spectral range. The combination of astrometry and spectroscopy has allowed us to investigate in detail the nature of some peculiar objects like the young, low-gravity dwarfs 0032-4405, 0357-4417, and 2213-2136; the unresolved binaries 0357-4417 and 1404-3159; the metal-poor dwarfs 1331-0116, 1928-4356, 2346-5928 and 2011-6201. Also, combining the spectra obtained with photometric data, parallaxes and atmospheric models, we derived effective temperature and bolometric luminosity for 21 of our targets. These new results seem to suggest a change in the slope of the $T_{\rm eff}$ - Spectral type sequence at the M/L spectral type transition. This feature could be due to the formation of dust clouds in the atmospheres of brown dwarfs, and the subsequent migration of the clouds into the photosphere. An increased sample of late-M and early-L with measured $T_{\rm eff}$ will help to constrain better the polynomial relation and understand the physics of the transition.

These 21 objects represent the first sub-sample of parallaxes obtained by PARSEC. The spectroscopic follow-up is in progress, to obtain NIR spectra of all the PARSEC targets that currently lack NIR spectroscopy (see AHA11 for the complete target list).

The new parallaxes, proper motions and spectra presented here and in AHA11 will contribute to the creation of a large database of brown dwarfs. The creation of this database is one of the outputs of the Interpretation and Parameterization of Extremely Red COOL objects (IPERCOOL) International Research Staff Exchange Scheme, hosted on the IPERCOOL website (http://ipercool.oato.inaf.it).

# Chapter 3: Spectroscopy of a large sample of L and T dwarfs from UKIDSS LAS

Part of the work presented in this chapter has been published in "The sub-stellar birth rate from UKIDSS", A. C. Day-Jones, F. Marocco, D. J. Pinfield, Z. H. Zhang, B. Burningham, N. Deacon, M. T. Ruiz, J. Gallardo, H. R. A. Jones, P. W. Lucas, J. S. Jenkins, J. I. Gomes, S. L. Folkes, and J. R. A. Clarke, Monthly Notices of the Royal Astronomical Society, Volume 430, Issue 2, p.1171-1187 (2013) and is reproduced by permission of the RAS.

The co-authors of the paper contributed entirely to Section 3.2 and partly to Section 3.3. Everything else is my own original work.

## 3.1 Introduction

The study of sub-stellar objects still presents a number of open questions. A very intriguing one is the understanding of the physical and chemical processes taking place at the transition between the spectral types L and T.

As described in Section 1.6.1, the sharp colour turnaround that characterizes the transition between the near-infrared types L7 to T5 (see Figure 1.7) is particularly challenging to model. The dust settling and the onset of the methane and molecular hydrogen absorption are now believed to be the main causes of the turnaround, but the details of these processes, in particular of the dust settling, are still not well understood. A number of different scenarios have been proposed (e.g. Tsuji & Nakajima, 2003; Knapp et al., 2004; Marley et al., 2002), but none of them could successfully reproduce the quickness and the sharpness of the turnaround (see Section 1.6.1 for a more detailed review). An important role is also played by atmospheric parameters like metallicity and surface gravity, which influence the nature and the settling of the dust clouds and can lead to the formation of very peculiar spectra (see Section 1.6 and references therein). Understanding in detail the effects of these parameters is another open question.

A significant contribution comes from the modern deep wide-field near-infrared surveys, like DENIS (Epchtein et al., 1999), SDSS (York et al., 2000), 2MASS (Skrutskie et al., 2006), UKIDSS (Lawrence et al., 2007), CFBDS (Delorme et al., 2008b), WISE (Wright et al., 2010), and VISTA (Emerson & Sutherland, 2002). Mapping thousands of square degrees to significant depths in both optical and infrared bands, these surveys provide huge datasets, and mining into them is the best way of finding large samples of brown dwarfs. The increase in numbers of known objects will give me the statistic significance necessary to better constrain the current structure and evolution models of L and T dwarfs.

In this chapter I present a detailed spectroscopic analysis of a sample of 196 late-M, L and T dwarfs selected from UKIDSS Large Area Survey (LAS). The spectra of the targets have been obtained with X-shooter on the Very Large Telescope (Vernet et al., 2011). Spectroscopy is a powerful tool to provide insights to the theory, as the formation of the observed spectra is heavily influenced by the physics and the chemistry of the

atmosphere. In particular the wide wavelength coverage delivered by X-shooter (0.3-2.45 $\mu$m) coupled with its good resolution makes it an ideal instrument for this kind of analysis, as it allows me to obtain both the optical and the near-infrared spectra of the targets at the same time. As these portions of the spectrum are sensitive to different parameters, their comparison can provide extremely useful insights in understanding the physics of the atmosphere of brown dwarfs.

## 3.2 Candidate selection

The objects presented here have been selected from the UKIDSS LAS DR7. The details of the targets selection are given in Day-Jones et al. (2013), and here I repeat the fundamental steps.

The sample consists of objects with declination $\leq 20°$ and brighter than 18.1 in J band. Field M dwarfs were removed by applying a colour cut of Y−J $> 0.8$ (Hewett et al., 2006).

Object whose ellipticity was larger than 0.45 were removed in order to ensure that selected objects were point sources. The ellipticity is defined as $1 - (b/a)$ where $a$ and $b$ are the semi-major and semi-minor axis of the PSF fit. The quality flags provided by the UKIDSS DR7 were used to remove cross-talk effects, objects that sit at the edge of the detector, saturated sources, and objects that fall in poor flat field regions. Both K band detections and non-detections were selected.

The preliminary list of candidates was then cross-matched against SDSS DR7 using a matching radius of $4''$ to select objects with optical counterparts. Objects with optical counterparts were selected according to the criteria below, based on those of (Schmidt et al., 2010b), who provide colours from an unbiased spectroscopically complete sample. Since the near-infrared colour selection effectively removes all contaminant field M dwarfs, this allows us to be more liberal with the redder sources (J−K $> 1.0$) in terms of $z$−J colour selection, and allows for larger uncertainties in the $i$ band as this sample is probing the faint end of SDSS. Y and J photometry were required to have errors not greater than $3\sigma$ and detections in H $\geq 14.5$, such that this search space would not have been probed by 2MASS. In addition, K-band non-detections were also considered, if their $z$−J colour passes the following criteria:

$z$−J $\geq 2.4$ and (J−K $\geq 1.0$ or no K detection)

OR

$z$−J $\geq 2.9$ and (J−K $< 1.0$ or no K detection)

Objects with the following were removed:

$i - z < 2.0$ and $\sigma_{(i-z)} < 0.35$

$i$−J $< 4.7$ and $\sigma_{(i-\mathrm{J})} < 0.2$

$z$−K $< 3.5$ and J−K $> 1.0$ and $\sigma_{(z-\mathrm{K})} < 0.2$.

As mid-T dwarfs typically have $z$−J $> 3.0$ (e.g. Pinfield et al., 2008), some objects will be too faint for detection in SDSS; thus these SDSS non-detections were included. All objects were then visually inspected to remove any possible mismatches

or cross-talk. The sample was also cross-matched with known L and T dwarfs in DwarfArchives.org and those that have spectral types $\geq$ L4 (to be consistent with completeness; see Section 4.2.1) were retained, giving a total sample size of 324 from 2000 deg$^2$ of ULAS (DR7) sky. From this final sample, 196 objects were followed-up with mid-resolution spectroscopy, and constitute the targets for the subsequent analysis I present in this thesis.

## 3.3 Observations and data reduction

The spectra of the 196 targets were obtained under ESO programs 086.C-0450(A/B), 087.C-0639(A/B), 088.C-0048(A/B), and 091.C-0452A. Sixty-eight spectra were presented in Day-Jones et al. (2013) and the others will be published in Marocco et al. (in prep.).

The targets were observed in echelle slit mode, which covers the wavelength range 0.30−2.50 $\mu$m. This is split into three separate arms, the UVB (0.30−0.55 $\mu$m), VIS (0.55−1.00 $\mu$m) and NIR (1.00−2.50 $\mu$m). The observations were taken using slit widths of 1.0 arcsec for the UVB arm and 0.9 arcsec for the VIS and NIR arms, and followed an ABBA pattern to allow sky subtraction. Individual integration times were set equal to 800, 1200, 1600 and 2000s for J $\leq$ 17, 17.5, 18, 18.1 respectively in the VIS arm, decreased by 70s in the UVB arm and increased by 90s in the NIR arm. I note that there is no significant flux detected in the UVB wavelength range for members of the sample. Telluric standards were observed following a target-telluric-target strategy, trying to minimize the airmass difference between the targets and the standards. Telluric stars were selected preferentially in the late-B to early-A spectral range, as these types of stars are essentially free of absorption features, except for H I lines.

I reduced the data using the ESO pipeline (version 2.0.0). The pipeline removes non-linear pixels, subtracts the bias (in the VIS arm) or dark frames (in the NIR arm) and divides the raw frames by flat-fields. Images are pairwise subtracted to remove sky background. The pipeline then extracts and merges the different orders in each arm, rectifying them using a multi-pinhole arc lamp (taken during the day-time calibration) and correcting for the flexure of the instrument using single-pinhole arc lamps (taken at night, one for each object observed). The response function for the instrument is computed using a spectrophotometric standard (generally observed at the beginning of the night) combined with a model of the atmospheric extinction at Cerro Paranal. The final response function is then applied to the observed targets to deliver the final flux calibrated spectra. Telluric stars are reduced in the same way, except that sky subtraction is done by fitting the background (as tellurics are not observed in nodding mode). The final products are one dimensional, wavelength and flux calibrated spectra, one for each arm. The spectra were telluric corrected using IDL routines, following a standard procedure: first, the telluric spectrum is cleared of H I absorption lines (by interpolating over them) and scaled to match the measured magnitudes; then it is divided by a black body curve for the appropriate temperature, to obtain the atmosphere response curve; finally the target spectrum is multiplied by the response curve obtained to correct for telluric absorption. The arms (VIS and NIR) were then merged by matching the flux level in the overlapping regions between them. The flux calibration was checked by determining the targets synthetic MKO YJHK magnitudes, that were compared to those obtained in the ULAS. Finally, each

spectrum was visually inspected to check for possible problems during the extraction or merging stage. The spectra were then binned (in the $\lambda$ direction) 40 times to produce an average S/N = 30 for resolution R = 880 and 510 in the VIS and NIR arms, respectively.

## 3.4 Results

Results of the observations are presented in Table 3.1. For each object I present short name, coordinates, photometry, the S/N achieved after binning the spectra down to a resolution of ∼800 and ∼500 in the VIS and NIR arm respectively (corresponding to a binning of 40 pixels in the wavelength direction), and the spectral type derived (see Section 3.4.1). The spectra are presented in Fig. 3.1 − 3.14, sorted in descending order of spectral type (i.e. from early to late). Figure 3.15 shows the signal-to-noise ratio (SNR) distribution in the sample. The blue histograms shows the distribution in the VIS arm, while the red histogram shows the distribution in the NIR arm. I have omitted the UVB arm as I do not detect any flux at wavelengths shorter than 0.6 $\mu$m. A dotted line indicate the SNR before binning, while a solid line indicates the distribution of the binned spectra. With typical SNR of 25−30 in the NIR arm, the spectra are suitable not only for spectral typing, but also for the reliable calculation of spectral indices and the identification of peculiar objects and unresolved binaries.

| Name | RA | Dec | Y | J | H | K | $i$ | $z$ | VIS SNR | NIR SNR | Spectral type | Ref. |
|---|---|---|---|---|---|---|---|---|---|---|---|---|
| BRLT1 | 00:06:13 | +15:40:21 | 18.953 | 17.875 | 16.712 | 16.142 | 24.161 | 20.608 | 5.00 | 30.02 | L9.0 ± 0.5 | 1 |
| BRLT2 | 00:10:41 | +01:00:13 | 19.361 | 18.089 | 17.457 | 16.709 | 22.215 | 20.796 | 7.48 | 21.56 | L1.0 ± 1.0 | 1 |
| BRLT3 | 00:18:37 | -00:25:59 | 18.730 | 17.667 | 16.607 | ... | 23.108 | 20.274 | 5.35 | 39.04 | L9.0 ± 1.0 | 1 |
| BRLT6 | 00:24:06 | +13:47:05 | 19.280 | 18.023 | 17.337 | 16.528 | 24.676 | 24.060 | 4.27 | 28.30 | L3.0 ± 1.0 | 1 |
| BRLT7 | 00:27:07 | +14:23:49 | 18.956 | 17.981 | 17.373 | 16.862 | 22.637 | 20.409 | 8.00 | 20.86 | M8.0 ± 1.0 | 1 |
| BRLT8 | 00:28:28 | +14:23:49 | 18.946 | 17.563 | 16.616 | 15.846 | 22.787 | 20.287 | 5.00 | 35.78 | L8.5 ± 0.5 | 1 |
| BRLT9 | 00:29:12 | +14:56:05 | 18.812 | 17.559 | 16.920 | 16.329 | 22.102 | 19.966 | 6.16 | 29.01 | L1.0 ± 1.0 | 1 |
| BRLT10 | 00:33:00 | +14:10:37 | 17.830 | 16.645 | 15.689 | 15.001 | 23.083 | 19.421 | 4.35 | 31.50 | L9.0 ± 0.5 | 2 |
| BRLT12 | 00:37:16 | -00:54:05 | 19.449 | 18.085 | 17.329 | 16.661 | 22.591 | 20.797 | 5.93 | 22.24 | L3.0 ± 1.0 | 1 |
| BRLT14 | 00:43:56 | +14:11:18 | 18.413 | 17.326 | 16.689 | 16.120 | 21.796 | 19.748 | 8.34 | 27.08 | L0.0 ± 0.5 | 1 |
| BRLT15 | 00:47:57 | +15:46:41 | 19.118 | 17.827 | 17.163 | 16.414 | ... | ... | 1.47 | 19.72 | T2.0 ± 2.0 | 1 |
| BRLT16 | 00:50:38 | -00:03:37 | 19.031 | 17.862 | 17.068 | 16.517 | 22.543 | 20.561 | 7.59 | 22.65 | L2.0 ± 1.0 | 1 |
| BRLT18 | 01:00:36 | +06:20:44 | 18.638 | 17.768 | 16.912 | 16.335 | ... | ... | 8.80 | 26.66 | L0.0 ± 1.0 | 1 |
| BRLT20 | 01:05:32 | +14:29:32 | 19.258 | 18.005 | 17.461 | 16.820 | 22.923 | 20.596 | 4.44 | 22.18 | L1.0 ± 1.0 | 1 |
| BRLT21 | 01:11:52 | -01:05:34 | 18.637 | 17.340 | 16.532 | 15.932 | 22.297 | 20.340 | 4.23 | 28.77 | L3.5 ± 0.5 | 1 |
| BRLT22 | 01:12:50 | +15:36:58 | 19.005 | 17.996 | 17.407 | 16.855 | ... | ... | 4.90 | 19.74 | M8.0 ± 0.5 | 1 |
| BRLT24 | 01:16:45 | +14:43:35 | 19.308 | 17.959 | 17.007 | 16.299 | ... | ... | 5.32 | 27.01 | L3.5 ± 0.5 | 1 |
| BRLT26 | 01:27:44 | +13:54:21 | 17.966 | 16.772 | 15.913 | 15.184 | 22.195 | 19.625 | 7.05 | 32.85 | L5.5 ± 0.5 | 3 |
| BRLT27 | 01:28:14 | -00:41:54 | 18.464 | 17.592 | 16.898 | 16.487 | 24.132 | 20.485 | 2.05 | 19.69 | T0.0 ± 0.5 | 1 |
| BRLT28 | 01:29:07 | +01:13:50 | 19.321 | 18.140 | 17.232 | 16.283 | ... | ... | 6.71 | 32.30 | L6.0 ± 0.5 | ... |
| BRLT30 | 01:32:44 | +05:52:32 | 17.764 | 16.414 | 15.480 | 14.750 | 21.327 | 19.302 | 8.54 | 32.98 | L5.0 ± 0.5 | 1 |
| BRLT31 | 01:36:20 | +07:17:38 | 19.460 | 18.008 | 17.101 | 16.473 | ... | ... | 6.94 | 26.73 | L4.0 ± 1.0 | 1 |
| BRLT32 | 01:38:08 | -01:04:17 | 19.320 | 18.006 | 17.331 | ... | 22.402 | 20.815 | 7.94 | 22.09 | L1.5 ± 0.5 | 1 |
| BRLT33 | 01:41:03 | +13:18:33 | 19.454 | 17.946 | 17.094 | 16.577 | 22.404 | 20.531 | 3.61 | 20.31 | L3.5 ± 0.5 | 1 |
| BRLT35 | 01:48:12 | +14:00:28 | 19.094 | 17.971 | 17.164 | 16.550 | 21.330 | 21.487 | 6.28 | 26.58 | M9.5 ± 0.5 | 1 |
| BRLT37 | 01:49:27 | +14:41:08 | 19.303 | 18.038 | 17.098 | 16.317 | 23.488 | 20.589 | 2.80 | 28.06 | L5.0 ± 0.5 | 1 |
| BRLT38 | 01:51:42 | +12:44:29 | 17.403 | 16.387 | 15.597 | 15.288 | ... | ... | 3.01 | 28.03 | T0.0 ± 0.5 | 2 |
| BRLT39 | 01:51:44 | +13:46:46 | 18.904 | 17.661 | 16.839 | 16.093 | 23.174 | 20.281 | 4.57 | 29.01 | L5.0 ± 1.0 | 1 |

Continued on the next page.

Continued from the previous page.

| Name | RA | Dec | Y | J | H | K | $i$ | $z$ | VIS SNR | NIR SNR | Spectral type | Ref. |
|---|---|---|---|---|---|---|---|---|---|---|---|---|
| BRLT42 | 02:00:03 | +06:58:08 | 19.110 | 17.934 | 17.203 | 16.716 | ... | ... | 6.78 | 20.25 | M9.0 ± 0.5 | 1 |
| BRLT44 | 02:03:33 | -01:08:12 | 18.992 | 17.692 | 16.886 | 16.268 | 24.024 | 20.467 | 4.26 | 29.06 | L5.0 ± 1.0 | 4 |
| BRLT45 | 02:05:30 | +14:21:14 | 19.140 | 17.993 | 17.266 | 16.932 | 25.172 | 20.699 | 3.21 | 15.89 | T1.0 ± 0.5 | 1 |
| BRLT46 | 02:06:04 | +05:49:59 | 18.977 | 17.915 | 17.412 | 16.800 | 22.314 | 20.391 | 4.30 | 15.84 | L0.5 ± 0.5 | 1 |
| BRLT48 | 02:47:03 | -01:07:01 | 19.191 | 17.765 | 16.827 | 15.993 | ... | ... | 4.91 | 28.75 | L4.5 ± 0.5 | 1 |
| BRLT49 | 02:52:44 | +01:06:18 | 19.450 | 18.150 | 17.892 | 17.424 | ... | ... | 5.32 | 26.64 | M9.0 ± 0.5 | ... |
| BRLT50 | 02:55:45 | +06:16:56 | 19.152 | 17.992 | 18.669 | ... | ... | ... | 3.17 | 5.94 | T6.0 ± 0.5 | 5 |
| BRLT51 | 02:59:41 | +05:49:35 | 19.278 | 18.024 | 17.189 | 16.480 | ... | ... | 2.80 | 22.53 | L3.0 ± 1.0 | 1 |
| BRLT52 | 03:14:52 | +04:53:46 | 18.591 | 17.302 | 16.387 | 15.589 | 22.368 | 20.366 | 7.59 | 27.56 | L5.5 ± 0.5 | 1 |
| BRLT56 | 03:20:00 | +06:17:41 | 19.242 | 17.785 | 17.034 | 16.396 | ... | ... | 6.15 | 25.23 | L1.5 ± 1.0 | 1 |
| BRLT57 | 03:20:42 | +06:18:37 | 19.272 | 18.059 | 17.479 | 16.905 | 22.423 | 20.489 | 5.95 | 22.29 | L0.0 ± 1.0 | 1 |
| BRLT58 | 03:21:43 | +05:45:24 | 18.557 | 17.333 | 16.608 | 15.967 | 22.419 | 20.077 | 7.87 | 24.04 | L4.0 ± 1.0 | 1 |
| BRLT60 | 03:23:54 | +06:13:52 | 19.003 | 17.638 | 16.989 | 16.312 | ... | ... | 6.55 | 26.34 | L1.0 ± 1.0 | 1 |
| BRLT62 | 03:30:06 | +05:56:53 | 19.512 | 17.948 | 16.843 | 15.948 | ... | ... | 5.44 | 27.61 | L5.0 ± 1.0 | 1 |
| BRLT63 | 03:30:28 | +05:36:27 | 19.291 | 18.110 | 17.572 | 16.722 | ... | ... | 5.13 | 24.19 | L1.0 ± 0.5 | ... |
| BRLT64 | 03:30:37 | +04:26:58 | 18.618 | 17.293 | 16.444 | 15.749 | 22.139 | 19.983 | 6.93 | 26.12 | L4.0 ± 0.5 | 1 |
| BRLT65 | 03:37:35 | +05:00:27 | 19.204 | 18.120 | 17.491 | 16.873 | ... | ... | 5.82 | 25.12 | M9.0 ± 0.5 | ... |
| BRLT66 | 03:41:50 | +04:23:25 | 18.287 | 16.847 | 15.947 | 15.198 | 21.902 | 19.778 | 9.35 | 27.97 | L5.0 ± 0.5 | 1 |
| BRLT67 | 08:00:55 | +19:38:38 | 18.993 | 17.713 | 16.959 | 16.247 | 22.401 | 20.583 | 10.73 | 32.07 | L1.0 ± 0.5 | ... |
| BRLT68 | 08:04:41 | +18:26:12 | 18.814 | 17.568 | 16.541 | 15.833 | 23.113 | 20.150 | 3.63 | 25.56 | L5.0 ± 0.5 | ... |
| BRLT69 | 08:24:28 | +05:57:43 | 18.724 | 17.491 | 16.891 | 16.258 | 22.492 | 20.177 | 7.25 | 25.88 | L1.0 ± 0.5 | ... |
| BRLT71 | 08:32:59 | +01:12:42 | 19.255 | 17.997 | 17.138 | 16.549 | ... | ... | 6.42 | 25.25 | L1.5 ± 0.5 | ... |
| BRLT72 | 08:33:35 | -01:44:55 | 18.674 | 17.703 | 17.011 | 16.388 | 22.463 | 20.218 | 7.58 | 31.33 | M9.0 ± 0.5 | ... |
| BRLT73 | 08:38:43 | +08:17:01 | 18.928 | 17.720 | 17.038 | 16.337 | 22.119 | 20.653 | 3.85 | 20.29 | L1.0 ± 0.5 | ... |
| BRLT74 | 08:43:02 | +00:12:47 | 18.791 | 17.758 | 16.798 | 16.288 | 23.253 | 20.330 | 1.97 | 19.27 | L9.5 ± 1.0 | ... |
| BRLT75 | 08:44:11 | -01:59:44 | 19.057 | 18.017 | 17.437 | 16.825 | 23.010 | 20.619 | 8.34 | 23.77 | M9.0 ± 1.0 | ... |
| BRLT76 | 08:47:10 | +02:04:13 | 19.772 | 18.180 | 17.164 | 16.410 | ... | ... | 4.81 | 28.24 | L5.5 ± 0.5 | ... |

Continued on the next page.

Continued from the previous page.

| Name | RA | Dec | Y | J | H | K | $i$ | $z$ | VIS SNR | NIR SNR | Spectral type | Ref. |
|---|---|---|---|---|---|---|---|---|---|---|---|---|
| BRLT78 | 08:48:50 | +07:15:12 | 18.956 | 18.020 | 17.417 | 16.757 | ... | ... | 8.98 | 24.90 | L1.0 ± 0.5 | ... |
| BRLT81 | 08:50:35 | +06:21:53 | 19.158 | 18.079 | 17.395 | 17.005 | ... | ... | 8.41 | 31.36 | M9.0 ± 0.5 | ... |
| BRLT82 | 08:53:12 | +03:21:48 | 19.119 | 17.905 | 17.040 | 16.432 | 22.872 | 20.494 | 8.83 | 27.74 | L1.0 ± 0.5 | ... |
| BRLT83 | 08:55:40 | -02:19:24 | 18.981 | 18.160 | 17.433 | 16.832 | ... | ... | 6.38 | 19.85 | M8.0 ± 0.5 | ... |
| BRLT84 | 08:56:00 | +00:30:48 | 18.954 | 17.540 | 16.777 | 15.997 | 22.058 | 20.357 | 5.84 | 26.50 | L3.5 ± 0.5 | ... |
| BRLT85 | 08:59:31 | +06:36:01 | 19.012 | 18.076 | 17.588 | 17.191 | ... | ... | 9.41 | 21.64 | M8.0 ± 0.5 | ... |
| BRLT87 | 09:05:22 | +10:06:55 | 18.202 | 17.082 | 16.389 | 16.074 | 23.327 | 19.969 | 8.12 | 29.28 | T0.0 ± 0.5 | ... |
| BRLT88 | 09:07:10 | -02:21:46 | 19.215 | 17.926 | 17.011 | 16.313 | ... | ... | 4.15 | 27.58 | L4.0 ± 1.0 | ... |
| BRLT91 | 09:15:44 | +05:31:04 | 18.083 | 16.963 | 16.581 | ... | 23.846 | 20.117 | 1.73 | 17.34 | T3.0 ± 0.5 | ... |
| BRLT92 | 09:17:41 | +00:42:54 | 18.716 | 17.607 | 16.889 | 16.157 | 22.693 | 20.211 | 7.78 | 30.74 | L1.0 ± 0.5 | ... |
| BRLT97 | 09:24:32 | +00:58:36 | 19.174 | 17.931 | 17.263 | 16.563 | 22.444 | 20.364 | 4.81 | 23.60 | L0.0 ± 1.0 | ... |
| BRLT98 | 09:26:25 | +07:11:41 | 18.526 | 17.481 | 17.386 | ... | ... | ... | 4.35 | 12.52 | T4.0 ± 0.5 | 6 |
| BRLT99 | 09:26:47 | -01:51:50 | 18.905 | 17.721 | 16.785 | 16.141 | ... | ... | 8.32 | 27.02 | L5.0 ± 0.5 | ... |
| BRLT101 | 09:26:59 | -00:56:11 | 19.255 | 17.972 | 17.369 | 16.893 | ... | ... | 7.04 | 25.65 | L3.0 ± 1.0 | ... |
| BRLT102 | 09:31:30 | -02:09:03 | 19.139 | 18.092 | 17.313 | 16.766 | ... | ... | 7.27 | 32.70 | L0.0 ± 0.5 | ... |
| BRLT103 | 09:35:13 | +01:23:47 | 18.514 | 17.354 | 16.595 | 16.062 | 22.357 | 20.226 | 7.61 | 23.69 | L5.5 ± 0.5 | ... |
| BRLT104 | 09:37:45 | +07:19:03 | 19.060 | 18.024 | 17.187 | 16.505 | 22.233 | 20.459 | 5.03 | 13.28 | M9.0 ± 0.5 | ... |
| BRLT105 | 09:39:31 | +06:53:10 | 18.083 | 16.787 | 15.863 | 15.160 | 21.697 | 19.616 | 7.73 | 32.87 | L5.0 ± 0.5 | ... |
| BRLT106 | 09:40:07 | +02:10:51 | 18.583 | 17.469 | 16.869 | 16.225 | ... | ... | 9.26 | 27.08 | M9.0 ± 0.5 | ... |
| BRLT108 | 09:41:37 | +09:42:14 | 18.883 | 17.511 | 16.458 | 15.552 | 23.163 | 20.422 | 8.92 | 35.42 | L6.5 ± 0.5 | ... |
| BRLT111 | 09:44:20 | +02:44:23 | 19.406 | 18.051 | 17.115 | 16.417 | ... | ... | 10.58 | 25.35 | L2.0 ± 0.5 | ... |
| BRLT112 | 09:47:42 | +07:42:32 | 18.822 | 17.760 | 17.062 | 16.404 | 22.408 | 20.502 | 8.43 | 22.14 | L1.0 ± 0.5 | ... |
| BRLT113 | 09:47:59 | +07:43:05 | 18.830 | 17.783 | 17.154 | 16.577 | 23.940 | 20.293 | 5.46 | 26.29 | M9.0 ± 0.5 | ... |
| BRLT114 | 09:51:27 | +07:57:57 | 18.723 | 17.620 | 16.635 | 15.866 | 22.609 | 20.150 | 7.93 | 38.68 | L6.0 ± 0.5 | ... |
| BRLT116 | 09:54:01 | +09:22:14 | 18.899 | 17.705 | 17.332 | 16.860 | ... | ... | 5.91 | 21.46 | T2.5 ± 0.5 | ... |
| BRLT117 | 09:56:07 | +08:21:16 | 19.301 | 17.982 | 17.096 | 16.463 | 23.155 | 20.451 | 9.43 | 29.42 | L5.0 ± 0.5 | ... |
| BRLT119 | 10:03:11 | +07:52:20 | 19.084 | 17.726 | 16.868 | 16.207 | ... | ... | 9.05 | 28.70 | L4.0 ± 0.5 | ... |

Continued on the next page.

Continued from the previous page.

| Name | RA | Dec | Y | J | H | K | $i$ | $z$ | VIS SNR | NIR SNR | Spectral type | Ref. |
|---|---|---|---|---|---|---|---|---|---|---|---|---|
| BRLT121 | 10:06:47 | +12:11:17 | 18.799 | 17.639 | 16.965 | 16.342 | 22.071 | 20.225 | 9.74 | 25.35 | L1.0 ± 0.5 | ... |
| BRLT122 | 10:07:04 | +01:30:17 | 18.963 | 17.693 | 16.949 | 16.259 | 22.265 | 20.123 | 7.77 | 21.10 | L1.0 ± 0.5 | ... |
| BRLT123 | 10:07:31 | +10:47:59 | 18.899 | 17.634 | 16.851 | 16.241 | 22.583 | 20.285 | 9.04 | 25.23 | L2.0 ± 0.5 | ... |
| BRLT129 | 10:16:19 | +00:00:28 | 18.672 | 17.442 | 16.553 | 15.756 | ... | ... | 6.47 | 39.09 | L5.0 ± 1.0 | ... |
| BRLT130 | 10:16:58 | -01:32:58 | 18.841 | 17.939 | 17.479 | 16.989 | ... | ... | 7.69 | 24.28 | L3.0 ± 1.0 | ... |
| BRLT131 | 10:21:10 | -03:04:20 | 17.037 | 15.916 | 15.578 | 15.373 | 23.577 | 19.297 | 3.15 | 20.90 | T3.0 ± 0.5 | 7 |
| BRLT133 | 10:35:54 | -01:21:26 | 19.007 | 17.872 | 17.317 | 16.738 | ... | ... | 10.77 | 27.30 | M9.0 ± 0.5 | ... |
| BRLT135 | 10:48:29 | +09:19:39 | 17.574 | 16.451 | 15.966 | 15.933 | 24.254 | 19.699 | 2.00 | 20.55 | T2.5 ± 0.5 | 8 |
| BRLT136 | 10:58:37 | +08:54:29 | 19.160 | 18.059 | 17.277 | 16.764 | 22.426 | 20.458 | 10.35 | 24.84 | L1.0 ± 1.0 | ... |
| BRLT137 | 11:19:29 | +00:21:33 | 18.806 | 17.501 | 16.652 | 15.935 | 22.336 | 20.179 | 4.94 | 20.79 | L4.5 ± 0.5 | ... |
| BRLT138 | 11:20:30 | -00:44:41 | 18.226 | 16.933 | 16.033 | 15.399 | 21.631 | 19.582 | 8.23 | 34.66 | L2.0 ± 1.0 | ... |
| BRLT139 | 11:20:43 | +09:04:30 | 19.146 | 17.829 | 17.143 | ... | ... | ... | 9.45 | 25.78 | L4.0 ± 1.0 | ... |
| BRLT140 | 11:31:51 | -00:26:21 | 19.277 | 18.077 | 17.474 | 16.907 | ... | ... | 9.02 | 27.84 | L0.0 ± 0.5 | ... |
| BRLT142 | 11:38:50 | -00:24:51 | 18.129 | 16.840 | 15.910 | 15.229 | 21.715 | 19.677 | 4.04 | 36.63 | L2.5 ± 0.5 | ... |
| BRLT144 | 11:41:05 | +09:16:48 | 18.658 | 17.354 | 16.684 | 16.091 | 22.471 | 20.041 | 7.91 | 24.33 | L5.0 ± 1.0 | ... |
| BRLT145 | 11:44:18 | +09:10:25 | 19.199 | 17.995 | 17.201 | 16.533 | 23.103 | 20.944 | 10.22 | 26.49 | L1.0 ± 0.5 | ... |
| BRLT147 | 11:57:59 | +09:22:01 | 17.985 | 16.840 | 16.439 | 16.272 | 25.500 | 19.879 | 2.01 | 16.30 | T3.0 ± 0.5 | 9 |
| BRLT149 | 12:00:10 | +12:08:21 | 18.976 | 17.584 | 16.795 | 16.216 | ... | ... | 5.36 | 25.62 | L6.0 ± 1.0 | ... |
| BRLT152 | 12:03:15 | +09:50:55 | 19.004 | 17.937 | 17.309 | 16.741 | 22.258 | 20.683 | 8.60 | 27.45 | L0.0 ± 0.5 | ... |
| BRLT153 | 12:03:24 | -01:56:56 | 18.816 | 17.726 | 17.208 | 16.708 | 22.381 | 20.356 | 8.55 | 25.22 | L1.0 ± 0.5 | ... |
| BRLT155 | 12:05:46 | +08:42:07 | 18.522 | 17.260 | 16.356 | 15.707 | 22.072 | 19.847 | 6.33 | 30.66 | L3.0 ± 1.0 | ... |
| BRLT159 | 12:09:43 | +06:53:33 | 19.460 | 18.096 | 17.166 | 16.590 | 23.362 | 20.845 | 6.46 | 30.35 | L9.0 ± 0.5 | ... |
| BRLT162 | 12:12:39 | +00:07:22 | 16.791 | 15.683 | 15.037 | 14.460 | 20.286 | 18.381 | 10.49 | 44.28 | L0.5 ± 0.5 | ... |
| BRLT163 | 12:13:21 | +15:02:35 | 18.776 | 17.647 | 16.865 | 16.203 | ... | ... | 7.79 | 25.27 | L1.0 ± 0.5 | ... |
| BRLT164 | 12:13:56 | +05:35:17 | 18.933 | 17.881 | 17.616 | 17.638 | ... | ... | 5.57 | 18.97 | T3.0 ± 0.5 | ... |
| BRLT165 | 12:18:17 | +13:49:54 | 19.147 | 17.953 | 17.320 | 16.599 | ... | ... | 8.32 | 24.48 | L2.0 ± 0.5 | ... |
| BRLT168 | 12:21:12 | +12:22:17 | 19.390 | 17.973 | 17.092 | 16.312 | 22.365 | 20.770 | 6.30 | 27.94 | L4.0 ± 0.5 | ... |

Continued on the next page.

Continued from the previous page.

| Name | RA | Dec | Y | J | H | K | $i$ | $z$ | VIS SNR | NIR SNR | Spectral type | Ref. |
|---|---|---|---|---|---|---|---|---|---|---|---|---|
| BRLT171 | 12:23:26 | +04:48:28 | 17.681 | 16.372 | 15.448 | 14.651 | 21.467 | 19.339 | 9.12 | 42.31 | L5.0 ± 0.5 | ... |
| BRLT176 | 12:30:13 | +07:17:18 | 18.821 | 17.564 | 16.794 | 16.109 | 22.606 | 20.248 | 4.05 | 27.45 | L4.0 ± 1.0 | ... |
| BRLT179 | 12:33:27 | +12:19:52 | 19.006 | 18.019 | 18.219 | ... | 22.337 | 22.421 | 2.53 | 7.29 | T4.5 ± 0.5 | 6 |
| BRLT181 | 12:34:34 | +01:07:42 | 19.113 | 17.823 | 17.093 | 16.379 | 22.604 | 20.578 | 5.29 | 24.59 | L1.0 ± 1.0 | ... |
| BRLT182 | 12:38:46 | +12:47:38 | 18.779 | 17.718 | 17.098 | 16.668 | ... | ... | 4.37 | 23.43 | T3.0 ± 0.5 | ... |
| BRLT186 | 12:40:53 | +11:29:40 | 16.595 | 15.508 | 14.828 | 14.242 | 21.519 | 18.195 | 13.58 | 47.07 | L1.0 ± 1.0 | ... |
| BRLT190 | 12:44:13 | +12:32:01 | 18.890 | 17.641 | 17.418 | 17.455 | ... | ... | 1.16 | 8.75 | T4.0 ± 0.5 | ... |
| BRLT197 | 13:04:36 | +15:42:53 | 18.611 | 17.189 | 16.440 | 15.863 | 23.610 | 20.210 | 2.38 | 21.55 | T2.0 ± 1.0 | ... |
| BRLT198 | 13:11:07 | -01:37:52 | 19.004 | 17.832 | 17.282 | 16.632 | 22.491 | 20.595 | 10.83 | 29.20 | L3.0 ± 1.0 | ... |
| BRLT202 | 13:13:07 | +12:35:41 | 18.577 | 17.425 | 16.907 | 16.504 | 23.616 | 20.715 | 1.97 | 20.74 | T2.5 ± 0.5 | ... |
| BRLT203 | 13:16:10 | +03:12:06 | 17.998 | 16.746 | 16.129 | 15.431 | 22.830 | 20.043 | 3.43 | 25.58 | T3.0 ± 1.0 | ... |
| BRLT206 | 13:24:10 | +02:50:41 | 19.394 | 18.072 | 17.254 | 16.655 | 22.671 | 20.675 | 9.16 | 26.18 | L2.0 ± 0.5 | ... |
| BRLT207 | 13:26:30 | -00:38:33 | 17.592 | 16.220 | 15.111 | 14.171 | 21.716 | 19.074 | 5.46 | 49.32 | L7.0 ± 0.5 | 10 |
| BRLT210 | 13:27:21 | +10:11:39 | 18.812 | 17.481 | 16.579 | 15.828 | 22.928 | 20.278 | 3.44 | 28.88 | L4.5 ± 0.5 | ... |
| BRLT212 | 13:31:49 | -01:17:01 | 16.497 | 15.330 | 14.670 | 14.050 | ... | ... | 10.56 | 32.34 | L6.0 ± 1.0 | 3 |
| BRLT216 | 13:43:23 | -01:08:44 | 18.479 | 17.428 | 16.714 | 16.224 | 21.869 | 20.056 | 8.53 | 33.27 | M9.0 ± 0.5 | ... |
| BRLT217 | 13:44:04 | +08:39:51 | 18.390 | 17.257 | 16.454 | 15.955 | 23.064 | 20.005 | 8.64 | 35.52 | T0.0 ± 0.5 | ... |
| BRLT218 | 13:44:15 | +09:24:05 | 18.624 | 17.287 | 16.301 | 15.460 | 22.786 | 20.206 | 9.08 | 33.20 | L6.0 ± 0.5 | ... |
| BRLT219 | 13:44:37 | +11:09:58 | 18.441 | 17.218 | 16.922 | 16.933 | 24.732 | 20.648 | 0.62 | 12.08 | T3.0 ± 0.5 | ... |
| BRLT220 | 13:46:13 | +08:25:03 | 19.356 | 18.004 | 17.257 | 16.499 | 22.836 | 20.433 | 9.37 | 27.53 | L2.0 ± 0.5 | ... |
| BRLT227 | 13:55:56 | +08:50:54 | 18.667 | 17.297 | 16.384 | 15.629 | 22.199 | 20.281 | 10.66 | 30.40 | L3.0 ± 0.5 | ... |
| BRLT229 | 13:58:49 | +01:47:46 | 18.493 | 17.620 | 16.995 | 16.520 | 22.004 | 20.070 | 9.59 | 30.86 | M8.0 ± 0.5 | ... |
| BRLT231 | 14:01:52 | +09:07:33 | 18.640 | 17.320 | 16.398 | 15.625 | 22.715 | 20.288 | 6.57 | 28.27 | L5.0 ± 0.5 | ... |
| BRLT232 | 14:02:56 | +08:00:55 | 17.990 | 16.836 | 16.203 | 15.706 | 22.965 | 19.938 | 1.99 | 25.79 | T2.5 ± 0.5 | 8 |
| BRLT234 | 14:12:04 | +12:16:10 | 17.540 | 16.325 | 15.851 | 15.430 | 21.322 | 19.150 | 7.82 | 30.39 | L4.0 ± 1.0 | ... |
| BRLT236 | 14:14:06 | +01:07:09 | 18.118 | 16.791 | 15.958 | 15.204 | 21.727 | 19.605 | 4.59 | 23.64 | L3.5 ± 0.5 | ... |
| BRLT237 | 14:17:10 | +13:17:37 | 18.051 | 16.689 | 15.911 | 15.208 | 21.678 | 19.637 | 7.68 | 26.76 | L5.0 ± 0.5 | ... |

Continued on the next page.

Continued from the previous page.

| Name | RA | Dec | Y | J | H | K | $i$ | $z$ | VIS SNR | NIR SNR | Spectral type | Ref. |
|---|---|---|---|---|---|---|---|---|---|---|---|---|
| BRLT240 | 14:23:00 | +04:10:26 | 18.818 | 17.385 | 16.548 | 15.796 | 22.215 | 20.056 | 6.46 | 31.67 | L3.0 ± 0.5 | ... |
| BRLT243 | 14:27:18 | +01:12:06 | 18.831 | 17.481 | 16.746 | 16.386 | 22.675 | 20.267 | 4.87 | 30.52 | T0.0 ± 0.5 | ... |
| BRLT247 | 14:32:57 | +12:28:09 | 18.626 | 17.630 | 16.911 | 16.356 | ... | ... | 7.53 | 23.19 | M9.0 ± 0.5 | ... |
| BRLT249 | 14:36:16 | +07:20:57 | 18.524 | 17.104 | 16.180 | 15.531 | 22.546 | 20.042 | 7.90 | 34.97 | L5.0 ± 0.5 | ... |
| BRLT250 | 14:36:24 | +01:42:58 | 18.980 | 17.603 | 16.785 | 16.061 | 22.865 | 20.446 | 8.46 | 32.04 | L1.0 ± 0.5 | ... |
| BRLT251 | 14:37:06 | +11:59:30 | 18.855 | 17.686 | 17.130 | 16.539 | 22.401 | 20.291 | 7.68 | 31.75 | L1.0 ± 0.5 | ... |
| BRLT253 | 14:41:52 | +04:37:39 | 18.443 | 17.326 | 16.784 | 16.407 | ... | ... | 8.42 | 28.94 | L1.0 ± 1.0 | ... |
| BRLT254 | 14:42:21 | +08:49:46 | 18.600 | 17.302 | 16.428 | 15.710 | 22.443 | 20.123 | 8.39 | 30.44 | L5.0 ± 0.5 | ... |
| BRLT258 | 14:46:01 | +00:24:51 | 16.895 | 15.584 | 14.656 | 13.921 | 20.759 | 18.572 | 3.51 | 26.13 | L5.0 ± 1.0 | 2 |
| BRLT260 | 14:48:13 | -00:00:19 | 18.870 | 17.597 | 17.121 | 16.553 | 22.480 | 20.492 | 6.89 | 29.53 | L2.0 ± 1.0 | ... |
| BRLT262 | 14:52:31 | +03:39:44 | 19.367 | 18.066 | 17.193 | 16.514 | ... | ... | 9.50 | 31.08 | L0.0 ± 0.5 | ... |
| BRLT265 | 14:55:42 | +00:22:24 | 18.864 | 17.607 | 16.727 | 15.975 | 22.459 | 20.169 | 7.40 | 26.40 | L2.0 ± 0.5 | ... |
| BRLT269 | 15:01:41 | -00:51:47 | 19.254 | 17.573 | 16.556 | 15.618 | ... | ... | 6.16 | 26.68 | L7.0 ± 0.5 | ... |
| BRLT270 | 15:05:32 | +01:02:33 | 18.635 | 17.441 | 16.865 | 16.433 | 22.730 | 20.099 | 7.85 | 25.51 | L2.0 ± 1.0 | ... |
| BRLT274 | 15:09:28 | +03:44:50 | 18.809 | 17.245 | 16.178 | 15.261 | ... | ... | 6.17 | 29.30 | L2.0 ± 0.5 | ... |
| BRLT275 | 15:11:15 | +06:07:41 | 17.220 | 15.877 | 15.182 | 14.439 | 21.672 | 19.200 | 3.98 | 23.51 | T2.0 ± 2.0 | 8 |
| BRLT276 | 15:11:46 | -02:17:27 | 18.584 | 17.419 | 16.779 | 16.235 | ... | ... | 8.36 | 34.20 | L0.0 ± 0.5 | ... |
| BRLT279 | 15:13:55 | -01:33:01 | 17.899 | 16.758 | 16.072 | 15.470 | 21.477 | 19.308 | 9.09 | 38.71 | L1.0 ± 0.5 | ... |
| BRLT281 | 15:16:03 | +02:59:28 | 17.959 | 16.877 | 16.075 | 15.437 | 22.996 | 19.709 | 9.25 | 37.53 | T0.0 ± 0.5 | 4 |
| BRLT283 | 15:16:50 | +08:36:07 | 18.741 | 17.348 | 16.705 | 16.258 | 22.693 | 20.374 | 7.09 | 27.39 | L5.0 ± 1.0 | ... |
| BRLT285 | 15:18:21 | +08:55:18 | 18.618 | 17.419 | 16.530 | 15.777 | 22.552 | 20.194 | 6.21 | 24.53 | L5.0 ± 0.5 | ... |
| BRLT286 | 15:19:13 | -00:00:30 | 18.193 | 17.206 | 17.066 | 16.968 | ... | ... | 8.38 | 27.74 | M8.0 ± 3.0 | ... |
| BRLT287 | 15:21:03 | +01:31:43 | 17.339 | 16.097 | 15.678 | 15.568 | 24.750 | 19.606 | 2.23 | 22.09 | T3.0 ± 0.5 | 4 |
| BRLT290 | 15:25:02 | +08:33:44 | 18.249 | 17.169 | 16.617 | 16.216 | 22.843 | 20.367 | 5.64 | 21.74 | T2.0 ± 0.5 | ... |
| BRLT295 | 15:31:28 | +07:37:55 | 17.851 | 16.606 | 16.021 | 15.445 | 21.547 | 19.457 | 6.07 | 31.26 | L4.0 ± 2.0 | ... |
| BRLT296 | 15:31:57 | +03:36:06 | 18.466 | 17.284 | 16.401 | 15.749 | 22.327 | 19.950 | 5.02 | 30.91 | L4.0 ± 0.5 | ... |
| BRLT297 | 15:32:57 | -02:25:11 | 19.128 | 17.646 | 16.827 | 16.056 | ... | ... | 4.69 | 25.33 | L4.5 ± 0.5 | ... |

Continued on the next page.

Continued from the previous page.

| Name | RA | Dec | Y | J | H | K | $i$ | $z$ | VIS SNR | NIR SNR | Spectral type | Ref. |
|---|---|---|---|---|---|---|---|---|---|---|---|---|
| BRLT299 | 15:40:39 | -00:12:57 | 17.837 | 16.625 | 15.813 | 15.174 | 21.660 | 19.342 | 4.73 | 40.48 | L4.0 ± 1.0 | ... |
| BRLT301 | 15:43:20 | +08:04:46 | 18.862 | 17.654 | 16.937 | 16.536 | 21.990 | 20.335 | 7.25 | 20.65 | L1.0 ± 0.5 | ... |
| BRLT302 | 15:44:49 | +09:42:57 | 18.802 | 17.671 | 16.979 | 16.367 | 22.722 | 20.258 | 7.40 | 20.23 | L4.0 ± 1.0 | ... |
| BRLT305 | 21:57:00 | +00:56:15 | 19.258 | 17.852 | 16.873 | 16.105 | 22.274 | 20.617 | 3.49 | 17.58 | L5.5 ± 1.0 | 1 |
| BRLT306 | 21:59:20 | +00:33:10 | 19.090 | 17.734 | 16.992 | 16.365 | 23.008 | 20.497 | 3.49 | 24.25 | L4.5 ± 0.5 | 1 |
| BRLT307 | 22:09:17 | -00:53:00 | 19.348 | 18.005 | 17.262 | 16.635 | 22.796 | 20.481 | 5.68 | 23.11 | L1.0 ± 0.5 | 1 |
| BRLT308 | 22:19:04 | +06:30:59 | 19.521 | 18.120 | 17.203 | 16.442 | ... | ... | 4.60 | 26.89 | L5.0 ± 0.5 | ... |
| BRLT309 | 22:27:11 | -00:45:47 | 19.501 | 18.110 | 16.612 | 15.323 | ... | ... | 3.47 | 37.51 | L7.0 ± 0.5 | 11 |
| BRLT311 | 22:29:58 | +01:02:17 | 19.106 | 17.884 | 17.498 | 17.217 | ... | ... | 1.82 | 14.40 | T3.0 ± 0.5 | 1 |
| BRLT312 | 22:33:48 | +00:22:14 | 19.119 | 18.068 | 17.360 | 16.640 | 21.933 | 21.517 | 3.58 | 20.80 | T0.0 ± 0.5 | 1 |
| BRLT313 | 22:36:37 | +01:11:32 | 18.447 | 17.109 | 16.239 | 15.474 | 22.178 | 20.148 | 6.02 | 33.56 | L3.5 ± 0.5 | 1 |
| BRLT314 | 22:37:57 | +07:16:57 | 18.870 | 17.490 | 16.447 | 15.655 | 23.195 | 20.464 | 2.92 | 30.49 | L7.5 ± 0.5 | 1 |
| BRLT315 | 22:40:52 | +00:08:22 | 19.275 | 17.819 | 17.117 | 16.576 | 22.285 | 20.258 | 3.04 | 22.23 | L1.0 ± 1.0 | 1 |
| BRLT316 | 22:49:23 | +07:15:28 | 19.638 | 18.089 | 17.541 | 16.854 | ... | ... | 4.23 | 19.82 | L1.0 ± 0.5 | 1 |
| BRLT317 | 22:50:16 | +08:08:22 | 16.669 | 15.502 | 15.047 | 14.512 | 20.356 | 18.242 | 9.45 | 41.47 | L3.0 ± 1.0 | 1 |
| BRLT318 | 22:51:15 | -00:07:24 | 19.208 | 17.950 | 17.353 | 16.493 | 22.113 | 21.147 | 6.86 | 20.87 | L1.0 ± 0.5 | 1 |
| BRLT319 | 22:56:25 | +06:21:53 | 19.442 | 18.140 | 17.933 | 17.651 | ... | ... | 2.07 | 14.22 | T3.0 ± 0.5 | ... |
| BRLT320 | 22:56:31 | +07:24:39 | 19.421 | 17.944 | 17.260 | 16.732 | 23.099 | 20.649 | 5.70 | 18.63 | M9.0 ± 0.5 | 1 |
| BRLT321 | 23:02:03 | +07:00:39 | 18.953 | 17.624 | 17.378 | 17.514 | ... | ... | 2.31 | 12.97 | T4.0 ± 0.5 | 1 |
| BRLT322 | 23:03:59 | +00:58:07 | 19.029 | 17.820 | 16.988 | 16.150 | 23.271 | 20.677 | 4.09 | 29.30 | L5.0 ± 0.5 | 1 |
| BRLT323 | 23:04:25 | +13:01:11 | 18.001 | 16.691 | 15.926 | 15.202 | 21.527 | 19.469 | 5.57 | 30.05 | L5.0 ± 1.0 | 1 |
| BRLT325 | 23:04:34 | +08:04:01 | 19.119 | 17.887 | 17.478 | 17.218 | ... | ... | 1.39 | 12.98 | T2.0 ± 1.0 | 1 |
| BRLT328 | 23:12:37 | +00:06:02 | 18.955 | 17.653 | 17.051 | 16.407 | 22.348 | 20.275 | 6.57 | 17.54 | L3.0 ± 1.0 | 1 |
| BRLT330 | 23:16:46 | +01:00:13 | 19.100 | 17.949 | 17.262 | 16.700 | 23.016 | 21.075 | 4.25 | 19.87 | L2.0 ± 1.0 | 1 |
| BRLT331 | 23:21:23 | -00:45:57 | 19.402 | 18.004 | 17.603 | 17.125 | 22.963 | 20.525 | 4.44 | 19.14 | L3.0 ± 1.0 | 1 |
| BRLT332 | 23:23:00 | +00:05:42 | 19.163 | 18.008 | 17.264 | 16.855 | 22.706 | 20.539 | 7.05 | 23.72 | L3.0 ± 1.0 | 1 |
| BRLT333 | 23:23:15 | +07:19:31 | 18.501 | 17.301 | 16.550 | 16.199 | 23.726 | 20.348 | 1.13 | 21.36 | T2.0 ± 0.5 | 1 |

Continued on the next page.

Continued from the previous page.

| Name | RA | Dec | Y | J | H | K | $i$ | $z$ | VIS SNR | NIR SNR | Spectral type | Ref. |
|---|---|---|---|---|---|---|---|---|---|---|---|---|
| BRLT334 | 23:27:16 | +15:17:30 | 17.541 | 16.202 | 15.357 | 14.683 | 21.297 | 19.170 | 3.39 | 31.77 | L3.5 ± 0.5 | 1 |
| BRLT335 | 23:27:32 | +01:02:53 | 19.261 | 18.068 | 17.235 | 16.608 | ... | ... | 5.69 | 22.66 | L4.0 ± 1.0 | 1 |
| BRLT338 | 23:30:02 | +14:03:30 | 18.592 | 17.366 | 16.792 | 16.104 | ... | ... | 6.57 | 19.58 | L1.0 ± 1.0 | 1 |
| BRLT340 | 23:39:43 | +07:53:27 | 19.840 | 18.130 | 17.333 | 16.542 | ... | ... | 3.20 | 23.92 | L4.0 ± 0.5 | ... |
| BRLT343 | 23:47:17 | -01:10:09 | 18.816 | 17.571 | 16.719 | 15.899 | 22.616 | 20.268 | 5.00 | 33.95 | L9.0 ± 1.0 | 1 |
| BRLT344 | 23:56:18 | +07:54:20 | 19.601 | 18.088 | 16.986 | 16.215 | ... | ... | 3.88 | 25.05 | T0.0 ± 1.0 | 1 |

Table 3.1: The objects observed. Discovery reference: (1) Day-Jones et al. (2013); (2) Geballe et al. (2002); (3) Hawley et al. (2002); (4) Knapp et al. (2004); (5) Burningham et al. (2013); (6) Burningham et al. (2010b); (7) Leggett et al. (2000); (8) Chiu et al. (2006); (9) Pinfield et al. (2008); (10) Fan et al. (2000); (11) Marocco et al. (2014). If no discovery reference is listed, the object is unpublished.

### 3.4.1 Spectral classification

Spectral types of the targets were determined via $\chi^2$ fitting with standard templates. The template spectra were taken from the SpeX-Prism online library[1]. Each of the targets was smoothed down to the resolution of the templates (R=120), and I excluded the noisy telluric bands when computing the statistic. I visually inspected the three best fit templates to check the accuracy of the fit and to identify possible peculiar objects (see Section 3.4.3). The spectral types obtained are listed in the second column of Table 3.2, along with the spectral indices determined for the spectra. The uncertainty on the spectral types was determined from the width of the $\chi^2$ distribution.

It must be noted at this point that the lower SNR in the red-optical portion of the spectrum results in the final spectral type being essentially based on the NIR spectrum. However, as discussed in Section 1.5.2, NIR and optical types are normally in good agreement, as demonstrated by many authors (e.g. Reid et al., 2001b; Testi et al., 2001; McLean et al., 2003).

Not surprisingly however, a number of objects in the sample did not provide good fit when compared to the standard templates. I discuss in the following sections how I identified the peculiar objects and how I assigned their spectral types.

| Name | Spectral type | $H_2O$-J | $H_2O$-H | $H_2O$-K | $CH_4$-J | $CH_4$-H | $CH_4$-K | K/J | H-dip |
|---|---|---|---|---|---|---|---|---|---|
| BRLT1 | L9.0 ± 0.5 | 0.73 | 0.71 | 0.89 | 0.75 | 1.04 | 0.78 | 0.60 | 0.50 |
| BRLT2 | L1.0 ± 1.0 | 0.94 | 0.79 | 1.11 | 0.81 | 1.08 | 1.07 | 0.41 | 0.48 |
| BRLT3 | L9.0 ± 1.0 | 0.76 | 0.70 | 0.88 | 0.74 | 1.05 | 0.90 | 0.58 | 0.51 |
| BRLT6 | L3.0 ± 1.0 | 0.85 | 0.80 | 1.02 | 0.83 | 1.11 | 1.08 | 0.47 | 0.48 |
| BRLT7 | M8.0 ± 1.0 | 0.96 | 0.88 | 1.19 | 0.87 | 1.03 | 0.95 | 0.35 | 0.49 |
| BRLT8 | L8.5 ± 0.5 | 0.71 | 0.76 | 0.87 | 0.78 | 1.04 | 0.90 | 0.67 | 0.50 |
| BRLT9 | L1.0 ± 1.0 | 0.96 | 0.84 | 1.00 | 0.86 | 1.03 | 0.95 | 0.37 | 0.48 |
| BRLT10 | L9.0 ± 0.5 | 0.67 | 0.70 | 0.79 | 0.77 | 1.05 | 0.85 | 0.64 | 0.51 |
| BRLT12 | L3.0 ± 1.0 | 0.75 | 0.79 | 1.00 | 0.75 | 1.05 | 1.03 | 0.44 | 0.48 |
| BRLT14 | L0.0 ± 0.5 | 0.97 | 0.85 | 1.14 | 0.86 | 1.02 | 1.06 | 0.37 | 0.48 |
| BRLT15 | T2.0 ± 2.0 | 0.50 | 0.61 | 0.82 | 0.58 | 0.92 | 0.76 | 0.53 | 0.47 |
| BRLT16 | L2.0 ± 1.0 | 0.91 | 0.80 | 0.96 | 0.83 | 0.93 | 0.96 | 0.42 | 0.45 |
| BRLT18 | L0.0 ± 1.0 | 1.03 | 0.91 | 1.07 | 0.95 | 1.00 | 0.98 | 0.39 | 0.49 |
| BRLT20 | L1.0 ± 1.0 | 0.87 | 0.77 | 1.03 | 0.76 | 0.99 | 0.94 | 0.32 | 0.48 |
| BRLT21 | L3.5 ± 0.5 | 0.83 | 0.75 | 0.95 | 0.81 | 1.01 | 0.98 | 0.46 | 0.48 |
| BRLT22 | M8.0 ± 0.5 | 1.01 | 0.89 | 1.20 | 0.87 | 1.07 | 0.93 | 0.32 | 0.51 |
| BRLT24 | L3.5 ± 0.5 | 0.80 | 0.74 | 0.99 | 0.81 | 1.00 | 0.99 | 0.47 | 0.47 |
| BRLT26 | L5.5 ± 0.5 | 0.80 | 0.72 | 0.91 | 0.81 | 1.07 | 0.97 | 0.53 | 0.49 |
| BRLT27 | T0.0 ± 0.5 | 0.63 | 0.65 | 0.78 | 0.63 | 1.01 | 0.59 | 0.43 | 0.50 |
| BRLT28 | L6.0 ± 0.5 | 0.72 | 0.69 | 0.88 | 0.79 | 1.04 | 0.91 | 0.62 | 0.48 |
| BRLT30 | L5.0 ± 0.5 | 0.75 | 0.75 | 0.95 | 0.79 | 1.08 | 1.02 | 0.51 | 0.48 |
| BRLT31 | L4.0 ± 1.0 | 0.74 | 0.70 | 0.92 | 0.78 | 1.04 | 0.86 | 0.51 | 0.50 |
| BRLT32 | L1.5 ± 0.5 | 0.86 | 0.79 | 1.08 | 0.83 | 1.04 | 1.05 | 0.41 | 0.49 |
| BRLT33 | L3.5 ± 0.5 | 0.82 | 0.74 | 0.96 | 0.81 | 0.94 | 0.94 | 0.42 | 0.48 |
| BRLT35 | M9.5 ± 0.5 | 0.98 | 0.88 | 1.08 | 0.93 | 1.01 | 1.04 | 0.40 | 0.49 |
| BRLT37 | L5.0 ± 0.5 | 0.71 | 0.71 | 0.85 | 0.76 | 1.10 | 0.96 | 0.53 | 0.51 |
| BRLT38 | T0.0 ± 0.5 | 0.66 | 0.65 | 0.77 | 0.68 | 0.96 | 0.67 | 0.41 | 0.51 |
| BRLT39 | L5.0 ± 1.0 | 0.80 | 0.75 | 0.93 | 0.78 | 1.07 | 0.95 | 0.46 | 0.49 |
| BRLT42 | M9.0 ± 0.5 | 1.05 | 0.95 | 1.20 | 0.96 | 1.00 | 0.96 | 0.43 | 0.49 |
| BRLT44 | L5.0 ± 1.0 | 0.73 | 0.76 | 0.84 | 0.74 | 1.01 | 0.82 | 0.53 | 0.50 |
| BRLT45 | T1.0 ± 0.5 | 0.58 | 0.61 | 0.72 | 0.64 | 0.89 | 0.57 | 0.42 | 0.47 |
| BRLT46 | L0.5 ± 0.5 | 0.92 | 0.76 | 1.14 | 0.81 | 1.13 | 1.08 | 0.30 | 0.49 |
| BRLT48 | L4.5 ± 0.5 | 0.78 | 0.77 | 1.05 | 0.81 | 1.20 | 1.09 | 0.56 | 0.49 |
| BRLT49 | M9.0 ± 0.5 | 0.99 | 0.87 | 1.09 | 0.86 | 1.00 | 1.06 | 0.36 | 0.49 |

Continued on the next page.

[1]http://pono.ucsd.edu/ adam/browndwarfs/spexprism/index.html

Continued from the previous page.

| Name | Spectral type | $H_2O$-J | $H_2O$-H | $H_2O$-K | $CH_4$-J | $CH_4$-H | $CH_4$-K | K/J | H-dip |
|---|---|---|---|---|---|---|---|---|---|
| BRLT50 | T6.0 ± 0.5 | 0.16 | 0.34 | 0.84 | 0.28 | 0.25 | 0.03 | 0.07 | 0.21 |
| BRLT51 | L3.0 ± 1.0 | 0.81 | 0.79 | 0.94 | 0.83 | 1.07 | 1.02 | 0.51 | 0.48 |
| BRLT52 | L5.5 ± 0.5 | 0.76 | 0.69 | 0.95 | 0.77 | 1.06 | 0.94 | 0.58 | 0.51 |
| BRLT56 | L1.5 ± 1.0 | 0.92 | 0.85 | 0.94 | 0.86 | 1.01 | 0.97 | 0.45 | 0.49 |
| BRLT57 | L0.0 ± 1.0 | 0.98 | 0.87 | 1.09 | 0.84 | 1.10 | 0.99 | 0.37 | 0.50 |
| BRLT58 | L4.0 ± 1.0 | 0.76 | 0.73 | 0.84 | 0.74 | 1.06 | 1.02 | 0.41 | 0.51 |
| BRLT60 | L1.0 ± 1.0 | 0.84 | 0.79 | 0.99 | 0.85 | 1.02 | 0.95 | 0.41 | 0.49 |
| BRLT62 | L5.0 ± 1.0 | 0.83 | 0.76 | 0.98 | 0.86 | 1.11 | 1.04 | 0.64 | 0.49 |
| BRLT63 | L1.0 ± 0.5 | 0.97 | 0.82 | 1.11 | 0.87 | 1.01 | 0.98 | 0.41 | 0.49 |
| BRLT64 | L4.0 ± 0.5 | 0.77 | 0.73 | 0.92 | 0.83 | 1.05 | 1.02 | 0.50 | 0.49 |
| BRLT65 | M9.0 ± 0.5 | 0.99 | 0.90 | 1.09 | 0.87 | 1.00 | 1.07 | 0.37 | 0.49 |
| BRLT66 | L5.0 ± 0.5 | 0.74 | 0.69 | 0.92 | 0.80 | 1.09 | 0.95 | 0.52 | 0.48 |
| BRLT67 | L1.0 ± 0.5 | 0.97 | 0.81 | 1.01 | 0.88 | 1.06 | 1.05 | 0.39 | 0.48 |
| BRLT68 | L5.0 ± 0.5 | 0.82 | 0.70 | 0.88 | 0.82 | 1.04 | 0.92 | 0.64 | 0.51 |
| BRLT69 | L1.0 ± 0.5 | 0.95 | 0.86 | 1.08 | 0.92 | 1.04 | 1.07 | 0.41 | 0.48 |
| BRLT71 | L1.5 ± 0.5 | 0.96 | 0.80 | 1.06 | 0.89 | 1.00 | 0.97 | 0.43 | 0.49 |
| BRLT72 | M9.0 ± 0.5 | 1.05 | 0.91 | 1.13 | 0.90 | 1.04 | 1.07 | 0.39 | 0.49 |
| BRLT73 | L1.0 ± 0.5 | 0.93 | 0.85 | 0.99 | 0.84 | 1.12 | 0.92 | 0.44 | 0.50 |
| BRLT74 | L9.5 ± 1.0 | 0.67 | 0.66 | 0.76 | 0.70 | 1.03 | 0.73 | 0.50 | 0.53 |
| BRLT75 | M9.0 ± 1.0 | 1.00 | 0.89 | 1.14 | 0.91 | 1.04 | 1.04 | 0.34 | 0.49 |
| BRLT76 | L5.5 ± 0.5 | 0.78 | 0.81 | 0.97 | 0.82 | 1.08 | 0.96 | 0.57 | 0.49 |
| BRLT78 | L1.0 ± 0.5 | 0.98 | 0.84 | 1.11 | 0.80 | 1.07 | 1.04 | 0.35 | 0.51 |
| BRLT81 | M9.0 ± 0.5 | 1.07 | 0.88 | 1.07 | 0.89 | 1.01 | 0.99 | 0.41 | 0.49 |
| BRLT82 | L1.0 ± 0.5 | 0.94 | 0.85 | 1.07 | 0.88 | 1.05 | 1.02 | 0.43 | 0.49 |
| BRLT83 | M8.0 ± 1.0 | 1.11 | 0.99 | 1.32 | 0.94 | 1.02 | 0.94 | 0.37 | 0.49 |
| BRLT84 | L3.5 ± 0.5 | 0.77 | 0.77 | 0.95 | 0.81 | 1.06 | 1.03 | 0.49 | 0.49 |
| BRLT85 | M8.0 ± 0.5 | 1.07 | 0.87 | 1.31 | 0.87 | 1.10 | 1.04 | 0.28 | 0.50 |
| BRLT87 | T0.0 ± 0.5 | 0.59 | 0.58 | 0.77 | 0.66 | 0.90 | 0.69 | 0.41 | 0.48 |
| BRLT88 | L4.0 ± 1.0 | 0.83 | 0.78 | 1.01 | 0.83 | 1.06 | 1.06 | 0.50 | 0.48 |
| BRLT91 | T3.0 ± 0.5 | 0.47 | 0.46 | 0.68 | 0.53 | 0.79 | 0.49 | 0.25 | 0.47 |
| BRLT92 | L1.0 ± 0.5 | 0.86 | 0.83 | 1.00 | 0.82 | 1.08 | 1.02 | 0.39 | 0.48 |
| BRLT97 | L0.0 ± 1.0 | 0.99 | 0.84 | 1.13 | 0.92 | 1.03 | 0.98 | 0.39 | 0.49 |
| BRLT98 | T4.0 ± 0.5 | 0.37 | 0.39 | 0.57 | 0.49 | 0.59 | 0.37 | 0.15 | 0.46 |
| BRLT99 | L5.0 ± 0.5 | 0.81 | 0.71 | 0.85 | 0.84 | 1.08 | 0.98 | 0.55 | 0.48 |
| BRLT101 | L3.0 ± 1.0 | 0.83 | 0.68 | 0.86 | 0.73 | 1.13 | 1.02 | 0.34 | 0.49 |
| BRLT102 | L0.0 ± 0.5 | 0.94 | 0.88 | 1.06 | 0.91 | 1.03 | 1.05 | 0.42 | 0.49 |
| BRLT103 | L5.5 ± 0.5 | 0.74 | 0.74 | 0.92 | 0.71 | 1.00 | 0.89 | 0.36 | 0.50 |
| BRLT104 | M9.0 ± 0.5 | 1.08 | 0.93 | 0.93 | 0.96 | 0.98 | 0.80 | 0.40 | 0.46 |
| BRLT105 | L5.0 ± 0.5 | 0.82 | 0.78 | 0.96 | 0.84 | 1.07 | 0.99 | 0.53 | 0.48 |
| BRLT106 | M9.0 ± 0.5 | 0.97 | 0.88 | 0.97 | 0.84 | 1.03 | 1.00 | 0.37 | 0.48 |
| BRLT108 | L6.5 ± 0.5 | 0.79 | 0.73 | 0.91 | 0.82 | 1.10 | 1.01 | 0.68 | 0.47 |
| BRLT111 | L2.0 ± 0.5 | 0.86 | 0.77 | 0.90 | 0.81 | 1.05 | 1.06 | 0.53 | 0.48 |
| BRLT112 | L1.0 ± 0.5 | 0.86 | 0.79 | 0.98 | 0.85 | 1.04 | 0.95 | 0.43 | 0.48 |
| BRLT113 | M9.0 ± 0.5 | 1.17 | 0.88 | 1.05 | 0.93 | 1.02 | 1.05 | 0.36 | 0.47 |
| BRLT114 | L6.0 ± 0.5 | 0.76 | 0.73 | 0.91 | 0.82 | 1.08 | 0.93 | 0.68 | 0.52 |
| BRLT116 | T2.5 ± 0.5 | 0.55 | 0.54 | 0.82 | 0.62 | 0.85 | 0.74 | 0.33 | 0.46 |
| BRLT117 | L5.0 ± 1.0 | 0.88 | 0.70 | 0.81 | 0.78 | 1.03 | 0.89 | 0.56 | 0.48 |
| BRLT119 | L4.0 ± 0.5 | 0.87 | 0.76 | 0.90 | 0.86 | 1.03 | 1.01 | 0.51 | 0.46 |
| BRLT121 | L1.0 ± 0.5 | 0.91 | 0.80 | 0.99 | 0.81 | 1.01 | 1.03 | 0.36 | 0.47 |
| BRLT122 | L1.0 ± 0.5 | 0.91 | 0.84 | 0.95 | 0.82 | 1.04 | 0.90 | 0.40 | 0.50 |
| BRLT123 | L2.0 ± 0.5 | 0.95 | 0.80 | 0.94 | 0.85 | 1.03 | 1.05 | 0.47 | 0.46 |
| BRLT129 | L5.0 ± 1.0 | 0.80 | 0.70 | 0.95 | 0.79 | 1.04 | 0.95 | 0.58 | 0.49 |
| BRLT130 | L3.0 ± 1.0 | 0.94 | 0.69 | 0.93 | 0.78 | 1.10 | 1.04 | 0.34 | 0.49 |
| BRLT131 | T3.0 ± 0.5 | 0.38 | 0.45 | 0.65 | 0.48 | 0.71 | 0.49 | 0.27 | 0.45 |
| BRLT133 | M9.0 ± 0.5 | 1.04 | 0.86 | 0.96 | 0.91 | 0.99 | 0.98 | 0.42 | 0.46 |
| BRLT135 | T2.5 ± 0.5 | 0.51 | 0.50 | 0.79 | 0.56 | 0.85 | 0.49 | 0.28 | 0.51 |

Continued on the next page.

Continued from the previous page.

| Name | Spectral type | $H_2O$-J | $H_2O$-H | $H_2O$-K | $CH_4$-J | $CH_4$-H | $CH_4$-K | K/J | H-dip |
|---|---|---|---|---|---|---|---|---|---|
| BRLT136 | L1.0 ± 1.0 | 0.93 | 0.87 | 0.96 | 0.86 | 1.06 | 1.02 | 0.37 | 0.48 |
| BRLT137 | L4.5 ± 0.5 | 0.76 | 0.72 | 0.88 | 0.75 | 1.04 | 0.91 | 0.52 | 0.50 |
| BRLT138 | L2.0 ± 1.0 | 0.88 | 0.82 | 0.97 | 0.86 | 1.06 | 0.98 | 0.50 | 0.49 |
| BRLT139 | L4.0 ± 1.0 | 0.80 | 0.74 | 0.84 | 0.73 | 1.04 | 0.95 | 0.41 | 0.49 |
| BRLT140 | L0.0 ± 0.5 | 0.94 | 0.86 | 0.96 | 0.84 | 1.07 | 1.00 | 0.41 | 0.48 |
| BRLT142 | L2.5 ± 0.5 | 0.85 | 0.82 | 0.97 | 0.85 | 1.08 | 0.98 | 0.54 | 0.49 |
| BRLT144 | L5.0 ± 1.0 | 0.86 | 0.68 | 0.84 | 0.81 | 0.97 | 0.93 | 0.46 | 0.47 |
| BRLT145 | L1.0 ± 0.5 | 0.93 | 0.83 | 1.01 | 0.84 | 1.02 | 0.99 | 0.42 | 0.49 |
| BRLT147 | T3.0 ± 0.5 | 0.44 | 0.49 | 0.64 | 0.48 | 0.79 | 0.50 | 0.26 | 0.45 |
| BRLT149 | L6.0 ± 1.0 | 0.78 | 0.68 | 0.83 | 0.77 | 1.04 | 0.98 | 0.43 | 0.49 |
| BRLT152 | L0.0 ± 0.5 | 1.05 | 0.91 | 0.99 | 0.91 | 1.03 | 1.03 | 0.41 | 0.49 |
| BRLT153 | L1.0 ± 0.5 | 0.91 | 0.84 | 1.02 | 0.82 | 1.06 | 1.02 | 0.34 | 0.48 |
| BRLT155 | L3.0 ± 1.0 | 0.86 | 0.75 | 1.05 | 0.88 | 1.09 | 1.00 | 0.50 | 0.49 |
| BRLT159 | L9.0 ± 0.5 | 0.73 | 0.67 | 0.80 | 0.78 | 1.02 | 0.89 | 0.62 | 0.50 |
| BRLT162 | L0.5 ± 0.5 | 0.97 | 0.86 | 1.11 | 0.84 | 1.06 | 1.06 | 0.35 | 0.49 |
| BRLT163 | L1.0 ± 0.5 | 0.83 | 0.83 | 1.02 | 0.90 | 1.05 | 1.09 | 0.44 | 0.48 |
| BRLT164 | T3.0 ± 0.5 | 0.54 | 0.53 | 0.71 | 0.57 | 0.70 | 0.39 | 0.24 | 0.46 |
| BRLT165 | L2.0 ± 0.5 | 0.92 | 0.86 | 0.95 | 0.90 | 1.04 | 1.03 | 0.46 | 0.50 |
| BRLT168 | L4.0 ± 0.5 | 0.79 | 0.75 | 0.92 | 0.80 | 1.09 | 1.03 | 0.56 | 0.46 |
| BRLT171 | L5.0 ± 0.5 | 0.79 | 0.74 | 0.94 | 0.82 | 1.08 | 1.00 | 0.55 | 0.49 |
| BRLT176 | L4.0 ± 1.0 | 0.87 | 0.77 | 0.96 | 0.79 | 1.01 | 0.96 | 0.44 | 0.49 |
| BRLT179 | T4.5 ± 0.5 | 0.32 | 0.48 | 0.48 | 0.43 | 0.45 | 0.26 | 0.07 | 0.43 |
| BRLT181 | L1.0 ± 1.0 | 1.09 | 0.88 | 1.09 | 0.89 | 1.03 | 1.01 | 0.42 | 0.49 |
| BRLT182 | T3.0 ± 0.5 | 0.51 | 0.50 | 0.74 | 0.57 | 0.79 | 0.61 | 0.37 | 0.44 |
| BRLT186 | L1.0 ± 1.0 | 0.92 | 0.85 | 1.04 | 0.85 | 1.04 | 1.03 | 0.39 | 0.49 |
| BRLT190 | T4.0 ± 0.5 | 0.34 | 0.47 | 0.54 | 0.48 | 0.54 | 0.19 | 0.22 | 0.36 |
| BRLT197 | T2.0 ± 1.0 | 0.54 | 0.64 | 0.87 | 0.66 | 0.88 | 0.70 | 0.44 | 0.47 |
| BRLT198 | L3.0 ± 1.0 | 0.90 | 0.80 | 1.06 | 0.84 | 1.06 | 1.04 | 0.39 | 0.47 |
| BRLT202 | T2.5 ± 0.5 | 0.45 | 0.57 | 0.81 | 0.52 | 0.79 | 0.60 | 0.32 | 0.44 |
| BRLT203 | T3.0 ± 1.0 | 0.39 | 0.58 | 0.82 | 0.53 | 0.81 | 0.74 | 0.46 | 0.44 |
| BRLT206 | L2.0 ± 0.5 | 0.90 | 0.83 | 0.91 | 0.82 | 1.06 | 1.10 | 0.45 | 0.48 |
| BRLT207 | L7.0 ± 0.5 | 0.70 | 0.73 | 0.99 | 0.82 | 1.08 | 0.97 | 0.83 | 0.50 |
| BRLT210 | L4.5 ± 0.5 | 0.77 | 0.75 | 0.96 | 0.82 | 1.09 | 1.01 | 0.54 | 0.49 |
| BRLT212 | L6.0 ± 1.0 | 0.73 | 0.66 | 0.83 | 0.68 | 1.08 | 0.91 | 0.37 | 0.51 |
| BRLT216 | M9.0 ± 0.5 | 1.10 | 0.88 | 1.07 | 0.90 | 1.00 | 0.99 | 0.39 | 0.49 |
| BRLT217 | T0.0 ± 0.5 | 0.69 | 0.66 | 0.89 | 0.75 | 0.94 | 0.78 | 0.50 | 0.52 |
| BRLT218 | L6.0 ± 0.5 | 0.79 | 0.71 | 0.95 | 0.80 | 1.13 | 1.04 | 0.62 | 0.52 |
| BRLT219 | T3.0 ± 0.5 | 0.43 | 0.46 | 0.73 | 0.52 | 0.68 | 0.40 | 0.26 | 0.44 |
| BRLT220 | L2.0 ± 0.5 | 0.89 | 0.77 | 0.83 | 0.85 | 1.09 | 1.07 | 0.51 | 0.47 |
| BRLT227 | L3.0 ± 0.5 | 0.83 | 0.76 | 0.91 | 0.85 | 1.10 | 1.07 | 0.55 | 0.50 |
| BRLT229 | M8.0 ± 0.5 | 1.23 | 0.95 | 1.01 | 0.95 | 1.05 | 1.04 | 0.37 | 0.50 |
| BRLT231 | L5.0 ± 0.5 | 0.87 | 0.77 | 0.91 | 0.85 | 1.07 | 1.00 | 0.59 | 0.49 |
| BRLT232 | T2.5 ± 0.5 | 0.51 | 0.58 | 0.78 | 0.56 | 0.81 | 0.70 | 0.38 | 0.45 |
| BRLT234 | L4.0 ± 1.0 | 0.74 | 0.67 | 0.87 | 0.64 | 1.09 | 0.95 | 0.26 | 0.50 |
| BRLT236 | L3.5 ± 0.5 | 0.82 | 0.71 | 0.93 | 0.76 | 1.07 | 0.97 | 0.43 | 0.49 |
| BRLT237 | L4.0 ± 1.0 | 0.84 | 0.69 | 0.88 | 0.84 | 1.09 | 0.99 | 0.49 | 0.51 |
| BRLT240 | L3.0 ± 0.5 | 0.94 | 0.82 | 0.93 | 0.90 | 1.05 | 1.05 | 0.55 | 0.47 |
| BRLT243 | T0.0 ± 0.5 | 0.70 | 0.60 | 0.73 | 0.69 | 1.01 | 0.76 | 0.50 | 0.51 |
| BRLT247 | M9.0 ± 0.5 | 1.09 | 0.90 | 1.09 | 0.93 | 0.97 | 1.00 | 0.41 | 0.48 |
| BRLT249 | L5.0 ± 0.5 | 0.84 | 0.71 | 0.84 | 0.84 | 1.05 | 0.92 | 0.57 | 0.50 |
| BRLT250 | L1.0 ± 0.5 | 0.85 | 0.77 | 0.83 | 0.79 | 1.05 | 0.94 | 0.46 | 0.49 |
| BRLT251 | L1.0 ± 0.5 | 0.92 | 0.80 | 0.94 | 0.80 | 1.00 | 0.94 | 0.34 | 0.48 |
| BRLT253 | L1.0 ± 1.0 | 0.89 | 0.71 | 0.86 | 0.72 | 1.09 | 0.99 | 0.27 | 0.48 |
| BRLT254 | L5.0 ± 0.5 | 0.84 | 0.82 | 0.95 | 0.89 | 1.06 | 1.04 | 0.54 | 0.49 |
| BRLT258 | L5.0 ± 1.0 | 0.80 | 0.72 | 0.90 | 0.80 | 1.03 | 0.89 | 0.53 | 0.49 |
| BRLT260 | L2.0 ± 1.0 | 0.80 | 0.70 | 0.89 | 0.71 | 1.11 | 1.00 | 0.29 | 0.49 |

Continued on the next page.

Continued from the previous page.

| Name | Spectral type | $H_2O$-J | $H_2O$-H | $H_2O$-K | $CH_4$-J | $CH_4$-H | $CH_4$-K | K/J | H-dip |
|---|---|---|---|---|---|---|---|---|---|
| BRLT262 | L0.0 ± 0.5 | 0.90 | 0.82 | 0.96 | 0.89 | 1.12 | 1.02 | 0.47 | 0.49 |
| BRLT265 | L2.0 ± 0.5 | 0.89 | 0.80 | 0.92 | 0.80 | 1.04 | 1.07 | 0.47 | 0.48 |
| BRLT269 | L7.0 ± 0.5 | 0.62 | 0.69 | 0.91 | 0.82 | 1.10 | 0.99 | 0.76 | 0.50 |
| BRLT270 | L2.0 ± 1.0 | 0.81 | 0.72 | 0.83 | 0.72 | 1.05 | 0.89 | 0.33 | 0.50 |
| BRLT274 | L2.0 ± 0.5 | 0.73 | 0.76 | 1.11 | 0.89 | 1.17 | 1.07 | 0.63 | 0.48 |
| BRLT275 | T2.0 ± 2.0 | 0.50 | 0.64 | 0.86 | 0.60 | 0.84 | 0.76 | 0.44 | 0.45 |
| BRLT276 | L0.0 ± 0.5 | 0.96 | 0.83 | 1.06 | 0.85 | 1.02 | 1.03 | 0.38 | 0.49 |
| BRLT279 | L1.0 ± 0.5 | 0.91 | 0.83 | 1.01 | 0.82 | 1.05 | 1.03 | 0.39 | 0.48 |
| BRLT281 | T0.0 ± 1.0 | 0.67 | 0.67 | 0.84 | 0.68 | 0.94 | 0.86 | 0.51 | 0.51 |
| BRLT283 | L5.0 ± 1.0 | 0.81 | 0.71 | 0.88 | 0.79 | 0.99 | 0.87 | 0.37 | 0.49 |
| BRLT285 | L5.0 ± 0.5 | 0.80 | 0.73 | 0.78 | 0.82 | 1.05 | 0.96 | 0.62 | 0.52 |
| BRLT286 | sdL4.0 ± 1.0 | 1.07 | 0.91 | 1.09 | 0.77 | 0.92 | 0.92 | 0.18 | 0.49 |
| BRLT287 | T3.0 ± 0.5 | 0.48 | 0.49 | 0.71 | 0.53 | 0.80 | 0.48 | 0.28 | 0.47 |
| BRLT290 | T2.0 ± 0.5 | 0.50 | 0.49 | 0.78 | 0.58 | 0.90 | 0.61 | 0.35 | 0.50 |
| BRLT295 | L4.0 ± 2.0 | 0.83 | 0.80 | 0.99 | 0.76 | 0.96 | 0.97 | 0.33 | 0.47 |
| BRLT296 | L4.0 ± 0.5 | 0.84 | 0.75 | 0.89 | 0.82 | 1.05 | 0.99 | 0.46 | 0.49 |
| BRLT297 | L4.5 ± 0.5 | 0.83 | 0.76 | 0.95 | 0.89 | 1.06 | 1.00 | 0.52 | 0.50 |
| BRLT299 | L4.0 ± 1.0 | 0.77 | 0.74 | 0.90 | 0.76 | 1.03 | 0.92 | 0.46 | 0.49 |
| BRLT301 | L1.0 ± 0.5 | 0.92 | 0.77 | 0.92 | 0.82 | 1.03 | 1.03 | 0.42 | 0.47 |
| BRLT302 | L4.0 ± 1.0 | 0.81 | 0.72 | 0.89 | 0.76 | 1.07 | 0.90 | 0.39 | 0.49 |
| BRLT305 | L5.5 ± 1.0 | 0.94 | 0.79 | 0.95 | 0.91 | 0.98 | 0.94 | 0.62 | 0.47 |
| BRLT306 | L4.5 ± 0.5 | 0.82 | 0.80 | 1.02 | 0.76 | 1.01 | 0.93 | 0.40 | 0.48 |
| BRLT307 | L1.0 ± 0.5 | 0.93 | 0.88 | 1.12 | 0.93 | 1.06 | 0.98 | 0.46 | 0.49 |
| BRLT308 | L5.0 ± 0.5 | 0.74 | 0.72 | 0.94 | 0.82 | 1.09 | 1.03 | 0.57 | 0.50 |
| BRLT309 | L7.0 ± 0.5 | 0.56 | 0.65 | 0.94 | 0.88 | 1.24 | 1.10 | 1.18 | 0.52 |
| BRLT311 | T3.0 ± 0.5 | 0.42 | 0.56 | 0.82 | 0.56 | 0.70 | 0.60 | 0.30 | 0.44 |
| BRLT312 | T0.0 ± 0.5 | 0.62 | 0.66 | 0.87 | 0.67 | 0.94 | 0.91 | 0.42 | 0.48 |
| BRLT313 | L3.5 ± 0.5 | 0.83 | 0.74 | 0.95 | 0.89 | 1.04 | 1.00 | 0.53 | 0.48 |
| BRLT314 | L7.5 ± 0.5 | 0.73 | 0.71 | 0.96 | 0.81 | 1.05 | 0.96 | 0.70 | 0.49 |
| BRLT315 | L1.0 ± 1.0 | 0.88 | 0.83 | 0.96 | 0.79 | 1.04 | 1.04 | 0.35 | 0.51 |
| BRLT316 | L1.0 ± 0.5 | 0.87 | 0.81 | 1.02 | 0.82 | 1.11 | 1.06 | 0.37 | 0.50 |
| BRLT317 | L3.0 ± 1.0 | 0.79 | 0.71 | 0.92 | 0.71 | 1.09 | 0.96 | 0.31 | 0.50 |
| BRLT318 | L1.0 ± 0.5 | 0.84 | 0.84 | 1.02 | 0.85 | 1.14 | 1.00 | 0.41 | 0.51 |
| BRLT319 | T3.0 ± 0.5 | 0.42 | 0.47 | 0.69 | 0.50 | 0.79 | 0.43 | 0.28 | 0.47 |
| BRLT320 | L1.0 ± 0.5 | 0.90 | 0.80 | 0.95 | 0.85 | 1.15 | 0.93 | 0.43 | 0.49 |
| BRLT321 | T4.0 ± 0.5 | 0.38 | 0.43 | 0.57 | 0.44 | 0.60 | 0.25 | 0.25 | 0.37 |
| BRLT322 | L5.0 ± 0.5 | 0.71 | 0.71 | 0.90 | 0.73 | 1.09 | 0.95 | 0.54 | 0.51 |
| BRLT323 | L5.0 ± 1.0 | 0.77 | 0.72 | 0.87 | 0.76 | 1.04 | 1.05 | 0.43 | 0.49 |
| BRLT325 | T2.0 ± 1.0 | 0.53 | 0.49 | 0.66 | 0.56 | 0.90 | 0.50 | 0.27 | 0.49 |
| BRLT328 | L3.0 ± 1.0 | 0.89 | 0.78 | 0.98 | 0.83 | 1.09 | 1.05 | 0.36 | 0.51 |
| BRLT330 | L2.0 ± 1.0 | 0.81 | 0.78 | 0.98 | 0.73 | 1.22 | 1.05 | 0.34 | 0.49 |
| BRLT331 | L3.0 ± 1.0 | 0.85 | 0.71 | 1.06 | 0.74 | 1.05 | 0.93 | 0.30 | 0.49 |
| BRLT332 | L3.0 ± 1.0 | 0.87 | 0.86 | 1.01 | 0.75 | 1.10 | 0.96 | 0.35 | 0.50 |
| BRLT333 | T2.0 ± 0.5 | 0.53 | 0.57 | 0.77 | 0.59 | 0.98 | 0.72 | 0.39 | 0.52 |
| BRLT334 | L3.5 ± 0.5 | 0.84 | 0.74 | 0.91 | 0.83 | 1.05 | 0.96 | 0.48 | 0.49 |
| BRLT335 | L4.0 ± 1.0 | 0.81 | 0.75 | 0.95 | 0.80 | 1.03 | 0.93 | 0.42 | 0.47 |
| BRLT338 | L1.0 ± 1.0 | 0.89 | 0.74 | 1.02 | 0.82 | 1.10 | 1.12 | 0.34 | 0.50 |
| BRLT340 | L4.0 ± 0.5 | 0.79 | 0.75 | 0.97 | 0.90 | 1.08 | 1.06 | 0.49 | 0.49 |
| BRLT343 | L9.0 ± 1.0 | 0.69 | 0.71 | 0.89 | 0.75 | 1.05 | 0.92 | 0.61 | 0.50 |
| BRLT344 | T0.0 ± 1.0 | 0.55 | 0.69 | 0.97 | 0.68 | 0.93 | 0.90 | 0.55 | 0.45 |

Table 3.2: Spectral indices for the objects in the sample.

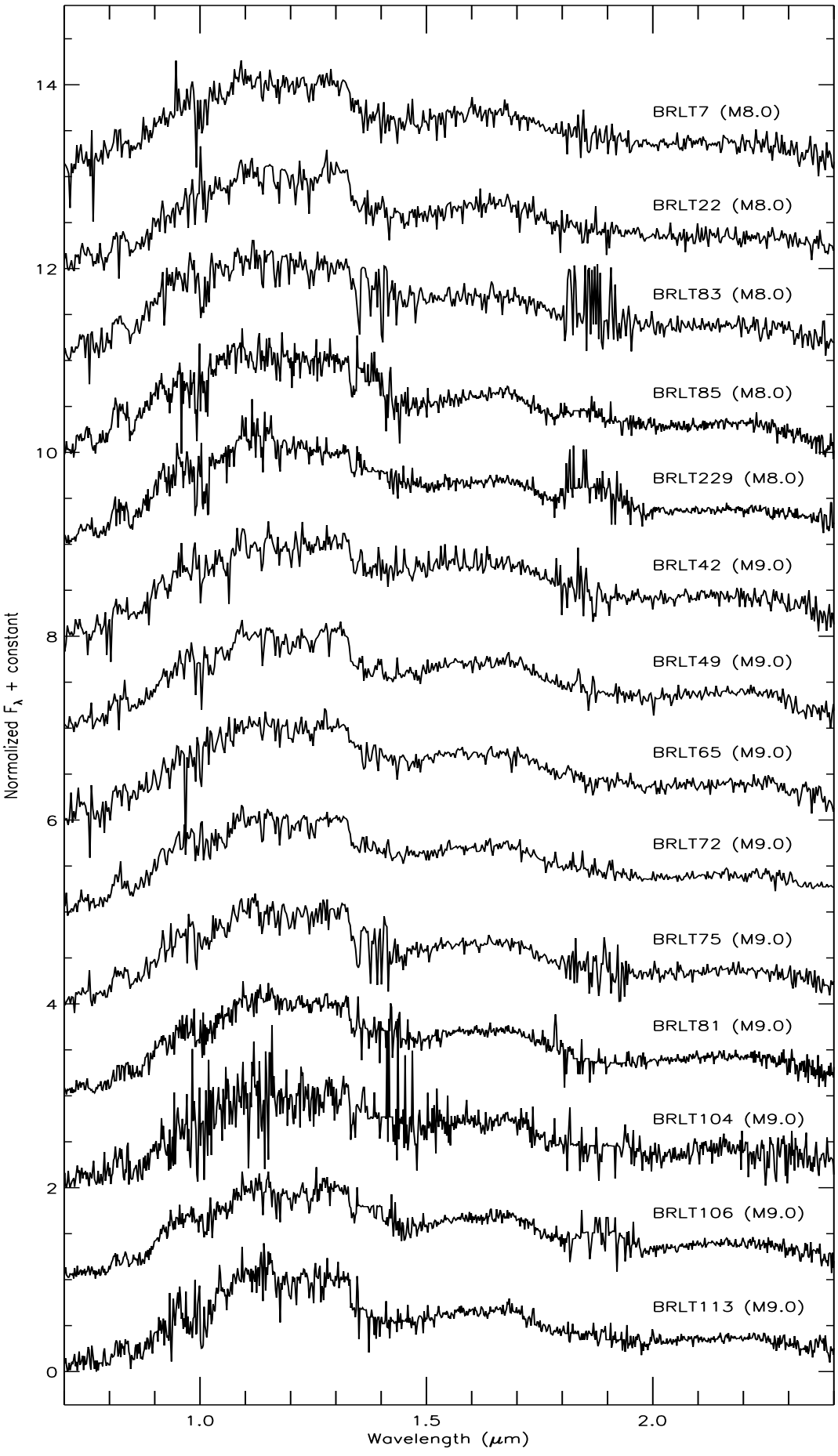


Fig. 3.1: The spectra of the objects presented here.

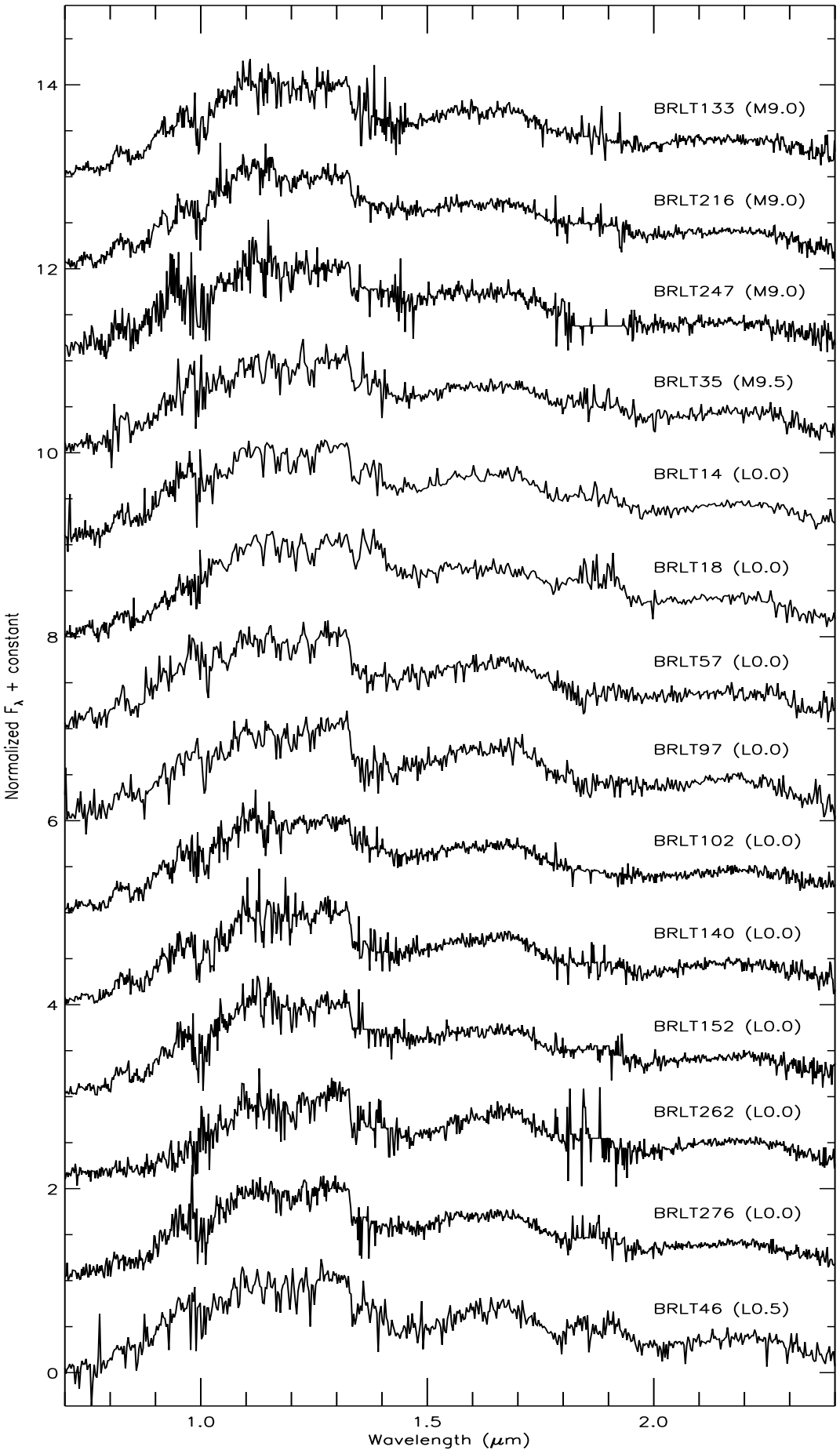


Fig. 3.2: The Xshooter spectra of the objects from the sample, sorted in ascending order of spectral type.

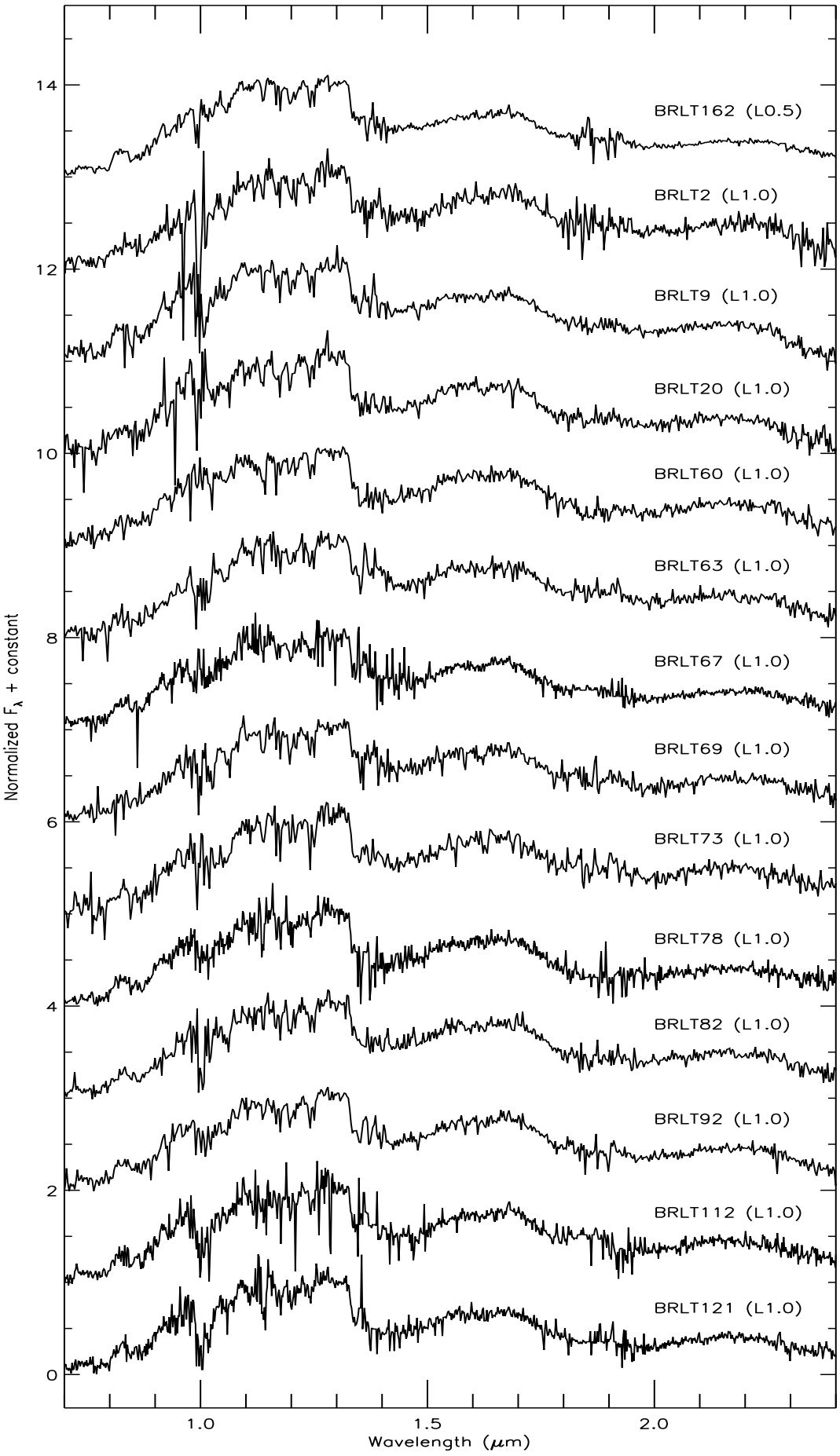


Fig. 3.3: The Xshooter spectra of the objects from the sample, sorted in ascending order of spectral type.

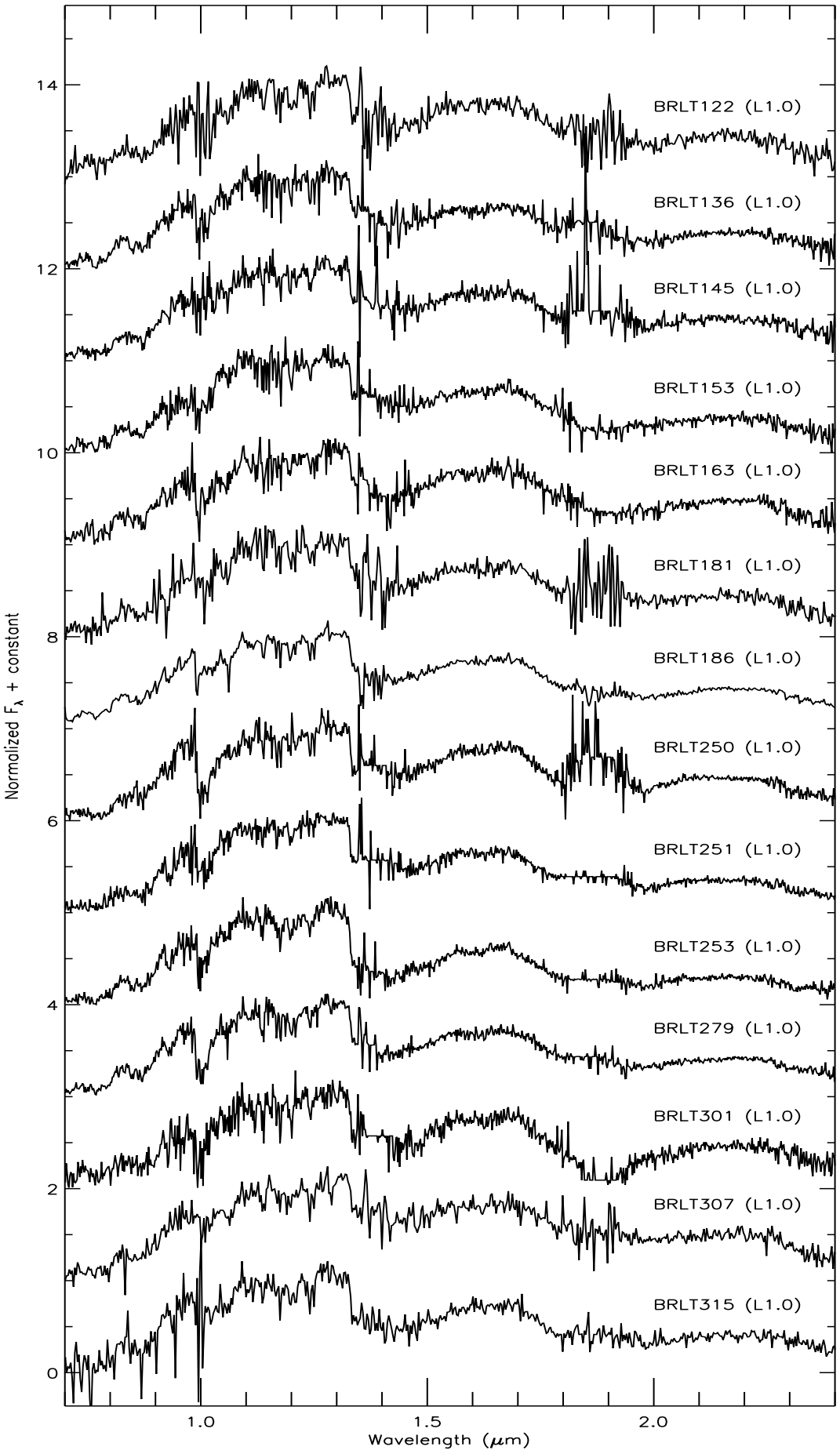


Fig. 3.4: The Xshooter spectra of the objects from the sample, sorted in ascending order of spectral type.

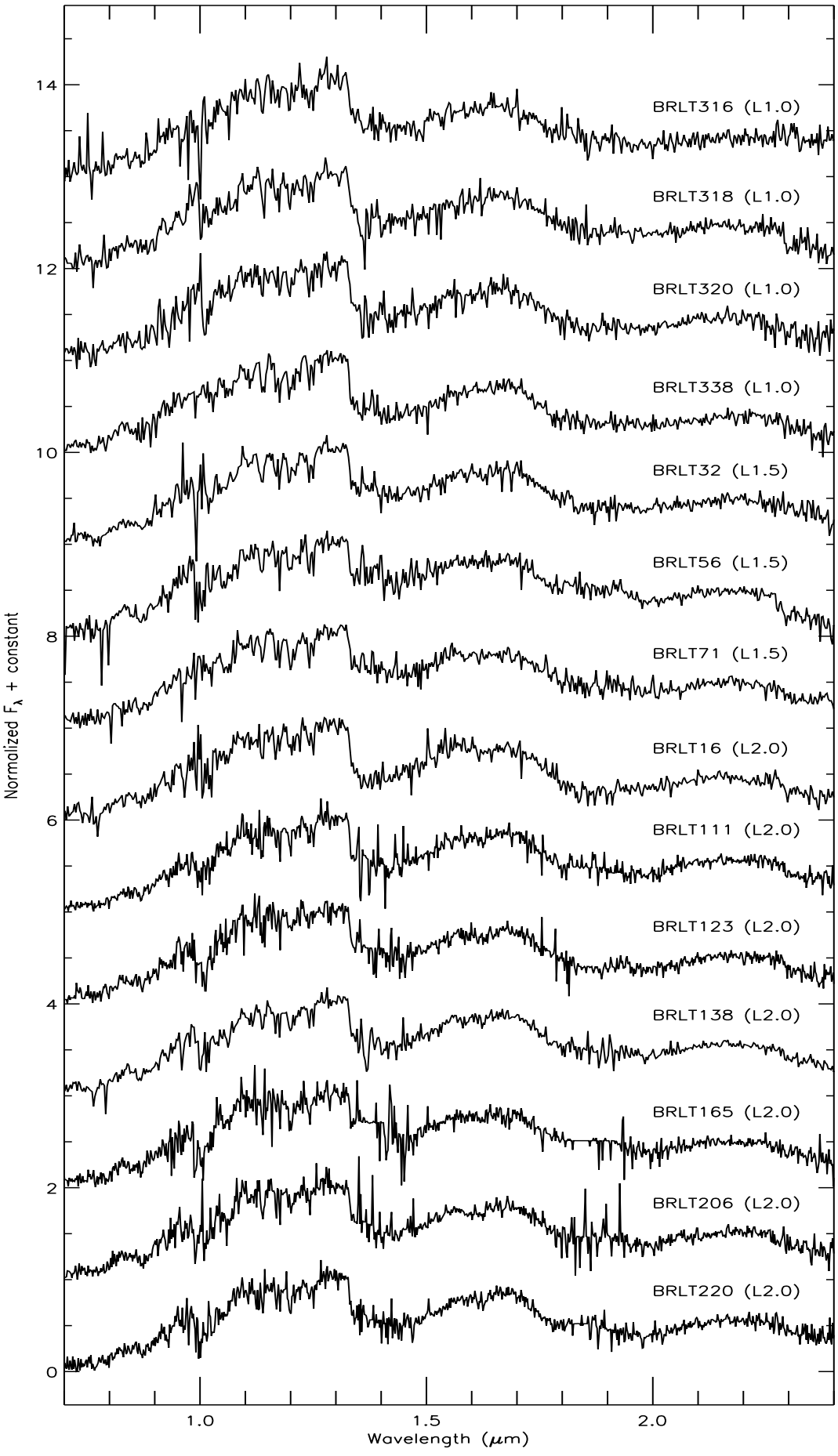


Fig. 3.5: The Xshooter spectra of the objects from the sample, sorted in ascending order of spectral type.

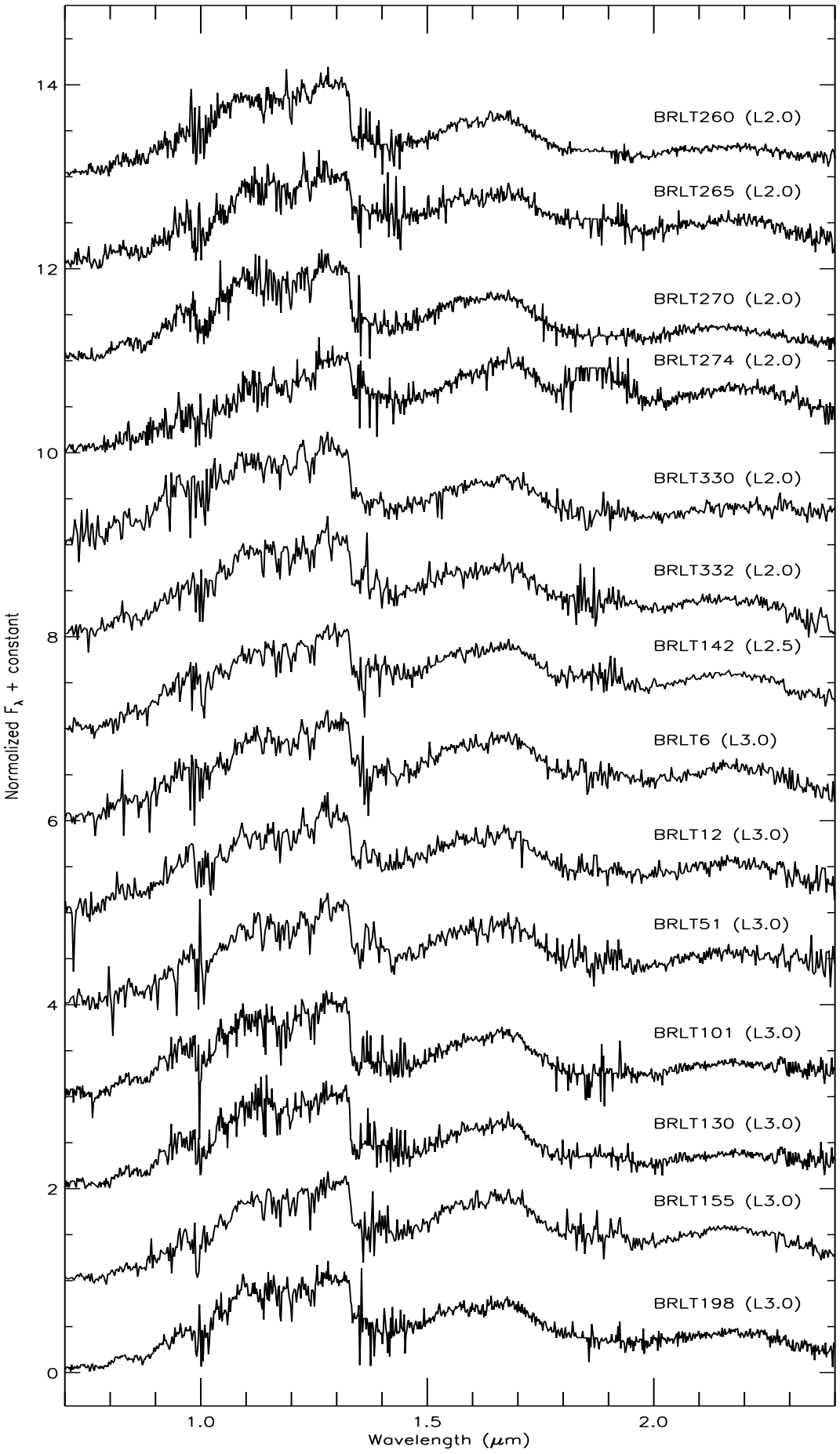


Fig. 3.6: The Xshooter spectra of the objects from the sample, sorted in ascending order of spectral type.

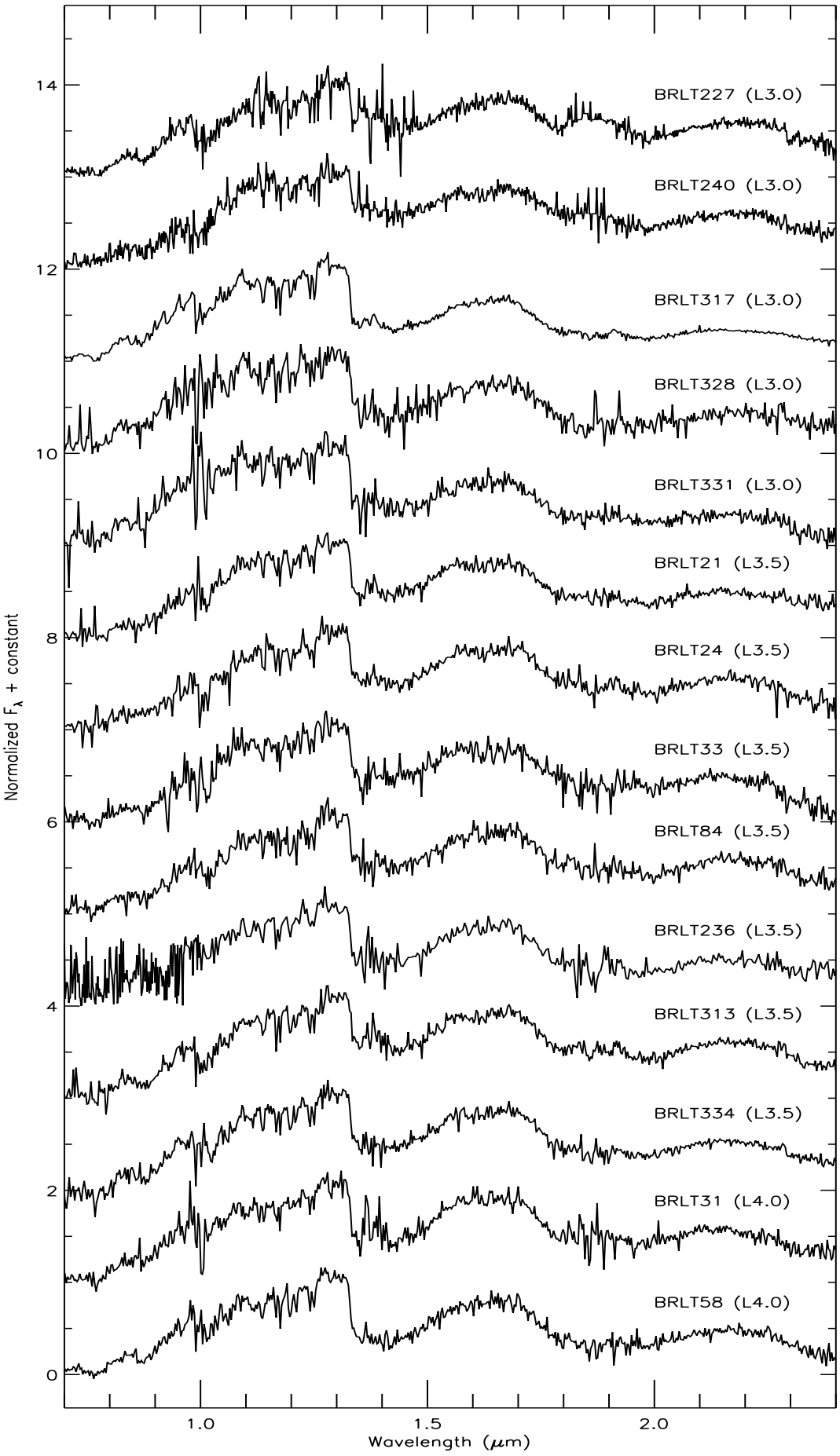


Fig. 3.7: The Xshooter spectra of the objects from the sample, sorted in ascending order of spectral type.

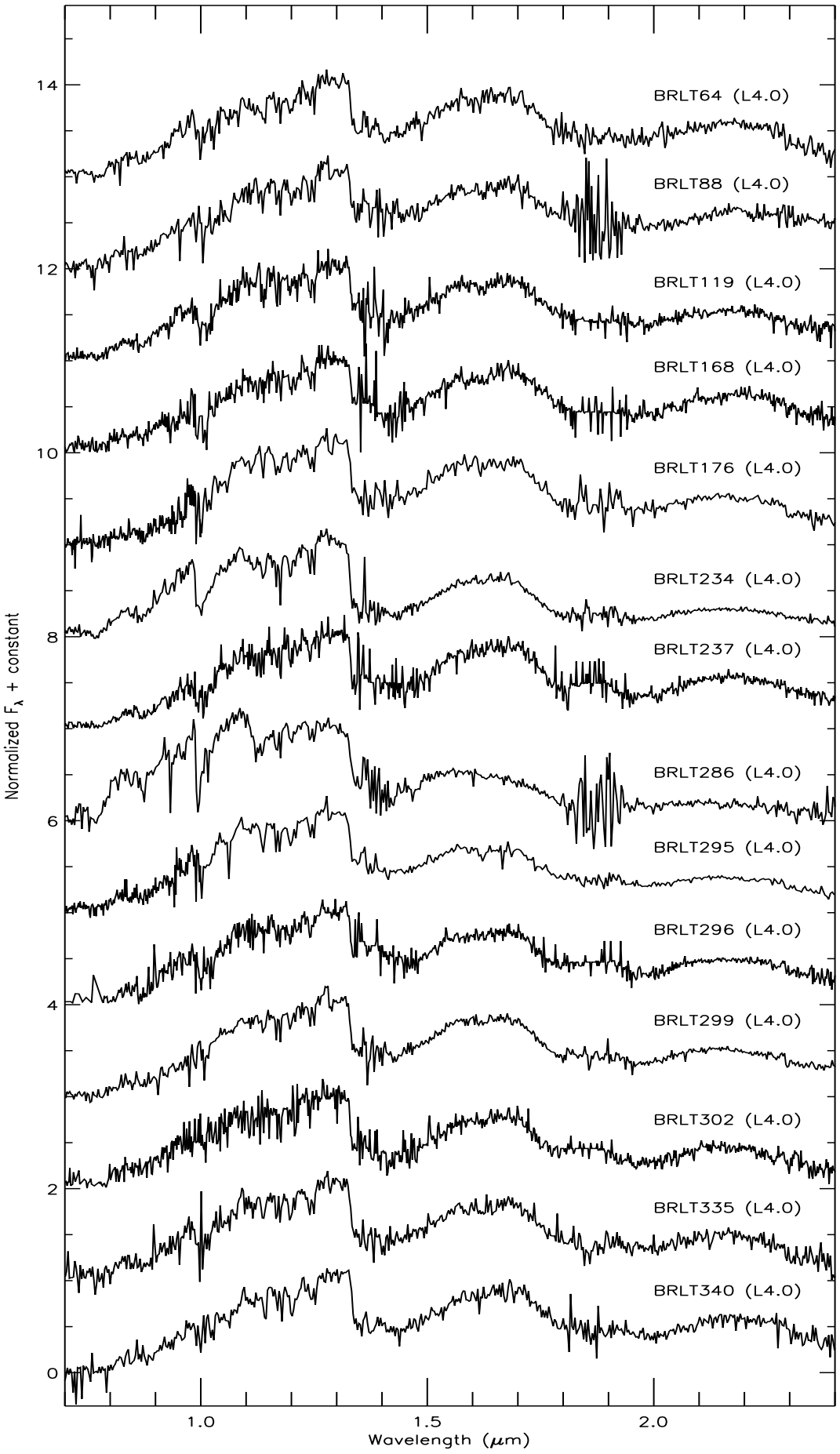


Fig. 3.8: The Xshooter spectra of the objects from the sample, sorted in ascending order of spectral type.

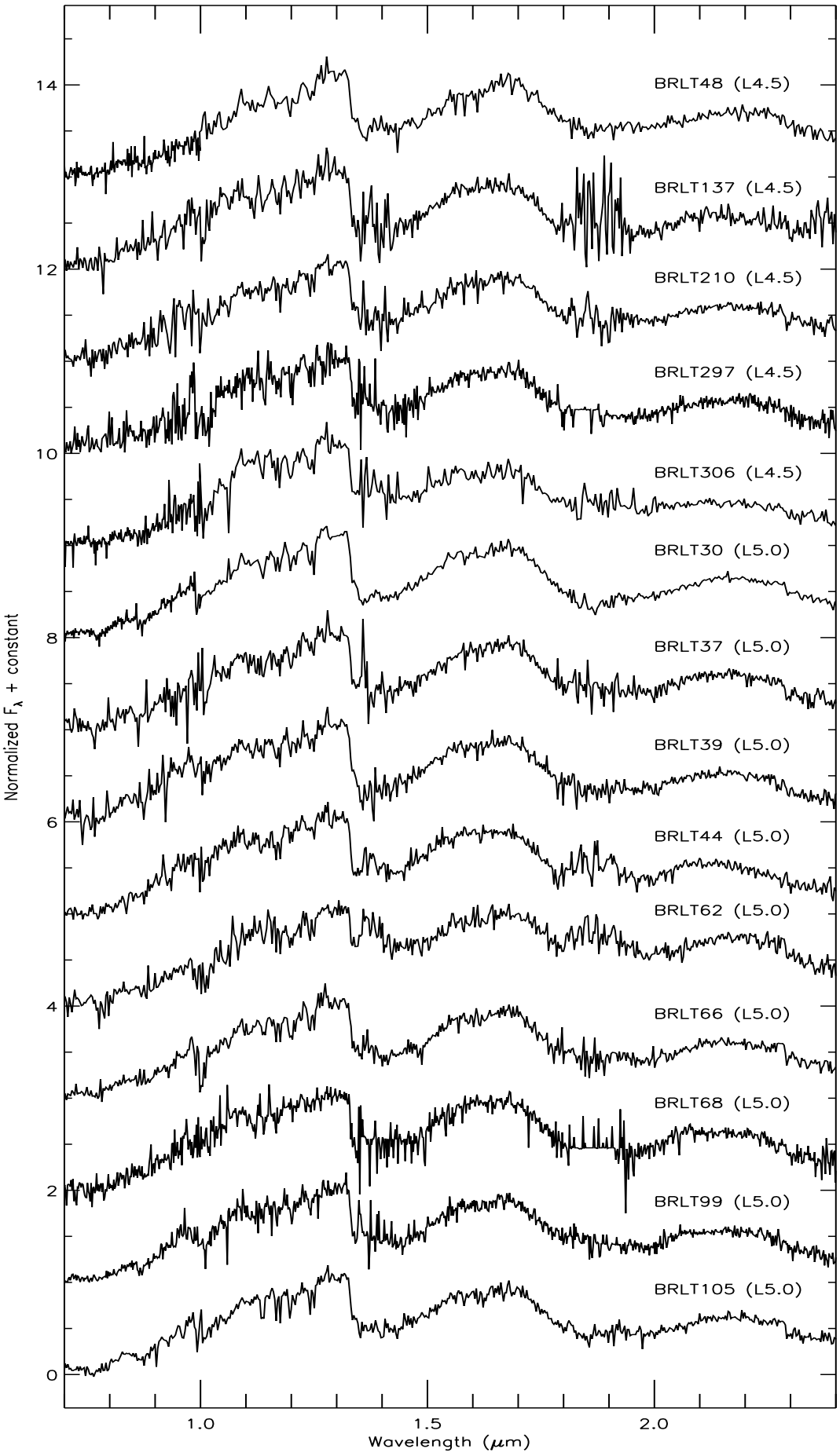


Fig. 3.9: The Xshooter spectra of the objects from the sample, sorted in ascending order of spectral type.

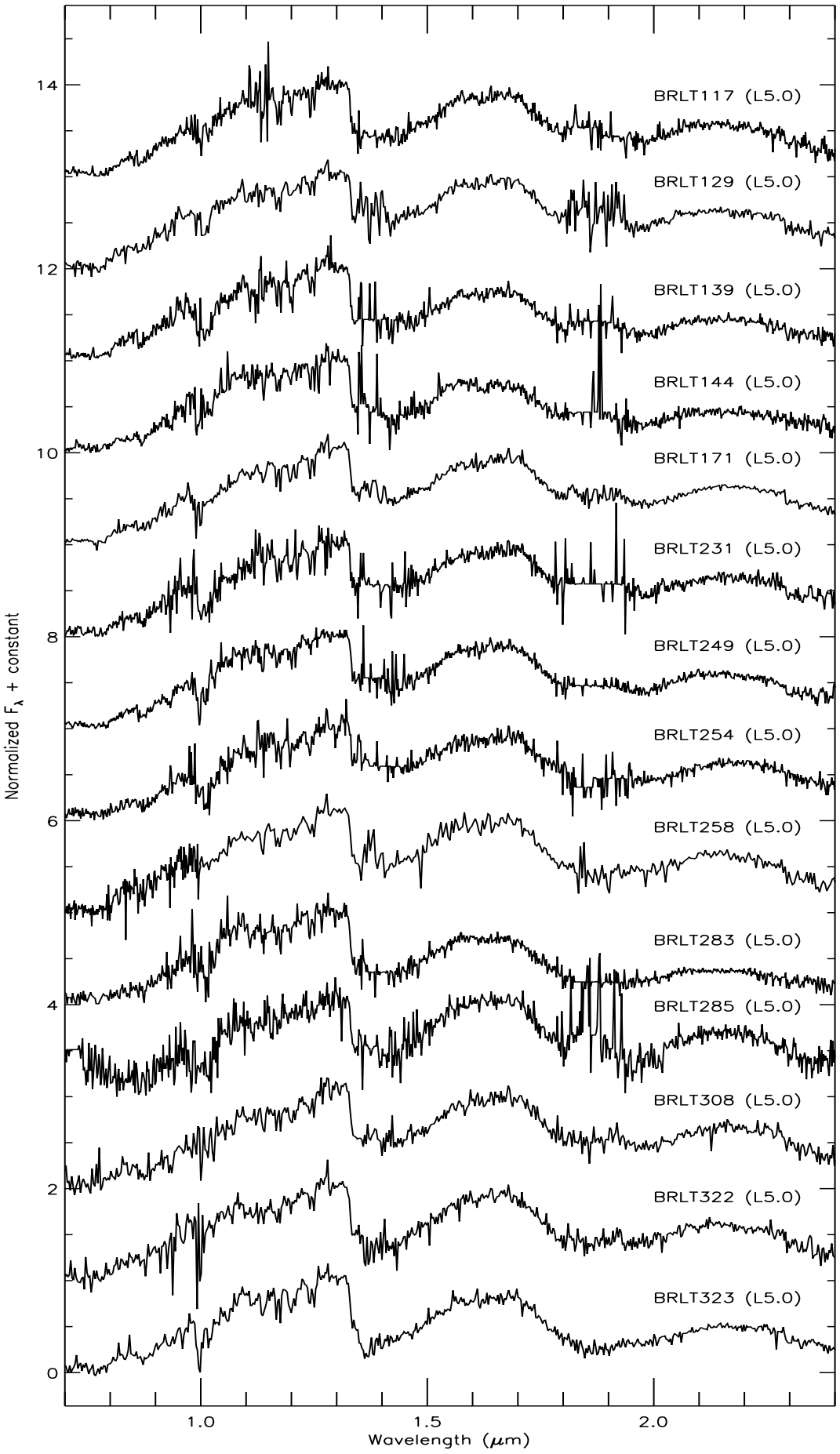


Fig. 3.10: The Xshooter spectra of the objects from the sample, sorted in ascending order of spectral type.

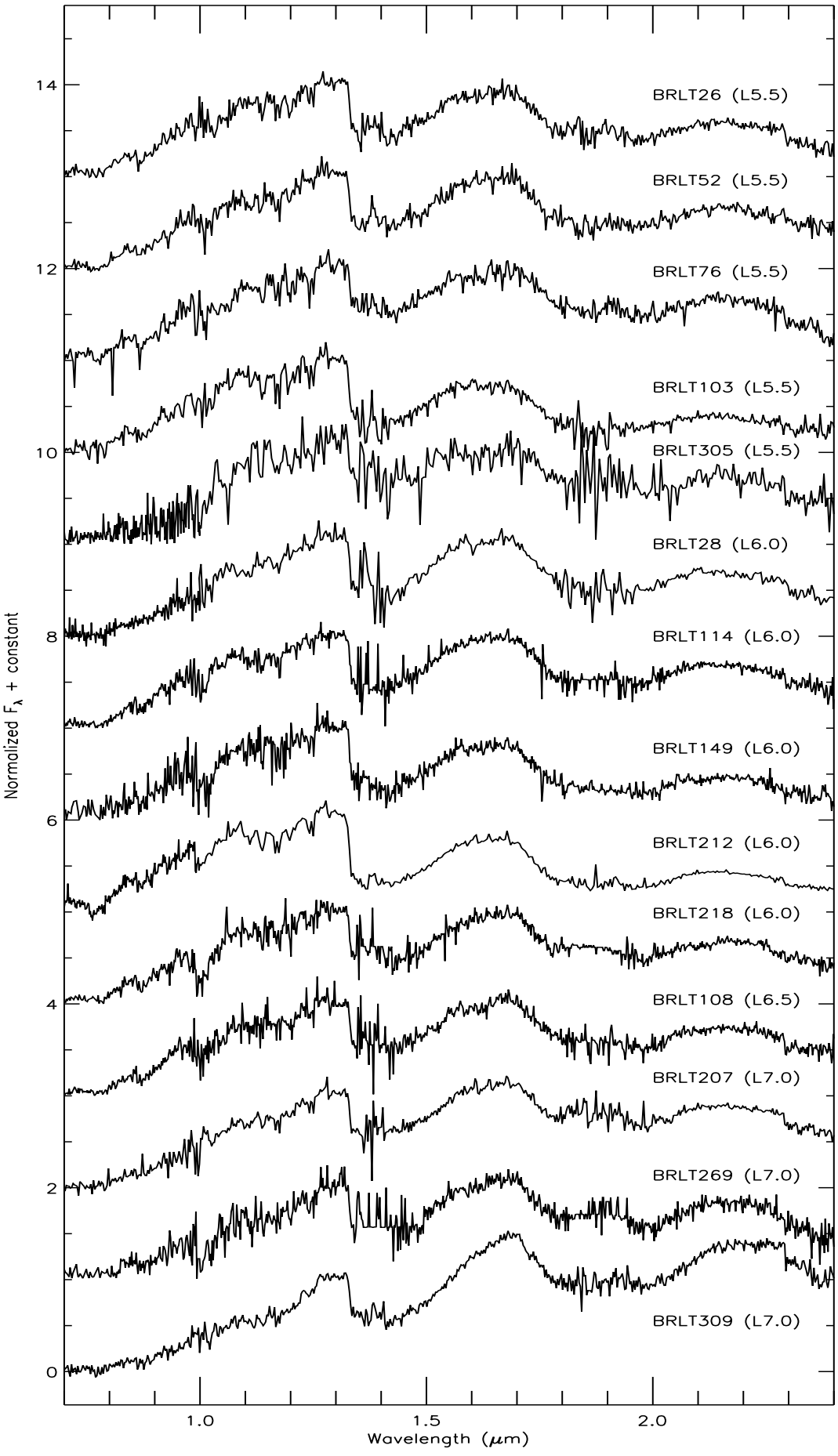


Fig. 3.11: The Xshooter spectra of the objects from the sample, sorted in ascending order of spectral type.

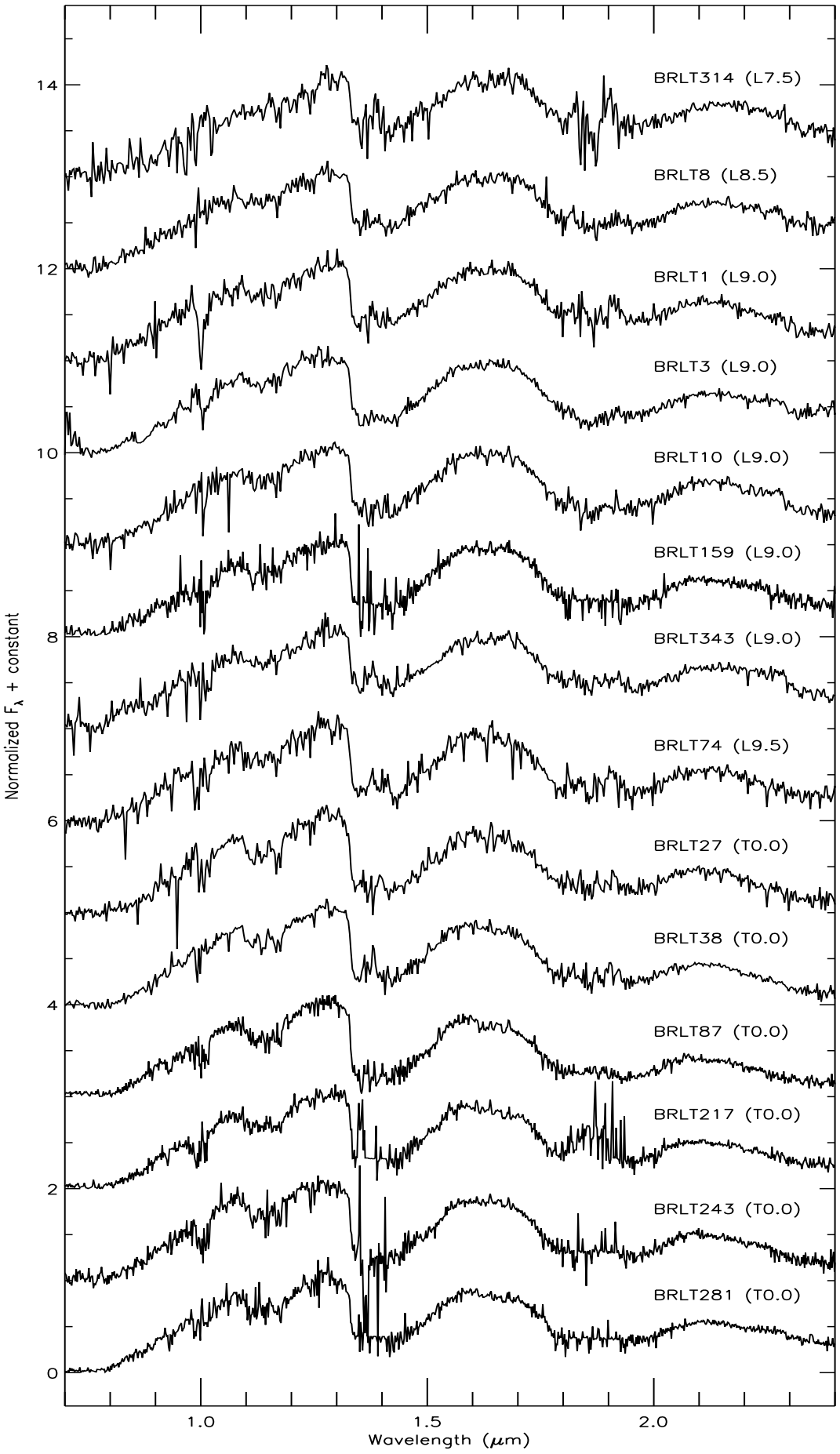


Fig. 3.12: The Xshooter spectra of the objects from the sample, sorted in ascending order of spectral type.

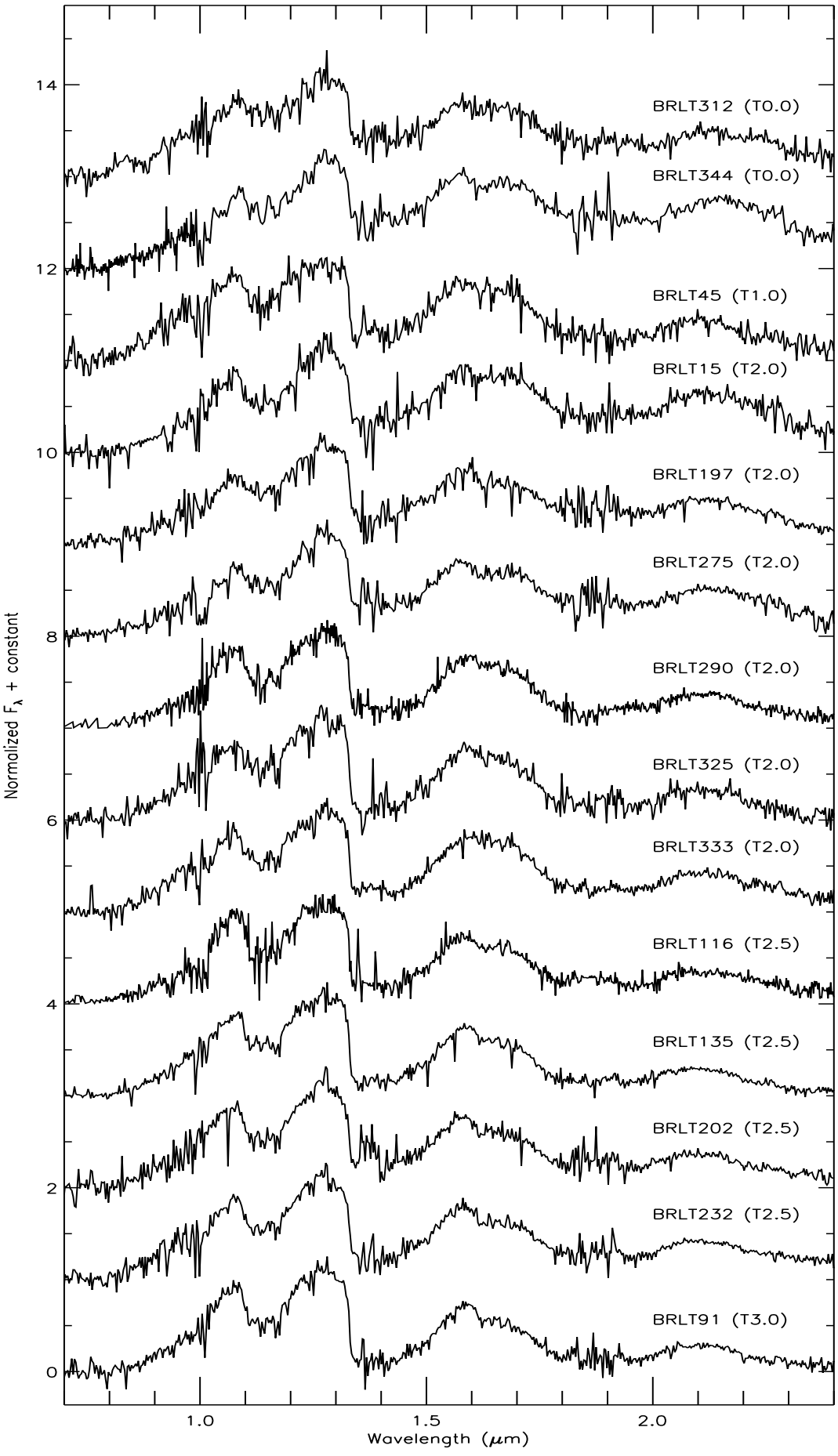


Fig. 3.13: The Xshooter spectra of the objects from the sample, sorted in ascending order of spectral type.

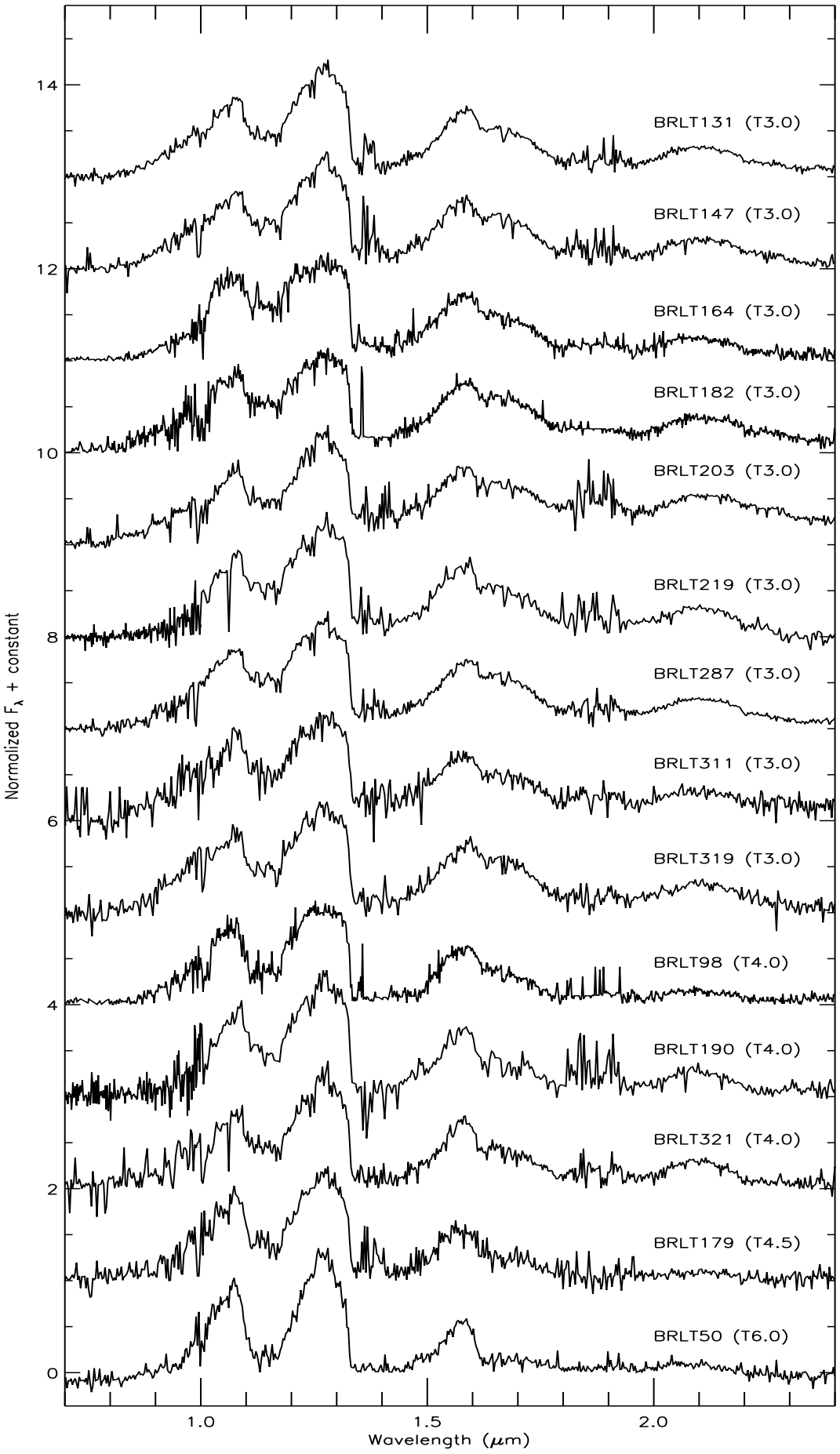


Fig. 3.14: The Xshooter spectra of the objects from the sample, sorted in ascending order of spectral type.

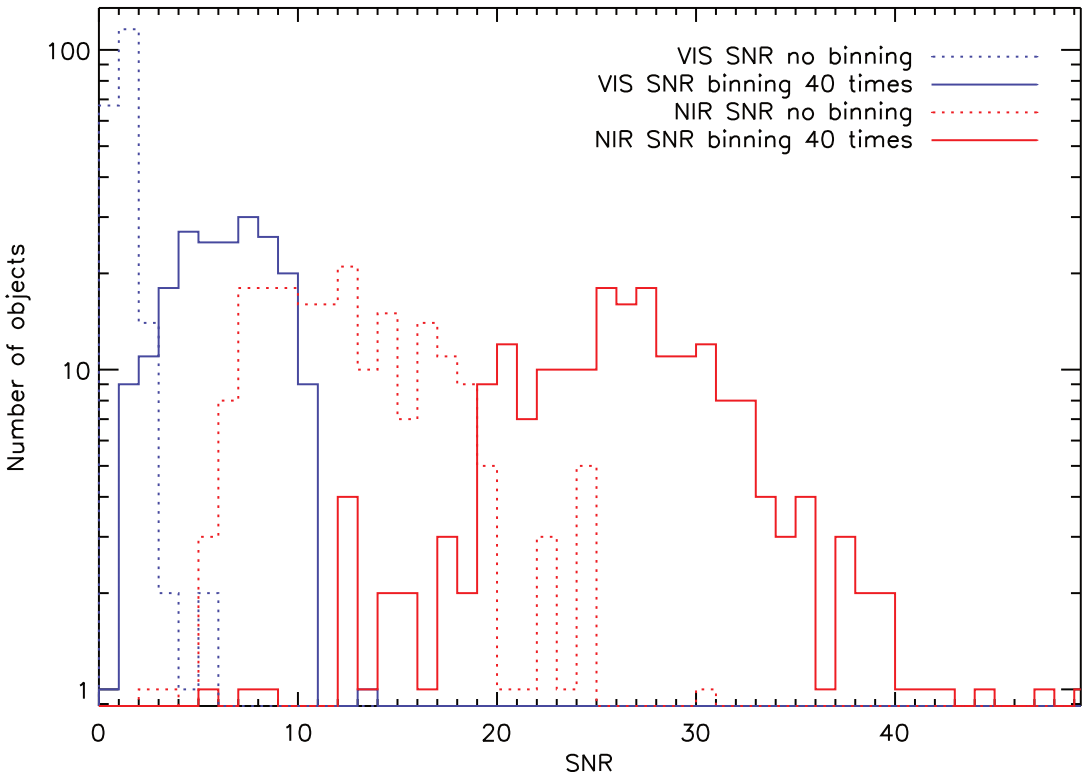


Fig. 3.15: The signal-to-noise ratio (SNR) distribution in the sample. With typical SNR of 25−30 in the NIR arm, the spectra are suitable for spectral typing, the reliable calculation of spectral indices and the identification of peculiar objects and unresolved binaries.

| Index | Numerator Range | Denominator Range | Feature |
|---|---|---|---|
| $H_2O$-$J$ | 1.14-1.165 | 1.26-1.285 | 1.15 $\mu$m $H_2O$ |
| $H_2O$-$H$ | 1.48-1.52 | 1.56-1.60 | 1.4 $\mu$m $H_2O$ |
| $H_2O$-$K$ | 1.975-1.995 | 2.08-2.10 | 1.9 $\mu$m $H_2O$ |
| $CH_4$-$J$ | 1.315-1.34 | 1.26-1.285 | 1.32 $\mu$m $CH_4$ |
| $CH_4$-$H$ | 1.635-1.675 | 1.56-1.60 | 1.65 $\mu$m $CH_4$ |
| $CH_4$-$K$ | 2.215-2.255 | 2.08-2.12 | 2.2 $\mu$m $CH_4$ |
| $K/J$ | 2.060-2.10 | 1.25-1.29 | $J$-$K$ colour |
| $H$-dip | 1.61-1.64 | 1.56-1.59 + 1.66-1.69 | 1.65 $\mu$m $CH_4$ |

Table 3.3: The spectral indices used to identify unresolved binary candidates. All the indices are defined in Burgasser et al. (2006a) except for $H$-dip which is defined in Burgasser et al. (2010).

### 3.4.2 Identification of unresolved binaries

One possible source of peculiarity in the spectra of brown dwarfs is binarity. Unresolved binaries are in fact characterized by odd spectra, which are the result of the combination of the two components of the system. This is particularly true in L/T transition pairs, where the two components have comparable brightness (see Figure 2.9 but significantly different spectra (e.g. Burgasser et al., 2010).

In order to select binary candidates within the sample, I follow the method described by Burgasser et al. (2010), who used a combination of index-index and index-spectral type diagrams to define a number of criteria to identify unresolved binary candidates.

By analysing the spectra of a set of known L/T unresolved binaries, Burgasser et al. (2010) identified a series of spectral peculiarities common to among these types of binaries. A sharp feature at 1.6$\mu$m (resulting from the overlap of FeH and $CH_4$ absorption bands), a stronger 1.6$\mu$m $CH_4$ absorption band compared to the 2.2$\mu$m $CH_4$ absorption band, a sharper 1.27$\mu$m peak (consequence of deeper $CH_4$ and $H_2O$ bands at $\sim$ 1.1$\mu$m), a slightly shifted 2.1$\mu$m peak, and an overall blue trend of the spectral energy distribution have been identified as the most prominent differences between the spectra of single objects and unresolved binaries.

The indices used to measure the strength of the aforementioned features are defined by Burgasser et al. (2006a) and Burgasser et al. (2010), and are summarized in Table 3.3. The selection criteria are based on the distribution of known unresolved binaries in a series of index-index plots. Looking at trends in individual indices and index ratios, Burgasser et al. (2010) identified six combinations of indices that clearly separate the known unresolved binaries from the rest of the L/T population. The selection criteria were set by visually defining regions in the chosen index-index plots that included the majority of the known binaries, while minimizing the number of non-binary objects selected. The selection therefore minimizes the number of false positives, but is *not* complete. The selection criteria are listed in Table 3.4. Objects that match two of the six criteria are called "weak candidates" while objects that match three or more criteria are called "strong candidates".

With this technique I was able to identify 39 binary candidates, consisting of 21 weak candidates and 18 strong candidates, that are listed in Table 3.5. The index-index and index-spectral type diagram used are presented in Figure 3.16, where strong candidates are marked with a diamond and weak candidates are marked with an asterisk.

To deconvolve the spectra of the binary candidates and determine the types of

| Abscissa | Ordinate | Inflection Points (x,y) |
|---|---|---|
| $H_2O$-$J$ | $H_2O$-$K$ | (0.325,0.5),(0.65,0.7) |
| $CH_4$-$H$ | $CH_4O$-$K$ | (0.6,0.35),(1,0.775) |
| $CH_4$-$H$ | $K/J$ | (0.65,0.25),(1,0.375) |
| $H_2O$-$H$ | $H$-dip | (0.5,0.49),(0.875,0.49) |
| SpT | $H_2O$-$J$/$H_2O$-$H$ | (L8.5,0.925),(T1.5,0.925),(T3.5,0.85) |
| SpT | $H_2O$-$J$/$CH_4$-$K$ | (L8.5,0.625),(T4.5,0.825) |

Table 3.4: The selection criteria used to identify unresolved binary candidates. Inflection points are defined in Burgasser et al. (2010).

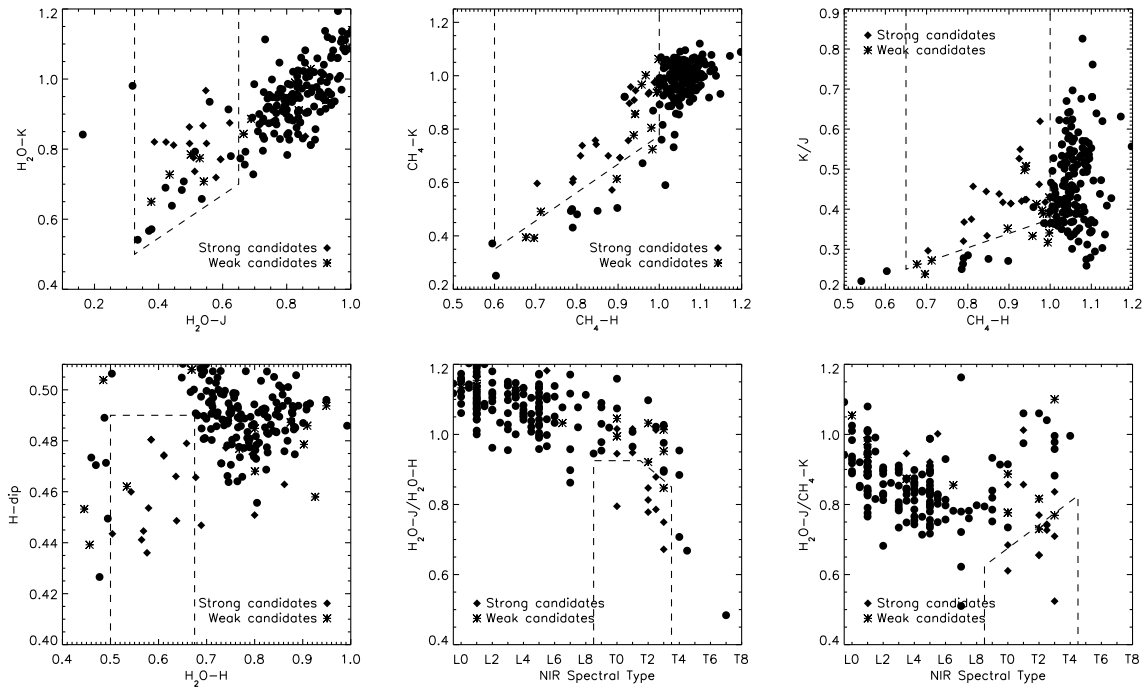


Fig. 3.16: The index-index and index-spectral type plots used for binary candidate selection. In each plot, the dashed line encloses the "selection box" for binary candidates.

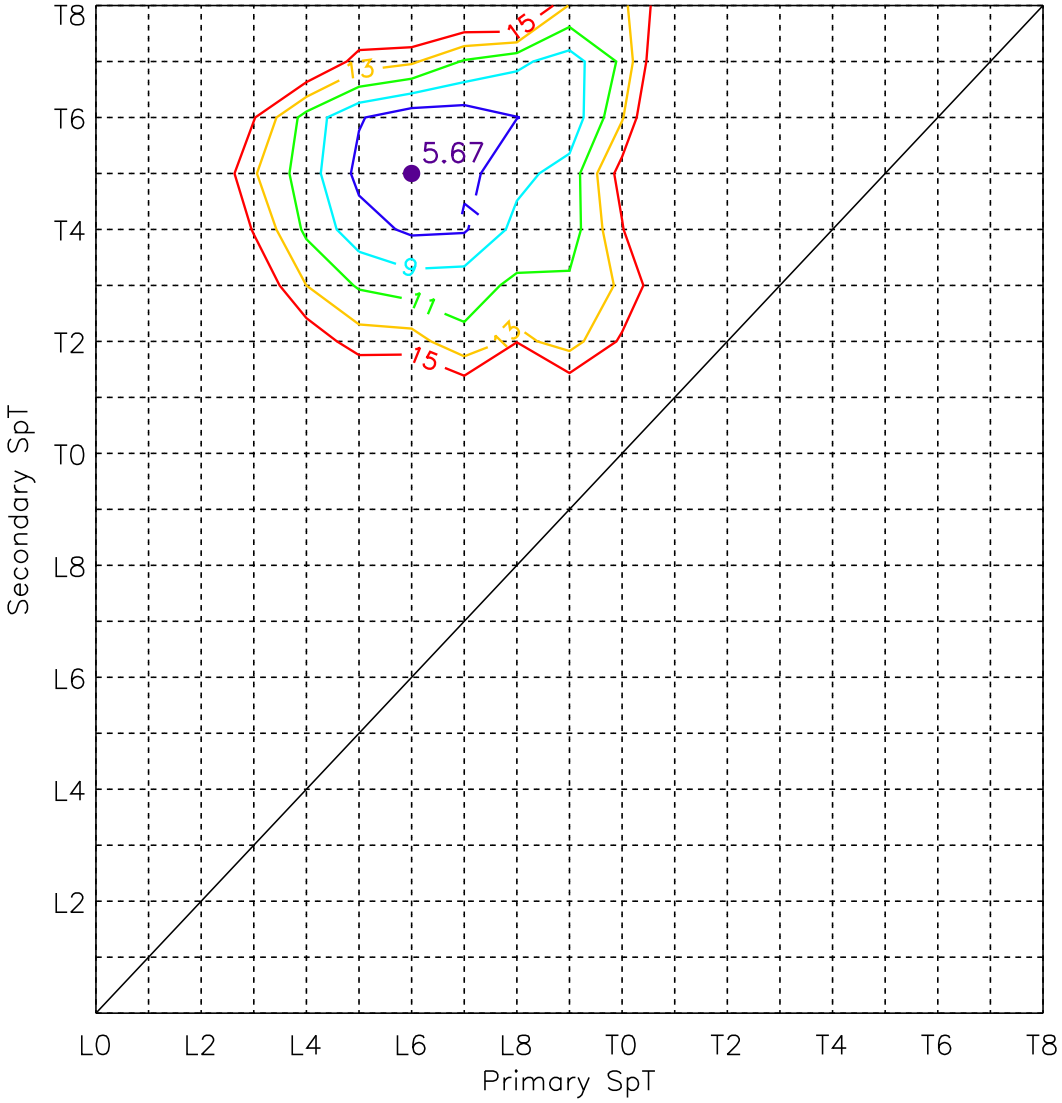


Fig. 3.17: The $\chi^2$ distribution for the deconvolution of BRLT203. For each primary+secondary combination I show the minimum $\chi^2$. The best fit is marked by a purple point, and the corresponding $\chi^2$ is shown.

the potential components I used the technique described in Day-Jones et al. (2013). I created a library of synthetic unresolved binaries combining the spectral templates taken from the already mentioned SpeX-Prism library. All the templates were scaled to a common flux level using the $M_J$-spectral type relation defined in Marocco et al. (2010) and combined. Each candidate was then fitted with this new set of templates using a $\chi^2$ fitting technique, after normalizing both of them at 1.28 $\mu$m. The fit are presented in Figure 3.18 – 3.27. An example of the $\chi^2$ distribution obtained is shown in Figure 3.17. For each primary+secondary combination I plot the minimum $\chi^2$ obtained (there are on average ∼60 templates for each point in the grid). The best fit is plotted as a purple dot and the corresponding $\chi^2$ is shown. The distribution is somewhat smooth and clearly converges towards a unique solution, without secondary minima.

The results of this fitting were compared to the results obtained using the standard templates with a one-sided F test, to assess the statistical significance of the deconvolution. If the ratio of the two chi-squared fits ($\eta$) is greater than the critical value

($\eta_{\rm crit}$ =1.15), this represents a 99% significance that the combined template fit is better than the standard template alone. The results are shown in Table 3.5 where for each target I present the best fit standard template (with the associated $\chi^2$), the best fit combined template (with $\chi^2$) and the $\eta$ value of the F test. As one can see, 20 out of 39 dwarfs give a statistically better fit using combined templates ($\eta > 1.15$) and are therefore the strongest binary candidates.

Three of these candidates have previously been identified as binaries or binary candidates. BRLT131 was resolved into its two component via HST imaging by Burgasser et al. (2006b), and their spectral types were estimated to be $\lesssim$T2 and T5 based on the resolved photometry. This is in good agreement with the results of my deconvolution, suggesting types T2.0 and T7.0. BRLT275 and BRLT281 were identified as strong binary candidates in Burgasser et al. (2010) and the spectral types of their deconvolution are L5.5+T5.0 for BRLT275 and L7.5+T2.5 for BRLT281. Again these results are in good agreement with mine, with the best fit template for BRLT275 being an L6.5+T5.5 and the best fit for BRLT281 being an L5.5+T3.0. BRLT275 was found to be $\sim$ 1 mag over-luminous compared to objects of similar "unresolved type" by Faherty et al. (2012), reinforcing the possibility of this object being a real binary.

For the other candidates, as clearly stated in Burgasser et al. (2010), the results of this fitting must be taken with caution and a definitive confirmation of the binarity of these objects must come from high resolution imaging, radial velocity monitoring or spectro-astrometry.

### 3.4.3 Identification of peculiar objects

As discussed in the introduction to this work, the most common origins of peculiarities in the spectra of brown dwarfs are unresolved binarity, and unusual values of surface gravity and metallicity. Assuming that all the unresolved binaries in the sample have been successfully identified in Section 3.4.2, I now analyse the SEDs of the remaining objects to identify peculiar dwarfs.

#### Subdwarfs

One of the most important sources of opacity in the atmospheres of cool stars and brown dwarfs is the Collision Induced Absorption (CIA) of molecular hydrogen. This is particularly true in the atmospheres of metal-poor and/or high surface gravity objects, where the lack of heavy elements and/or the higher atmospheric pressure enhance the CIA (Borysow et al., 1997). The spectra of metal deficient/high gravity objects appear therefore particularly blue compared to solar metallicity/low gravity ones, as the CIA suppresses significantly the emergent flux in the H and K bands. Other peculiar signatures of metal deficiency/high gravity are an enhancement of the hydride absorption bands (CaH and FeH in particular) and of the alkali metals (Na I, K I, Cs I, and Rb I). This may be somewhat counter-intuitive but, since the lack of heavy elements prevents the formation of dust, a smaller fraction of alkali is "trapped" into dust grains, and therefore their lines are stronger.

A reduced metal content and a high surface gravity are generally associated with old ages. As in the early stages our Galaxy was composed of gas with a significantly reduced content of heavy elements, brown dwarfs formed at that stage would have a much lower metallicity compared to younger objects. Similarly, very old object would have had the time to contract to their final radii, and to cool down significantly

| Target name | Single template best fit ($\chi^2$) | Combined template best fit ($\chi^2$) | F-test $\eta$ |
|---|---|---|---|
| Strong candidates | | | |
| BRLT15 | T2.0 (14.83) | L8.0+T7.0 (3.69) | 4.02 |
| BRLT16 | L3.5 (3.74) | L3.0+T3.0 (3.60) | 1.04 |
| BRLT33 | L3.5 (6.08) | L3.0+T4.0 (4.42) | 1.37 |
| BRLT45 | T1.0 (6.26) | T1.0+T3.0 (6.76) | 0.92 |
| BRLT87 | T1.0 (4.96) | T0.0+T2.0 (3.91) | 1.27 |
| BRLT116 | T2.5 (7.58) | L9.5+T3.0 (6.78) | 1.12 |
| BRLT133 | M9.0 (8.51) | L1.0+L1.5 (10.99) | 0.77 |
| BRLT144 | L5.0 (12.27) | L2.0+T3.0 (11.80) | 1.04 |
| BRLT182 | T3.0 (6.59) | L9.0+T4.5 (5.74) | 1.15 |
| BRLT197 | T2.0 (10.88) | L7.0+T5.5 (6.33) | 1.72 |
| BRLT202 | T2.5 (7.62) | L7.5+T5.0 (5.82) | 1.31 |
| BRLT203 | T3.0 (15.90) | L6.0+T5.0 (5.67) | 2.80 |
| BRLT232 | T2.5 (6.52) | L7.0+T5.0 (4.02) | 1.62 |
| BRLT275 | T2.0 (12.38) | L6.5+T5.5 (6.02) | 2.05 |
| BRLT305 | L5.5 (7.03) | L5.0+L6.0 (8.91) | 0.79 |
| BRLT311 | T3.0 (9.33) | T1.0+T5.0 (7.27) | 1.28 |
| BRLT312 | T0.0 (6.50) | L5.0+T4.0 (5.39) | 1.20 |
| BRLT344 | T0.0 (5.80) | L7.0+T7.0 (3.59) | 1.62 |
| Weak candidates | | | |
| BRLT18 | L0.0 (37.43) | L1.5+L2.5 (42.29) | 0.88 |
| BRLT20 | L1.0 (12.05) | L1.0+T5.5 (9.32) | 1.29 |
| BRLT42 | M9.0 (5.23) | M9.0+L1.0 (3.39) | 1.54 |
| BRLT49 | M9.0 (4.65) | L1.0+T8.0 (6.31) | 0.74 |
| BRLT60 | L1.0 (2.30) | L1.0+T3.0 (2.18) | 1.06 |
| BRLT71 | L1.5 (5.80) | L1.0+L1.5 (5.82) | 0.99 |
| BRLT91 | T3.0 (3.71) | T3.0+T4.0 (3.41) | 1.09 |
| BRLT103 | L5.5 (8.66) | L5.0+T3.0 (5.97) | 1.45 |
| BRLT104 | M9.0 (26.58) | L1.5+T8.0 (32.18) | 0.83 |
| BRLT131 | T3.0 (2.95) | T2.0+T7.0 (2.25) | 1.31 |
| BRLT164 | T3.0 (7.23) | T2.0+T3.0 (6.17) | 1.17 |
| BRLT176 | L4.0 (7.15) | L4.0+T1.0 (6.76) | 1.06 |
| BRLT217 | T0.0 (11.81) | L5.0+T2.0 (10.60) | 1.11 |
| BRLT219 | T3.0 (9.51) | T2.5+T4.0 (8.26) | 1.15 |
| BRLT247 | M9.0 (12.75) | L1.0+L1.5 (17.95) | 0.71 |
| BRLT251 | L1.0 (9.03) | L1.5+T5.0 (6.41) | 1.41 |
| BRLT281 | T0.0 (5.03) | L5.5+T3.0 (3.77) | 1.33 |
| BRLT290 | T2.0 (4.77) | T2.0+T3.0 (4.45) | 1.07 |
| BRLT295 | L4.0 (13.23) | L1.5+T5.5 (8.94) | 1.48 |
| BRLT333 | T2.0 (4.43) | L8.5+T2.5 (3.32) | 1.33 |
| BRLT335 | L4.0 (4.63) | L3.0+T3.0 (4.28) | 1.08 |

Table 3.5: The results of the spectral fitting of the binary candidates with combined templates.

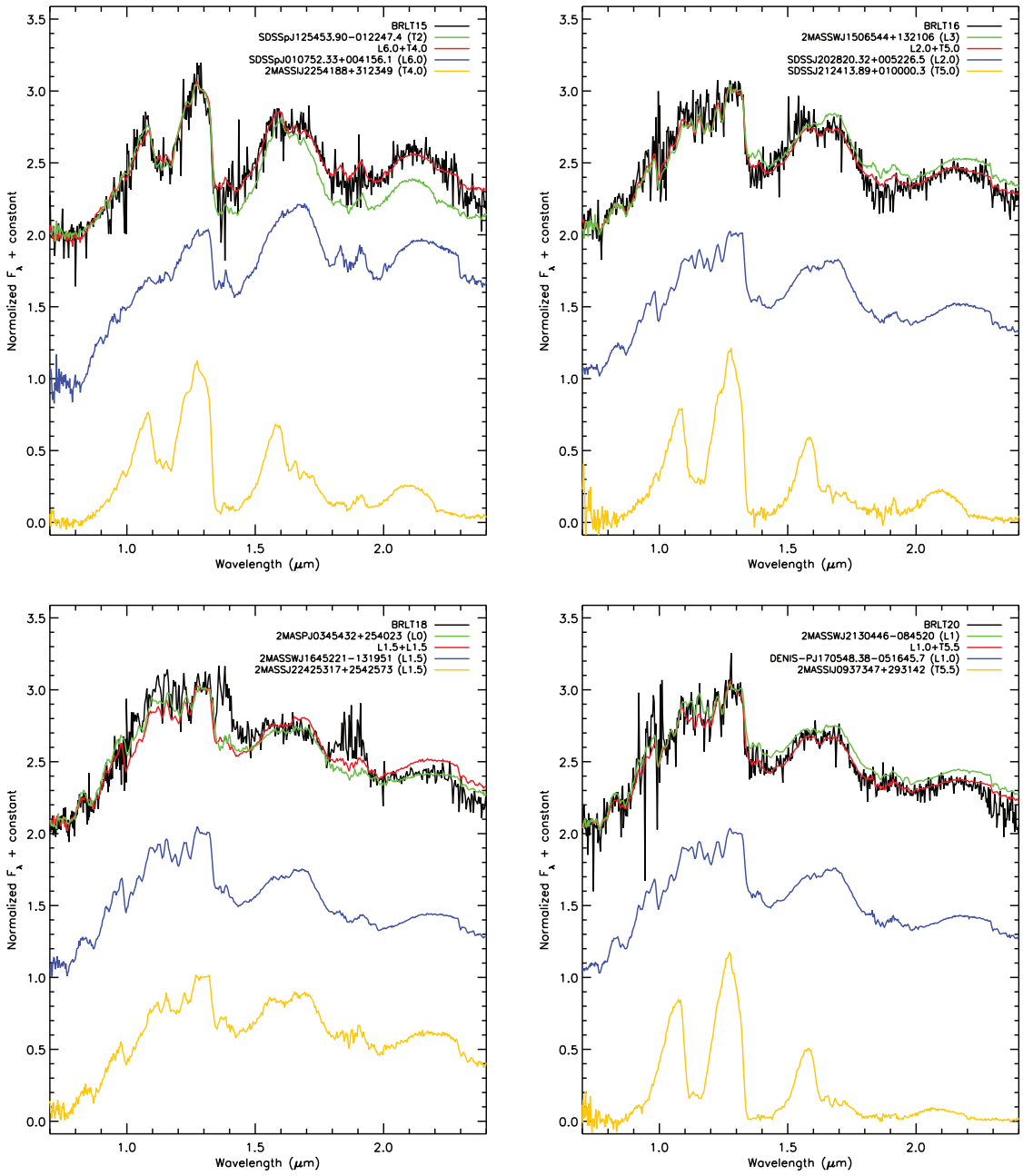


Fig. 3.18: The spectral deconvolution of the binary candidates.

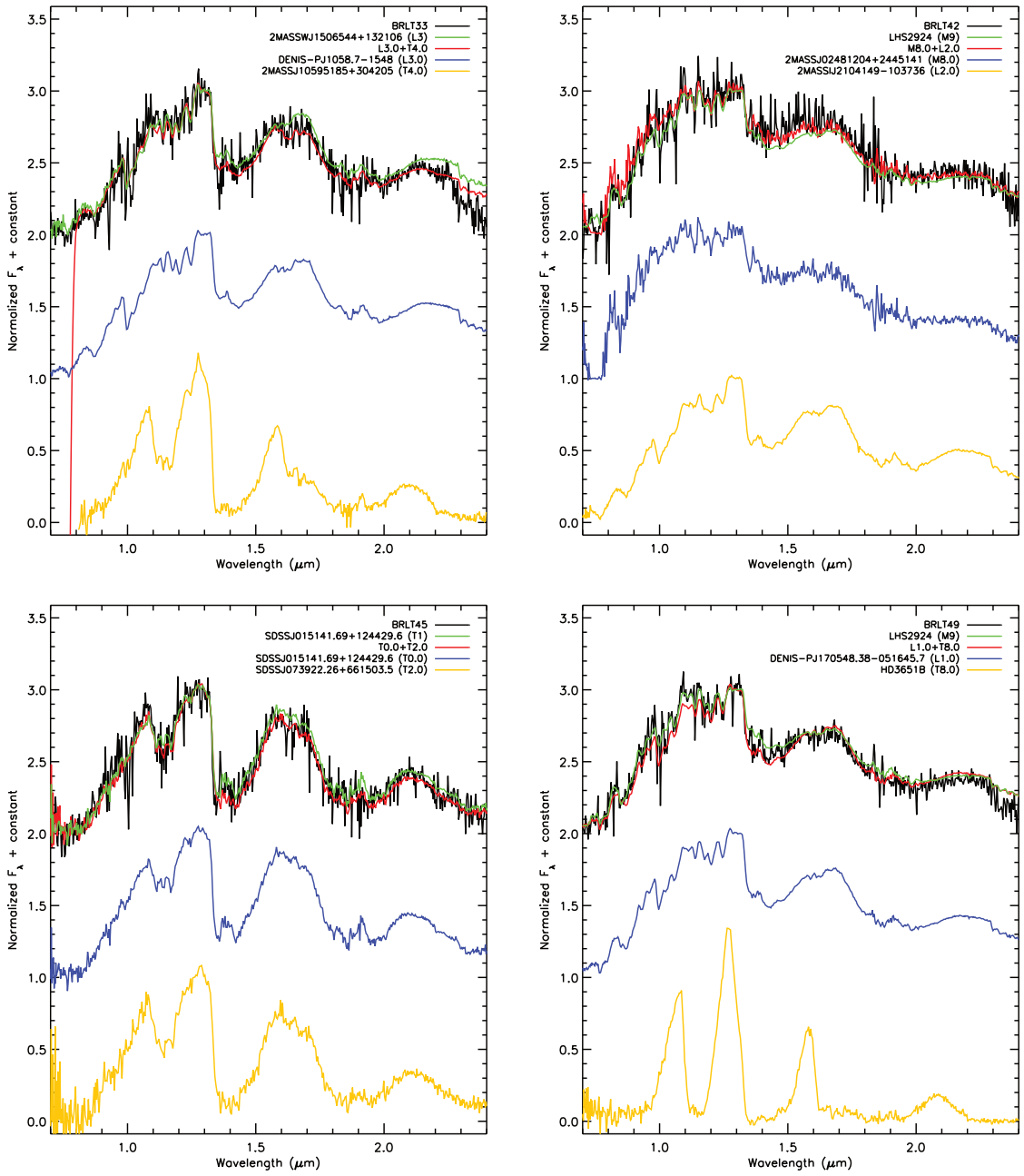


Fig. 3.19: The spectral deconvolution of the binary candidates.

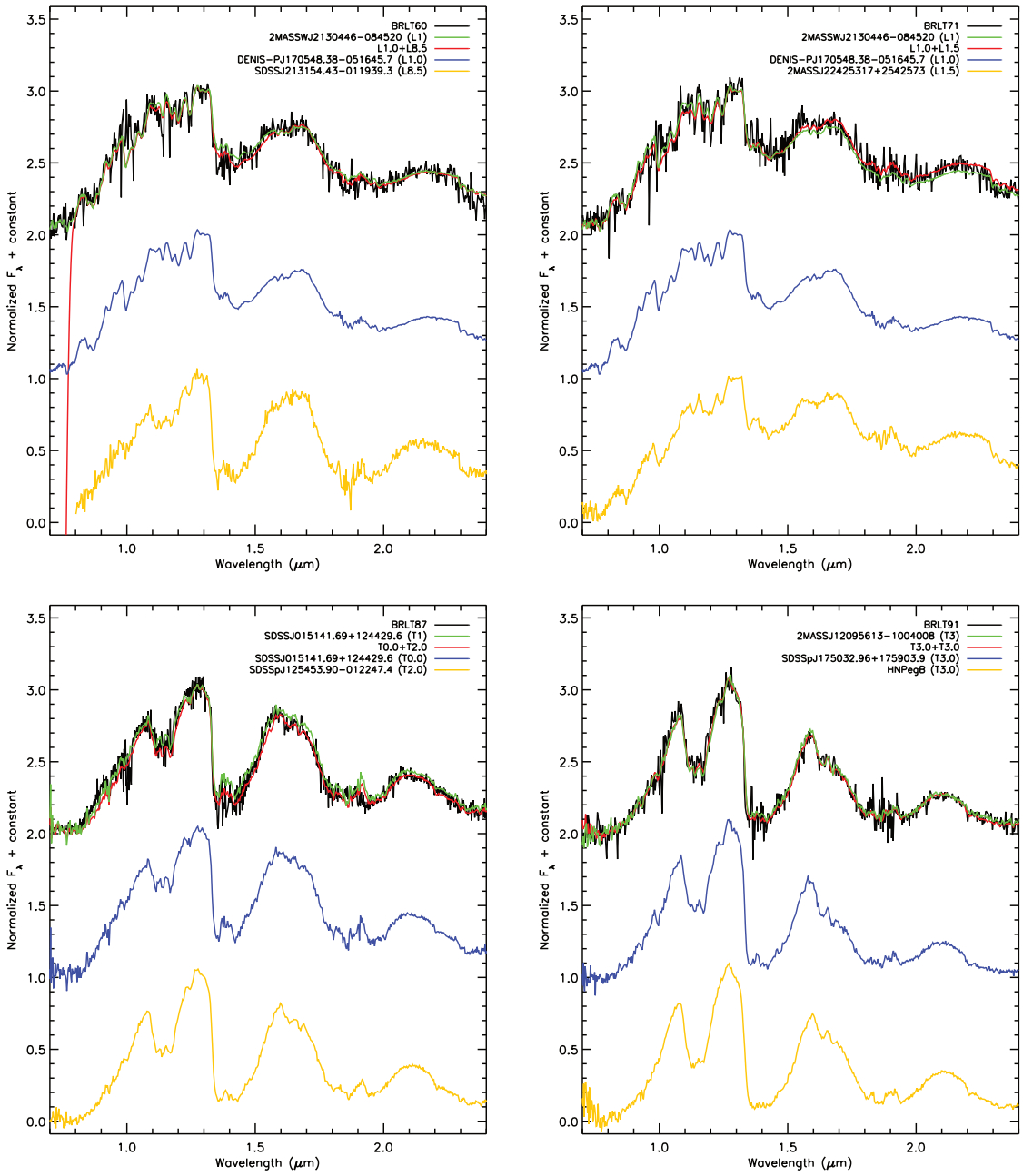


Fig. 3.20: The spectral deconvolution of the binary candidates.

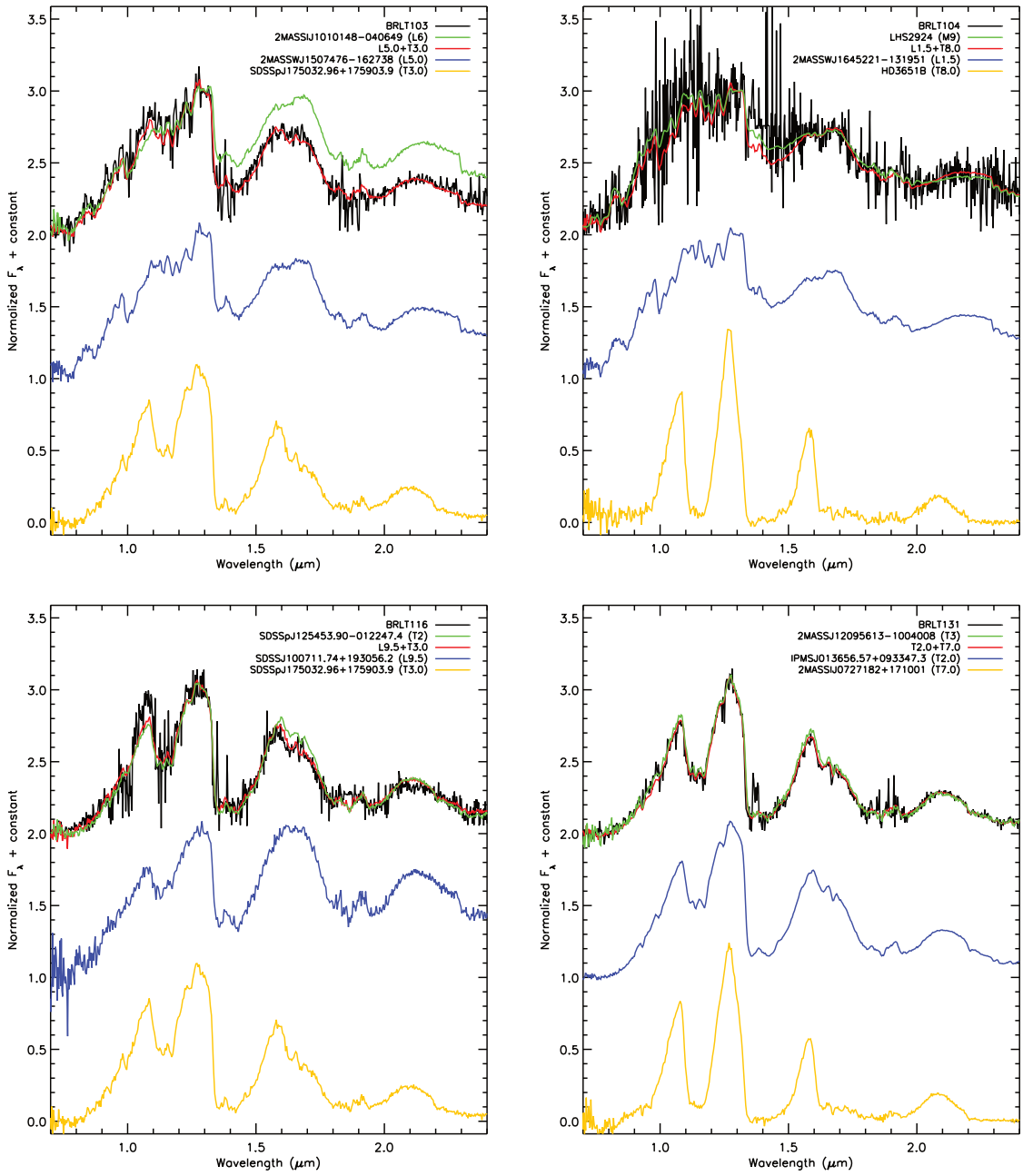


Fig. 3.21: The spectral deconvolution of the binary candidates.

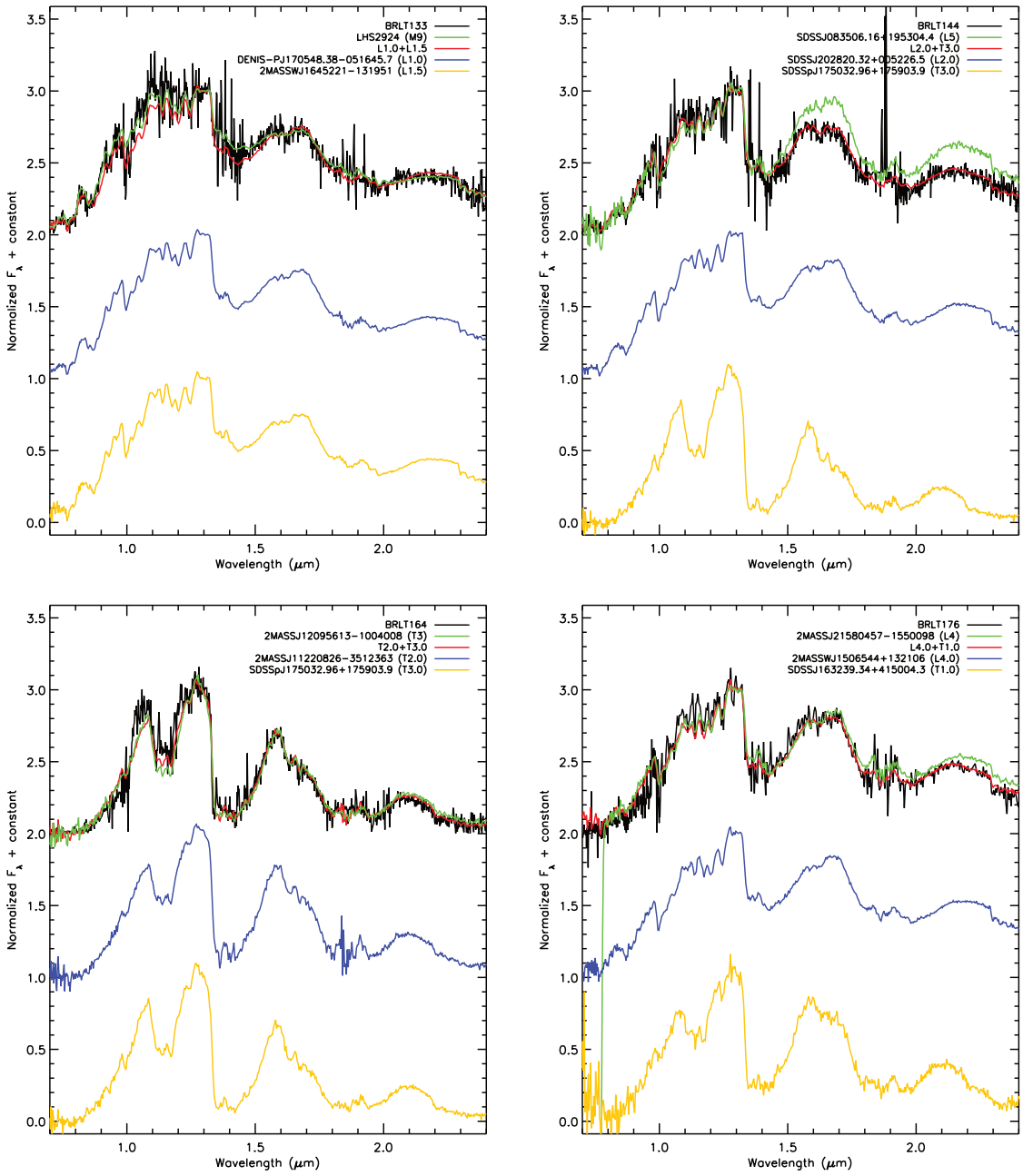


Fig. 3.22: The spectral deconvolution of the binary candidates.

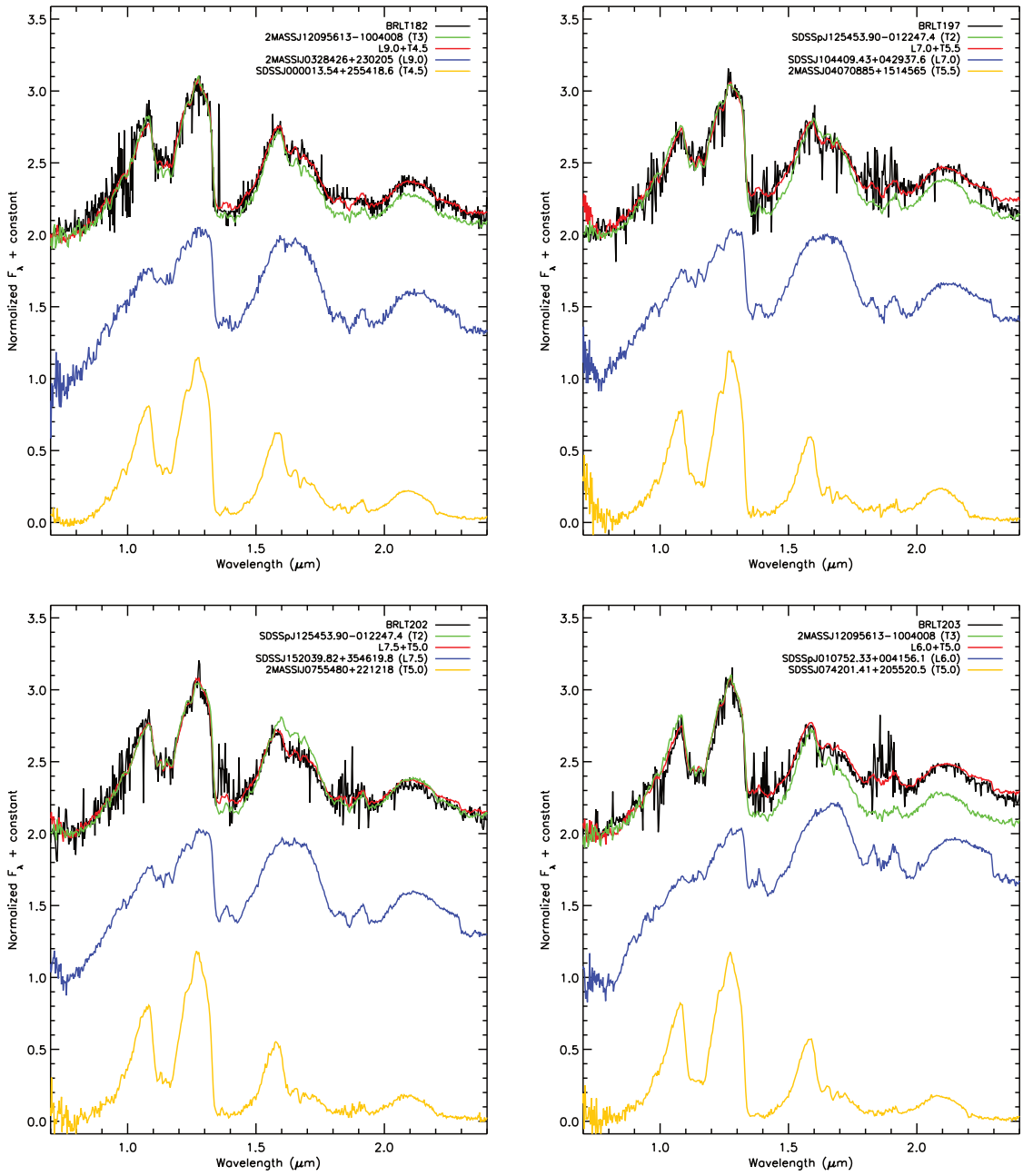


Fig. 3.23: The spectral deconvolution of the binary candidates.

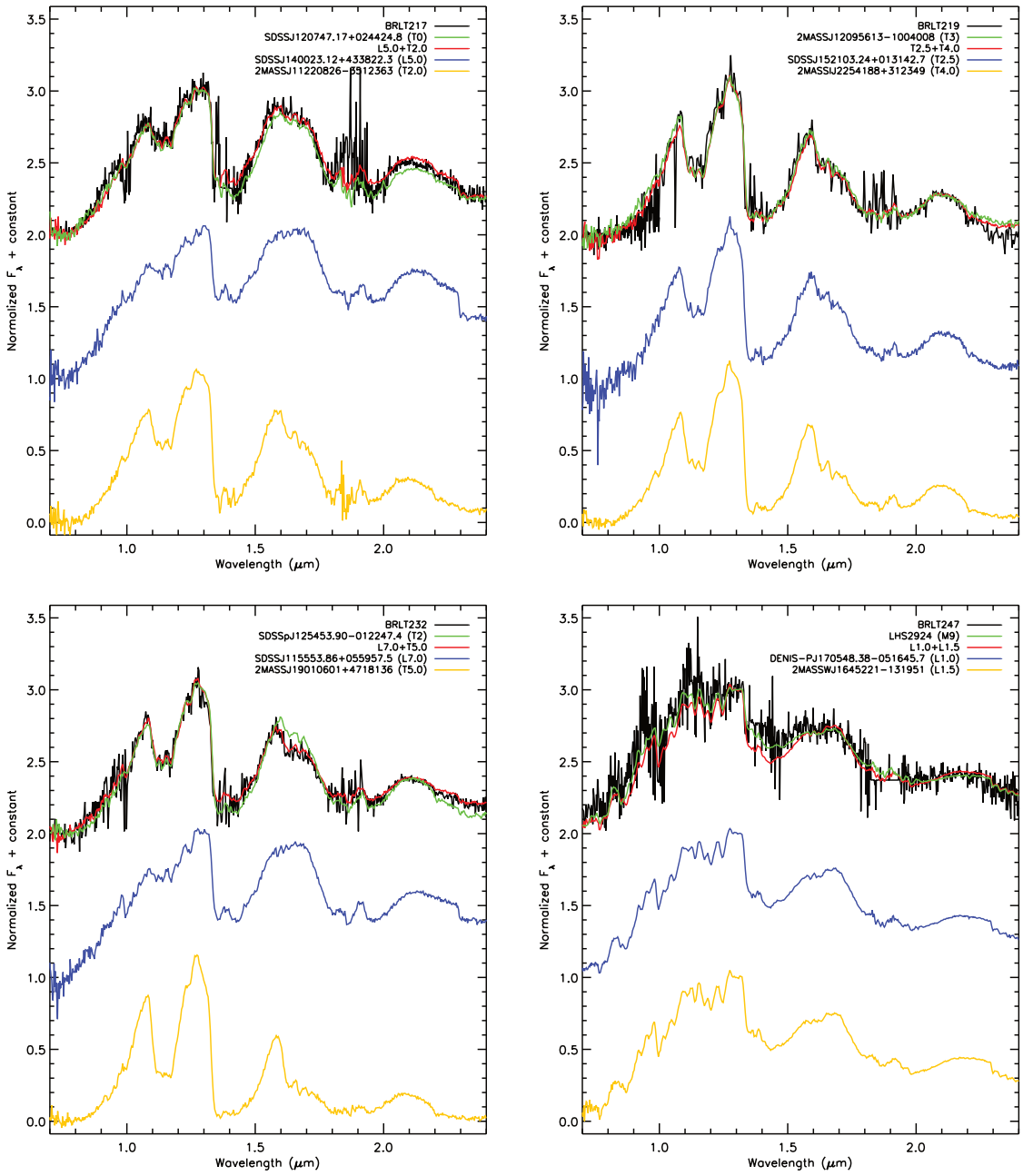


Fig. 3.24: The spectral deconvolution of the binary candidates.

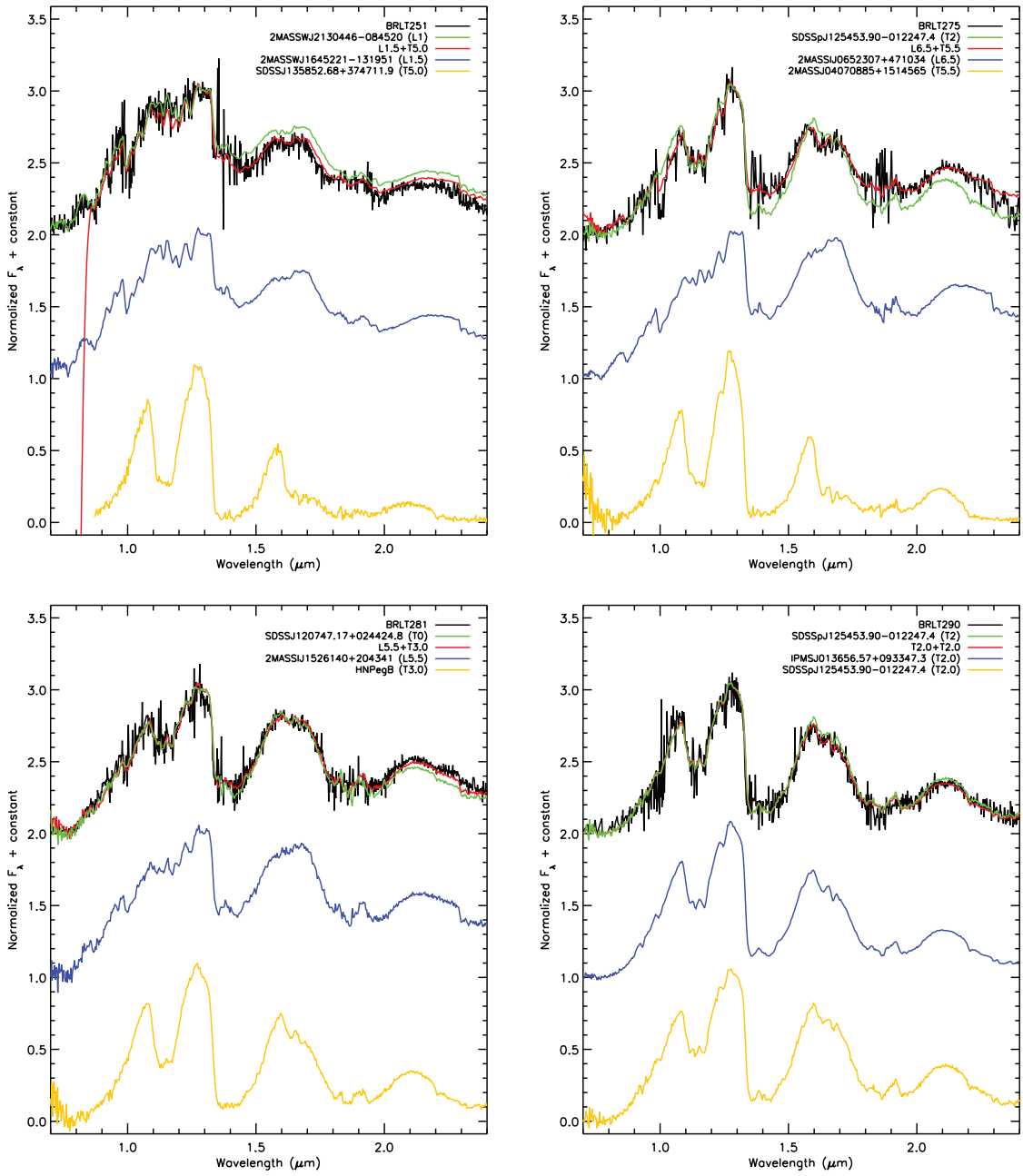


Fig. 3.25: The spectral deconvolution of the binary candidates.

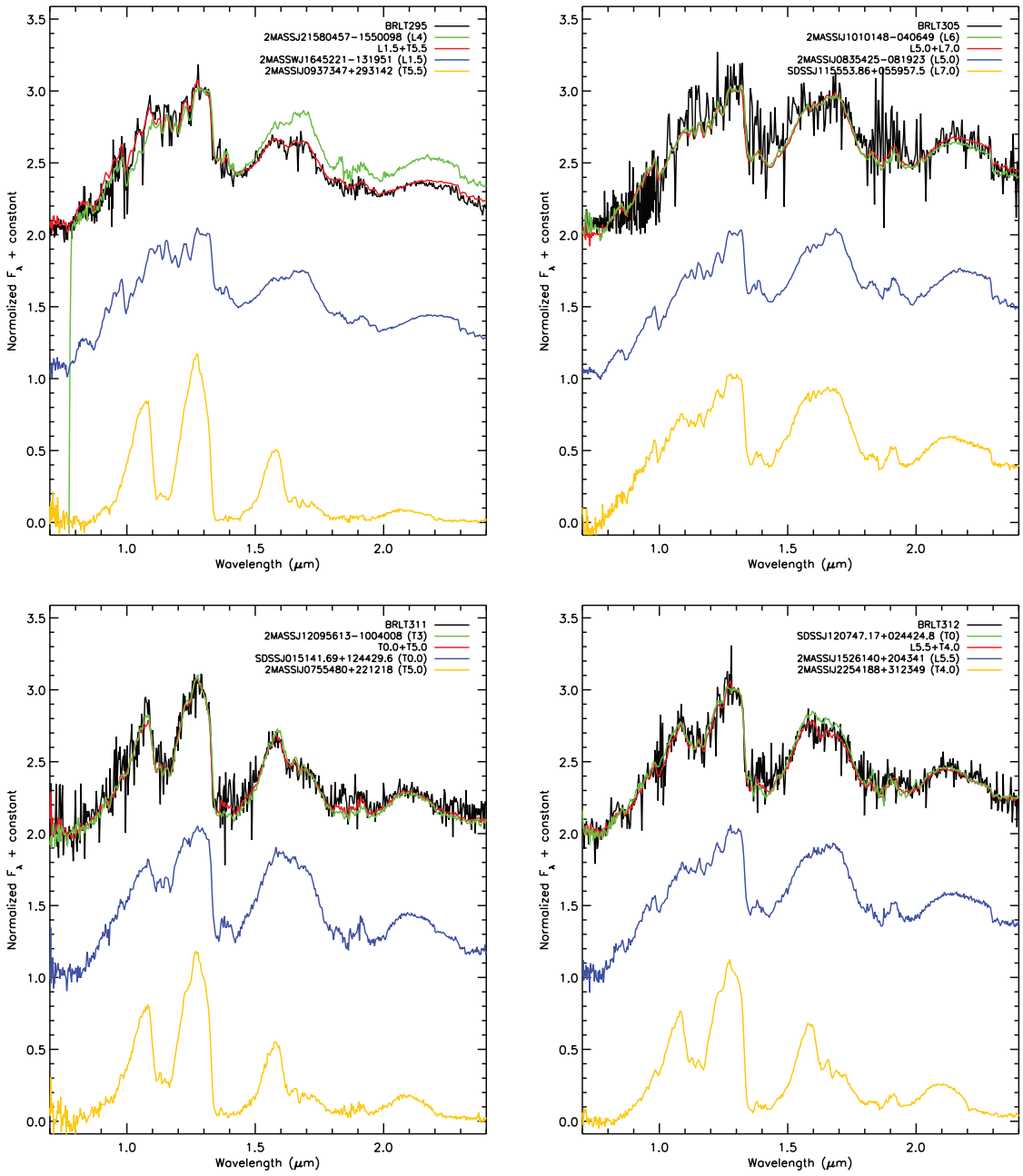


Fig. 3.26: The spectral deconvolution of the binary candidates.

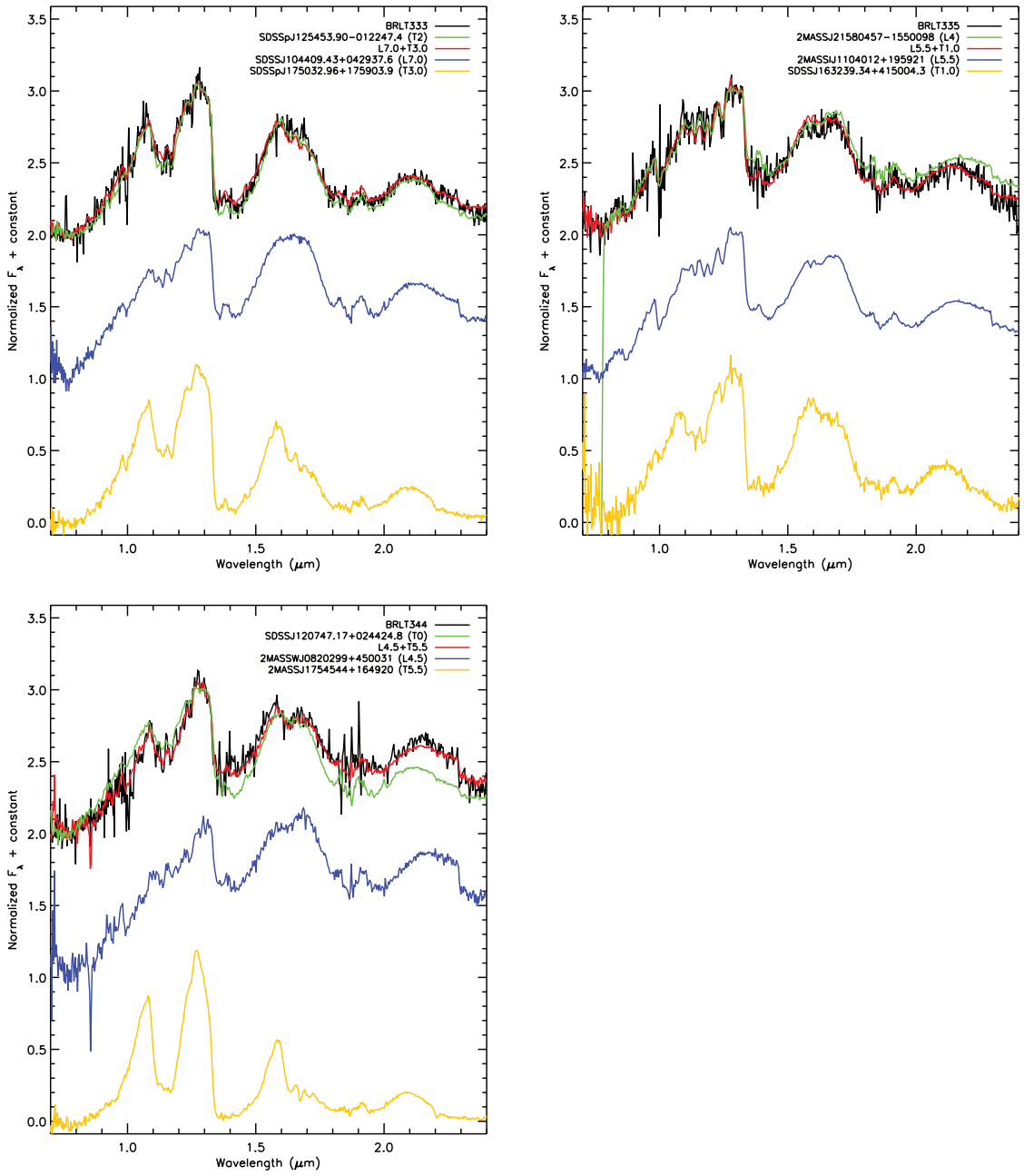


Fig. 3.27: The spectral deconvolution of the binary candidates.

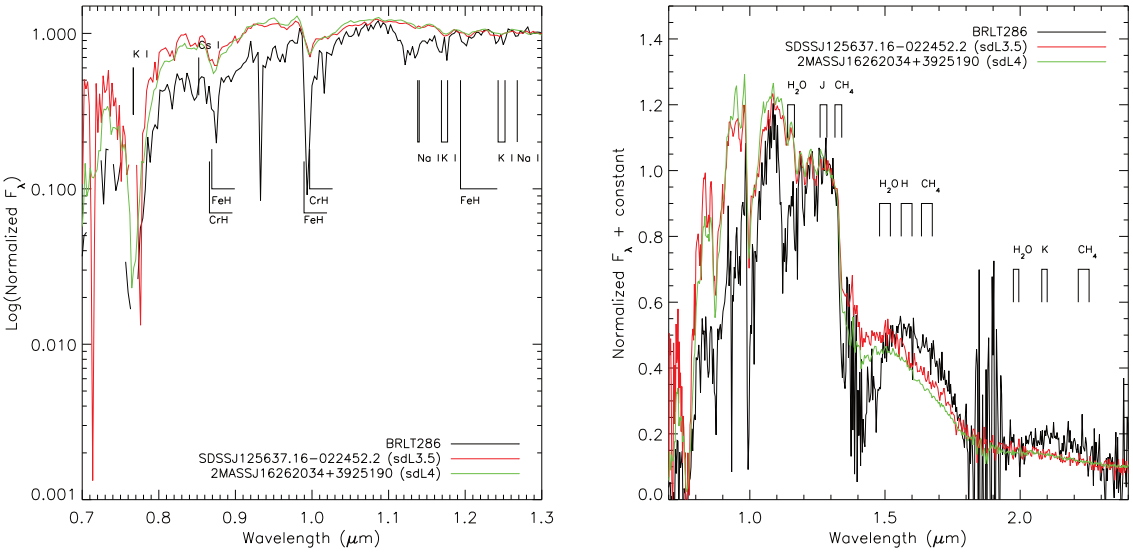


Fig. 3.28: The spectrum of BRLT286. *Left panel*: a zoom of the optical and J band spectrum (0.7−1.3 $\mu$m). *Right panel*: the entire spectrum of the object (0.7−2.45 $\mu$m). Overplotted for comparison the spectra of the sdL3.5 SDSS J125637.16−022452.2 (in red) and of the sdL4.0 2MASS J16262034+3925190 (in green). Major absorption features are labelled.

compared to objects of similar mass. Therefore they fall in the same spectral subclass with younger and smaller (i.e. of lower mass) brown dwarfs, but being more massive show higher surface gravity.

Old, metal-poor, high gravity objects are generally referred to as "sub-dwarfs". A classification scheme for these objects in the near-infrared has not yet been established, mostly because of the lack of a significant sample of such objects (see Table 8 in Kirkpatrick et al., 2010, for a complete census of brown dwarfs classified as sub-dwarfs).

Comparing the spectra of the targets with standard templates and with the available spectra of known L sub-dwarfs I identified one possible sub-dwarfs, BRLT286. The object shows all the "trademarks" of metal poor dwarfs: an extremely suppressed H and K band spectrum, with very little flux at wavelength longer than $\sim 2\mu$m; enhanced flux in the red optical and J band; strong Na I and K I lines; extremely deep FeH and CrH absorption bands. I show the spectrum of BRLT286 in Figure 3.28 along with two known sub-dwarfs: the sdL3.5 SDSS J125637.16−022452.2 and the sdL4 2MASS J16262034+3925190. It is evident that the target is not as extreme as the two plotted sub-dwarfs, as its H and K band spectrum is slightly brighter while the optical and J band is much fainter than in the sub-dwarfs, signs of a less prominent CIA and of a slightly higher dust content of the photosphere. Since there is no established spectral classification of L sub-dwarfs, I classify BRLT286 as sdL4.0 ± 1.0 given its high resemblance to the plotted sub-dwarfs.

### Unusually blue L dwarfs

A number of objects in the sample show unusually blue infrared colours, but do not present any clear sign of metal depletion, hence they cannot be classified as sub-dwarfs. In particular, they do not present significant enhancement of the the alkali absorption lines, while they still show significant suppression of the H and K band flux, and in some cases strong FeH and CrH absorption bands.

Previous studies of the kinematics of such peculiar objects (e.g. Faherty et al., 2009; Kirkpatrick et al., 2010) have pointed out that blue L dwarfs could be part of an older population compared to "normal" L dwarfs, but not as old as the halo population. The metal abundances of these peculiar objects would then be reduced, but not enough to be labelled as sub-dwarfs.

A problem that arises immediately is how to classify these targets, as their spectra diverge significantly from those of standard objects. I adopted an hybrid way of classifying the blue L dwarfs in the sample. I fit the spectra of the targets with the standard templates, but instead of normalizing both the target and the template at a chosen point, I cut the spectra in three parts, roughly corresponding to the optical + J band, H band, and K band, and then separately normalize and fit these three parts. The final spectral type is given by the template that fits best the three separate portions.

To check the robustness of this method I compare in Figure **??** the results obtained for BRLT212, since this object is in common with the PARSEC sample presented in Chapter 2. On the left hand side I show the best-fit spectrum identified using the by-eye approach described in Chapter 2, while on the right hand side I show the best fit obtained with the new method introduced here. The L1.0 standard, selected via by-eye matching, fits well the optical and $J$ band spectrum, underestimating however the depth of the $H_2O$ absorption band at $\sim 1.15\mu$m. The $H$ and $K$ band on the other hand are poorly fit, with much stronger $H_2O$ absorption bands in the target, indicative of a later spectral type. The L6.0 fits much better these two regions of the spectrum, as well as the $H_2O$ absorption band at $\sim 1.15\mu$m, but fails to match accurately the flux level in the red-optical and $J$ band. However, this discrepancy can be explained assuming that the target is a metal-poor object. In a low metallicity atmosphere dust formation is hampered, so the total dust opacity is reduced. A reduced dust opacity results in bluer colours, since observations can probe deeper into the photosphere of the object, where the temperature and pressure are higher. The effect of the CIA on the emergent spectrum is therefore higher and the overall spectral energy distribution is bluer. A spectral type of L6.0 is also consistent with the spectral indices and the absolute magnitudes of the target (see Figures 2.9 and 2.11). I therefore conclude that this new approach is a more accurate and reliable way to determine the spectral type for peculiar objects.

The spectra of the blue L dwarfs identified here are presented in Figures 3.30 - 3.32. For each object I overplot in red the best fit standard template. The targets generally present suppressed H and K band fluxes, and enhanced J bands. The H and K band suppression can be an indication of an enhancement of the CIA, which is the proxy of metal depletion or high surface gravity, and this would be in agreement with the hypothesis of Faherty et al. (2009), suggesting the membership of peculiar L dwarfs to a slightly older population.

Another common feature in all the blue L dwarfs is the presence of very strong $H_2O$ absorption bands. When looking at Figure 3.35, it is evident how blue L dwarfs tend to lie below the "main sequence" in the three plots on the left, with $H_2O$ based indices typical of objects of later spectral type. This could be the effect of a reduced dust content in these metal poor atmospheres, that makes water the main source of opacity.

A general consideration that arises from the analysis of the spectra of the new sub-dwarfs is that the spectral indices measuring the water bands depth are particularly good to pick up the sub-dwarfs, as can be seen by the spectra of the targets and those of the standard templates (Figures 3.30 to 3.32). The three water indices ($H_2O$-J, $H_2O$-H,

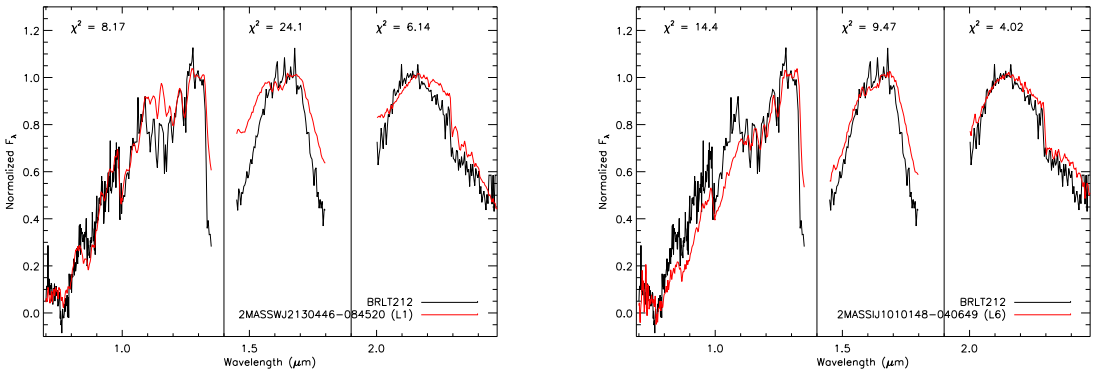


Fig. 3.29: The spectrum of BRLT212 compared to the best-fit templates obtained folllowing two methods. *Left*: the best fit obtained via by-eye matching (see Section 2.3.2). *Right*: the best fit obtained via spectral fitting (see text for details). The L6.0 standard provides a better match to the $H$ and $K$ band spectra, while the L1.0 fits better the red-optical and $J$ band. This is an indication of metal depletion.

and $H_2O$-K) lie in regions where the flux ratio diverges significantly from unity, while the other indices, and in particular $CH_4$-J, $CH_4$-H, and $CH_4$-K pick up features that are much less influenced by metal depletion.

It must be noted at this point that an alternative explanation for unusually blue L dwarfs is unresolved binarity. The presence of a close T type companion would produce a similar effect. However, only one of the new blue L dwarfs matches the selection criteria for binaries (BRLT16), and its fit with unresolved binary templates is not significantly better than the one with a single template (see Section 2.3.3). I therefore conclude that the sample of blue L dwarfs is entirely made of intrinsically blue objects.

### Blue T dwarfs

As for the blue L dwarfs, I identified 2 peculiar T dwarfs which show H and K band suppression.

A number of unusually blue T dwarfs have been presented in Murray et al. (2011), who selected the peculiar objects based on their MKO photometry. One of the two objects identified here, BRLT179, was indeed part of that sample. The spectra of the two blue T dwarfs in the sample are presented in Figure 3.33. Both of them show a very suppressed K band flux, which is indicative of an enhanced CIA. Whether this enhancement is due to low metallicity or to a higher surface gravity is still a matter of debate (see for instance Murray et al., 2011). A way to distinguish between the two cases is the analysis of the kinematics of the brown dwarfs, as thick disk or halo-like space velocities would be suggestive of a metal-poor nature, while in the case of a thin disk-like space motion high gravity would be the preferred explanation.

*BRLT50*: the general shape of the spectrum of this object is well fitted by the T6 standard SDSSp J162414.37+002915.6. However, the peak of the J and H band are slightly lower in the target, and the K band is clearly suppressed, all hints to metal depletion. The kinematics can generally offer insights into the interpretation of the nature of peculiar objects like this one, but with no measured proper motion, I cannot address the possibility of this object belonging to a older disk population.

*BRLT179*: I assigned a spectral type of T4.5 to this object as the T5 standard

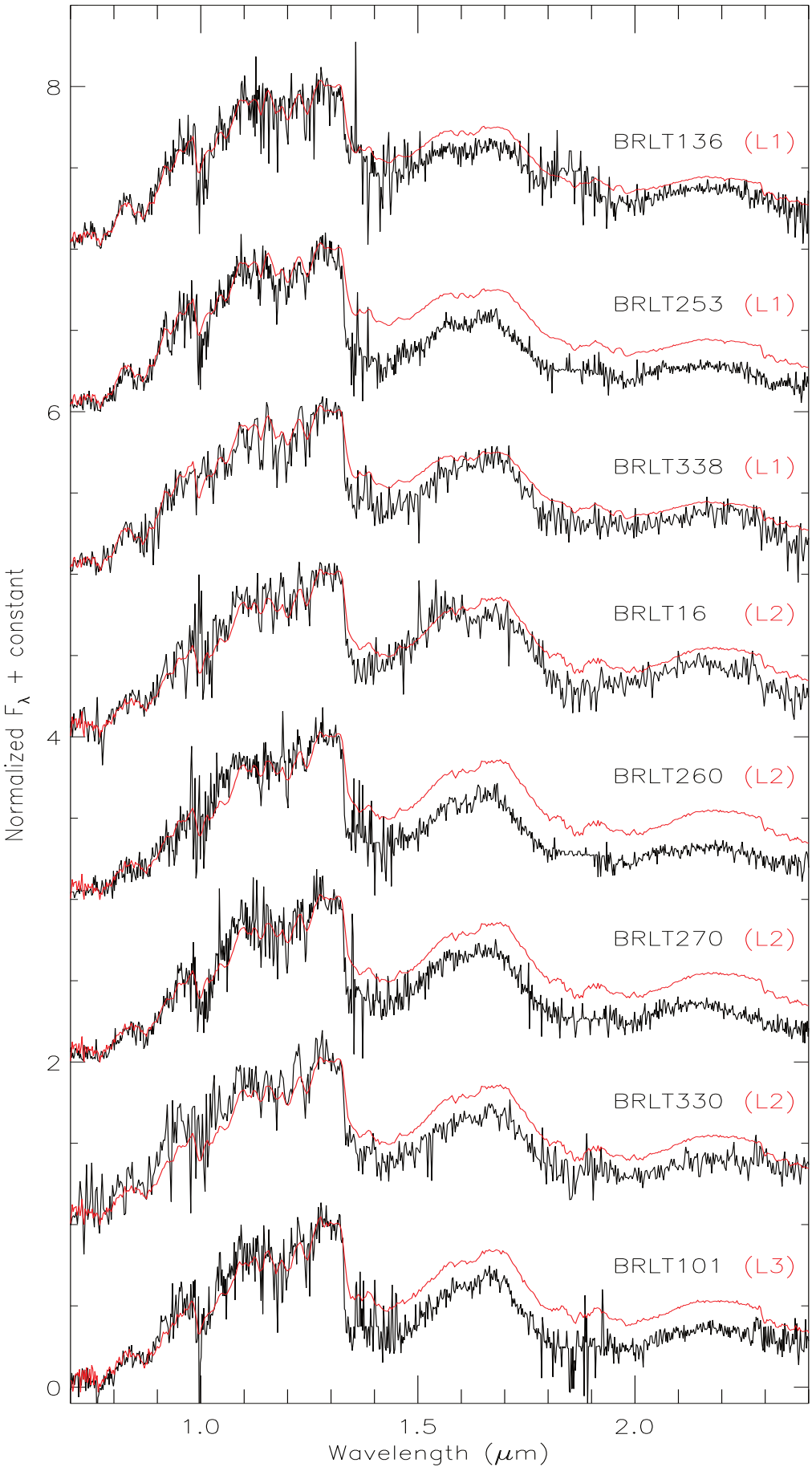


Fig. 3.30: The spectra of the peculiar blue L dwarfs. Overplotted in red I show the best fit template for each target.

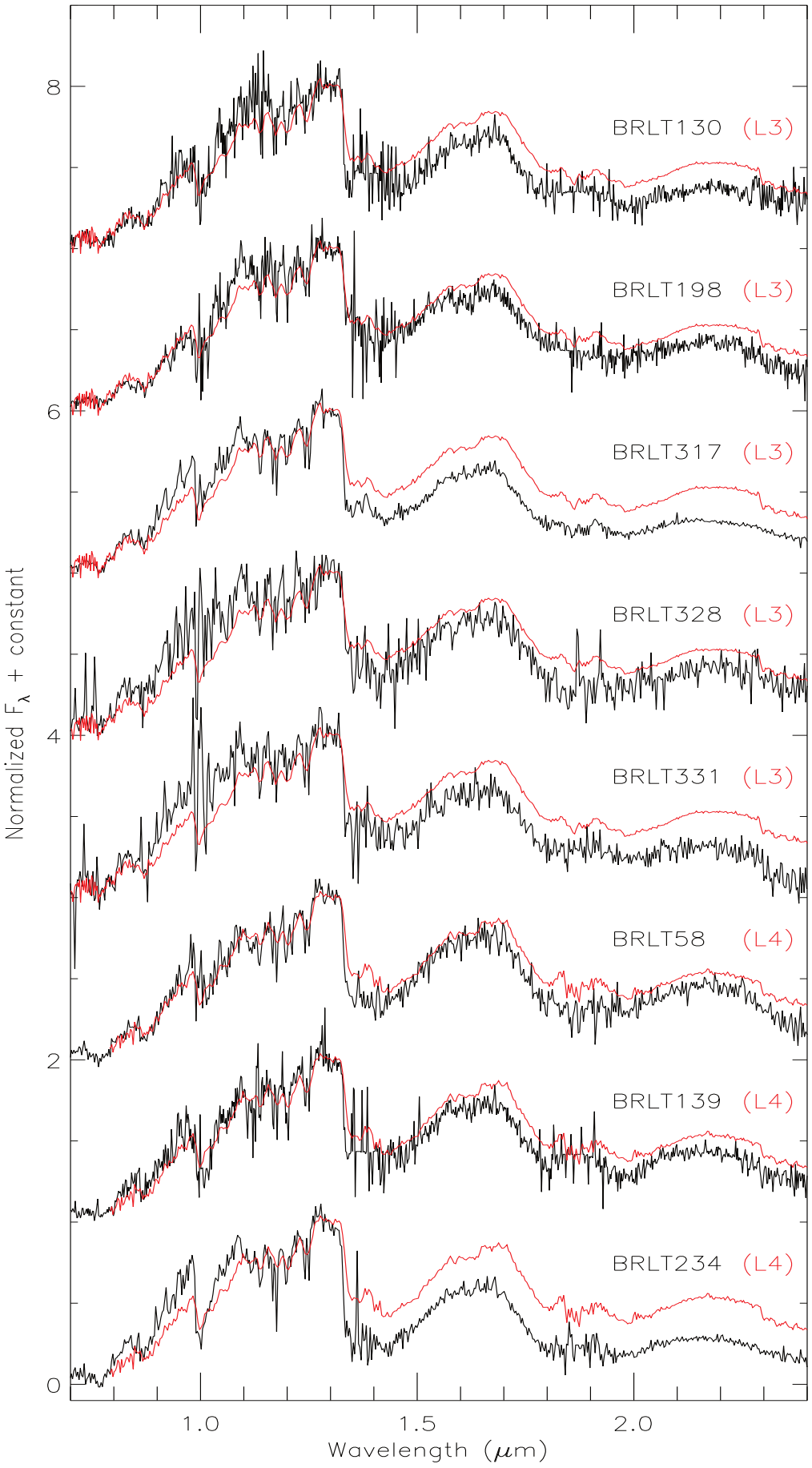


Fig. 3.31: The spectra of the peculiar blue L dwarfs. Overplotted in red I show the best fit template for each target.

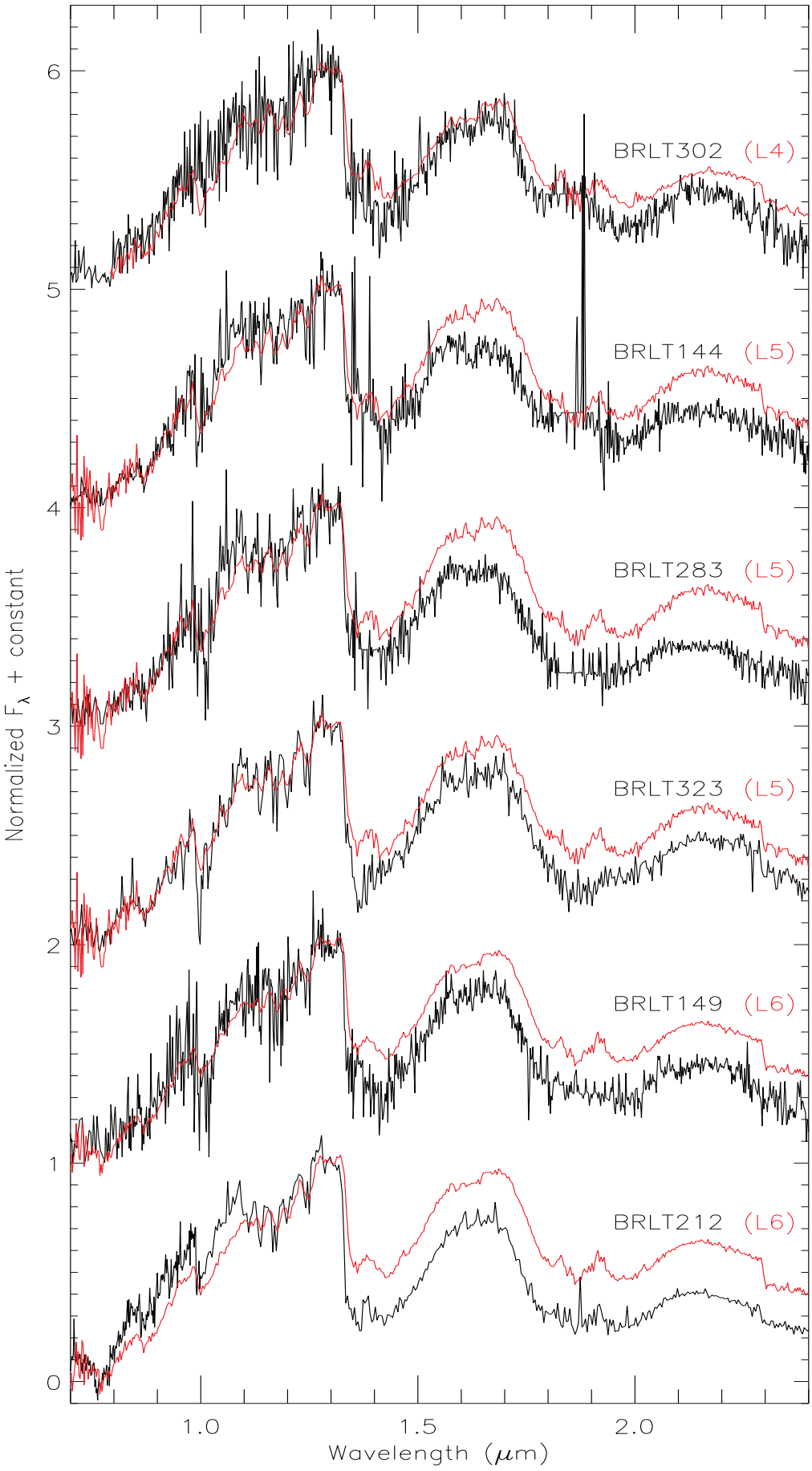


Fig. 3.32: The spectra of the peculiar blue L dwarfs. Overplotted in red I show the best fit template for each target.

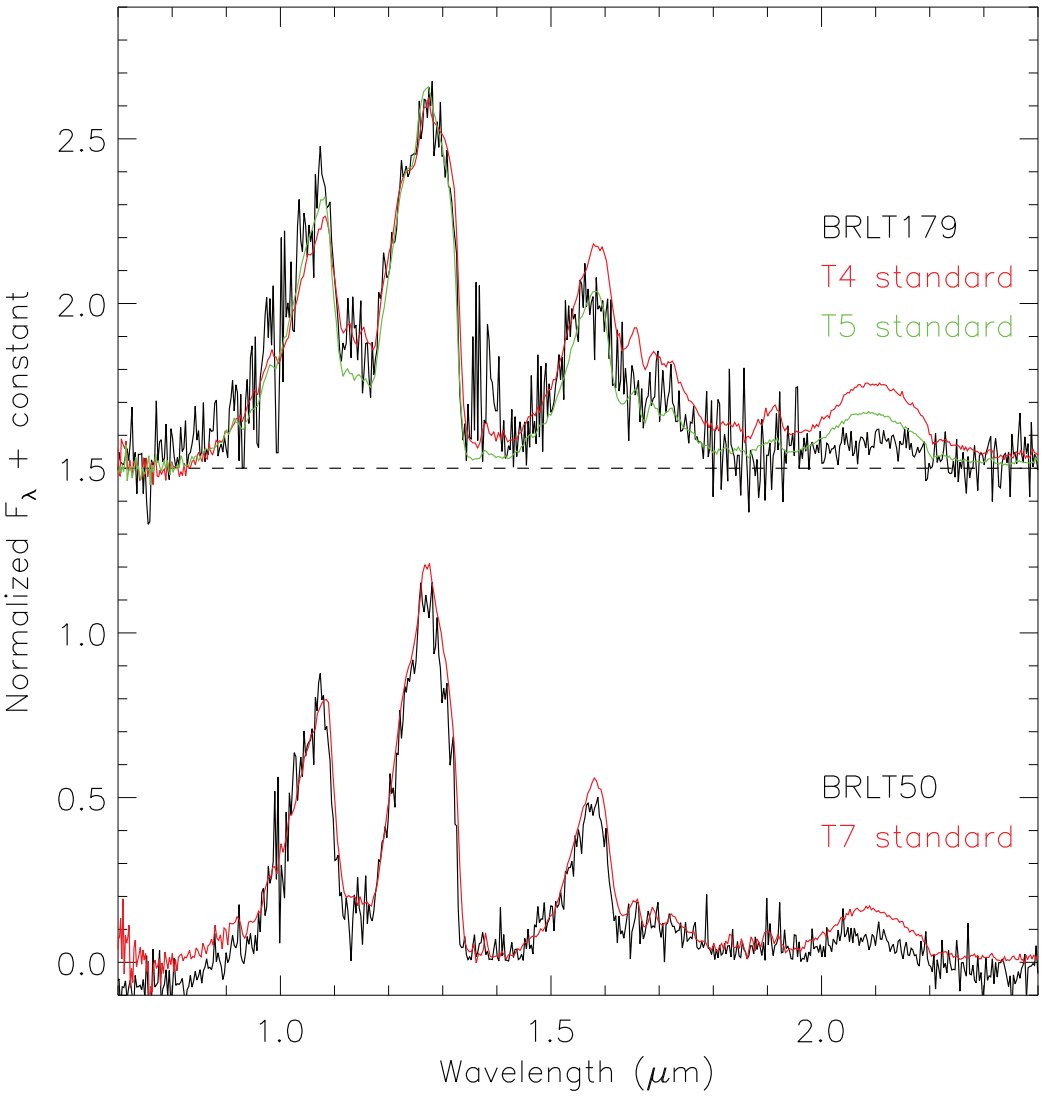


Fig. 3.33: The spectra of the peculiar blue T dwarfs. Overplotted in red I show the best fit template for each target.

reproduces quite well the general shape of the SED in the 0.7−1.8 $\mu$m range, except for the depth of the H2O absorption at 1.15 and 1.35 $\mu$m. These features are much better fitted by the T4 standard. The flux level in the K band is extremely suppressed, with almost no flux left. The assigned spectral type is 1 subtype later than the one given in Burningham et al. (2010b), but that is based on a 1.05−1.35 $\mu$m spectrum only. The kinematics analysis of BRLT179 performed by Murray et al. (2011) suggests a young disk nature for this object, which is somewhat surprising as BRLT179 is the second bluest T dwarf known (J−K = -1.2 ± 0.1), and its K band spectrum is strongly suppressed. This apparent inconsistency is in common with the bluest T dwarf known, SDSS J1416+1348B (Burningham et al., 2010a; Scholz, 2010) which has young disk kinematics as well.

### Low gravity and unusually red L dwarfs

While unusually blue infrared colours are generally tracers of reduced metallicity or high surface gravity, unusually red spectra are the product of an increased metal content or a low surface gravity (which is typical of young objects). I refer the reader to Section 1.6.2 and references therein for a more detailed description of the spectral signatures associated (or believed to be associated) with these two atmospheric parameters, and the classification scheme developed for this type of objects.

I identified 3 peculiar red L dwarfs within the sample, and their spectra can be found in Figure 3.34. A discussion of their characteristics is in the following paragraphs.

*BRLT22* and *BRLT85*: these two late M dwarfs show the peculiar signs of low gravity objects. Specifically they have a somewhat triangular shaped H band, and shallower alkali lines in the J band (in particular in BRLT85). Both objects also show stronger water absorption when compared to the standard template (overplotted in red in Figure 3.34). In both cases the low gravity M8 template matches better the SED of the target. The gravity classification scheme defined in Allers & Liu (2013) gives a classification of INT-G for BRLT22 and LOW-G for BRLT85, further highlighting the peculiar nature of these two targets. A definitive confirmation has to come from the kinematics, possibly associating the targets to known young moving groups in the solar neighbourhood.

*BRLT309*: it is the reddest object in the sample, and one of the two reddest brown dwarfs known (depending on the colour considered). I assign a spectral type of L7 as the corresponding standard provides the closest match to the separately normalized J, H, and K band peaks. Its spectrum however diverges significantly from the standard in the optical and in particular in the H and K band. The reduced flux at $\lambda < 1.2$ $\mu$m, the triangular shape of the H and K band peak and their enhancement, and the very strong CO feature are all hallmarks of increased dust opacity. The general shape of the spectrum shows a significant resemblance to that of the proposed very low gravity L7 standard (plotted in green in Figure 3.34). The Allers & Liu (2013) gravity classification for BRLT309 however is FLD-G. A more detailed description of the characteristics of this object, and a more in-depth analysis of its properties can be found in Chapter 5.

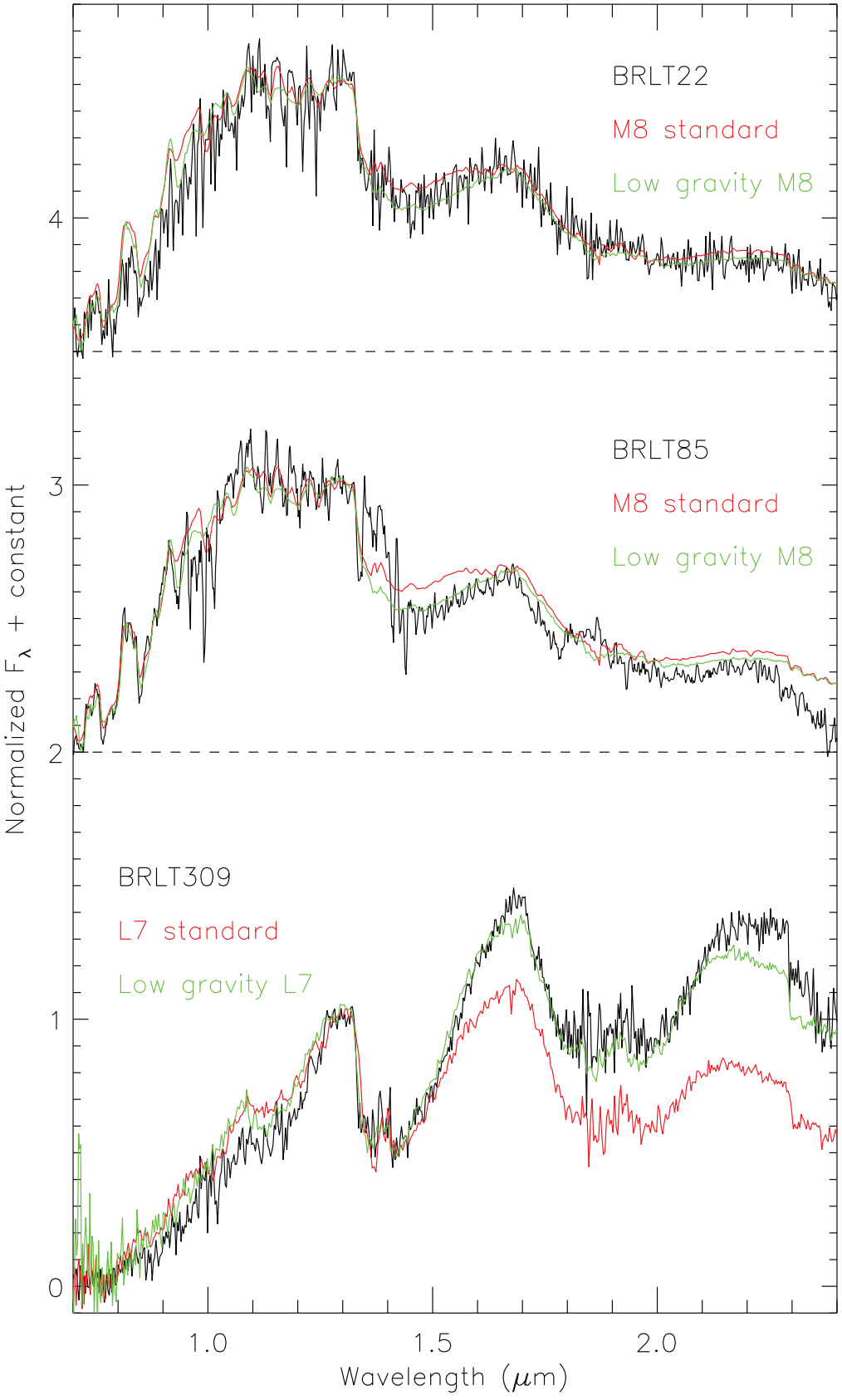


Fig. 3.34: The spectra of the peculiar red L dwarfs. Overplotted in red and green I show the best fit field standard and the best fit low gravity standard

## 3.5 Spectral indices and equivalent width

A way to quantify the evolution of spectral features across the spectral sequence is to use spectral indices to measure their strength. The spectral indices calculated for the targets are presented in Table 3.2, and plotted in Figure 3.35 and 3.36. The peculiar objects identified in the previous section are plotted in colour.

In Figure 3.35 one can see how the indices measuring the *relative* strength of the water absorption bands (the three plots on the left hand side) correlate very well with spectral types. Blue L dwarfs tend to have stronger water absorption bands and their indices therefore are typical of later type objects (as late as T0−T1 in some cases), lying below the "main sequence". A purely index-based classification for these objects could therefore lead to systematically later types. The sub-dwarf candidate on the other hand is above the sequence, not because it has shallower water bands (see Figure 3.28), but because the flux in the H and K band is suppressed by the CIA and therefore the relative depth of those bands is shallower.

The right hand side of Figure 3.35 shows the indices measuring the *relative* depth of the methane absorption bands. Not surprisingly, the correlation between those indices and spectral type is valid only in the T dwarf range, as there is no methane absorption in L dwarfs.

In Figure 3.36 I present a series of index-index plots. It is easy to spot the "main sequence", from the late-Ms and early-Ls on the top-right to the mid-Ts in the bottom-left corner of each plot. Once again, the methane indices do not correlate in the L dwarfs regime, with all of the L dwarfs clustered in the 0.8−1.0 range for each methane index. When looking at the left hand side of the figure, blue L dwarfs tend to be clustered below the sequence, further stressing the unusual strength of their water absorption bands, while blue T dwarfs sit above it. In particular the two blue T dwarfs have very high values of the $H_2O$-K index, which is the effect of their extreme flux suppression in the K band. With very little flux left, their K band spectra are almost flat, and their corresponding indices tend to one. The extremely red L dwarf is also slightly above the sequence, but its position is not as extreme as suggested by its photometry. This is in agreement with its FLD-G classification.

While these indices give an indication of the evolution of broad molecular absorption bands, to measure the strength of narrow atomic lines I calculated their equivalent width. As discussed in Section 1.5 the main atomic lines in the spectra of brown dwarfs are Na I and K I. I calculated the equivalent width of the Na I doublet at 1.139 $\mu$m, and the K I lines at 1.169, 1.177, 1.244, and 1.253 $\mu$m, as these are the strongest and best detected lines.

To measure the equivalent width, I fit each doublet and the region of the spectrum around it using a double gaussian profile. I decided to fit the doublets together since the lines are too close to allow for a separate fit, as one would have to restrict the region to fit too much, leading to a more uncertain determination of the continuum. The continuum is a parameter of the fit, and is assumed to be changing linearly as a function of wavelength. This is to take into account that, especially in late type objects, some of the lines considered do not fall in regions of flat continuum. The centre of the lines is also a parameter of the fit, but the separation between them is fixed and assumed to be equal to the tabulated separation. The equation describing each doublet is therefore:

$$F(\lambda) = F_0 + \lambda \times C + a_1 e^{(\lambda-\lambda_1)^2/2\sigma_1^2} + a_2 e^{(\lambda-(\lambda_1+\Delta\lambda))^2/2\sigma_2^2} \quad (3.1)$$

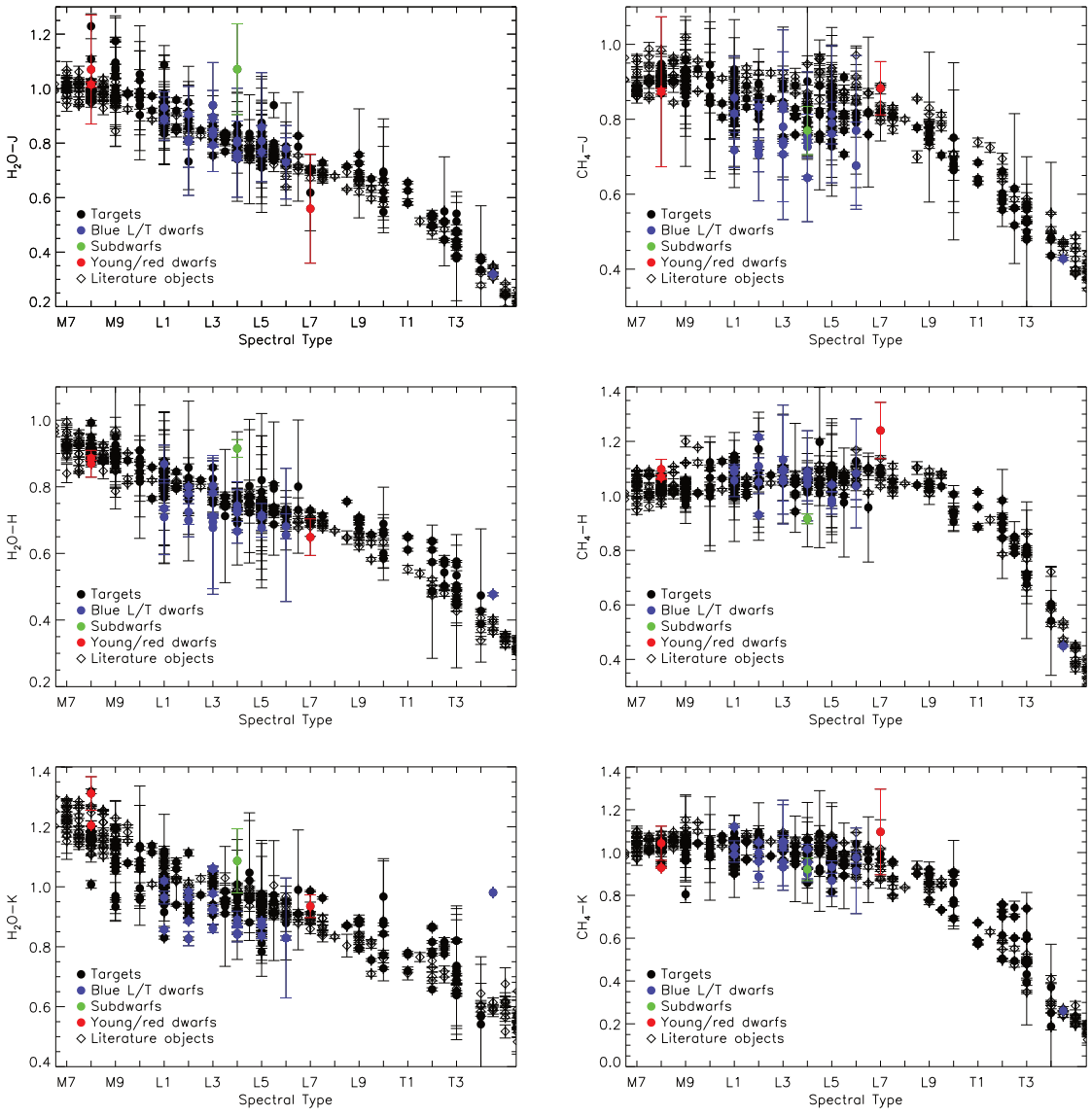


Fig. 3.35: The spectral indices as a function of spectral type. Peculiar objects are plotted in colours. The spectral indices calculated for a series of known L and T dwarfs from the literature are overplotted for reference.

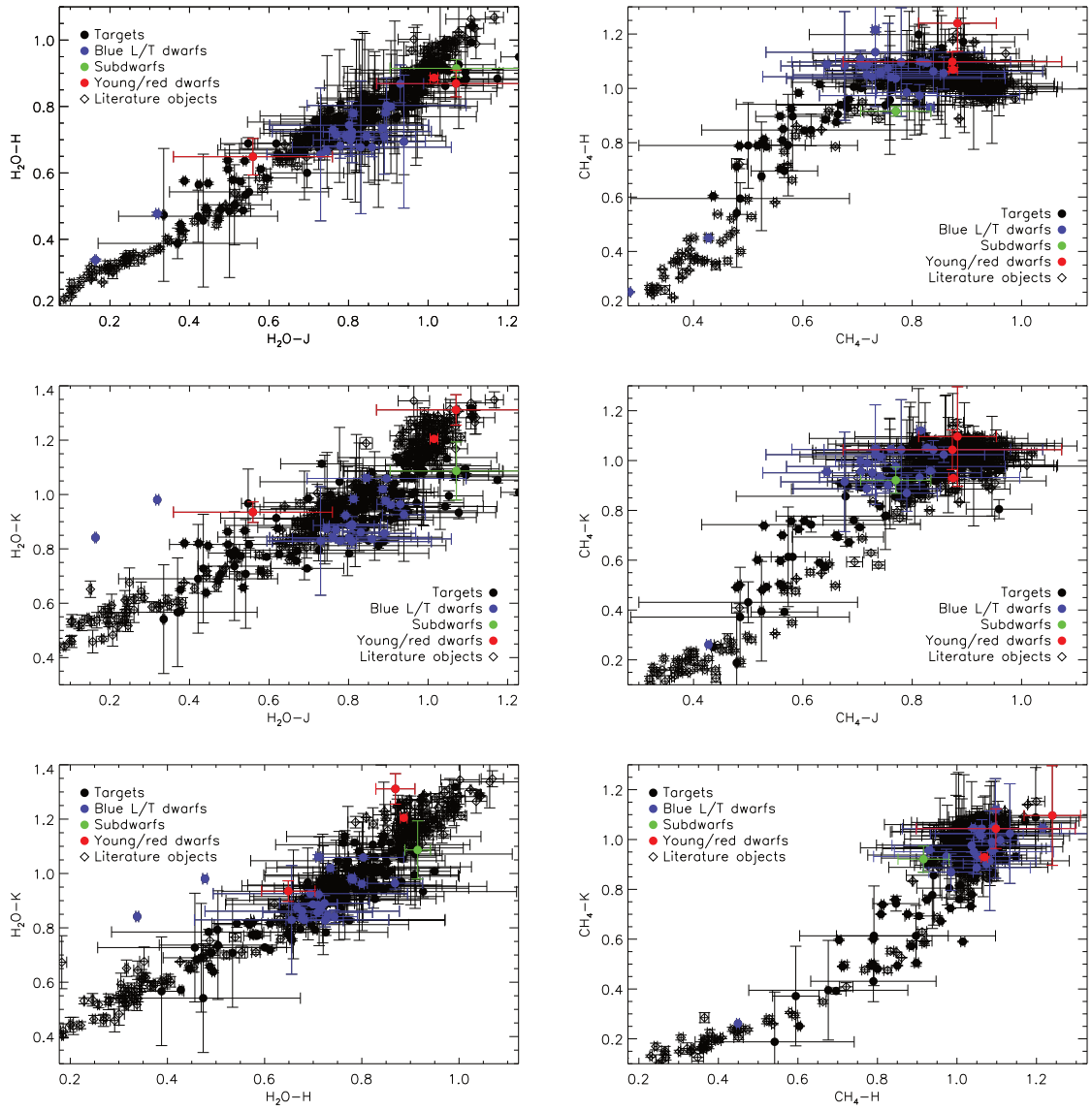


Fig. 3.36: Index-index plots. Peculiar objects are plotted in colours. The spectral indices calculated for a series of known L and T dwarfs from the literature are overplottedfor reference. The "main sequence" is clearly visible from the top-right to the bottom-left corner of each plot.

where $F_0$ and $C$ are the two parameters describing the continuum, $\lambda_1$ is the centre of the first line in the doublet, $\Delta\lambda$ is the separation between the two lines, $\sigma_1$ and $\sigma_2$ are the width of the two lines, and $a_1$ and $a_2$ are intensity of the two lines, i.e. the minimum flux at the centre of the lines. $F_0, C, \lambda_1, a_1, a_2, \sigma_1$ and $\sigma_2$ are all parameters of the fit.

The equivalent width measured for the targets are presented in Table 3.6 and plotted as a function of effective temperature in Figure 3.37. Since the Na I doublet at 1.139 $\mu$m is partly blended, the values presented are the total equivalent width of the doublet. The effective temperature of an object was determined from its spectral type using the type-to-temperature conversion presented in Chapter 2. Objects with very low signal to noise, or with dubious detection of the lines have been omitted. Measurements with relative errors larger than 0.33 are plotted as open circles, while those with relative errors better than 0.33 are plotted as filled circles. Overplotted for reference are the equivalent width calculated for the BT-Settl atmospheric models (Allard et al., 2011) for solar metallicity, and three different values of surface gravity. The equivalent widths show a large scatter, and there is no clear separation between blue/red L and T dwarfs and the rest of the sample.

The models suggest that the lines should reach their maximum strength at $T_{\rm eff} \sim$ 2000 K, and then slowly get weaker towards lower temperature. Looking at the values from the sample, only the K I lines at 1.244 and 1.253 $\mu$m follow the expected trend, while the Na I doublet and the K I lines at 1.169 and 1.177 $\mu$m remain strong even at temperatures as low as ∼1200 K. However the discrepant measurements tend to have very large associated errors. This is because the mentioned lines fall in regions of growing $H_2O$ and $CH_4$ absorption, so in late type (i.e. low $T_{\rm eff}$) objects the signal-to-noise ratio in those areas decreases sharply, and the fit to the doublet get less reliable. This would not be a problem in the atmospheric models, nor for the K I lines at 1.244 and 1.253 $\mu$m since they fall in a region where water and methane absorption is less prominent, and therefore follow the expected trend.

| Name | Spectral type | Equivalent width (Å) | | | | |
|---|---|---|---|---|---|---|
| | | Na I 1.139$\mu$m | K I 1.169$\mu$m | K I 1.177$\mu$m | K I 1.244$\mu$m | K I 1.253$\mu$m |
| BRLT1 | L9.0 ± 0.5 | *0.90* | 8.52 | 3.83 | 2.50 | 2.73 |
| BRLT2 | L1.0 ± 1.0 | 6.79 | 5.23 | 4.77 | 9.27 | 2.38 |
| BRLT3 | L9.0 ± 1.0 | *1.33* | 3.95 | 4.72 | *0.57* | 3.87 |
| BRLT6 | L3.0 ± 1.0 | 6.88 | 2.15 | 2.70 | 9.36 | 2.58 |
| BRLT7 | M8.0 ± 1.0 | 6.41 | *1.26* | 5.69 | 3.04 | 4.95 |
| BRLT8 | L8.5 ± 0.5 | *3.50* | 5.46 | 1.92 | 1.68 | 3.89 |
| BRLT9 | L1.0 ± 1.0 | 7.38 | 4.97 | 8.39 | 5.20 | 6.09 |
| BRLT10 | L9.0 ± 0.5 | *2.41* | 2.42 | 3.52 | *0.67* | *1.32* |
| BRLT12 | L3.0 ± 1.0 | 4.24 | 2.82 | 8.70 | 5.39 | 5.61 |
| BRLT14 | L0.0 ± 0.5 | ... | ... | ... | ... | ... |
| BRLT15 | T2.0 ± 2.0 | ... | *4.29* | *2.20* | 1.57 | 2.66 |
| BRLT16 | L2.0 ± 1.0 | 6.92 | 6.76 | 4.91 | 5.89 | 2.72 |
| BRLT18 | L0.0 ± 1.0 | ... | ... | ... | ... | ... |
| BRLT20 | L1.0 ± 1.0 | 5.90 | 5.08 | 8.69 | 5.77 | 2.06 |
| BRLT21 | L3.5 ± 0.5 | 8.09 | 4.08 | 9.37 | 7.41 | 8.32 |
| BRLT22 | M8.0 ± 0.5 | 4.41 | 6.26 | 5.04 | 6.27 | ... |
| BRLT24 | L3.5 ± 0.5 | 12.53 | 3.42 | 6.94 | 5.96 | 6.70 |

Continued on the next page.

Continued from the previous page.

| Name | Spectral type | Equivalent width (Å) | | | | |
|---|---|---|---|---|---|---|
| | | Na I 1.139$\mu$m | K I 1.169$\mu$m | K I 1.177$\mu$m | K I 1.244$\mu$m | K I 1.253$\mu$m |
| BRLT26 | L5.5 ± 0.5 | 8.97 | 5.77 | 5.57 | 4.03 | 2.66 |
| BRLT27 | T0.0 ± 0.5 | *3.55* | *5.59* | *3.87* | 5.78 | *1.67* |
| BRLT28 | L6.0 ± 0.5 | ... | *5.62* | *5.65* | ... | ... |
| BRLT30 | L5.0 ± 0.5 | ... | ... | ... | *4.72* | ... |
| BRLT31 | L4.0 ± 1.0 | 3.32 | 4.61 | 6.50 | 5.72 | 4.59 |
| BRLT32 | L1.5 ± 0.5 | 7.89 | 3.63 | 9.26 | 9.26 | 6.69 |
| BRLT33 | L3.5 ± 0.5 | 4.41 | *0.87* | 9.33 | 9.04 | 4.65 |
| BRLT35 | M9.5 ± 0.5 | 9.89 | 4.11 | 7.79 | 5.19 | 3.75 |
| BRLT37 | L5.0 ± 0.5 | 8.38 | 3.00 | 6.83 | 6.46 | 5.72 |
| BRLT38 | T0.0 ± 0.5 | *5.33* | *2.69* | *3.04* | 1.36 | 2.95 |
| BRLT39 | L5.0 ± 1.0 | 3.29 | 6.08 | 7.12 | 5.18 | 7.94 |
| BRLT42 | M9.0 ± 0.5 | 8.58 | *0.81* | 5.57 | 1.68 | 3.40 |
| BRLT44 | L5.0 ± 1.0 | 2.02 | 7.24 | 7.71 | 3.34 | 3.00 |
| BRLT45 | T1.0 ± 0.5 | *1.07* | *0.73* | *2.63* | 1.88 | 3.14 |
| BRLT46 | L0.5 ± 0.5 | 9.54 | 8.13 | 7.45 | 10.87 | 3.50 |
| BRLT48 | L4.5 ± 0.5 | ... | ... | ... | ... | ... |
| BRLT49 | M9.0 ± 0.5 | ... | *2.72* | *5.23* | *3.95* | *5.04* |
| BRLT50 | T6.0 ± 0.5 | ... | ... | ... | ... | ... |
| BRLT51 | L3.0 ± 1.0 | 11.88 | 4.20 | 4.86 | 9.75 | 2.31 |
| BRLT52 | L5.5 ± 0.5 | ... | 6.53 | 7.08 | *1.24* | 3.51 |
| BRLT56 | L1.5 ± 1.0 | 5.34 | 4.89 | 9.50 | 7.13 | 4.33 |
| BRLT57 | L0.0 ± 1.0 | 5.53 | 4.35 | 4.29 | 7.53 | 3.09 |
| BRLT58 | L4.0 ± 1.0 | 5.26 | 4.51 | 11.05 | 9.47 | 4.71 |
| BRLT60 | L1.0 ± 1.0 | 12.12 | 5.83 | 2.94 | 9.67 | 2.43 |
| BRLT62 | L5.0 ± 1.0 | 9.46 | 4.39 | 6.54 | 7.42 | 3.37 |
| BRLT63 | L1.0 ± 0.5 | *6.03* | *3.11* | *5.03* | *6.67* | *6.96* |
| BRLT64 | L4.0 ± 0.5 | 10.78 | 2.56 | 6.51 | ... | 5.02 |
| BRLT65 | M9.0 ± 0.5 | ... | ... | 5.44 | *4.58* | *5.82* |
| BRLT66 | L5.0 ± 0.5 | 7.67 | 3.95 | 5.28 | 6.04 | 4.49 |
| BRLT67 | L1.0 ± 0.5 | *8.17* | *4.98* | *3.20* | *7.99* | *8.89* |
| BRLT68 | L5.0 ± 0.5 | *14.65* | *4.99* | ... | ... | *3.22* |
| BRLT69 | L1.0 ± 0.5 | 9.03 | 2.97 | 5.19 | 5.65 | 5.35 |
| BRLT71 | L1.5 ± 0.5 | 9.86 | 7.50 | 8.03 | 6.84 | 2.80 |
| BRLT72 | M9.0 ± 0.5 | 7.66 | 2.06 | 7.81 | 4.20 | 4.75 |
| BRLT73 | L1.0 ± 0.5 | 9.70 | 6.78 | 9.71 | 12.73 | 6.47 |
| BRLT74 | L9.5 ± 1.0 | *3.04* | 8.25 | 2.12 | 3.74 | 3.16 |
| BRLT75 | M9.0 ± 1.0 | 5.80 | 5.32 | 4.95 | 4.26 | *0.29* |
| BRLT76 | L5.5 ± 0.5 | 9.98 | 7.26 | 6.58 | 9.89 | 2.55 |
| BRLT78 | L1.0 ± 0.5 | 15.59 | 8.53 | *14.00* | *8.82* | ... |
| BRLT81 | M9.0 ± 0.5 | *4.43* | *2.52* | *4.94* | *7.57* | ... |
| BRLT82 | L1.0 ± 0.5 | 7.93 | 3.65 | 7.38 | 7.66 | 3.86 |
| BRLT83 | M8.0 ± 1.0 | 7.97 | 6.65 | 5.46 | 5.51 | 5.07 |
| BRLT84 | L3.5 ± 0.5 | 7.73 | ... | 4.77 | 2.07 | 1.93 |
| BRLT85 | M8.0 ± 0.5 | *5.84* | *5.77* | *4.03* | *5.36* | ... |

Continued on the next page.

Continued from the previous page.

| Name | Spectral type | Equivalent width (Å) | | | | |
|---|---|---|---|---|---|---|
| | | Na I 1.139$\mu$m | K I 1.169$\mu$m | K I 1.177$\mu$m | K I 1.244$\mu$m | K I 1.253$\mu$m |
| BRLT87 | T0.0 ± 0.5 | *1.96* | *2.74* | *6.58* | ... | ... |
| BRLT88 | L4.0 ± 1.0 | 5.57 | 7.69 | 7.89 | 4.77 | 3.30 |
| BRLT91 | T3.0 ± 0.5 | *4.00* | *6.22* | *2.96* | *0.62* | 4.17 |
| BRLT92 | L1.0 ± 0.5 | 6.48 | 3.16 | 6.49 | 7.47 | 3.77 |
| BRLT97 | L0.0 ± 1.0 | 2.60 | 5.46 | 6.33 | 6.02 | 2.30 |
| BRLT98 | T4.0 ± 0.5 | ... | *8.21* | *5.37* | ... | ... |
| BRLT99 | L5.0 ± 0.5 | ... | *8.47* | *6.21* | *5.50* | ... |
| BRLT101 | L3.0 ± 0.5 | 18.71 | *7.25* | 13.16 | 12.27 | ... |
| BRLT102 | L0.0 ± 0.5 | 14.15 | *6.53* | 12.87 | ... | ... |
| BRLT103 | L5.5 ± 0.5 | 10.30 | 9.66 | 7.30 | 6.31 | 4.27 |
| BRLT104 | M9.0 ± 0.5 | 21.60 | 9.47 | *1.81* | *12.72* | *6.38* |
| BRLT105 | L5.0 ± 0.5 | 7.70 | 6.49 | 6.97 | 6.64 | 3.53 |
| BRLT106 | M9.0 ± 0.5 | *7.32* | *8.73* | *8.72* | 17.21 | ... |
| BRLT108 | L6.5 ± 0.5 | ... | ... | *2.14* | *11.95* | ... |
| BRLT111 | L2.0 ± 0.5 | *5.89* | *5.12* | 11.27 | ... | *11.96* |
| BRLT112 | L1.0 ± 0.5 | *6.48* | ... | 9.63 | *15.86* | *4.92* |
| BRLT113 | M9.0 ± 0.5 | ... | *7.86* | *15.20* | 11.86 | *6.69* |
| BRLT114 | L6.0 ± 0.5 | *6.29* | ... | 14.17 | ... | *5.59* |
| BRLT116 | T2.5 ± 0.5 | ... | *4.81* | ... | ... | ... |
| BRLT117 | L5.0 ± 0.5 | *2.56* | *13.99* | 13.90 | *9.77* | *8.93* |
| BRLT119 | L4.0 ± 0.5 | *19.11* | *5.58* | *5.31* | *10.97* | *16.48* |
| BRLT121 | L1.0 ± 0.5 | 29.10 | *8.06* | 12.60 | *8.68* | ... |
| BRLT122 | L1.0 ± 0.5 | 10.63 | 4.97 | 9.10 | 6.53 | *1.04* |
| BRLT123 | L2.0 ± 0.5 | 18.71 | ... | *11.03* | ... | *1.89* |
| BRLT129 | L5.0 ± 1.0 | 3.13 | 7.27 | 6.11 | 3.19 | 3.86 |
| BRLT130 | L3.0 ± 0.5 | 20.06 | 10.64 | 8.77 | *3.99* | ... |
| BRLT131 | T3.0 ± 0.5 | *4.47* | *4.07* | *3.07* | 3.79 | 3.09 |
| BRLT133 | M9.0 ± 0.5 | 10.02 | *3.52* | *5.27* | *8.43* | ... |
| BRLT135 | T2.5 ± 0.5 | *1.87* | *3.86* | *3.57* | ... | 1.32 |
| BRLT136 | L1.0 ± 1.0 | *6.10* | *5.32* | 12.74 | *5.37* | ... |
| BRLT137 | L4.5 ± 0.5 | 8.36 | 7.98 | 6.09 | 1.71 | 4.66 |
| BRLT138 | L2.0 ± 1.0 | 8.16 | 3.67 | 4.97 | 4.23 | 2.98 |
| BRLT139 | L5.0 ± 0.5 | *7.14* | *7.92* | 12.15 | *13.20* | *7.34* |
| BRLT140 | L0.0 ± 0.5 | 15.30 | *3.56* | *10.37* | ... | *1.69* |
| BRLT142 | L2.5 ± 0.5 | 4.49 | 6.25 | 5.65 | 4.64 | 3.15 |
| BRLT144 | L5.0 ± 0.5 | ... | *10.26* | *4.40* | *13.78* | *6.10* |
| BRLT145 | L1.0 ± 0.5 | *7.44* | *5.15* | *9.39* | *15.89* | ... |
| BRLT147 | T3.0 ± 0.5 | ... | *5.72* | *5.02* | 1.82 | 2.28 |
| BRLT149 | L6.0 ± 0.5 | 12.64 | *4.46* | ... | ... | *13.19* |
| BRLT152 | L0.0 ± 0.5 | 13.29 | *3.42* | *10.16* | ... | *8.06* |
| BRLT153 | L1.0 ± 0.5 | *3.69* | *3.85* | *10.86* | *12.93* | ... |
| BRLT155 | L3.0 ± 1.0 | 11.26 | 2.45 | 5.72 | 8.17 | ... |
| BRLT159 | L9.0 ± 0.5 | ... | *4.61* | *9.62* | ... | ... |
| BRLT162 | L0.5 ± 0.5 | 7.51 | 2.79 | 5.51 | 5.62 | 3.77 |

Continued on the next page.

Continued from the previous page.

| Name | Spectral type | Equivalent width (Å) | | | | |
|---|---|---|---|---|---|---|
| | | Na I 1.139$\mu$m | K I 1.169$\mu$m | K I 1.177$\mu$m | K I 1.244$\mu$m | K I 1.253$\mu$m |
| BRLT163 | L1.0 ± 0.5 | 19.13 | *5.04* | *5.45* | *7.36* | *6.29* |
| BRLT164 | T3.0 ± 0.5 | *3.14* | ... | *6.96* | *2.72* | ... |
| BRLT165 | L2.0 ± 0.5 | *1.63* | ... | ... | *14.47* | 5.52 |
| BRLT168 | L4.0 ± 0.5 | 6.73 | *4.78* | *9.16* | 12.21 | *12.93* |
| BRLT171 | L5.0 ± 0.5 | 7.22 | 5.79 | 5.95 | 4.61 | 3.26 |
| BRLT176 | L4.0 ± 1.0 | ... | ... | ... | ... | ... |
| BRLT179 | T4.5 ± 0.5 | ... | ... | ... | ... | ... |
| BRLT181 | L1.0 ± 1.0 | 7.28 | 7.31 | 6.98 | 4.58 | 3.60 |
| BRLT182 | T3.0 ± 0.5 | *3.02* | *2.93* | *5.61* | *3.18* | *7.41* |
| BRLT186 | L1.0 ± 1.0 | 7.48 | 2.24 | 5.39 | 4.51 | 2.92 |
| BRLT190 | T4.0 ± 0.5 | ... | ... | ... | ... | ... |
| BRLT197 | T2.0 ± 1.0 | *2.84* | *4.87* | *3.53* | 6.65 | 2.85 |
| BRLT198 | L3.0 ± 0.5 | *2.07* | *5.90* | 16.15 | *8.15* | *8.87* |
| BRLT202 | T2.5 ± 0.5 | *4.49* | *4.41* | *3.57* | 1.82 | 2.02 |
| BRLT203 | T3.0 ± 1.0 | *4.15* | *3.20* | *3.63* | 4.05 | *1.01* |
| BRLT206 | L2.0 ± 0.5 | 16.86 | *4.89* | 8.94 | *7.47* | *3.43* |
| BRLT207 | L7.0 ± 0.5 | 6.14 | 4.55 | 3.75 | 2.88 | 2.19 |
| BRLT210 | L4.5 ± 0.5 | 4.74 | 3.75 | 8.24 | 6.16 | 2.32 |
| BRLT212 | L6.0 ± 2.0 | *4.46* | ... | ... | *3.52* | ... |
| BRLT216 | M9.0 ± 0.5 | ... | 6.66 | *6.84* | *3.07* | ... |
| BRLT217 | T0.0 ± 0.5 | ... | ... | *4.93* | *3.43* | ... |
| BRLT218 | L6.0 ± 0.5 | *6.97* | *6.01* | *11.66* | *3.17* | *5.89* |
| BRLT219 | T3.0 ± 0.5 | ... | ... | ... | ... | ... |
| BRLT220 | L2.0 ± 0.5 | *4.01* | *7.71* | *7.76* | ... | *8.67* |
| BRLT227 | L3.0 ± 0.5 | *8.12* | *5.75* | 16.46 | *7.24* | *6.59* |
| BRLT229 | M8.0 ± 0.5 | *5.02* | ... | 11.39 | *4.85* | *2.87* |
| BRLT231 | L5.0 ± 0.5 | *6.58* | *12.85* | *9.54* | *15.08* | *10.09* |
| BRLT232 | T2.5 ± 0.5 | *2.74* | *4.51* | *2.32* | 3.42 | 1.71 |
| BRLT234 | L4.0 ± 1.0 | 9.44 | 7.80 | 12.22 | 7.10 | 4.57 |
| BRLT236 | L3.5 ± 0.5 | ... | ... | ... | ... | ... |
| BRLT237 | L4.0 ± 1.0 | *6.12* | *4.88* | 14.21 | *6.18* | ... |
| BRLT240 | L3.0 ± 0.5 | 13.35 | 7.40 | 11.84 | ... | *2.69* |
| BRLT243 | T0.0 ± 0.5 | *6.55* | ... | ... | *7.99* | *4.86* |
| BRLT247 | M9.0 ± 0.5 | 16.42 | *3.70* | 16.27 | *9.29* | ... |
| BRLT249 | L5.0 ± 0.5 | *4.02* | *7.47* | ... | ... | ... |
| BRLT250 | L1.0 ± 0.5 | *5.99* | *9.14* | *8.69* | *6.73* | *6.40* |
| BRLT251 | L1.0 ± 0.5 | *4.05* | ... | *3.27* | ... | *6.88* |
| BRLT253 | L1.0 ± 0.5 | *1.03* | *5.08* | 13.56 | *5.89* | ... |
| BRLT254 | L5.0 ± 0.5 | *9.96* | ... | 13.09 | ... | ... |
| BRLT258 | L5.0 ± 1.0 | ... | ... | ... | ... | ... |
| BRLT260 | L2.0 ± 0.5 | 15.49 | 4.18 | *8.72* | *3.77* | ... |
| BRLT262 | L0.0 ± 0.5 | 5.80 | *3.06* | 10.26 | 10.55 | *7.30* |
| BRLT265 | L2.0 ± 0.5 | *8.94* | *2.86* | 8.95 | 11.27 | 8.38 |
| BRLT269 | L7.0 ± 0.5 | *14.63* | ... | *5.99* | *7.25* | ... |

Continued on the next page.

Continued from the previous page.

| Name | Spectral type | Equivalent width (Å) | | | | |
|---|---|---|---|---|---|---|
| | | Na I 1.139$\mu$m | K I 1.169$\mu$m | K I 1.177$\mu$m | K I 1.244$\mu$m | K I 1.253$\mu$m |
| BRLT270 | L2.0 ± 0.5 | 12.43 | *6.30* | *8.25* | *15.34* | ... |
| BRLT274 | L2.0 ± 0.5 | ... | *2.74* | *5.22* | *13.52* | *6.16* |
| BRLT275 | T2.0 ± 2.0 | *4.64* | *2.16* | *3.69* | 6.13 | 4.94 |
| BRLT276 | L0.0 ± 0.5 | ... | ... | 7.91 | *2.96* | ... |
| BRLT279 | L1.0 ± 0.5 | *8.03* | *4.44* | *7.97* | *5.10* | ... |
| BRLT281 | T0.0 ± 1.0 | *7.44* | ... | *5.68* | ... | ... |
| BRLT283 | L5.0 ± 0.5 | 8.11 | *5.03* | 13.08 | *9.28* | *7.37* |
| BRLT285 | L5.0 ± 0.5 | *3.25* | *7.24* | ... | ... | 8.77 |
| BRLT286 | L4.0 ± 0.5 | ... | ... | *5.61* | *5.37* | ... |
| BRLT287 | T3.0 ± 0.5 | *3.48* | *3.73* | *3.63* | 3.09 | 3.58 |
| BRLT290 | T2.0 ± 0.5 | *10.65* | *3.05* | *5.31* | ... | ... |
| BRLT295 | L4.0 ± 2.0 | ... | ... | ... | *5.07* | ... |
| BRLT296 | L4.0 ± 0.5 | *4.88* | *4.97* | *3.42* | 16.10 | *3.07* |
| BRLT297 | L4.5 ± 0.5 | 22.31 | 7.22 | *5.03* | ... | *10.87* |
| BRLT299 | L4.0 ± 1.0 | 7.06 | 5.02 | 5.73 | 5.28 | 3.10 |
| BRLT301 | L1.0 ± 0.5 | *9.14* | *8.24* | *18.21* | *11.62* | ... |
| BRLT302 | L4.0 ± 0.5 | *2.08* | 7.14 | 16.35 | *3.20* | ... |
| BRLT305 | L5.5 ± 1.0 | ... | ... | ... | ... | ... |
| BRLT306 | L4.5 ± 1.0 | ... | ... | ... | ... | ... |
| BRLT307 | L1.0 ± 0.5 | 9.93 | *0.99* | 2.40 | 8.40 | 3.16 |
| BRLT308 | L5.0 ± 0.5 | *7.27* | ... | *5.15* | ... | ... |
| BRLT309 | L7.0 ± 0.5 | *6.11* | *6.35* | *2.00* | ... | ... |
| BRLT311 | T3.0 ± 0.5 | *4.25* | *0.55* | *1.36* | *1.09* | 2.25 |
| BRLT312 | T0.0 ± 0.5 | *6.46* | *2.57* | *4.47* | 7.28 | 4.52 |
| BRLT313 | L3.5 ± 0.5 | 8.72 | 10.48 | 6.12 | 4.73 | *1.41* |
| BRLT314 | L7.5 ± 0.5 | 6.82 | 7.46 | 6.24 | 3.20 | 2.73 |
| BRLT315 | L1.0 ± 1.0 | 5.33 | 1.56 | 8.78 | 6.81 | 5.95 |
| BRLT316 | L1.0 ± 0.5 | 12.46 | 2.74 | 3.19 | 2.69 | 5.79 |
| BRLT317 | L3.0 ± 1.0 | 9.77 | 6.95 | 9.81 | 4.57 | 8.67 |
| BRLT318 | L1.0 ± 0.5 | 14.36 | 6.33 | 6.22 | 6.20 | 6.10 |
| BRLT319 | T3.0 ± 0.5 | *4.19* | *7.52* | *3.21* | ... | *5.84* |
| BRLT320 | L1.0 ± 0.5 | 4.90 | *0.90* | 8.12 | 6.34 | *1.88* |
| BRLT321 | T4.0 ± 0.5 | *2.85* | *5.28* | *4.99* | 5.73 | 2.26 |
| BRLT322 | L5.0 ± 0.5 | 3.48 | 4.19 | 4.20 | 6.66 | 5.10 |
| BRLT323 | L5.0 ± 1.0 | 7.97 | 7.54 | 6.30 | 6.35 | 7.85 |
| BRLT325 | T2.0 ± 1.0 | *3.35* | *8.20* | *5.85* | 7.34 | 4.93 |
| BRLT328 | L3.0 ± 1.0 | 7.78 | 9.25 | 8.12 | 7.30 | 2.85 |
| BRLT330 | L2.0 ± 1.0 | 7.53 | 2.97 | 7.51 | 4.76 | 4.40 |
| BRLT331 | L3.0 ± 1.0 | 11.68 | 4.10 | 7.02 | 3.56 | 8.74 |
| BRLT332 | L2.0 ± 1.0 | 6.67 | 7.44 | 6.96 | 4.92 | 6.05 |
| BRLT333 | T2.0 ± 0.5 | *2.92* | *5.06* | *3.55* | ... | 5.24 |
| BRLT334 | L3.5 ± 0.5 | 7.51 | 5.26 | 6.19 | 6.27 | 4.74 |
| BRLT335 | L4.0 ± 1.0 | 8.62 | 4.56 | 6.62 | 7.05 | 5.50 |
| BRLT338 | L1.0 ± 1.0 | 13.70 | 8.90 | 10.46 | 6.94 | 2.44 |

Continued on the next page.

Continued from the previous page.

| Name | Spectral type | Equivalent width (Å) | | | | |
|---|---|---|---|---|---|---|
| | | Na I 1.139$\mu$m | K I 1.169$\mu$m | K I 1.177$\mu$m | K I 1.244$\mu$m | K I 1.253$\mu$m |
| BRLT340 | L4.0 ± 0.5 | *11.60* | ... | *6.78* | *7.30* | *6.37* |
| BRLT343 | L9.0 ± 1.0 | *2.24* | 7.31 | *0.62* | 4.02 | *1.53* |
| BRLT344 | T0.0 ± 1.0 | *5.87* | *4.36* | ... | 2.80 | 2.73 |

Table 3.6: The equivalent width obtained from the spectra. Missing entries indicate the non detection of the line, due either to the line being too weak or the spectrum being too noisy. Numbers in *italics* indicate measurements with relative errors larger than 0.33.

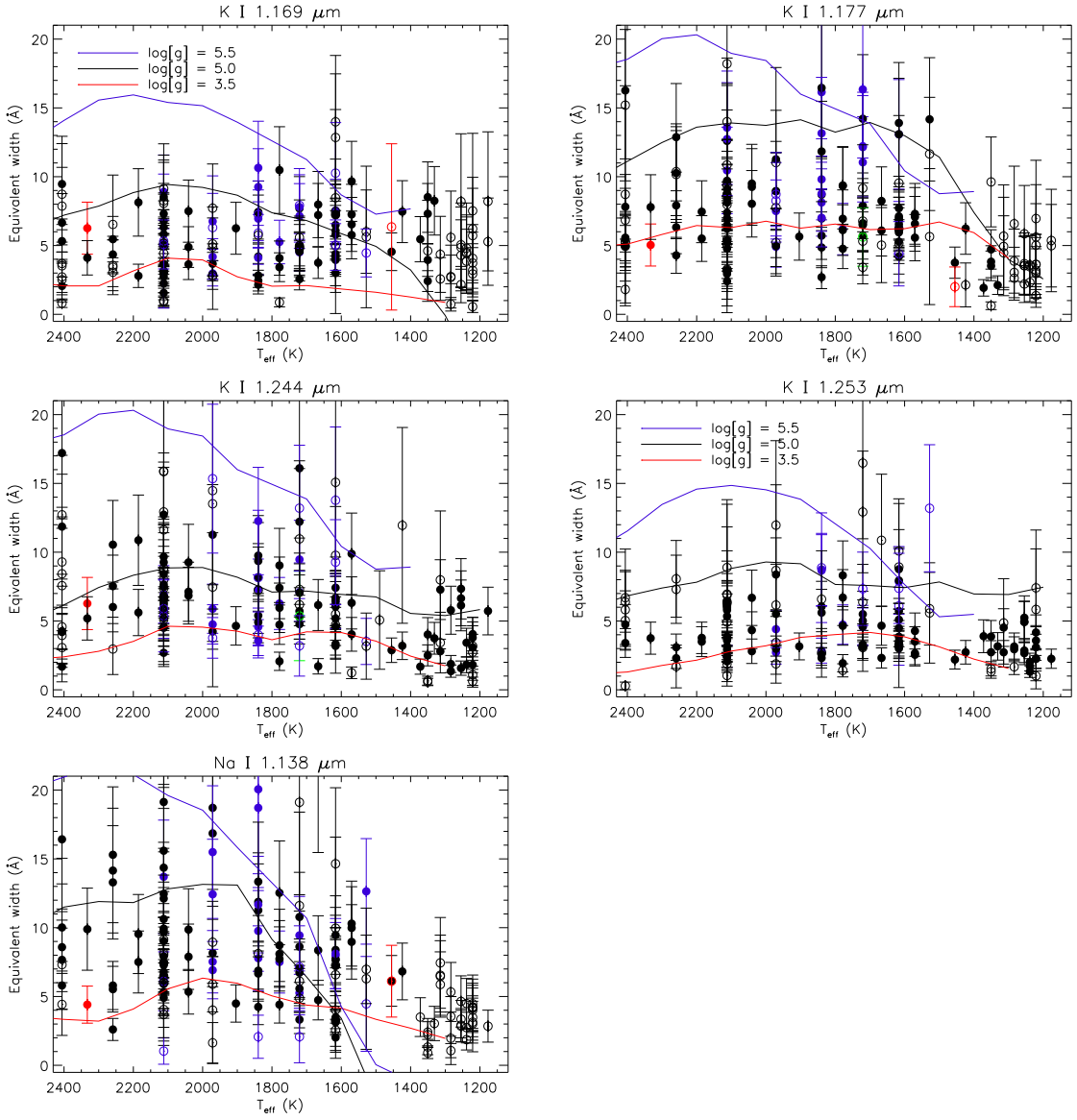


Fig. 3.37: The equivalent width of Na I and K I lines as a function of spectral type. Measurements with relative errors larger than 0.33 are plotted as filled circles. Peculiar objects are labelled following the same colour scheme of Figure 3.35 and 3.36. Overplotted for comparison are the equivalent width measured from the BT-Settl atmospheric models (Allard et al., 2011) for solar metallicity. The red line corresponds to a surface gravity log(g) = 3.5, the black line to log(g) = 5.0 and the blue line to log(g) = 5.5.

# Chapter 4: Constraining the sub-stellar birthrate

Part of the work presented in this chapter has been published in "The sub-stellar birth rate from UKIDSS", A. C. Day-Jones, F. Marocco, D. J. Pinfield, Z. H. Zhang, B. Burningham, N. Deacon, M. T. Ruiz, J. Gallardo, H. R. A. Jones, P. W. Lucas, J. S. Jenkins, J. I. Gomes, S. L. Folkes, and J. R. A. Clarke, Monthly Notices of the Royal Astronomical Society, Volume 430, Issue 2, p.1171-1187 (2013) and is reproduced by permission of the RAS.

The co-authors of the paper contributed partly to Section 4.2.1 and partly to Section 4.3. Everything else is my own original work.

## 4.1 Introduction

Extending the Salpeter mass function (Salpeter, 1955) to sub-stellar objects one would expect many more brown dwarfs than stars, which are not seen by observations of late M and L dwarfs (e.g. Reid et al., 2002a). As discussed in Section 1.4, the formation mechanism of brown dwarfs and giant planets is not well understood. To distinguish between the competing/complementing scenarios proposed it is fundamental to constrain the mass function and formation history in the sub-stellar regime.

Young clusters and associations have been the target of many campaigns measuring the sub-stellar IMF, since their known ages and metallicities allow the use of a mass-luminosity relation based on the cluster age (e.g. Lodieu et al., 2011, 2009, 2007; Caballero, 2009; Luhman et al., 2009; Alves de Oliveira et al., 2013, 2012). Although these clusters allow a relatively direct measurement of the sub-stellar IMF, they still present some problems, since the initial conditions and accretion histories of individual objects introduce uncertainties regarding the ages, and hence masses, of such young objects (e.g. Baraffe, 2010). Moreover, very high and variable extinction increases contamination by reddening field stars. Evolutionary models are also very uncertain at young ages, and the effect of magnetic activity or episodic accretion on the determination of luminosity are not yet fully understood. Finally, some of these regions are still forming stars, introducing further uncertainties and possible biases (see e.g. Alves de Oliveira, 2013).

Studying the IMF of the field populations has significant advantages, since there is a larger number of benchmark systems, and therefore the evolutionary and atmospheric models are more mature. Reddening is not an issue, given that even the deepest surveys can only probe the solar neighbourhood. On the other hand, as it is difficult to determine the age of field brown dwarfs, unless they have fiducial constraints on their age as binaries (e.g. Burningham et al., 2011, 2010a, 2009; Zhang et al., 2010; Day-Jones et al., 2011; Scholz et al., 2003; Gomes et al., 2013; Delorme et al., 2013) or as members of moving groups (e.g. Gagné et al., 2014; Malo et al., 2014, 2013; Clarke et al., 2010; Gálvez-Ortiz et al., 2010), estimating the mass function of field brown dwarfs requires knowledge of their formation history. This is often assumed to be the same as that for stars (i.e. constant with time Miller & Scalo, 1979), but is unconstrained in the sub-stellar regime. The assessment of completeness, contamination, and other observational biases can introduce further uncertainties.

Several groups have made measurements of the sub-stellar mass function in the field. These have all generally been with small sample sizes or cover only L dwarfs (e.g Cruz et al., 2007) or only T dwarfs (e.g. Metchev et al., 2008; Burningham et al., 2013; Kirkpatrick et al., 2012; Reylé et al., 2010). Those that have considered the full temperature regime across the L and T dwarf spectral types (e.g. Reylé et al., 2010) suffer from large associated errors and large bin sizes in order to get large enough sampling.

In order to characterize the form of the sub-stellar formation history, a large sample of brown dwarfs is required. With modern large-scale near- and mid-infrared surveys, such as the DENIS (Epchtein et al., 1999), SDSS (York et al., 2000), 2MASS (Skrutskie et al., 2006), UKIDSS (Lawrence et al., 2007), VISTA (Emerson & Sutherland, 2002), and WISE (Wright et al., 2010), which have identified large numbers of brown dwarfs it is now possible to provide the necessary sample of such objects. However, surveys such as 2MASS and SDSS were more sensitive to the detection of L dwarfs and produced only a few tens of early T dwarfs. As such they could not provide the population needed to study and constrain the birth rate. The ULAS probes to greater depth across the L and T dwarf spectral types and can provide a statistically robust sample spanning the mid-L to mid-T region, which is most sensitive to the effects of the form of the formation history.

This chapter outlines the efforts to use the sample of mid-L−mid-T dwarfs described in Chapter 3 to empirically constrain the Galactic brown dwarf formation history. This sample is an obvious choice because it covers a large spectral type range (crucially focused on the L-T transition) with a good sampling of each spectral type bin, and it is complete (see Section 4.2.1), unbiased (see Section 3.2) and uncontaminated, since its members have been followed up with spectroscopy. These qualities allow me to attempt for the first time to constrain the sub-stellar formation history.

## 4.2 Determining the space density of L/T transition dwarfs

The spectroscopic follow-up of the full sample is incomplete, with only 196 objects observed out of 324. However, there are area of sky where the follow-up is been completed: between RA = 15h50m to 9h20m the follow-up is complete down to the limit of J = 18.1; between RA = 9h20m to 12h20m the follow-up is complete down to J = 17.87; finally between RA = 12h20m to 15h50m the follow-up is complete down to J = 17.7. These RA ranges correspond to an area of ∼620, 375 and 712 deg$^2$ in ULAS DR7, and account for 88, 29, and 50 objects respectively. So in order to determine the space density of brown dwarfs avoiding contamination into the sample, I considered only the three sub-samples above.

To determine the volume sampled I calculated the maximum distance at which an objects of a given spectral type could have been detected (assuming the given magnitude limit), using the $M_J$-NIR spectral type relation from Marocco et al. (2010). With this distance limit I then calculated the volume sampled by each spectral type bin, and the corresponding space density of objects.

The derived space densities were then corrected for the Malmquist and Eddington biases following the approach described in Pinfield et al. (2008). The Eddington bias is caused by the photometric uncertainties on the magnitudes of objects near our cut (i.e. J < 18.1). However, since the magnitude cut imposed is bright (it corresponds to a

$\sim 12\sigma$ detection in the ULAS), the uncertainties at the J = 18.1 limit are typically less than $\sigma = 0.05$ and therefore the Eddington bias correction is less than 1 per cent. This is negligible compared to the other sources of uncertainty. I estimated the Malmquist bias correction considering the mean scatter of the sample of known L and T dwarfs around the adopted $M_J$-NIR spectral type relation. This represents an increase in the volume sampled of 22 per cent.

To increase the number of object per bin, and therefore reduce the poissonian errors, I binned up the sample in four spectral type bins: L0-L3, L4-L6, L7-T0, and T1-T4. These bins correspond roughly to effective temperature ranges of $\sim$150 K.

### 4.2.1 Completeness

In order to calculate the completeness of the sample,first we need to estimate the number of objects lost due to missed detections. As stated above, the imposed magnitude limit (J < 18.1) is bright compared to the limit of the ULAS, and therefore I do not expect to lose any object because of missed detections. This is well demonstrated by Figure 4.1 where I show the number of objects detected in the original ULAS images as a function of MKO J magnitude. The number of faint sources increases $\propto 10^{nJ}$ (note that the y axis is in logarithmic scale), where J is the apparent magnitude and n $\leq$ 0.6, from J $\sim$ 14 up to J $\sim$ 19 (as a consequence of the larger volume probed at fainter magnitudes, Mihalas & Binney, 1981), where it sharply drops. The dotted line is my fit to the bright tail of the distribution, i.e. for 14 <J< 17. Extrapolating the fit up to J=18.1 and comparing the "expected" number of objects with the measured one gives a completeness of > 99%. The number of objects lost due to incomplete detection in therefore negligible.

Another possible issue, especially when searching for faint objects, is the possible blending with bright sources. However the typical object density in the fields considered is very low, because I am probing regions outside the galactic plane, therefore blending should not be an issue. To quantitatively assess its impact I adopted the following approach. I used the ULAS J band images containing the selected objects. I run the Cambridge Astronomy Survey Unit (CASU) pipeline on the images to detect and extract all the sources in the field. I then doubled the number of objects in every image by taking a 20×20 pixels cut out around every object and copying it into a random position in the image, re-scaling it appropriately to blend the background level and avoid artefacts. I then re-run the CASU pipeline on the images and compared the number of sources identified (as a function of their J magnitude) with the number of sources in the original images. One would obviously expect to detect twice as many objects in the new synthetic images, with no dependence on the objects magnitude. This is indeed the case, as can be seen in Figure 4.1, where the number of detected objects in the synthetic images is plotted in red. With an average number of sources detected in the synthetic images of $\sim$1.987 times the number of sources detected in the original images, and no clear dependence on the J magnitude, the incompleteness due to objects blending is 0.3%, which is again negligible compared to the other causes of incompleteness considered below.

To assess the completeness of the photometric selection criteria, the sample it was compared to a control sample of known L and T dwarfs taken from www.DwarfArchives.org, for a magnitude limit of J $\leq$ 16, removing any objects that are known to be members of unresolved binary systems. The control sample was cross-matched with the ULAS and SDSS in order to obtain photometry on the same colour system as the selection

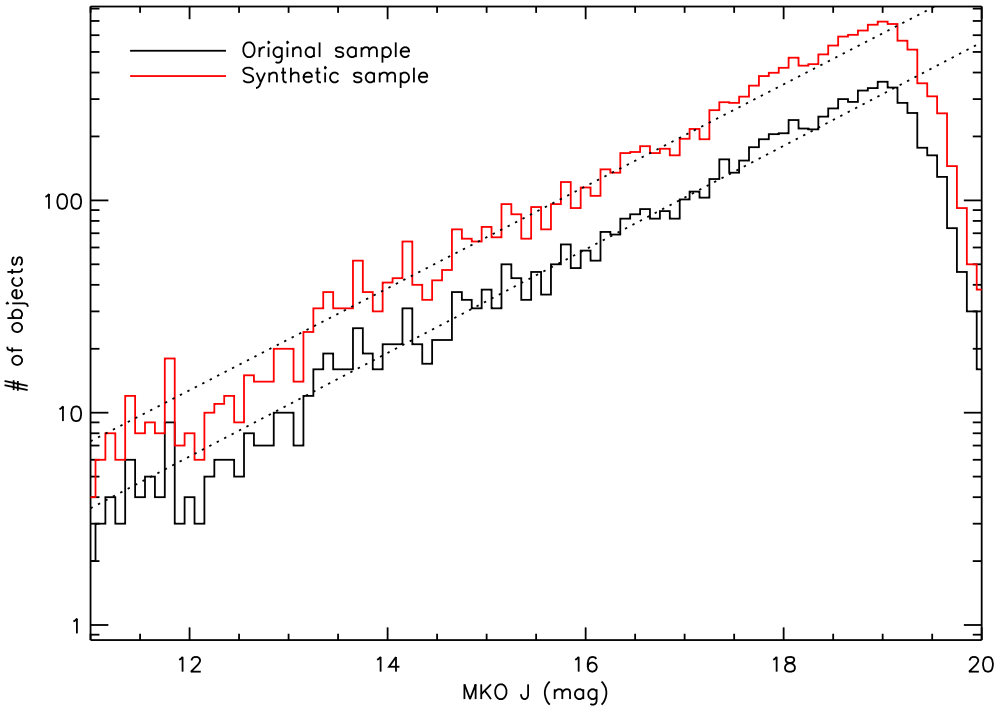


Fig. 4.1: The number of objects detected as a function of the J magnitude in the images used for the sample selection. The black histogram shows the results for the original images, while the red histogram shows the results in the synthetic images created by duplicating the number of objects. The dotted lines represent a fit to the bright tail of the distribution, i.e. for $14 < J < 17$.

criteria used. The same set of colour cuts described in Section 3.2 was imposed to reveal the level of completeness of the sample selection. We retain all of the L4 dwarfs from the control sample, but only some of the L0-L3 dwarfs, indicating that the sample selection is complete for L4 spectral types and later. Similarly, the selection is largely incomplete beyond spectral types of T5. I therefore only consider the three spectral type bins covering the L4−T4 range.

The loss of objects due to photometric scattering of colours was also considered. For L4-L6 types one would expect to lose 3.7 dwarfs, this corresponds to a completeness level of 88%. The L7-T0 range would lose 0.55 dwarfs, corresponding to a 94% completeness; for T1-T4 the expected loss is 0.05 dwarfs, corresponding to a completeness of 99%.

Pixel-noise correlation is not an issue, as demonstrated by Andrews et al. (2014), who estimated the randomness of background noise in the ULAS images by visually selecting 11 empty 7×7 pixel regions from the mosaics. They computed the standard deviation of the mean pixel value of each region (calling it $q$) and compared it against a similar calculation after randomly swapping pixels between regions. A $q/q_{\rm swapped}$ of 1 indicates perfectly uncorrelated noise while $q/q_{\rm swapped} \gg 1$ is due to non-pixel scale systematic variations. For ULAS images they found $q/q_{\rm swapped} \sim 1$.

### 4.2.2 Correction for unresolved binarity

I also corrected the results for the presence of binaries by first considering objects identified as possible binaries (Section 3.4.2) for which the spectral deconvolution gives a statistically better fit. I derived the J magnitude of the two components given the unresolved photometry and the two spectral types determined with the deconvolution, and removed from the sample all companions and those primaries that would fall beyond the magnitude limit.

To assess the completeness of this correction I performed numerical simulations, using the spectra templates taken from the SpeX-Prism library. The spectra were combined to create a sample of synthetic unresolved binaries, following the procedure described in Day-Jones et al. (2013) and in Section 3.4.2 of this work. The synthetic templates were "degraded" to the typical SNR of the observed spectra by adding gaussian noise. I then run the binary identification process on each of the synthetic binaries to calculate the rate of successful detections. To avoid false positive detections in low mass ratio binaries, when fitting a given synthetic binary I removed from the template list all the synthetic binaries that had the same primary as the "target" one. For example, when fitting the synthetic binary SDSS J165329.69+623136.5 + 2MASSI J0415195−093506 (L1.0 + T8.0) I removed from the set of templates all the synthetic binaries that had SDSS J165329.69+623136.5 as a primary. This is because one can expect that the synthetic L1.0 + T8.0 SDSS J165329.69+623136.5 + HD 3651B would fit better the target than an L1.0 template alone, not because the synthetic binary genuinely fits better, but because the contribution from the T8.0 component is negligible and I would essentially be fitting the L1.0 component with itself.

The results are shown in Figure 4.2, where I plot the fraction of synthetic binaries retrieved as a function of the spectral type of the two components. Interpolated contour level are overplotted to ease the reading of the figure. As expected, the technique is most efficient at the L/T transition, and the fraction of detected binaries steeply declines when moving towards very low mass ratios and early type binaries. Equal spectral type binaries are also not detectable with this method. Overplotted as

| Spectral | $q$ <1 | | $q$ =1 | |
|---|---|---|---|---|
| type range | Binary fraction | Binaries | Binary fraction | Binaries |
| L4−L6 | 11% | 5.8 | 13% | 7.0 |
| L7−T0 | 34% | 7.1 | 40% | 8.5 |
| T1−T4 | 19% | 4.7 | 23% | 5.6 |

Table 4.1: The derived binary fraction. For each spectral type range I indicate the binary fraction and the expected number of binaries in the sample.

black circles are the binary candidates identified in Section 3.4.2. Not surprisingly the candidates are concentrated mostly in the high detection fraction area.

The sample of binary candidates is probably contaminated by peculiar objects, and therefore the derived binary fraction is somewhat higher than the "true" one. To assess the level of contamination I run the binary identification method on a sample of L and T dwarfs that have been previously targeted by high-resolution imaging campaigns, and have not showed evidences of binarity. The control sample consists of 40 objects covering the L0.0 to T7.5 spectral range, and includes objects taken from Bouy et al. (2003), Gizis et al. (2003), and Burgasser et al. (2003c). Two out of 40 objects are flagged as binaries by the detection method, implying a level of contamination of 5%.

I can now use the detected binaries to constrain the binary fraction. To do that I combine the detection probability from Figure 4.2 with the mass-ratio distribution of sub-stellar binaries from Figure 1.12. First of all I correct the observed number of binaries for contamination using the fraction derived above, and then for completeness using the detection probability; all these binaries have mass ratio $q$ <1, if not they would have equal spectral type; using the distribution from Figure 1.12 I could estimate the number of undetected equal mass/equal spectral type binaries and therefore derive the binary fraction, *however* the exact mass ratio of a system depends on its age, which is unconstrained. So I can only correct the number of observed binaries using the ratio between the number of $q$=1 binaries over the number of $q$ <1 binaries, which is ∼1.2.

The numbers derived are presented in Table 4.1. I calculated the binary fraction in the three spectral types ranges considered above (i.e. L4-L6, L7-T0, and T1-T4). The fraction is 24% in the L4-L6 range but rises to ∼70% in the L7-T0 range, before dropping down to ∼40% in the early T regime. This could be partly due to an underestimate of the number of equal spectral type binaries in the early L regime, due to the fact that the detected binary candidates lie in the $q \ll 1$ range, and the ratio of $(q = 1)/(q \ll 1)$ binaries is higher than the assumed value of ∼1.2.

On the other hand, the binary fraction obtained for the L-T transition is much higher than measured by high-resolution imaging and radial velocity surveys (see Section 1.7.1), typically detecting a binary fraction of ∼10-20%. The reason for this discrepancy could be in a higher false positive ratio than estimated here. The control sample used to determine the contamination is in fact limited (only 40 objects) and the L-T transition in particular is poorly sampled. When correcting my derived space densities for unresolved binarity I will therefore use both the binary fraction I measured, and the values published in the literature.

To take into account the presence of the undetected equal spectral type binaries, which would fall beyond the J limit if they were single objects, I used the definition of

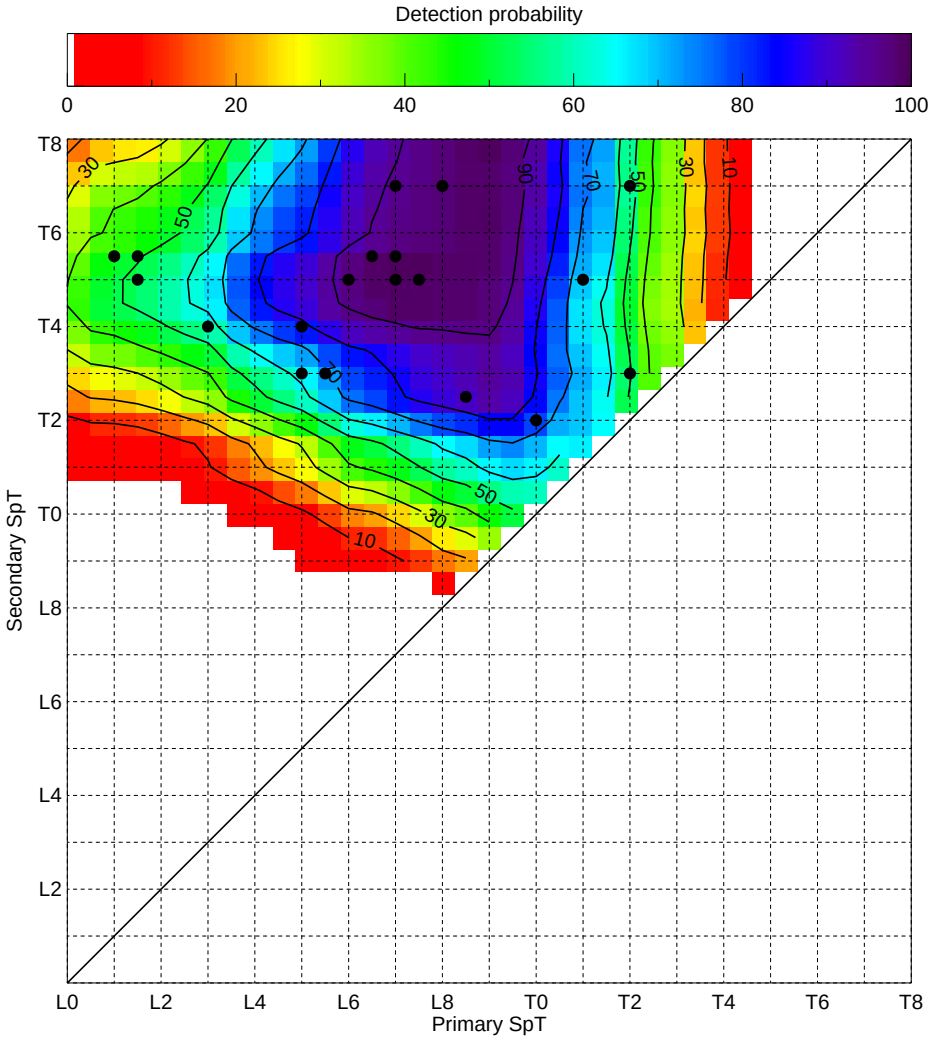


Fig. 4.2: The detection probability for unresolved binaries as a function of the spectral types of the two components, using the detection and deconvolution technique described in Section 3.4.2. Interpolated contour level are overplotted to ease the reading of the figure. Overplotted as black circles are the binary candidates identified in Section 3.4.2.

"observed binary fraction" given by Burgasser et al. (2003c),

$$\frac{N_B}{N_m} = \frac{\gamma}{\gamma + (1/\mathrm{BF}) - 1} \tag{4.1}$$

where $N_B$ and $N_m$ are the observed binaries and the total number of objects, respectively, BF is the "true" binary fraction, and $\gamma$ is the fractional increase in volume due to inclusion of binaries in the sample. The number of binaries that fall within the magnitude limit ($N_D$) is

$$\frac{N_D}{N_B} = \frac{\gamma - 1}{\gamma} \tag{4.2}$$

Therefore, the fraction of objects to be excluded from the sample ($f_{\mathrm{excl}}$) is

$$f_{\mathrm{excl}} = \frac{N_B}{N_m}\frac{N_D}{N_B} = \frac{\gamma - 1}{\gamma + (1/\mathrm{BF}) - 1} \tag{4.3}$$

For equal spectral type binaries $\gamma = 2\sqrt{2}$. This can be derived by writing the volume probed by a magnitude limited sample ($V$) as

$$V = \frac{4}{3}\pi\, 10^{\frac{3}{5}(m-M+5)} \tag{4.4}$$

where $m$ is the magnitude limit and $M$ is the absolute magnitude of the target considered. The absolute magnitude of an unresolved binary is

$$M_{\mathrm{bin}} = M_{\mathrm{single}} - \frac{5}{2}\, log_{10}(2) \tag{4.5}$$

so given the magnitude limit $m$ the volume probed by binaries is

$$V_{\mathrm{bin}} = \frac{4}{3}\pi\, 10^{\frac{3}{5}(m-M_{\mathrm{single}}+\frac{5}{2}\, log_{10}(2)+5)} = V_{\mathrm{single}} \times 10^{\frac{3}{2}\, log_{10}(2)} \tag{4.6}$$

and the fractional increase in volume $\gamma$ is therefore $V_{\mathrm{bin}}/V_{\mathrm{single}} = 2\sqrt{2}$.

As stated above, the final correction applied was derived assuming BF$= 26 \pm 13\%$, i.e. the mid point between the upper and lower limit derived in this work, and BF$= 14 \pm 10\%$, i.e. the weighted average of the values presented in Section 1.7.1. The corrections applied are therefore $f_{\mathrm{excl}} = 0.30 \pm 0.10$ and $f_{\mathrm{excl}} = 0.18 \pm 0.12$.

## 4.3 Comparison with numerical simulations

I compared the space densities obtained above with the results of numerical simulations computed assuming different IMFs and birth rates. Details of the simulations are presented in Deacon & Hambly (2006) and are briefly summarized here.

They assume an exponential IMF in the form

$$\Psi(M) \propto M^{-\alpha}\left(pc^{-3}M_{\odot}^{-1}\right) \tag{4.7}$$

where is the number of objects per unit volume in a given mass interval. They also assumed an exponential birth rate of the form

$$b(t) \propto e^{-\beta t} \tag{4.8}$$

where $t$ is in Gyr and $\beta$ is the inverse of the scale time $\tau$ (in Gyr, since the galaxy was formed). Each simulated object was assigned an age based on the birth rate and a mass based on the IMF, giving a final creation function $C$ given by the equation

$$C(M,t) = \Psi(M)\frac{b(t)}{T_G} \tag{4.9}$$

where $T_G$ is the age of the Galaxy. $C$ is therefore the number of objects created per unit time per unit mass. The evolution of each object and its parameters (i.e. $T_{\rm eff}$ and absolute magnitudes) were calculated using the evolutionary models from Baraffe et al. (1998). Any model-dependent systematics would be introduced, but these should not affect the overall trend. The $T_{\rm eff}$ of an object was then converted into a spectral type using the $T_{\rm eff}$-NIR spectral type relation presented in (Stephens et al., 2009, equation 3). The number densities obtained for each bin were finally normalized to 0.0024 pc$^{-3}$ in the 0.1-0.09 $M_\odot$ mass range, according to Deacon et al. (2008). I must point out at this point that all objects in these simulations are assumed to be single objects and therefore the derived space densities are for primary brown dwarfs. I consider the simulations for five different values of $\beta$ (-0.2, -0.1, 0.0, +0.1, +0.2 corresponding to $\tau$ = -5, -10, $\infty$, +10, +5 Gyr, respectively) and five values of $\alpha$ (0.0, -0.5, -1.0, -1.5, -2.0). The results obtained for $\alpha$ = 0.0, -1.0, -2.0 and $\beta$ = 0.0, 0.2, 0.5 are shown in Figure 4.3, where different colours represent different values of $\alpha$ and different line styles represent different values of $\beta$.

I compare the calculated space densities, taking into account the completeness and contribution from unresolved binaries, with those presented by various authors in the literature. I considered five different studies: Cruz et al. (2007), Metchev et al. (2008), Reylé et al. (2010), Kirkpatrick et al. (2012), Burningham et al. (2013), and Day-Jones et al. (2013).

The Cruz et al. (2007) space densities probe down to the 2MASS limit (J = ∼16) and cover the M9-L8 dwarfs, likely suffering from incompleteness at the later types due to colour scattering. The binary correction uses the observed binary fraction of ∼ 17% derived via high-resolution imaging of their sample. Metchev et al. (2008) cross-matched 2MASS with SDSS DR1 and used a series of colour selection criteria to select a sample of L and T dwarfs down to $z \leq$21. The correction for binarity accounts only for equal mass/ equal spectral type binaries in reason of the strong peak in the $q$ distribution (see Figure 1.12). The adopted binary fraction is assumed to decline from 50% in the T0-T2.5 range, down to 21% in the T3-T5.5 range, to 13% in the T6-T8 range, and is therefore comparable to the numbers derived here. Reylé et al. (2010) used CFBDS to select and classify a sample of ∼100 >L5 dwarfs down to $z'$ <22.5, a comparable depth to this sample. They chose not make any correction for binarity, given the large uncertainty in the measured binary fraction. Kirkpatrick et al. (2012) focused on the late T and Y dwarfs, using the WISE-selected sample of nearby objects. Assuming a binary fraction of 30% and correcting for the incompleteness at the faint end of their sample, they derive the space density in the T6 to Y0.5 range. The Burningham et al. (2013) space densities use the same $M_{\rm J}$-spectral type relations I adopted. They correct for binarity assuming an upper limit on the binary fraction of 45% (Maxted & Jeffries, 2005) and a lower limit of 5% Burgasser et al. (2003c), hence deriving two values of the space density in each spectral type bin. They also probe down to a magnitude limit comparable to this sample. Finally, the Day-Jones et al. (2013) represent an early result from this sample, obtained from the sub-sample falling in the RA = 22h to 4h range. The only difference in the treatment of the data

| Reference | Spectral type range | Space density ($\times 10^{-3}$ pc$^{-3}$) |
|---|---|---|
| Cruz et al. (2007) | L0-L3 | $1.7 \pm 0.4$ |
| | L3.5-L8 | $2.2 \pm 0.4$ |
| Metchev et al. (2008) | T0-T2.5 | $0.86^{+0.48}_{-0.44}$ |
| | T3-T5.5 | $1.4^{+0.8}_{-0.8}$ |
| | T6-T8 | $4.7^{+3.1}_{-2.8}$ |
| Reylé et al. (2010) | L5-T0 | $2.0^{+0.8}_{-0.7}$ |
| | T0.5-T5.5 | $1.4^{+0.3}_{-0.2}$ |
| | T6-T8 | $5.3^{+3.1}_{-2.2}$ |
| Kirkpatrick et al. (2012) | T6-T6.5 | 1.1 |
| | T7-T7.5 | 0.93 |
| | T8-T8.5 | 1.4 |
| | T9-T9.5 | 1.6 |
| Burningham et al. (2013) | T6-T6.5 | $0.39 \pm 0.22 - 0.71 \pm 0.40$ |
| | T7-T7.5 | $0.56 \pm 0.32 - 1.02 \pm 0.64$ |
| | T8-T8.5 | $2.05 \pm 1.21 - 3.79 \pm 2.24$ |
| Day-Jones et al. (2013) | L4-L6.5 | $0.53 \pm 0.10 - 0.88 \pm 0.16$ |
| | L7-T0.5 | $0.56 \pm 0.10 - 0.94 \pm 0.16$ |
| | T1-T4.5 | $0.42 \pm 0.16 - 0.71 \pm 0.27$ |
| This thesis, BF = 26 ± 13 | L4-L6.5 | $0.85 \pm 0.55$ |
| | L7-T0.5 | $0.73 \pm 0.47$ |
| | T1-T4.5 | $0.74 \pm 0.48$ |
| This thesis, BF = 14 ± 10 | L4-L6.5 | $1.00 \pm 0.64$ |
| | L7-T0.5 | $0.85 \pm 0.55$ |
| | T1-T4.5 | $0.88 \pm 0.56$ |

Table 4.2: The space density derived here compared to values presented in the literature. The numbers are integrated over the spectral range quoted in the second column.

is in the binary correction, since in Day-Jones et al. (2013) we followed the approach of Burningham et al. (2013) and derived two values for each spectral type range.

My results and those listed above are summarized in Table 4.2, and in Figure 4.3. It is important to notice that the numbers in Table 4.2 are *integrated* over the spectral range quoted, while those plotted in Figure 4.3 are *per spectral type*, to allow a direct comparison with the simulations. A first look at the plot shows that my space densities do not differ drastically (within uncertainties) from those previously measured and discussed earlier. The differences between my derived densities and those previously published are mostly due to the use of different $M_J$-SpT conversions and different binary fractions by the various groups.

The most prominent feature is the apparent absence of a significant drop in the number of objects between L7 and T4. The number of L-T transition dwarfs decreases, but not as much as expected. For the predicted theoretical deficit to be realised a higher binary fraction than assumed for the L-T transition would be necessary. That would lead to a larger correction and therefore to lower space densities. Conversely, a lower binary fraction at early types would bring up the density of objects in the L4-L6 range increasing the drop.

However, this second scenario would lead to a preference for $\alpha > 0$, which would be inconsistent with the results for late type objects, that consistently point towards $\alpha < 0$. On the other hand, $\alpha > 0$ is found also in nearby young clusters (e.g. Casewell

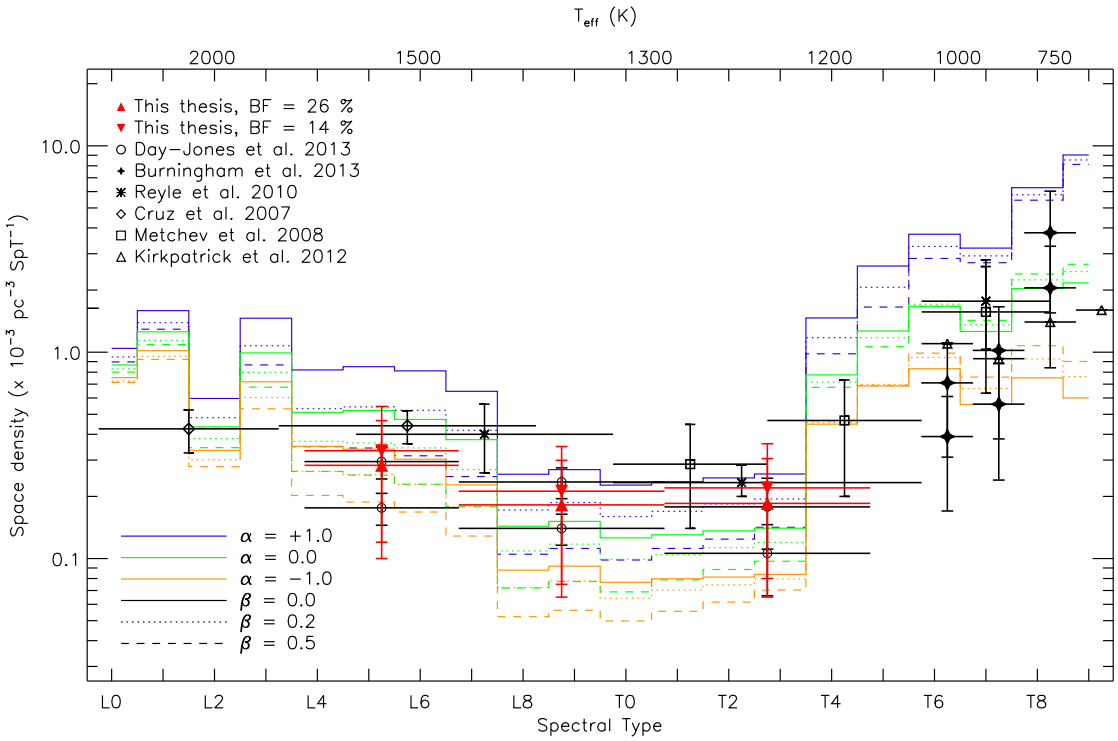


Fig. 4.3: A comparison between measured space densities of L and T dwarfs with simulations from Deacon & Hambly (2006) with $\alpha$ = +1.0, 0.0, -1.0 and $\beta$ = 0.0, 0.2, 0.5. On the top axis I show an indicative temperature scale.

et al., 2007; Bastian et al., 2010) and by microlensing surveys ($\alpha = 0.49^{+0.24}_{-0.27}$ Sumi et al., 2011).

Either the binary fraction in the L-T transition is much higher than currently estimated, reconciling the results in the two mass regimes, or objects in the high-mass end and low-mass end form in different environments, with the high mass L dwarfs forming predominantly in dense clusters (i.e. resulting in an $\alpha > 0$ IMF) and the low mass T dwarfs forming in low density environments, leading to a $\alpha < 0$ IMF. Another possibility, as suggested by Burningham et al. (2013) is that the cooling times assumed to transform the IMF into field luminosity function are affected by systematic errors.

As regards the formation history, it is not currently possible to place robust constraints on the birth rate with this sub-sample. One of the largest sources of uncertainties is the binary fraction. This could be resolved with the follow-up of the unresolved binary candidates, by either AO imaging or radial velocity.

The other main source of uncertainty is the absolute magnitude−spectral type calibration. Although based on an increasing number of objects with well measured parallaxes, the scatter around the current polynomial relation is still large, with typical rms of 0.4 magnitudes (Dupuy & Liu, 2012), and this propagates into a factor of ∼1.5 in the volume sampled. In this respect, the final results for PARSEC (see Chapter 2) will help to further improve the current calibration, reducing the uncertainty to the intrinsic scatter of the brown dwarf population.

# Chapter 5: The extremely red L dwarf ULAS J222711−004547 - dominated by dust.

This chapter is a version of "The extremely red L dwarf ULAS J222711−004547 - dominated by dust", F. Marocco, A. C. Day-Jones, P. W. Lucas, H. R. A. Jones, R. L. Smart, Z. H. Zhang, J. I. Gomes, B. Burningham, D. J. Pinfield, R. Raddi, and L. Smith, Monthly Notices of the Royal Astronomical Society, Volume 439, Issue 1, p.372-386 (2014), and is reproduced by permission of the RAS.

The co-authors of the paper contributed partly to Section 5.5.2. Everything else is my own original work.

## 5.1 Introduction

As described in Chapter 1, there is no unique mass − spectral type relation for sub-stellar objects. For example, an L spectral class bin might be populated by an old low-mass star, a young high mass brown dwarfs, or even a very young planetary mass object.

Spectroscopy can provide useful insights to break this age-mass-luminosity degeneracy. Young brown dwarfs have in fact low surface gravity, as they have not contracted to their final radii, and some spectral features have been found to be sensitive to variations in the surface gravity. In particular, L dwarfs in young clusters show weak CaH, K I, and Na I absorption, and strong VO bands in their optical spectra (Cruz et al., 2009, and references therein). Near-infrared spectra show peaked $H$-band and a general flux excess towards longer wavelength (e.g. Lucas et al., 2001; Lodieu et al., 2008). As a result, young brown dwarfs appear very red in terms of infrared colours.

Recent kinematic studies however have suggested that field objects showing signs of youth in their spectra could instead be relatively old (Kirkpatrick et al., 2010; Faherty et al., 2012). The peculiar morphology of their spectra therefore is not an effect of low surface gravity, but could instead be caused by an excess of dust in their photosphere (Cushing et al., 2008) due to an higher-than-average metallicity (e.g. Leggett et al., 2007; Looper et al., 2008b; Stephens et al., 2009). The nature of these objects, generally referred to as "unusually red L dwarfs" (hereafter URLs, e.g. Gizis et al., 2012) is not fully understood yet, in part because of the lack of such objects discovered so far. There are indeed only nine identified URLs: the L1pec 2MASS J13313310+3407583 (Reid et al., 2008b; Kirkpatrick et al., 2010); the L5pec 2MASS J18212815+1414010 (Looper et al., 2008b) and 2MASS J23512200+3010540 (Kirkpatrick et al., 2010); the L6.5pec 2MASS J21481628+4003593 (Looper et al., 2008b) and 2MASS J23174712−4838501 (Reid et al., 2008b; Kirkpatrick et al., 2010); the L7.5pec WISEP J004701.06+680352.1 (Gizis et al., 2012); the recently discovered L7.5 WISE J104915.57−531906.1A (Luhman, 2013; Burgasser et al., 2013); finally the L9pec WISEPA J020625.26+264023.6 and WISEPA J164715.59+563208.2 (Kirkpatrick et al., 2011).

Planetary-mass objects show similar near-infrared colours, like 2M1207b ($J - K_s = 3.1$, Chauvin et al., 2004), PSO J318.5338−22.8603 ($J - K_s = 2.84$, Liu et al., 2013) and the HR8799 planets (Marois et al., 2008), and their photometric and spectroscopic

properties are believed to be heavily influenced by the atmospheric condensates (e.g. Madhusudhan et al., 2011). URLs can therefore be considered a "bridge" between brown dwarfs and giant planets atmospheres, thus a useful test-bed for the atmospheric models. Also, these objects can be used as probes to understand the physics of dust clouds, and to disentangle the effects of surface gravity and metallicity in the L type temperature regime.

In this contribution we present a new example of this class of objects, discovered in the United Kingdom Infrared Deep Sky Survey (UKIDSS) Large Area Survey (LAS): ULAS J222711−004547. With a spectral type of L7pec (see Section 5.2), this object marks an extreme in the L/T transition, where the role of dust and condensates clouds becomes fundamental (e.g. Burrows et al., 2011, 2006; Allard et al., 2001). The processes leading to the formation and subsequent disruption of said clouds, which determine the transition from L to T class objects, are still poorly understood. Constraining the effect of surface gravity and metallicity in these processes is an open challenge, with the different assumptions adopted in modern atmospheric models leading to significantly different results (especially for peculiar objects, see Section 5.6). ULAS J222711−004547 represents a new opportunity to investigate this interesting stage in the evolution of sub-stellar objects.

In Section 5.2 we present the spectrum obtained for our target, and discuss its peculiarities. In Section 5.3 we compare the photometry of ULAS J222711−004547 with the population of known brown dwarfs. In Section 5.4 we calculate the target's proper motion, using the data available in the literature. In Section 5.5 we de-redden the spectrum of ULAS J222711−004547 using extinction laws for different dust species, and we derive a typical grain size for the dust particles. In Section 5.6 we compare its spectrum with atmospheric models. Finally in Section 5.7 we summarize and discuss the results obtained.

## 5.2 Spectroscopic follow-up

### 5.2.1 Observations & data reduction

ULAS J222711−004547 was selected from DR7 of the UKIDSS LAS, as part of the large spectroscopic campaign to constrain the sub-stellar birth rate presented in Chapter 3 and 4. The candidate selection process is described in details in Section 3.2, where the reader can find details on the colour cuts and the quality criteria applied.

We obtained a medium resolution spectrum of ULAS J222711−004547 using XSHOOTER on UT2 at the VLT. The target was observed on the night of 2011-10-03 under the ESO program 088.C-0048 (P.I. A. C. Day-Jones), using a slit width of 1.0" in the UVB arm and 0.9" in the VIS and NIR arms. These correspond to a resolution of 5100 in the UVB arm, 8800 in the VIS arm and 5100 in the NIR arm. The object was visible in the 20 s acquisition image, and was placed on the centre of the slit. We took eight exposures in an ABBA nodded sequence, with individual exposure times of 230 s, 300 s and 390 s in the three arms. To allow for telluric correction, we observed the B7V star HIP014143 immediately after the target, matching the airmass of the observation. The data have been reduced following the procedure described in Section 3.3

The spectrum obtained for ULAS J222711−004547 is plotted in Figure 5.1. We only show the 0.55-2.5 $\mu$m range, as we do not detect any flux at shorter wavelengths. The median SNR in the four main wavelength ranges (red-optical, $z$-band, $J$-band, $H$-

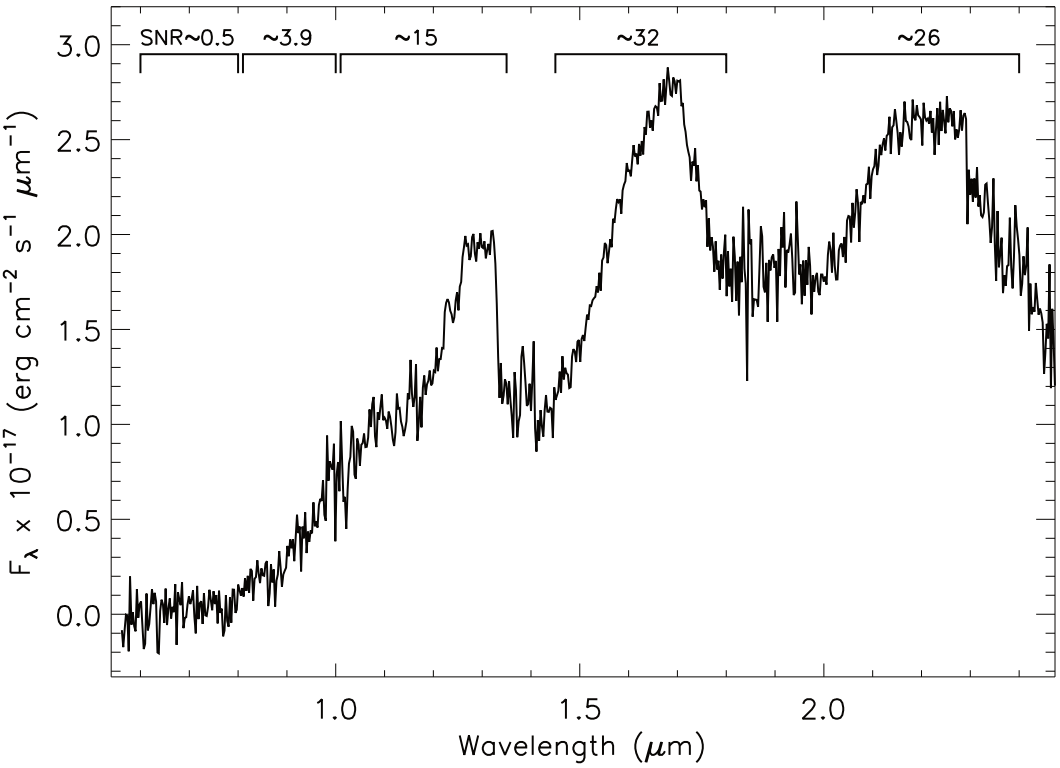


Fig. 5.1: The spectrum of ULAS J222711−004547. At the top of the Figure we indicate the median SNR in each wavelength range.

band, and $K$-band) is indicated above the spectrum. Unlike normal L and T dwarfs, the spectrum peaks in the $H$-band, with the $K$-band reaching almost the same flux level. The optical and $J$-band are very smooth, and the CO absorption at 2.3 $\mu$m appears weaker than in other L/T transition dwarfs. The flux level at 2.2 to 2.28 $\mu$m is higher than in normal late-L dwarfs, an indication of a reduced Collision Induced Absorption (CIA) of $H_2$ or a reduced absorption from $CH_4$, the two major sources of opacity at these wavelengths (e.g. Tokunaga & Kobayashi, 1999; McLean et al., 2003). A more detailed description of the spectral features of ULAS J222711−004547 is given in the following sections.

### 5.2.2 Spectral typing

Given the peculiarity of the spectrum of ULAS J222711−004547, we cannot apply the standard spectral typing systems developed for L and T dwarfs (Kirkpatrick et al., 1999; Burgasser et al., 2006a). To assign a spectral type to our target we therefore split its spectrum into three separate portions: optical+$J$-band (0.7-1.35 $\mu$m), $H$-band (1.45-1.8 $\mu$m), and $K$-band (2.0-2.5 $\mu$m). We normalized the three portions separately to remove the steep red slope, and we compared them to the spectra of standard L and T dwarfs, treated the same way[1]. In all three portions, the best fit is given by the L7 standard 2MASSI J0103320+193536, but the match between the two spectra remains poor. We show the three portions of the spectrum with the best fit

[1]All the spectra were taken from the Spex-Prism online library: http://pono.ucsd.edu/∼adam/browndwarfs/spexprism

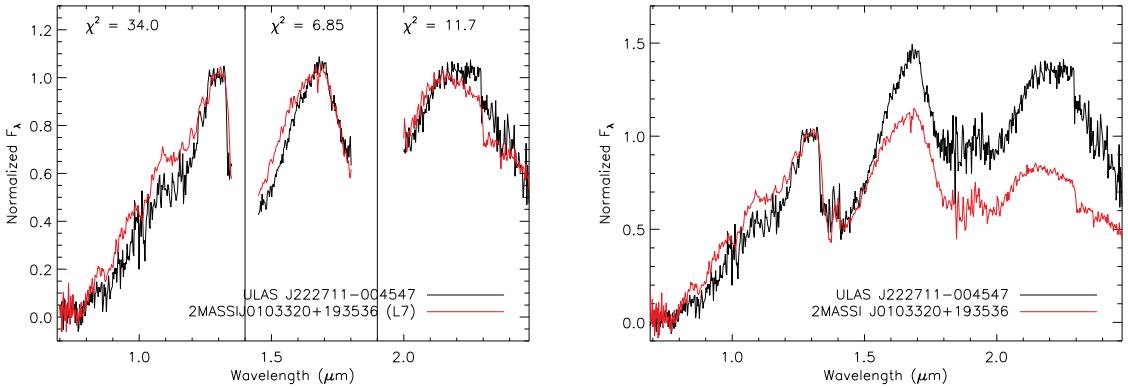


Fig. 5.2: The spectrum of ULAS J222711−004547 (black) compared to the L7 standard 2MASSI J0103320+193536 (red). *Left:* both spectra are normalized to 1 in each portion. *Right:* both spectra are normalized to 1 at 1.28 $\mu$m.

standard template on the left panel of Figure 5.2. If we compare directly the spectrum of ULAS J222711−004547 with 2MASSI J0103320+193536 (normalizing the complete spectra to 1 at 1.28 $\mu$m) we note immediately that our target is much redder than the standard, with an increased flux level in the $H$ and $K$ bands, as we can see in the right panel of Figure 5.2. We therefore classify ULAS J222711−004547 as L7pec, following the notation described in Kirkpatrick et al. (2010, Section 5.2).

A way to confirm its spectral type is to compare ULAS J222711−004547 directly with known peculiar red L dwarfs. Figure 5.3 shows a comparison of its spectrum with the red L dwarfs 2MASS J035523.37+113343.7, 2MASS J21481628+4003593, WISEP J004701.06−680352.1, and 2MASSW J2244316+204343. The main absorption features are marked on the plot to ease the interpretation. Our target appears redder than all of the other peculiar L dwarfs. Its MKO $J - K$ is 2.79±0.06, thus is the reddest measured of any field brown dwarf (see Section 4). The L5$\gamma$ 2MASS J035523.37+113343.7 looks very similar to our target in the optical and $J$-band, but has weaker water absorption bands at ∼1.4 and 1.9 $\mu$m, as expected in a earlier type dwarf. The $H$-band of ULAS J222711−004547 looks less peaked than that of the L5$\gamma$, which could be an indication of higher surface gravity, but as pointed out by Allers & Liu (2013) the "peakiness" of the $H$-band is not a wholly reliable indicator because it has been seen in dusty L dwarfs that are not young. Our target also appears much brighter than the L5$\gamma$ in the $K$-band, which is again expected in a later type dwarf. The L6.5pec 2MASS J21481628+4003593 reproduces very well the shape and flux level of the optical and $J$-band of ULAS J222711−004547. It also matches the relative depth of the water absorption bands, not surprisingly given the very small difference in spectral type. On the other hand, our target appears significantly redder in the $H$ and $K$-band, and with a weaker FeH absorption feature at ∼ 1.6 $\mu$m. These could be evidence for an enhanced dust content in the photosphere of ULAS J222711−004547. The L7.5pec WISEP J004701.06−680352.1 and 2MASSW J2244316+204343 look similar to our target in the optical and $J$-band, but with less pronounced FeH absorption bands, a generally smoother continuum, and a slight flux excess between ∼0.9 and 1.1 $\mu$m. Both objects also show stronger $H_2O$ absorption at ∼ 1.1 $\mu$m. All these differences are consistent with their slightly later spectral types. The $H$-band is well fitted, but ULAS J222711−004547 presents a slight flux excess at the peak of the band. Our target is also brighter than both L7.5pec in the $K$-band, with a plateau in flux between

$\sim$2.1 $\mu$m and the CO band head. An enhanced dust content of the photosphere and a slightly suppressed molecular hydrogen CIA in ULAS J222711−004547 could be the cause of these discrepancies. An enhanced dust content would result in a higher opacity in the red-optical portion of the spectrum, suppressing the emergent flux. A reduced CIA on the other hand would reduce the opacity in the $H$ and $K$ band, allowing more flux to emerge. Overall, the combined effect would be a general strong reddening of the spectrum, like what we observe in ULAS J222711−004547 (see Section 5.5).

Using the XSHOOTER spectrum we also determined spectral indices for our target. The indices are those used for spectral classification, as defined in Geballe et al. (2002) and Burgasser et al. (2006a), and the gravity-sensitive indices defined in Allers & Liu (2013). The values obtained for ULAS J222711−004547 are listed in Table 5.1, along with reference values for "field" and low gravity L7s (where available). Some of those indices are outside the defined ranges for spectral typing, except the $H_2O$ 1.5 $\mu$m index which indicates a spectral type of L8, the $CH_4$ 2.2 $\mu$m which indicates a spectral type of L5, and the $H_2O$−H which indicates a spectral type of T0. We then applied the gravity classification method defined in Allers & Liu (2013, Table 9 and 10). The method is based on assigning "scores" of 0, 1 or 2 to different spectral features based on their strength. Specifically, the features considered are the FeH absorption bands at 0.998 and 1.2 $\mu$m (whose strength is measured by the $FeH_z$ and $FeH_J$ indices respectively), the VO absorption band at 1.058 $\mu$m (measured by the $VO_z$ index), the alkali lines (measuring the equivalent width of the Na I line at 1.1396 $\mu$m and of the K I lines at 1.1692, 1.1778, and 1.2529 $\mu$m), and the "peakiness" of the $H$-band (measured by the $H$-cont index). The criteria to assign the scores are defined only for given spectral type ranges, and for some features do not extend down to L7. In those cases we assign a qualitative score based on a direct comparison of our target indices with the values plotted in Allers & Liu (2013) for known low-gravity objects. We assign a score of 1 to the FeH absorption features based on the $FeH_J$ index only, as the $FeH_z$ feature falls in the very noisy region of the spectrum, at the edge of the VIS and NIR arms, where the flux calibration of our spectrum is less reliable. We assign a score of 0 to the VO feature as its index falls exactly on the line defining the average value for normal field dwarfs (see Allers & Liu, 2013, Figure 20). Finally, the alkali lines give an average score of 0 while the $H$-cont index gives a score of 2 (based on the criteria defined in Table 9 and 10 of Allers & Liu, 2013). The median score for ULAS J222711−004547 is therefore 0.5, and so we classify it as a field-gravity dwarf (hereafter FLD-G), i.e. the surface gravity is consistent with normal field dwarfs. This finding is in agreement with the results of Allers & Liu (2013), where they classified all the URLs in their sample as FLD-G dwarfs.

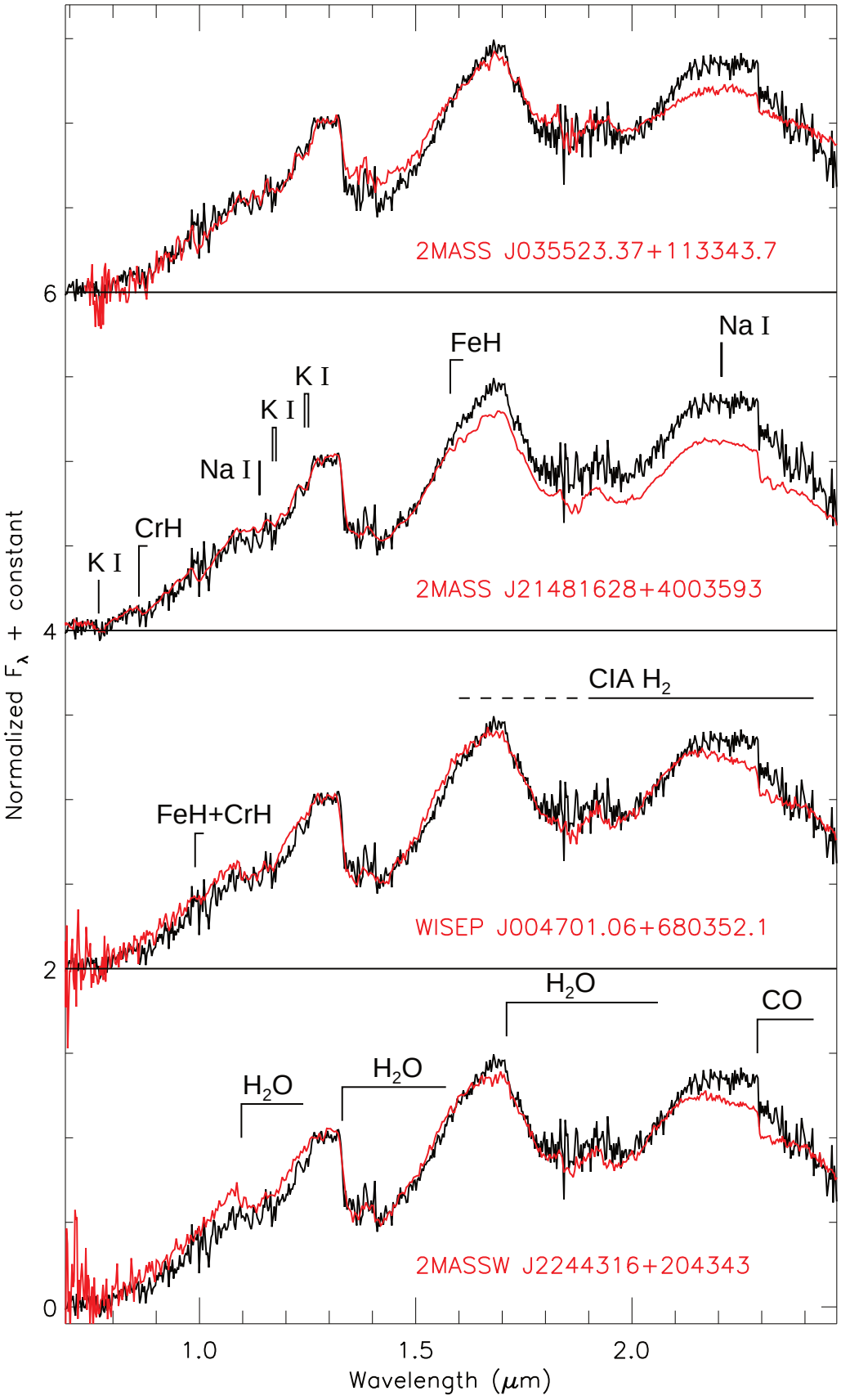


Fig. 5.3: The spectrum of ULAS J222711−004547 compared to the known red L dwarfs 2MASS J035523.37+113343.7 (L5$\gamma$), 2MASS J21481628+4003593 (L6.5pec), WISEP J004701.06−680352.1 (L7.5pec), and 2MASSW J2244316+204343 (L7.5pec). All the spectra are normalized to 1 at 1.28 $\mu$m.

| Index | Value | | |
|---|---|---|---|
| | Target | Field L7 | Low gravity L7 |
| $H_2O-J$ | 0.58±0.14 | $\gtrsim$ 0.70 | ... |
| $H_2O-H$ | 0.66±0.08 | $\gtrsim$ 0.70 | ... |
| $H_2O$ 1.5 $\mu$m | 1.71±0.23 | 1.65-1.70 | ... |
| $H_2O-K$ | 0.95±0.12 | $\gtrsim$ 0.70 | ... |
| $CH_4$ 2.2 $\mu$m | 0.98±0.13 | 1.075-1.125 | ... |
| $FeH_J$ | 1.00±0.17 | ∼1.1 | ... |
| $VO_z$ | 0.97±0.15 | ∼0.97-1.00 | > 1.00 |
| K $I_J$ | 1.02±0.10 | 1.01-1.07 | < 1.01 |
| *H*-cont | 0.97±0.07 | < 0.888 | ≥ 0.888 |
| Spectral | Equivalent Width (Å) | | |
| Feature | Target | Field L7 | Low gravity L7 |
| Na I 1.138 $\mu$m | 8.12±0.44 | > 3.175 | ≤ 3.175 |
| K I 1.169 $\mu$m | 12.65±0.87 | > 6.496 | ≤ 6.496 |
| K I 1.177 $\mu$m | 11.21±0.88 | > 8.154 | ≤ 8.154 |
| K I 1.253 $\mu$m | 7.78±0.69 | > 4.545 | ≤ 4.545 |

Table 5.1: Spectral indices and equivalent widths for ULAS J222711−004547. The indices are defined in Geballe et al. (2002), Burgasser et al. (2006a), and Allers & Liu (2013). Where available, comparison values for "field" and low gravity L7s are given.

## 5.3 Photometric properties

We obtained the photometry of ULAS J222711−004547 from the UKIDSS LAS (Lawrence et al., 2007), the 2MASS Point Source Catalogue (Skrutskie et al., 2006), the *WISE* All-Sky Data Release (Wright et al., 2010), and the *NEOWISE* Post-Cryo Data Release (Mainzer et al., 2012). The object is undetected in 2MASS *J*-band, so we determined its synthetic magnitude in that band from the measured spectrum. We checked the accuracy of our synthetic value by comparing it with the magnitude obtained converting its UKIDSS MKO *J*-band magnitude using the equations presented in Stephens & Leggett (2004). The two values are in good agreement with each other (18.27±0.06 vs. 18.25±0.04) and we therefore assume as our final 2MASS *J*-band magnitude 18.26±0.05.

We also obtained a NTT/SOFI *J*-band image of ULAS J222711−004547. The observations were made on the night of 2013-06-22 as part of the NPARSEC program (ESO 186.C-0756 P.I. R. L. Smart) and the observing strategy is fully described in Smart et al. (2013). Briefly we observed with a nine point dither pattern of 4 × 30 s exposures (i.e. NDIT=4, DIT=30 s) for a total integration time of 18 minutes. This was coadded using the *jitter* software, and centroids and instrumental magnitudes were found from the resulting coadded image using the *SExtractor* barycenter and psf fitting procedures (Bertin & Arnouts, 1996). We calculated the zero point of the field using the measured 2MASS *J*-band magnitudes from the 2MASS Point Source Catalogue (hereafter PSC) of the reference stars in the field, converting them in ESO/SOFI magnitudes using the equations presented in Carpenter (2001). The SOFI *J*-band magnitude for ULAS J222711−004547 is 18.13 ± 0.05. This value agrees with the 2MASS synthetic value, although only at the $2\sigma$ level. This slight discrepancy could be due to the NTT/SOFI *J*-band filter bandpass including the telluric absorption bands, whose variability affects differently the early type stars used for photometric

calibration and the brown dwarf.

There is no clear evidence for variability in the *WISE* single exposures in $W1$ and $W2$, nor in the *NEOWISE* single exposures in $W1$ and $W2$.

In Figure 5.4 and 5.5 we compare the photometry of ULAS J222711−004547 with known "normal", low-gravity, and unusually red L dwarfs from the literature. We note that our target appears much redder than any of the known late-L dwarfs, and it is still redder than most of the other known low-gravity and unusually red L dwarfs (see Figure 5.4). It is particularly interesting to notice in Figure 5.5, that our target marks the end of the L-dwarf sequence (running from bottom-left to top-right in the four panels) further stressing its extreme nature, and that its photometry is very similar to the recently discovered free-floating planetary-mass L7 PSO J318.5338−22.8603 (Liu et al., 2013).

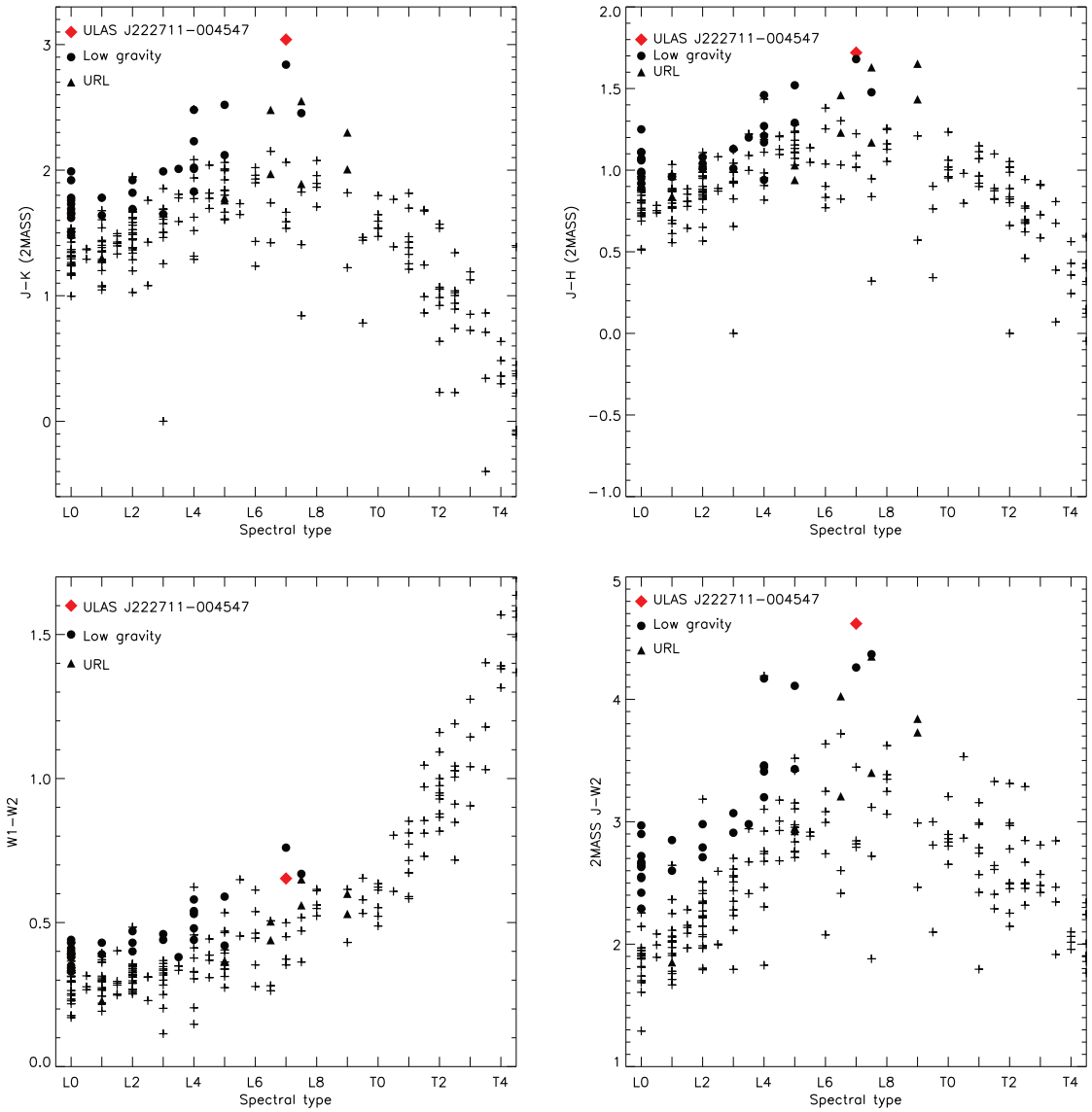


Fig. 5.4: Colour − spectral type diagrams comparing the photometry of ULAS J222711−004547 with other known L and T dwarfs. "Normal" field objects are plotted as crosses, known low-gravity dwarfs as circles, and unusually red L dwarfs (URLs) as triangles. ULAS J222711−004547 is plotted as a red diamond.

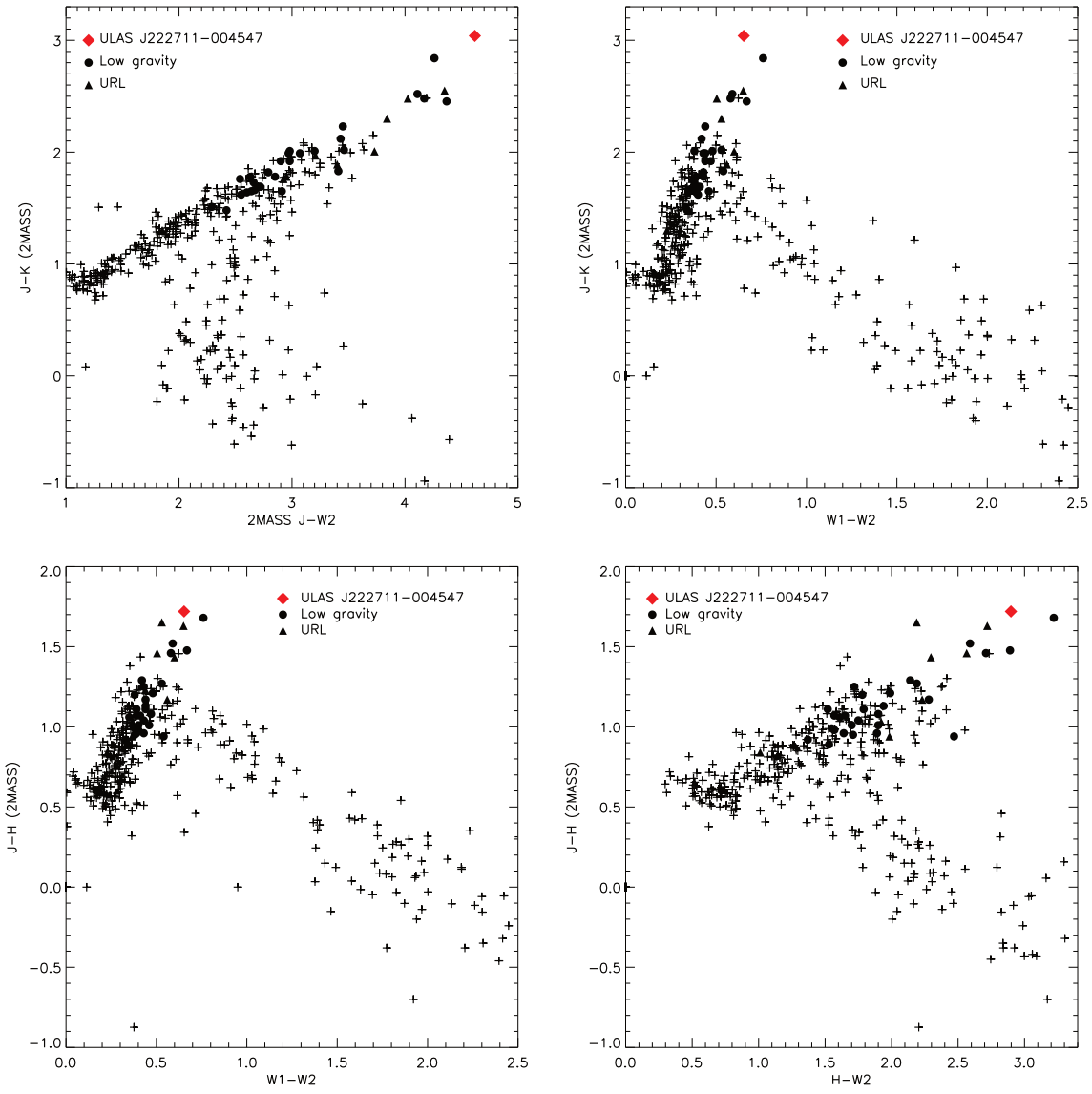


Fig. 5.5: Colour − colour diagrams comparing the photometry of ULAS J222711−004547 with other known L and T dwarfs. L dwarfs form a sequence running from bottom-left to top-right in each panel. Plotting symbols follow the same convention of Figure 5.4.

## 5.4 Astrometry

Other than in UKIDSS $YJHK$ bands, ULAS J222711−004547 is detected in 2MASS $H$ and $K$-band, and in *WISE* $W1$-$W2$-$W3$. In Figure 5.6 we present the 2MASS $K$-band, UKIDSS $K$-band, and *WISE* $W2$-band images of our target. We also show the SDSS $z$-band image of the field, but we note that ULAS J222711−004547 is undetected. The object just outside the edge of the circle marking the expected position of the target is a different source, and its very faint counterpart can be seen in the UKIDSS $K$ band as well. With a total baseline of more than 11 yr between the 2MASS and *WISE* images, we can estimate the proper motion of our target. A linear fit to the measured positions in 2MASS, UKIDSS and *WISE* gives a proper motion of $\mu_\alpha \cos\delta = 100 \pm 16$ mas yr$^{-1}$ and $\mu_\delta$ = -30 ± 16 mas yr$^{-1}$.

We tried to estimate the photometric distance to our target using the calibration published in Dupuy & Liu (2012). However, the peculiarity of ULAS J222711−004547 makes the estimation unreliable, as the calibrations presented in the literature are applicable only to standard objects. It has indeed been pointed out by Faherty et al. (2012) that unusually red L dwarfs tend to be underluminous compared to the average absolute magnitude of their spectral type by up to 1.0 mag. Moreover, their non-standard colours cause them to "move" up and down in an absolute magnitude − spectral type plot. This results in the photometric distances given by the different magnitudes to be inconsistent with each other, spanning from 68 ± 12 pc if using MKO $M_Y$ to 31 ± 5 pc when using *WISE* $M_{W2}$. The value obtained using *WISE* $M_{W2}$ should be the most accurate, as the flux at 4.6 $\mu$m should be much less impacted by dust.

We tested the possibility of the object being a member of one of the known young moving groups (hereafter MG) using the convergent-point method (e.g. Clarke et al., 2010; de Bruijne, 1999, and references therein). We de-composed the proper motion of ULAS J222711−004547 into a component towards the convergent point of the MG ($\mu_\parallel$) and one perpendicular to that direction ($\mu_\perp$). For a MG member $\mu_\parallel$ must be positive while $\mu_\perp$ should ideally be zero. However, given the measurement errors on the proper motion of the target, and the intrinsic velocity dispersion of the MG, one should expect non-zero $\mu_\perp$. We calculated $\mu_\parallel$ and $\mu_\perp$ for our target relative to 13 known MGs, whose convergent points were taken from Mamajek (2013). The results obtained are listed in Table 5.2. The large uncertainties on the proper motion components and the weak constraint on the distance to ULAS J222711−004547 prevent us from drawing any firm conclusion. It appears however unlikely for the target to be member of any of the MGs considered, given its significant $\mu_\perp$. Even assuming the smaller distance estimate (31 ± 5 pc) the $\mu_\perp$ obtained corresponds in fact to peculiar velocities larger than 3 km s$^{-1}$, and generally above the 3$\sigma$ velocity dispersion of the MGs. Our results are in agreement with the Bayesian Analysis for Nearby Young AssociatioNs (BANYAN, Malo et al., 2013) online tool, that returns a probability of 97% of the object being a field "old" dwarf.

Finally, we searched for common proper motion companions to ULAS J222711−004547. We assumed the shortest distance estimate (31 ± 5 pc) and we looked for objects within 25000 AU from our target, with proper motion components within 2$\sigma$ from those of ULAS J222711−004547. We used the PPMXL, LSPM, rNLTT, HIPPARCOS, TYCHO2 and UCAC4 catalogues, and we did not find any common proper motion companion to our target.

A summary of the properties of ULAS J222711−004547 is given in Table 5.3, where

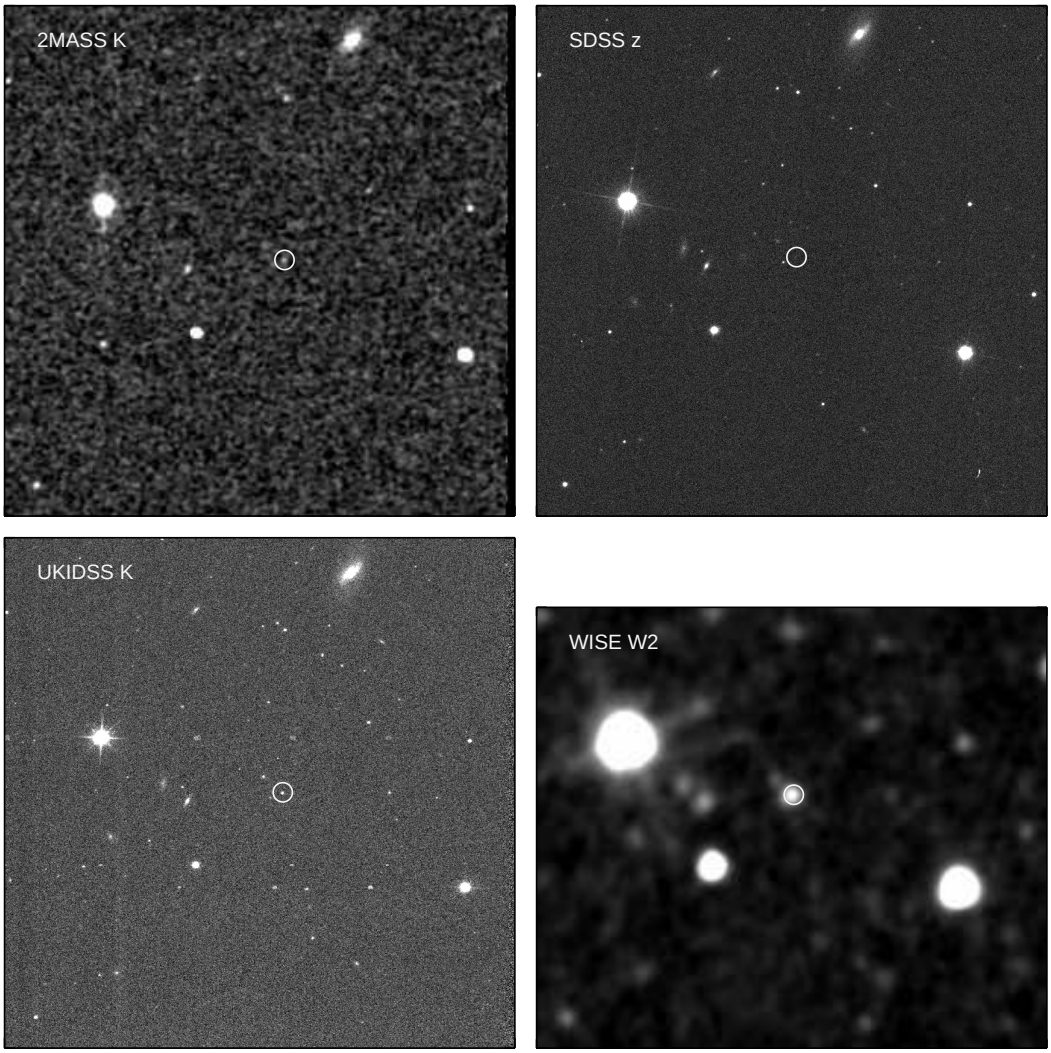


Fig. 5.6: Finder charts for ULAS J222711−004547. The object position in each frame is marked with a circle. All images are oriented with north up and east left and are 5×5 arcmin, except the *WISE* $W2$ image which is 5×4.3 arcmin. The target is undetected in the SDSS $z$-band.

Table 5.2: Convergent point calculations for ULAS J222711−004547.

| Group | $\mu_{\parallel}$ (mas yr$^{-1}$) | $\mu_{\perp}$ (mas yr$^{-1}$) |
|---|---|---|
| 32 Ori | 101 | 26 |
| AB Dor | 89 | 53 |
| Alessi 13 | 102 | 23 |
| Argus | 100 | -28 |
| $\beta$ Pic | 100 | 27 |
| Carina-Near | 102 | -21 |
| Columba | 101 | 25 |
| Coma Ber | 98 | 36 |
| $\eta$ Cha | 97 | 37 |
| Hyades | 96 | -42 |
| Tucana | 100 | 29 |
| TW Hya | 102 | 24 |
| UMa (Sirius) | -65 | 82 |

The uncertainty on $\mu_{\parallel}$ and $\mu_{\perp}$ is $\pm$16 mas yr$^{-1}$.

we present coordinates, the available photometry, spectral type, proper motion, and the photometric distance range.

Table 5.3: Summary of the properties of ULAS J222711−004547.

| Parameter | Value |
|---|---|
| RA (J2000) | 22:27:10.8 |
| Dec (J2000) | -00:45:47.3 |
| SDSS $z$ | $> 20.8$ |
| MKO Y | 19.50 ± 0.11 |
| MKO J | 18.11 ± 0.06 |
| MKO H | 16.61 ± 0.03 |
| MKO K | 15.32 ± 0.02 |
| 2MASS J | *18.26 ± 0.05*[a] |
| ESO/SOFI J | 18.13 ± 0.05 |
| 2MASS H | 16.54 ± 0.26 |
| 2MASS K | 15.22 ± 0.16 |
| *WISE* $W1$ | 14.295 ± 0.031 |
| *NEOWISE* $W1$ | 14.332 ± 0.020 |
| *WISE* $W2$ | 13.642 ± 0.041 |
| *NEOWISE* $W2$ | 13.599 ± 0.031 |
| *WISE* $W3$ | 12.283 ± 0.409 |
| *WISE* $W4$ | $> 8.592$ |
| Spectral type | L7pec |
| $\mu_\alpha \cos\delta$ (mas yr$^{-1}$) | 100 ± 16 |
| $\mu_\delta$ (mas yr$^{-1}$) | -30 ± 16 |
| $d_{\rm phot}$ (pc) | 31 − 68 |

Note: (a) Synthetic value, derived from the measured spectrum.

## 5.5 De-reddening

The extremely red colours and spectra of red L dwarfs could be caused by thicker clouds (Cushing et al., 2008). Such thicker condensate clouds are believed to be associated with low surface gravity or high metallicity (e.g. Leggett et al., 2007; Looper et al., 2008b; Stephens et al., 2009). We note that the extinction cross sections of condensate clouds are very sensitive to the characteristic size of the particles so in this context "thicker clouds" may mean a higher optical depth due to slightly larger particles rather than a structural difference in a cloud layer.

Low surface gravity is a sign of youth, and in L dwarfs is marked by triangular-shaped $H$-band spectra (e.g. Lucas et al., 2001). In the case of ULAS J222711−004547, the $H$-band looks indeed slightly triangular compared to the standard L7 (see Figure 5.2). The effect is however not as strong as seen in known young objects like 2MASS J03552337+1133437 (Cruz et al., 2009) and 2MASS J01225093−2439505 (Bowler et al., 2013) . Other signs of youth, like the Li I absorption doublet at 6708 Å and the H$\alpha$ emission at 6563 Å are not seen in the spectrum of our target. Their absence however does not rule out the possibility that ULAS J222711−004547 is a young field brown dwarf, as pointed out by Cruz et al. (2009) and Kirkpatrick et al. (2008). Also, the kinematics of this object does not match any of the known young moving groups (see Section 5.4), and it is therefore unlikely that ULAS J222711−004547 is very young.

### 5.5.1 Checking for interstellar reddening

A way to determine the effect of dust clouds and their role in the formation of the spectra of peculiar red L dwarfs is to de-redden the spectra applying wavelength dependent corrections (e.g. Gizis et al., 2012). We de-reddened the spectrum of ULAS J222711−004547 using two different reddening curves: the Cardelli et al. (1989) and the more recent Fitzpatrick (1999), assuming the standard value $R(V) = 3.1$. For each reddening curve we selected the best colour excess E(B-V) − standard template combination via $\chi^2$ minimization. In both cases the best fit is given by the L7 standard with a colour excess of E(B-V)=1.1. The results are shown in Figure 5.7 where we compare the normalized spectrum of ULAS J222711−004547 before and after the de-reddening with the standard L7 dwarf 2MASSI J0103320+193536. Since there is no significant difference between the results obtained with the two different extinction laws, we only show the correction obtained with the Fitzpatrick (1999) curve. The de-reddened version of the spectrum resembles closely to the L7 standard, but still shows a more peaked $H$-band, due to its blue-wing being fainter, i.e. the water absorption at 1.4 $\mu$m being stronger, than in 2MASSI J0103320+193536. The $K$-band flux is also slightly enhanced, especially in its red end. We note in particular a "bump" between 2.1 and 2.3 $\mu$m, and a weaker CO absorption compared to the L7 standard. This result is quite remarkable and surprising when considering how different the interstellar dust and the atmospheric clouds of brown dwarfs are.

There is of course the possibility that the reddening of the spectrum is due to interstellar dust clouds. However this is improbable as the object is at a distance of less than 70 pc (see Section 5.4) and that the asymptotic reddening for the field is E(B-V) = 0.068, which corresponds to an integrated extinction of approximately 0.061 mag, 0.039 mag, and 0.025 mag in the $J$, $H$, and $K$ band respectively. Reddening and extinction for the field were obtained using the Galactic Dust Reddening and

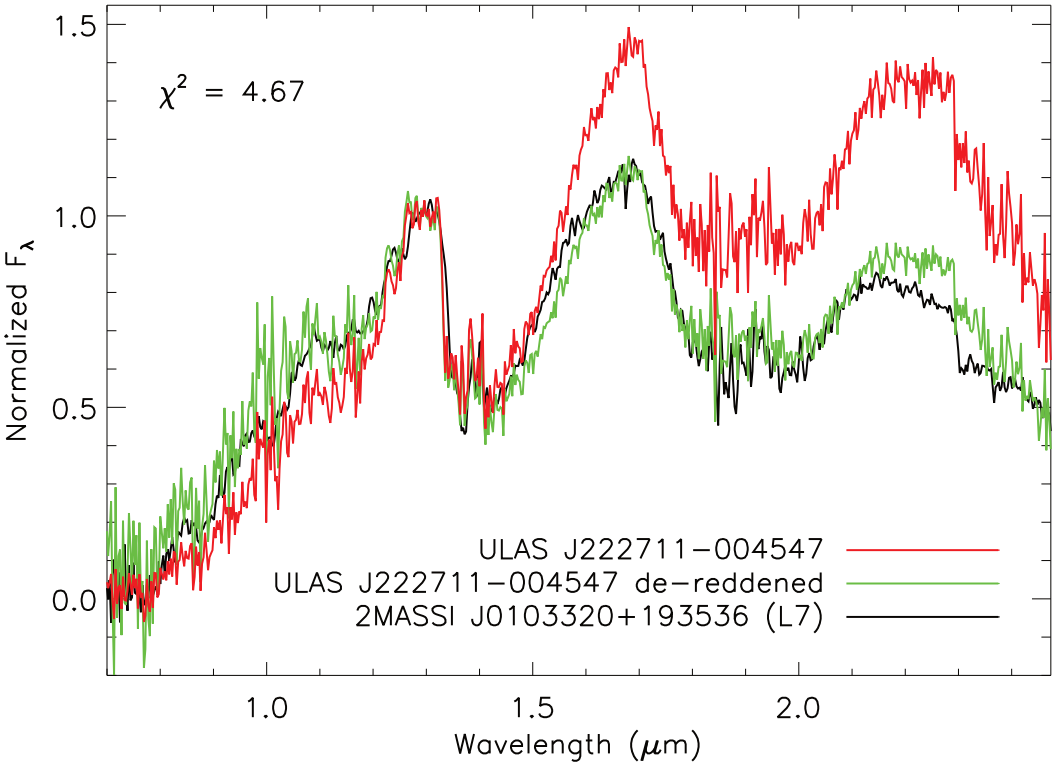


Fig. 5.7: The spectrum of ULAS J222711−004547 (black) and its de-reddened version (green) compared to the L7 standard 2MASSI J0103320+193536 (red). The spectrum has been de-reddened applying the Fitzpatrick (1999) extinction curve with a colour excess of E(B-V)=1.1.

Extinction service[2], which is based on the results of Schlegel et al. (1998). We note that the value of E(B-V) measured for the field is almost constant, with $\Delta$ E(B-V) = 0.01 over an area of 2×2 square degrees. This rules out peculiar properties of the interstellar medium and the presence of molecular clouds along the line of sight, and therefore justifies the use of $R(V) = 3.1$.

### 5.5.2 De-reddening with dust typical of L dwarfs

The surprisingly good results given by the method described above, motivated us to calculate more specific extinction curves, for the dust species that are typical of the atmospheres of brown dwarfs. In this contribution we have considered corundum ($Al_2O_3$), enstatite ($MgSiO_3$), and iron, as they are thought to be the most abundant in late-L dwarfs (e.g. Morley et al., 2012, and references therein). For each dust species we calculated the extinction cross section as a function of wavelength using an adapted version of the Mie scattering code of Bohren & Huffman (1983). Following Seager et al. (2000), optical constants were taken from Dorschner et al. (1995), for enstatite; Koike et al. (1995), for corundum; and Ordal et al. (1985), for iron. For corundum we used the "ISAS" particles given in Koike et al. (1995), since this yields a single scattering albedo spectrum consistent with that shown by Seager et al. (2000).

We have calculated the extinction for a range of characteristic grain radii (hereafter $r$) from 0.05 to 1.00 um. For each $r$ we used a Gaussian size distribution with a width $\sqrt{2}\sigma = 0.1 \times r$. This size distribution is wide enough to smooth over the interference effects that arise in Mie scattering. In reality, there is likely to be a broader distribution of grain sizes but the extinction curve is dominated by grains close to $r$, so it is useful to consider a characteristic size, even though it may not dominate the mass. For example, the scattering cross section of particles much smaller then the wavelength is proportional to the sixth power of the grain size (due to the Rayleigh-like fourth power in efficiency, combined with the physical cross section increasing with the square of radius). Therefore the size distribution would have to be very steep for the smaller particles to contribute significantly.

The range of $r$ that we consider is constrained by basic considerations of light scattering physics and by the fact that particles larger than 1 $\mu$m are expected to drop out of the photosphere. If the size parameter $x = 2\pi r/\lambda$ of optically dominant grains is much bigger than 1 in the wavelength range under consideration, then the extinction is expected to be "grey", with little or no reddening effect. If $r < 0.05$ $\mu$m then it approaches the small grain limit, and no changes to the extinction curve would be expected if the grains were smaller.

We then de-reddened the spectrum of ULAS J222711−004547 using the extinction curves and fit it to the already mentioned L7 spectroscopic standard 2MASSI J0103320+193536. The fit has two free parameters: other than the grain size $r$, the normalization of the extinction curve at 2.20 $\mu$m (i.e. $A_K$). In Figure 5.8 we show the best fit obtained for each dust species. Corundum and enstatite (top-left and top-right panel of Figure 5.8) give a very good fit for typical grain sizes of 0.45-0.50 $\mu$m. The de-reddened spectrum matches almost perfectly the standard, with only slight discrepancies in the CO absorption band at 2.3 $\mu$m and in the CrH band at 0.86 $\mu$m. The best fit grain size for iron is 0.20 $\mu$m (bottom-left panel of Figure 5.8), but the quality of the fit is significantly poorer. While the NIR portion is quite well matched, the optical and J-band

[2]http://irsa.ipac.caltech.edu/applications/DUST/

appear much fainter than in the standard. All the dust species give a best-fit $A_K$ of 0.20-0.22, which corresponds to $\tau_K$ = 0.18-0.20. The de-reddened *WISE* photometry gives a $W1-W2 = 0.62$ (using the corundum or enstatite extinction curve), and 0.63 (using the iron extinction curve). The *WISE* colours are still redder than the average even after de-reddening them, because the extinction curves we derived decline steeply as a function of wavelength, and the difference between the extinctions at 3.4 and 4.6 $\mu$m is therefore negligible.

A complication is that there is a strong peak in the extinction cross section when the grain size is a little smaller than the wavelength of observation (e.g. Figure 15 of Lucas & Roche, 1998). The strength of this peak and the corresponding size parameter depend on the shape and refractive index of the particles. This has the consequence that grains that are a bit smaller than the maximum size can have a significant effect at shorter wavelengths. For this reason we have attempted to de-redden with a power law size distribution of iron grains, in order to determine whether the poor fit to iron is due to the unusual optical properties of this metal or to the fact the large refractive index of iron causes smaller grains in the distribution to have a more noticeable effect. We determined extinction curves for exponents between 0 and -7.00 with steps of 0.25. We assume a fixed minimum grain size of 0.05 $\mu$m, while the maximum grain size $r_{max}$ at which we truncate the power law is a parameter of the fit (as well as $A_K$ and the exponent of the power law).

The best-fit obtained is shown in bottom-right panel of Figure 5.8. The maximum grain size obtained is 0.30 $\mu$m with $A_K$ = 0.30 and a power law index of -2.50. The quality of the fit obtained is equal to that obtained with corundum and enstatite, and much better than the fit obtained assuming a narrow gaussian distribution around the characteristic $r$. This indicates that given its large refractive index, the size distribution of iron cannot be neglected when computing its extinction.

### 5.5.3 Testing the method on other Unusually Red L dwarfs

To test the reliability of our method, we applied it to the other URLs plotted in Figure 5.3. An example of the fits obtained is shown in Figure 5.9 where we plot 2MASS J035523.37+113343.7, 2MASS J21481628+4003593, WISEP J004701.06−680352.1, and 2MASSW J2244316+204343 (from top to bottom), dereddened with corundum. Overplotted in red are the corresponding standard templates used. WISEP J004701.06−680352.1, and 2MASSW J2244316+204343 give results that are very similar to those obtained for ULAS J222711−004547. The best-fit grain size for corundum and enstatite is slightly larger (r = 0.50-0.60 $\mu$m for $A_K \sim 0.5$) and the quality of the fit to the L7 standard is surprisingly good. De-reddening using iron gives a best-fit grain size of 0.20 $\mu$m for both objects ($A_K \sim 0.3$), but the quality of the fit to the red-optical part of the spectrum is again poorer. The best-fit parameters for 2MASS J21481628+4003593 against the L6 standard are identical to those given by our target, i.e. r = 0.45-0.50 $\mu$m with $A_K$ = 0.22-0.24 for corundum and enstatite, and r = 0.20 $\mu$m and $A_K$ = 0.20 using iron. The quality of the fit to the standard in this case is very good also for the de-reddening using iron, with a very good match to the entire spectrum. The consistency of these results strengthens the validity and the significance of our approach, further highlighting the importance of dust in the photosphere of URLs.

The fits obtained for 2MASS J035523.37+113343.7 against the L5 standard are poorer. The best-fit grain sizes obtained for corundum, enstatite and iron are comparable to those obtained for the other URLs (0.40, 0.50, and 0.15 $\mu$m respectively,

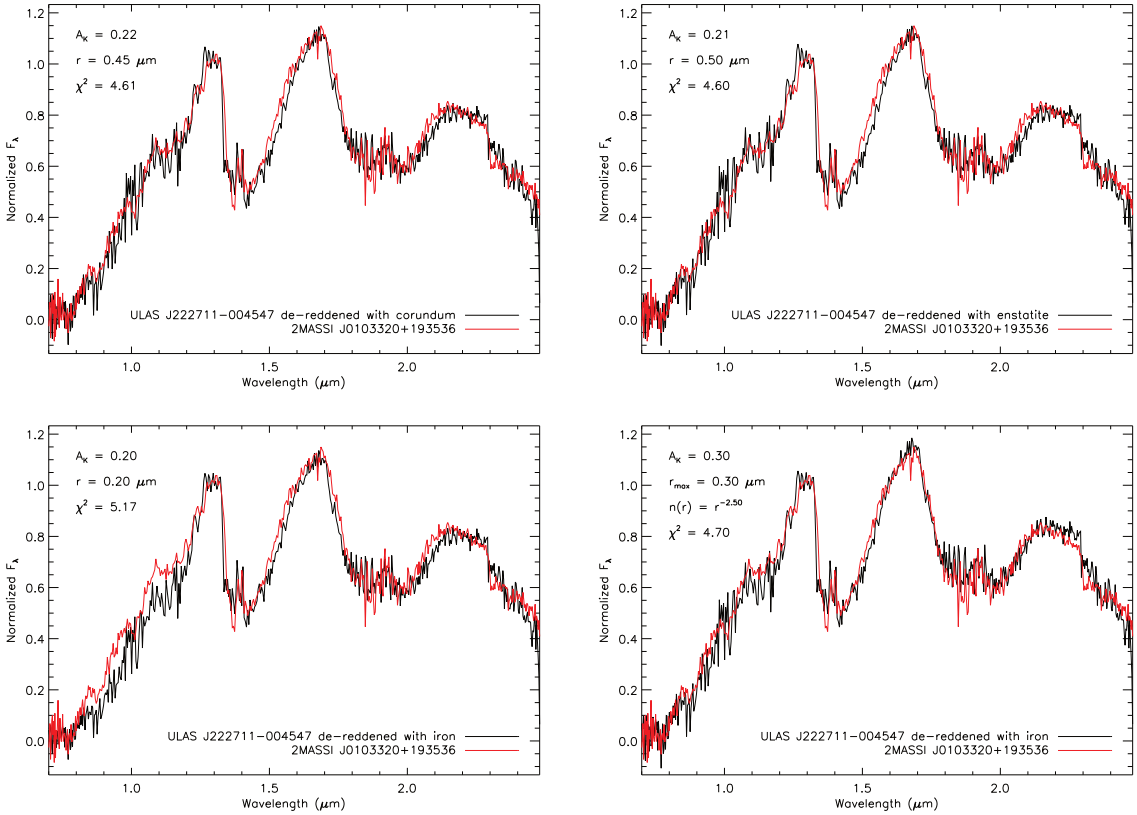


Fig. 5.8: The spectrum of ULAS J222711−004547 (black line) de-reddened using extinction curves for corundum (top-left), enstatite (top-right) and iron assuming a typical grain size (bottom-left) and iron assuming a power law grain size distribution (bottom right) compared to the L7 standard 2MASSI J0103320+193536 (red line). The best fit parameters are shown in the top left corner of each panel.

with $A_K$ = 0.26, 0.32, and 0.19). However, the de-reddened spectrum resembles closely that of the standard in the red-optical and $J$-band, but the standard has stronger $H_2O$ and CO absorption, a less peaked $H$-band, and it is brighter in the $K$-band. The poorer results obtained for this object could be due to a combination of two factors. First, 2MASS J035523.37+113343.7 is classified as very-low gravity in Allers & Liu (2013), and it is likely to be a member of the AB Doradus moving group (Faherty et al., 2013b). Therefore, to fully explain its spectral peculiarities low gravity cannot be neglected, and a simple dust de-reddening is not sufficient. Second, this object is of a slightly earlier spectral type compared to the other URLs considered, and the role of dust clouds in its photosphere is intrinsically less dominant.

### 5.5.4 De-reddening using different templates

We have also de-reddened the spectrum of ULAS J222711−004547 using different comparison dwarfs. Instead of the L7 standard, we used the L7 2MASS J09153413+0422045, which is slightly bluer than the standard, and the d/sdL7 2MASS J14162409+1348267, which is a known slightly metal-poor dwarf (Bowler et al., 2010; Schmidt et al., 2010a). The fit to 2MASS J09153413+0422045 gives typical grain sizes slightly larger but consistent with those obtained with the fit against the L7 standard. We obtain r = 0.50, 0.60, and 0.20 $\mu$m for corundum, enstatite and iron respectively. The main difference between the two fits is, not surprisingly, the larger $A_K$ given by the bluer template, in the range 0.35 to 0.60. The quality of the fit is still extremely good for the entire spectrum. When fitting the d/sdL7 2MASS J14162409+1348267 we obtain the same typical grain sizes, but a higher extinction $A_K$ = 0.79, 0.95, and 0.56 for corundum, enstatite and iron respectively. The quality of the fit remains quite good for corundum and enstatite, except for the $H$-band peak that appears too triangular compared to the d/sdL7. De-reddeing with iron gives a very poor fit at wavelengths shorter than 1.2 $\mu$m, and a good fit to the rest of the spectrum. The results are shown in Figure 5.10 where we show the spectrum of ULAS J222711−004547 de-reddened using the corundum extinction curve. The two different standards that we used are overplotted in red for comparison.

These surprisingly good results suggest that the differences in photometry and spectra seen in objects of similar spectral types (especially at late-L type, e.g. Zhang et al., 2013a) could be explained almost entirely by assuming differences in the optical thickness and depth of the cloud deck.

The results of this de-reddening however have to be taken with caution. In fact we do not use the extinction curves in a defined structure or medium but simply apply them directly to the observed spectrum. This is equivalent to adding a layer of cold dust at the top of the brown dwarf's photosphere, neglecting the effect of scattering (i.e. scattered photons are considered to disappear as if they were absorbed), and without taking into account any effect that the extra dust would cause on the atmosphere of the object (e.g. elements depletion, backwarming effect, etc.). Physically, the dust layer as fitted here could be located anywhere above the photosphere, and the fitted extinction $A_K$ represents the effect of this dust layer over and above the normal extinction effect of dust in the spectroscopic standard. More realistically, at least some of the additional dust in the red L dwarf is likely to be mixed in with the photosphere, which would mean that the $A_K$ parameter is under-estimated. In fact, it is not necessary for the

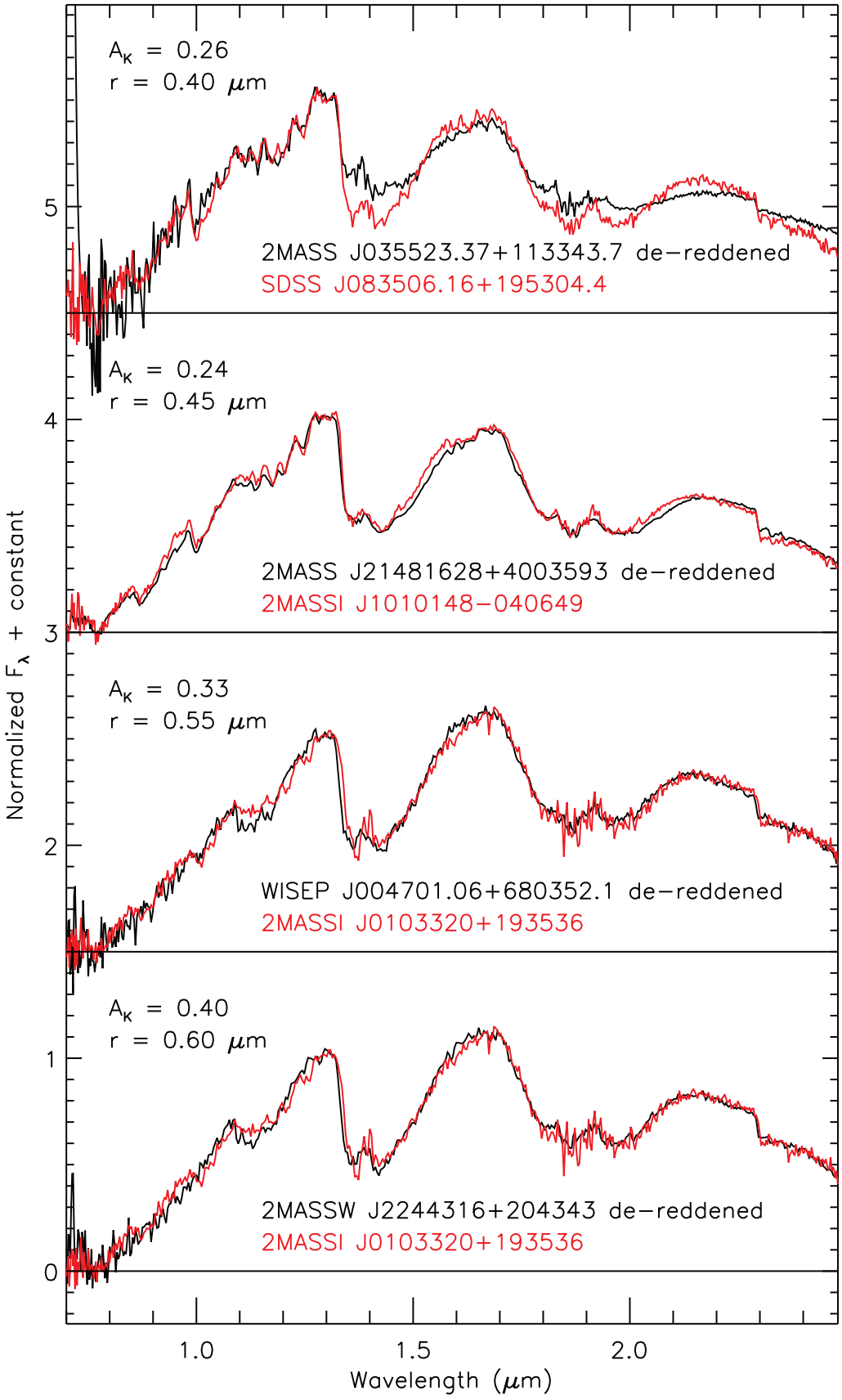


Fig. 5.9: The spectra of 2MASS J035523.37+113343.7, 2MASS J21481628+4003593, WISEP J004701.06−680352.1, and 2MASSW J2244316+204343 (from top to bottom), de-reddened with corundum. Overplotted in red are the corresponding standard templates used. The best fit parameters for each object are indicated on the left-hand side.

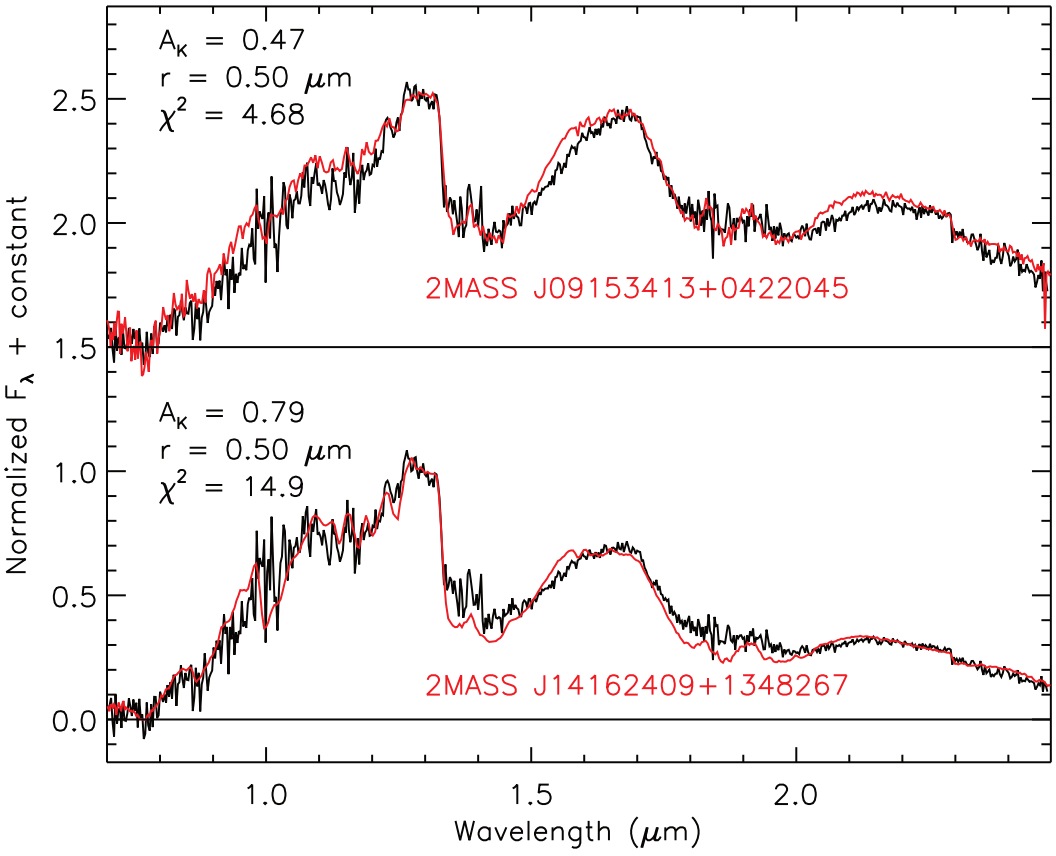


Fig. 5.10: The spectrum of ULAS J222711−004547 de-reddened with corundum, compared to the slightly blue L7 2MASS J09153413+0422045 (top), and the d/sdL7 2MASS J14162409+1348267 (bottom). The best fit parameters for each fit are indicated on the left-hand side.

dust in red L dwarfs to be located at a different altitude than in normal L dwarfs. It is only necessary for it to have higher optical depth, perhaps due to larger grain size, or a higher space density of particles, rather than a physically thicker cloud layer.

A larger typical dust grain size in the photosphere can naturally arise from lower gravity, which would increase the maximum grain size that can remain suspended in the photosphere. However, in ULAS J222711−004547 there is no clear evidence for low gravity (see Section 5.2.2), so the explanation could be a higher than solar metallicity.

## 5.6 Model fitting

We fit the spectrum of ULAS J222711−004547 with a set of atmospheric models to try to understand the origin of its very red infrared colours. We used the BT-Settl and BT-Dusty models from Allard et al. (2011), the A and AE models from Madhusudhan et al. (2011), and the Unified Cloudy Models (hereafter UCM) from Tsuji (2002); Tsuji et al. (2004); Tsuji (2005). For each set of models, we selected the best fit one via $\chi^2$ fitting. The results are shown in Figure 5.11 where we present the fit to the entire spectrum, and a zoom to the optical+$J$-band, $H$-band, and $K$-band respectively (separately normalized to 1 at their peaks). At the top of each panel, we plot for comparison the fit given by the L7 standard reddened using the extinction curve for corundum derived in Section 5.5.

### 5.6.1 BT-Dusty and BT-Settl models

In the BT-Dusty and BT-Settl models dust species abundances are calculated assuming chemical equilibrium. In the BT-Dusty models, no gravitational settling is considered, and the clouds are homogeneously distributed in the atmosphere of the brown dwarf. In the BT-Settl models instead, the dust grains sediment towards the lower layers of the photosphere, slowly depleting the upper layers. The cloud coverage is still assumed to be homogeneous. The dust grain size is determined by the equilibrium between the growth of the grains and their mixing and sedimentation. For the typical atmospheric parameters of late-L dwarfs, this results in grains with a diameter from ∼1 up to ∼10 $\mu$m. The mixing time scale is computed by extrapolating the results of hydrodynamical simulations of late-M dwarfs by Ludwig et al. (2002) at lower temperatures. We can see in Figure 5.11 (top-left panel) that the BT models fit quite well the overall slope of the spectrum, with only the Dusty models appearing slightly bluer than the target in the $K$-band. However, the main absorption features (i.e. the $H_2O$ and CO bands, see Figure 5.11, bottom-right panel) are poorly reproduced. The best fit parameters are very different: the Dusty models suggest $T_{\rm eff}$ = 1800 K (typical of early L-dwarfs) and log(g) = 5.0, while the Settl models give $T_{\rm eff}$ = 1500 K (typical of L5−L6 dwarfs) and log(g) = 3.5. This difference is a direct consequence of the different treatment of dust in the photosphere: the Dusty models, neglecting by assumption the dust settling, do not require low gravity to reach very red colours, while the Settl models do, to allow a greater dust content and at a higher altitude.

### 5.6.2 A and AE models

Madhusudhan et al. (2011) describe the cloud decks in the atmosphere assuming that the dust particle density follows the gas-phase pressure profile, with different "shape

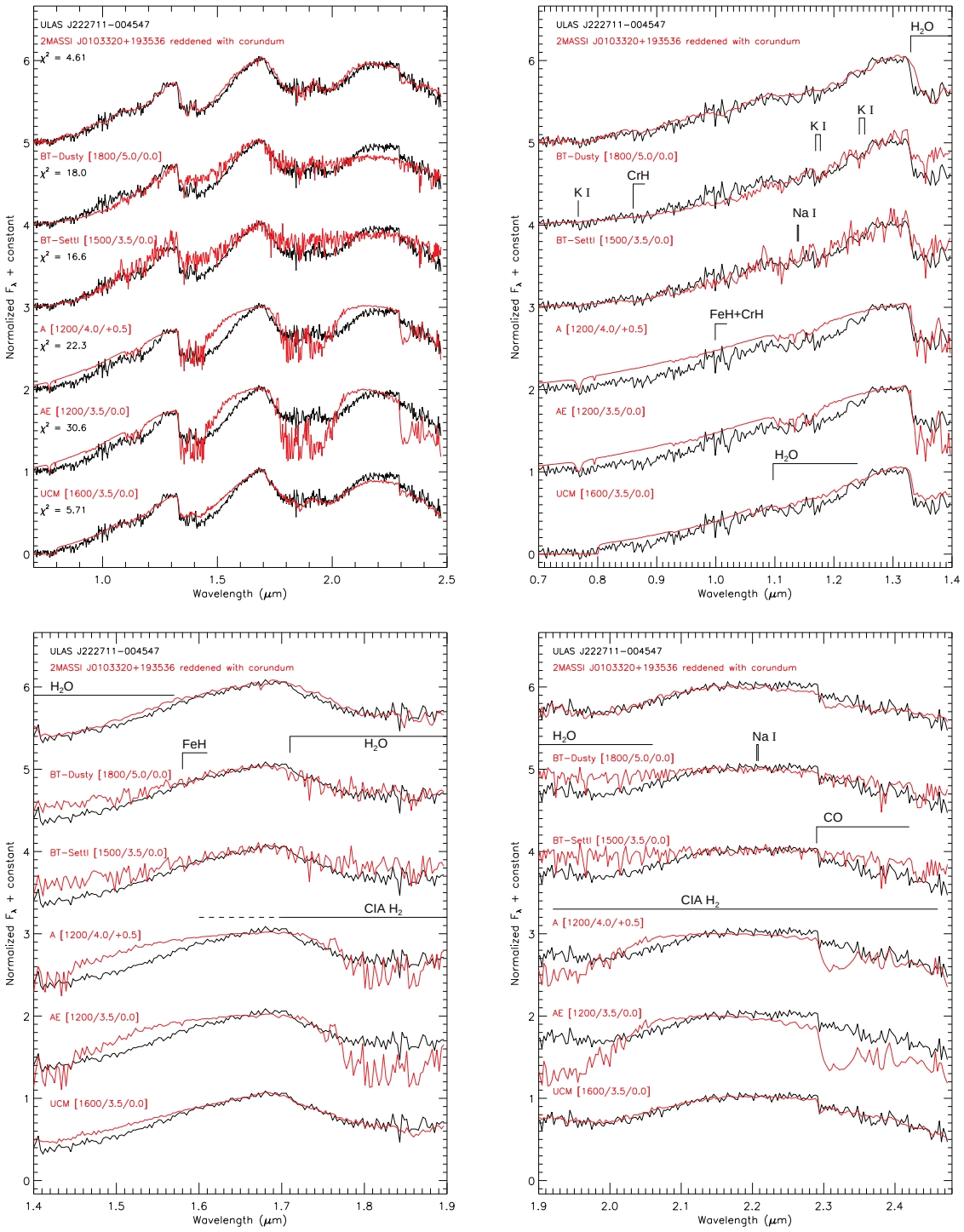


Fig. 5.11: The spectrum of ULAS J222711−004547 compared to atmospheric models. The models used are the BT-Settl and BT-Dusty (Allard et al., 2011), the A and AE models (Madhusudhan et al., 2011), and the UCM models (Tsuji, 2002; Tsuji et al., 2004; Tsuji, 2005). For each model we indicate in bracket effective temperature, surface gravity and metallicity, following the scheme [$T_{\rm eff}$/log(g)/[Fe/H]]. For comparison, we show at the top of each panel the fit given by the L7 standard reddened with our corundum extinction curve. *Top-left*: the complete spectrum. *Top-right*: a zoom into the optical+$J$-band portion of the spectrum. *Bottom-left*: a zoom into the $H$-band portion of the spectrum. *Bottom-right*: a zoom into the $K$-band portion of the spectrum.

functions" to modulate the top and bottom cut-off of the clouds. In the E models, both cut-offs are very sharp; in the A models, the bottom cut-off is very sharp, while there is no top cut-off (i.e. the clouds extend all the way to the top of the atmosphere); the AE models represent an intermediate scenario, with a sharp cut-off at the bottom, and a shallow exponential cut-off at the top. The authors assumed the Deirmendjian size distribution for the dust particles (Sudarsky et al., 2000) with modal particle sizes of 1, 30, 60, and 100 $\mu$m. In Figures 5.11 we show only the A and AE models, as the E models provide a very poor fit. Both models tend to overestimate the flux in the "blue" portion of the spectrum (at wavelengths shorter than 1.3 $\mu$m) and also do not reproduce appropriately the shape of the $H$ and $K$-band. The strength of the CO absorption at 2.3 $\mu$m in this case is overestimated. The A model matches well the strength of the water absorption at 1.4 and 1.9 $\mu$m, while the AE model tends to overestimate the strength of both. We note that the best-fit Madhusudhan et al. (2011) models consider only forsterite clouds. The opacity spectrum of forsterite is very different from that of corundum and enstatite (whose extinction curves provide an excellent fit to the standard), and this could partly explain the poor quality of the fit at short wavelengths. Also, the modal grain sizes adopted vary between 1 and 100 $\mu$m, much larger than what is suggested by our de-reddening. Such large grains would give a more "grey" extinction in the NIR range, resulting in less reddening. This could explain the very low best-fit $T_{\rm eff}$ (1200 K, typical of standard mid T-dwarfs), as this lower temperature implies an intrinsically redder spectrum, which is needed to fit the colours of ULAS J222711−004547.

### 5.6.3 Unified Cloudy Models

In the UCM dust grains are assumed to form at the condensation temperature ($T_{\rm cond}$ ≈2000 K) and then grow until they reach their critical radius (at the critical temperature $T_{\rm cr}$), at which point they precipitate below the photosphere. The dust clouds are therefore segregated in the portion of the photosphere where $T_{\rm cr} \lesssim T \lesssim T_{\rm cond}$. In objects with higher $T_{\rm eff}$ (i.e. L dwarfs) the clouds are located higher in the photosphere, and therefore impact more the spectrum. The dust opacities are calculated assuming grains with a fixed radius of 0.01 $\mu$m, and considering only corundum, enstatite and iron. As we can see in Figure 5.11, the UCM fits properly the flux level in the $H$ and $K$-band, but as in the BT-Settl models, the strength of the CO absorption at 2.3 $\mu$m and of the water band at 1.4 $\mu$m is underestimated. The $H$-band appears too triangular compared to the observed one. Also, we can see in Figure 5.11 (top-right panel) that the red-optical portion looks too smooth compared to the observed spectrum, and is slightly over-luminous. The best-fit parameters are $T_{\rm eff}$ = 1600 K and log(g) = 3.5, in good agreement with the BT-Settl models. The best-fit $T_{\rm cr}$ is 1600 K, which means that the cloud deck extends all the way to the top of the photosphere.

In summary, all the best-fit models imply a low gravity of log(g) $\simeq$ 3.5−4.0 (with the exception of the BT-Dusty models), in contrast with the index-based classification as FLD-G. The temperature predicted varies significantly, from 1200 K up to 1800 K. This wide range of temperatures can be due to the different approaches to dust treatment adopted by the models considered, further highlighting the importance of condensates in the atmosphere of this red L dwarf. Another parameter that can play a role is metallicity. We must note at this point that the model grids used here are

largely incomplete in the sense that they generally offer only solar metallicity spectra. A higher metallicity would facilitate the formation of dust, and could explain the remaining differences between ULAS J222711−004547 and the synthetic spectra shown here. As regards the dust cloud's distribution, all the best fit models imply a fully dusty photosphere, with the dust clouds extending all the way to the top of the atmosphere, although their density is assumed to be modulated in different ways, therefore resembling to our de-reddening scenario, where the dust is essentially added on the top of the dwarf's atmosphere (for a more complete review and comparison of the different atmospheric models, and their dust cloud modelling, we refer the reader to Helling et al., 2008, in particular their Figures 2 and 5).

## 5.7 Conclusions

We report the discovery of a new peculiar L dwarf, ULAS J222711−004547. This object fits into the category of "unusually red L dwarfs", showing very red infrared colours while not displaying any particular sign of youth. Its kinematics in fact do not point towards membership of any of the known young moving groups, and its spectrum does not show the "trademarks" of young brown dwarfs. The index-based classification developed by Allers & Liu (2013) suggests that the object has surface gravity consistent with the field population of L dwarfs. Current atmospheric models however suggest a low gravity nature for ULAS J222711−004547, but fail to reproduce properly its spectrum. The most poorly reproduced feature are the water vapour absorption band at 1.4 $\mu$m, the "peakiness" of the $H$-band, and the CO absorption band at 2.3 $\mu$m. It is not excluded that a non-standard, higher-than-solar metallicity could explain these discrepancies.

However, applying a simple de-reddening curve, the spectrum of ULAS J222711−004547 becomes remarkably similar to the spectra of the L7 spectroscopic standards. This result is rather surprising, as the atmospheric clouds of brown dwarfs are quite different in terms of dust grain size and density compared to the interstellar dust. Refining our de-reddening approach by using extinction curves for the most abundant dust species in the atmospheres of L dwarfs (corundum, enstatite, and iron) allowed us to obtain even higher quality fits, not only for our target but for other URLs as well. It appears that the differences in NIR colours and spectra of late-L dwarfs could be almost entirely explained by assuming a higher dust content in the photospheres of the redder objects. If our simple model is taken at face value, the grain size in the atmosphere would be typically $\sim$0.5 $\mu$m. An important point to stress is that the models that better fit the spectrum and photometry of ULAS J222711−004547 are characterized by fully dusty photospheres, with the clouds extending all the way to the top of the atmosphere. This is to some extent similar to our simple de-reddening, where the dust is essentially located above the atmosphere, and suggests that URLs and giant planets are characterized by thick clouds in the uppermost layers of the atmosphere, probably caused by a combination of slightly low gravity and high metallicity.

Further study of ULAS J222711−004547 and other red L dwarfs will help to understand better the role of dust clouds in ultracool atmospheres, their formation and subsequent disruption, and will lead to a better understanding of the atmospheric dynamics of gas giant planets. Variability studies in particular can help to understand the cloud dynamics in the atmosphere of these peculiar objects, highlighting the role of dust in shaping the spectra of URLs. A more detailed and rigorous modeling of

the reddening induced by the dust excess will be the key to understand the nature of this objects, and could potentially lead to more robust observational constraints on the grain size distribution and abundances in the atmospheres of brown dwarfs.

# Chapter 6: Conclusions and Future Work

The systematic and homogeneous parameterization of large samples of L and T dwarfs is the only way forward in our understanding of the physics of sub-stellar objects. While the initial efforts were devoted (and partially still are) to the discovery of new extreme objects, pushing the boundary of our knowledge to colder and colder dwarfs, sub-stellar astrophysics has now reached a more mature stage in which the facilities available allow for a more systematic study of statistically significant samples. Large area surveys like DENIS, SDSS, 2MASS, UKIDSS, WISE, and more recently VISTA and PANSTARRS, have uncovered more than 1500 brown dwarfs at the time of writing, allowing a more comprehensive analysis of the general properties of the sub-stellar population rather than individual objects.

In this thesis I tried to address some of the open questions via spectroscopic analysis of large samples of L and T dwarfs, combining the spectroscopic information with other available data. The main goals I tried to achieve are a more robust calibration of the magnitude and temperature sequence, and to place a constraint on the IMF and formation history of brown dwarfs.

A better calibration of the absolute magnitude and temperature sequence is necessary in order to determine the luminosity function of brown dwarfs and, therefore the IMF and formation history. As seen in Chapter 4 one of the predominant sources of uncertainty in measuring the space density of a magnitude limited sample is the estimate of the volume probed, i.e. of the photometric distance limit. PARSEC, described in Chapter 2 and in Marocco et al. (2013), will provide a better calibration than the existing one, especially at early types, where the scatter in the absolute magnitude sequence appears to be larger. It is worth mentioning at this point that a significant contribution towards this goal will come from the ESA mission Gaia, that will provide high precision parallaxes (and proper motions), for a few hundred early L dwarfs. Combined with photometry and spectroscopy the astrometric information becomes invaluable, as it can lead to measurements of bolometric luminosity and effective temperature (see Section 2.5), the identification of common proper motions pairs (Section 2.6.4 and 2.6.5), unresolved binaries (Section 2.3.3), and members of young moving groups (Section 2.4).

Similarly, a better calibration of the temperature sequence is necessary in order to compare the results of observational efforts with numerical simulations, as one would always have to convert somehow the observed spectral types into physical parameters, primarily effective temperature, and possibly surface gravity and metallicity. The preliminary results presented in this thesis and in Marocco et al. (2013) suggest that the effective temperature sequence might become shallower at the transition between M and L type dwarfs, possibly because the formation of dust in the photosphere causes a more rapid evolution of the spectral features.

In this respect large spectroscopic campaigns like the one described in Chapter 3 are fundamental to build up statistical significant samples of homogeneously classified objects, reducing the scatter in the calibration by identifying peculiar objects and binaries. And this leads to the second point to be addressed if we wish to constrain the IMF and formation history: the uncertainty in the binary fraction of sub-stellar objects. The sample of potential binaries identified in Chapter 3 can be used to put

stronger constraints on the binary fraction in the L-T transition. The binary candidates presented here are in fact selected in an homogeneous way and from a photometrically complete, magnitude limited, large sample. However we need to assess the contamination from peculiar objects, and the only robust way to do it is to follow-up the binary candidates. High-resolution imaging or radial velocity monitoring can reveal whether these are real binaries or not. Multiple systems are not only important to constrain the luminosity function, but are also precious benchmark systems, as they can lead to dynamical mass measurements (via astrometric monitoring, e.g. Dupuy et al., 2009) and radii measurements (if they form eclipsing pairs Stassun et al., 2006). Direct measurements of both quantities are fundamental to test evolutionary models.

According to the proverb "it is the exception that proves the rule", peculiar objects like ULAS J2227114−004547 are often the key to improve our understanding of the atmospheric physics of sub-stellar objects. While the preliminary constraints on the grain size derived in Chapter 5 and Marocco et al. (2014) are still rough estimates and potentially affected by a number of systematics, the important point to take away is that variations in the dust opacity (i.e. in the dust content) can account almost entirely for differences between red and blue extremes of a given spectral class. This somewhat diminishes the role of CIA, traditionally retained as the primary responsible for the suppression/enhancement of the H and K band flux in L and T dwarfs. Moreover, the surprisingly good results obtained with the de-reddening method, suggest that the dust clouds in peculiar red objects are predominantly located in the high layers of the photosphere. Improved kinematics for ULAS J2227114−004547 could help understand better its nature, by possibly placing it into one of the nearby young clusters. That would determine whether the increased dust opacity is a consequence of reduced surface gravity, or if the reason has to be found somewhere else, possibly in an enhanced metal content of the photosphere.

With the full exploitation of present surveys, and new facilities like SPHERE and GPI, sub-stellar astrophysics is constantly progressing towards the solution of its remaining open questions, by revealing larger and larger populations of L, T, and Y dwarfs. New optical and near-infrared spectrographs like CARMENES, ESPRESSO, and SPIRou will allow us to characterize the atmospheres of brown dwarf and giant exoplanets in further details, allowing a more in-depth analysis of the complex physics and chemistry in ultra-cool atmospheres. The already mentioned ESA/Gaia mission will provide extremely precise astrometry for thousands of L dwarfs, allowing not only for a better calibrations of the absolute magnitude sequence, but also finding literally thousands of binaries and members of moving groups (i.e. benchmark systems) through the comparison of stellar kinematics and those of brown dwarfs seen, and also not seen by Gaia but observed in ground surveys.

On the theoretical side, atmospheric models are becoming more and more accurate, and model grids are exploring a larger parameter space, partly thanks to the constant progress in computer power, but also thanks to the inclusion in the calculations of new, more complete molecular databases like ExoMol.

Further ahead in the future, LSST, E-ELT, GMT and JWST will constitute another giant leap forward, probing the sky to deeper magnitudes and therefore pushing the boundaries of our observations down to even fainter objects, allowing the direct imaging of the coldest constituents of the brown dwarf and exoplanets population.

# References


Abel, M. & Frommhold, L. 2013, Canadian Journal of Physics, 91, 857 [ADS]

Ackerman, A. S. & Marley, M. S. 2001, ApJ, 556, 872 [ADS]

Ahmic, M., Jayawardhana, R., Brandeker, A., Scholz, A., van Kerkwijk, M. H., Delgado-Donate, E., & Froebrich, D. 2007, ApJ, 671, 2074 [ADS]

Allard, F., Hauschildt, P. H., Alexander, D. R., & Starrfield, S. 1997, ARA&A, 35, 137 [ADS]

Allard, F., Hauschildt, P. H., Alexander, D. R., Tamanai, A., & Schweitzer, A. 2001, ApJ, 556, 357 [ADS]

Allard, F., Homeier, D., & Freytag, B. 2011, in Astronomical Society of the Pacific Conference Series, Vol. 448, 16th Cambridge Workshop on Cool Stars, Stellar Systems, and the Sun, 91 [ADS]

Allen, P. R., Koerner, D. W., Reid, I. N., & Trilling, D. E. 2005, ApJ, 625, 385 [ADS]

Allers, K. N. & Liu, M. C. 2013, ApJ, 772, 79 [ADS]

Alves de Oliveira, C. 2013, Mem. Soc. Astron. Italiana, 84, 905 [ADS]

Alves de Oliveira, C., Ábrahám, P., Marton, G., Pinte, C., Kiss, C., Kun, M., Kóspál, Á., André, P., & Könyves, V. 2013, A&A, 559, A126 [ADS]

Alves de Oliveira, C., Moraux, E., Bouvier, J., & Bouy, H. 2012, A&A, 539, A151 [ADS]

André, P., Ward-Thompson, D., & Greaves, J. 2012, Science, 337, 69 [ADS]

Andrei, A. H., Smart, R. L., Penna, J. L., d'Avila, V. A., Bucciarelli, B., Camargo, J. I. B., Crosta, M. T., Daprà, M., Goldman, B., Jones, H. R. A., Lattanzi, M. G., Nicastro, L., Pinfield, D. J., da Silva Neto, D. N., & Teixeira, R. 2011, AJ, 141, 54 [ADS]

Andrews, S. K., Kelvin, L. S., Driver, S. P., & Robotham, A. S. G. 2014, PASA, 31, 4 [ADS]

Bakos, G. Á., Sahu, K. C., & Németh, P. 2002, ApJS, 141, 187 [ADS]

Baraffe, I. 2010, Highlights of Astronomy, 15, 755 [ADS]

Baraffe, I., Chabrier, G., Allard, F., & Hauschildt, P. H. 1998, A&A, 337, 403 [ADS]

Baraffe, I., Chabrier, G., Barman, T. S., Allard, F., & Hauschildt, P. H. 2003, A&A, 402, 701 [ADS]

Barman, T. S., Macintosh, B., Konopacky, Q. M., & Marois, C. 2011, ApJ, 735, L39 [ADS]

Basri, G., Marcy, G. W., & Graham, J. R. 1996, ApJ, 458, 600 [ADS]

Basri, G. & Reiners, A. 2006, AJ, 132, 663 [ADS]

Bastian, N., Covey, K. R., & Meyer, M. R. 2010, ARA&A, 48, 339 [ADS]

Bate, M. R. 2012, MNRAS, 419, 3115 [ADS]

—. 2014, ArXiv e-prints [ADS]

Bate, M. R., Bonnell, I. A., & Bromm, V. 2002, MNRAS, 332, L65 [ADS]

—. 2003, MNRAS, 339, 577 [ADS]

Becklin, E. E. & Zuckerman, B. 1988, Nature, 336, 656 [ADS]

Bensby, T., Feltzing, S., & Lundström, I. 2003, A&A, 410, 527 [ADS]

Bertin, E. & Arnouts, S. 1996, A&AS, 117, 393 [ADS]

Bessell, M. S. 1995, PASP, 107, 672 [ADS]

Beuzit, J.-L., Ségransan, D., Forveille, T., Udry, S., Delfosse, X., Mayor, M., Perrier, C., Hainaut, M.-C., Roddier, C., Roddier, F., & Martín, E. L. 2004, A&A, 425, 997 [ADS]

Boffin, H. M. J., Watkins, S. J., Bhattal, A. S., Francis, N., & Whitworth, A. P. 1998, MNRAS, 300, 1189 [ADS]

Bohren, C. F. & Huffman, D. R. 1983, Absorption and scattering of light by small particles (John Wiley & Sons) [ADS]

Borysow, A., Jorgensen, U. G., & Zheng, C. 1997, A&A, 324, 185 [ADS]

Bouy, H., Brandner, W., Martín, E. L., Delfosse, X., Allard, F., & Basri, G. 2003, AJ, 126, 1526 [ADS]

Bouy, H., Martín, E. L., Brandner, W., Forveille, T., Delfosse, X., Huélamo, N., Basri, G., Girard, J., Zapatero Osorio, M.-R., Stumpf, M., Ghez, A., Valdivielso, L., Marchis, F., Burgasser, A. J., & Cruz, K. 2008, A&A, 481, 757 [ADS]

Bowler, B. P., Liu, M. C., & Dupuy, T. J. 2010, ApJ, 710, 45 [ADS]

Bowler, B. P., Liu, M. C., Shkolnik, E. L., & Dupuy, T. J. 2013, ApJ, 774, 55 [ADS]

Burgasser, A. J. 2001, PhD thesis, Department of Physics, California Institute of Technology [ADS]

—. 2004, ApJS, 155, 191 [ADS]

—. 2013, Astronomische Nachrichten, 334, 32 [ADS]

Burgasser, A. J., Cruz, K. L., Cushing, M., Gelino, C. R., Looper, D. L., Faherty, J. K., Kirkpatrick, J. D., & Reid, I. N. 2010, ApJ, 710, 1142 [ADS]

Burgasser, A. J., Geballe, T. R., Leggett, S. K., Kirkpatrick, J. D., & Golimowski, D. A. 2006a, ApJ, 637, 1067 [ADS]

Burgasser, A. J., Kirkpatrick, J. D., Burrows, A., Liebert, J., Reid, I. N., Gizis, J. E., McGovern, M. R., Prato, L., & McLean, I. S. 2003a, ApJ, 592, 1186 [ADS]

Burgasser, A. J., Kirkpatrick, J. D., Cruz, K. L., Reid, I. N., Leggett, S. K., Liebert, J., Burrows, A., & Brown, M. E. 2006b, ApJS, 166, 585 [ADS]

Burgasser, A. J., Kirkpatrick, J. D., Cutri, R. M., McCallon, H., Kopan, G., Gizis, J. E., Liebert, J., Reid, I. N., Brown, M. E., Monet, D. G., Dahn, C. C., Beichman, C. A., & Skrutskie, M. F. 2000, ApJ, 531, L57 [ADS]

Burgasser, A. J., Kirkpatrick, J. D., Liebert, J., & Burrows, A. 2003b, ApJ, 594, 510 [ADS]

Burgasser, A. J., Kirkpatrick, J. D., Reid, I. N., Brown, M. E., Miskey, C. L., & Gizis, J. E. 2003c, ApJ, 586, 512 [ADS]

Burgasser, A. J., Marley, M. S., Ackerman, A. S., Saumon, D., Lodders, K., Dahn, C. C., Harris, H. C., & Kirkpatrick, J. D. 2002, ApJ, 571, L151 [ADS]

Burgasser, A. J., Reid, I. N., Siegler, N., Close, L., Allen, P., Lowrance, P., & Gizis, J. 2007, Protostars and Planets V, 427 [ADS]

Burgasser, A. J., Sheppard, S. S., & Luhman, K. L. 2013, ApJ, 772, 129 [ADS]

Burningham, B., Cardoso, C. V., Smith, L., Leggett, S. K., Smart, R. L., Mann, A. W., Dhital, S., Lucas, P. W., Tinney, C. G., Pinfield, D. J., Zhang, Z., Morley, C., Saumon, D., Aller, K., Littlefair, S. P., Homeier, D., Lodieu, N., Deacon, N., Marley, M. S., van Spaandonk, L., Baker, D., Allard, F., Andrei, A. H., Canty, J., Clarke, J., Day-Jones, A. C., Dupuy, T., Fortney, J. J., Gomes, J., Ishii, M., Jones, H. R. A., Liu, M., Magazzú, A., Marocco, F., Murray, D. N., Rojas-Ayala, B., & Tamura, M. 2013, MNRAS, 433, 457 [ADS]

Burningham, B., Leggett, S. K., Homeier, D., Saumon, D., Lucas, P. W., Pinfield, D. J., Tinney, C. G., Allard, F., Marley, M. S., Jones, H. R. A., Murray, D. N., Ishii, M., Day-Jones, A., Gomes, J., & Zhang, Z. H. 2011, MNRAS, 414, 3590 [ADS]

Burningham, B., Leggett, S. K., Lucas, P. W., Pinfield, D. J., Smart, R. L., Day-Jones, A. C., Jones, H. R. A., Murray, D., Nickson, E., Tamura, M., Zhang, Z., Lodieu, N., Tinney, C. G., & Osorio, M. R. Z. 2010a, MNRAS, 404, 1952 [ADS]

Burningham, B., Pinfield, D. J., Leggett, S. K., Tamura, M., Lucas, P. W., Homeier, D., Day-Jones, A., Jones, H. R. A., Clarke, J. R. A., Ishii, M., Kuzuhara, M., Lodieu, N., Zapatero Osorio, M. R., Venemans, B. P., Mortlock, D. J., Barrado Y Navascués, D., Martin, E. L., & Magazzù, A. 2008, MNRAS, 391, 320 [ADS]

Burningham, B., Pinfield, D. J., Leggett, S. K., Tinney, C. G., Liu, M. C., Homeier, D., West, A. A., Day-Jones, A., Huelamo, N., Dupuy, T. J., Zhang, Z., Murray, D. N., Lodieu, N., Barrado Y Navascués, D., Folkes, S., Galvez-Ortiz, M. C., Jones, H. R. A., Lucas, P. W., Calderon, M. M., & Tamura, M. 2009, MNRAS, 395, 1237 [ADS]

Burningham, B., Pinfield, D. J., Lucas, P. W., Leggett, S. K., Deacon, N. R., Tamura, M., Tinney, C. G., Lodieu, N., Zhang, Z. H., Huelamo, N., Jones, H. R. A., Murray, D. N., Mortlock, D. J., Patel, M., Barrado Y Navascués, D., Zapatero Osorio, M. R., Ishii, M., Kuzuhara, M., & Smart, R. L. 2010b, MNRAS, 406, 1885 [ADS]

Burningham, B., Smith, L., Cardoso, C. V., Lucas, P. W., Burgasser, A. J., Jones, H. R. A., & Smart, R. L. 2014, ArXiv e-prints [ADS]

Burrows, A., Heng, K., & Nampaisarn, T. 2011, ApJ, 736, 47 [ADS]

Burrows, A., Hubbard, W. B., Lunine, J. I., & Liebert, J. 2001, Reviews of Modern Physics, 73, 719 [ADS]

Burrows, A., Hubbard, W. B., Saumon, D., & Lunine, J. I. 1993, ApJ, 406, 158 [ADS]

Burrows, A., Marley, M., Hubbard, W. B., Lunine, J. I., Guillot, T., Saumon, D., Freedman, R., Sudarsky, D., & Sharp, C. 1997, ApJ, 491, 856 [ADS]

Burrows, A. & Sharp, C. M. 1999, ApJ, 512, 843 [ADS]

Burrows, A., Sudarsky, D., & Hubeny, I. 2006, ApJ, 640, 1063 [ADS]

Burrows, A., Sudarsky, D., & Lunine, J. I. 2003, ApJ, 596, 587 [ADS]

Burrows, A. & Volobuyev, M. 2003, ApJ, 583, 985 [ADS]

Caballero, J. A. 2009, in American Institute of Physics Conference Series, Vol. 1094, 15th Cambridge Workshop on Cool Stars, Stellar Systems, and the Sun, 912–915 [ADS]

Cardelli, J. A., Clayton, G. C., & Mathis, J. S. 1989, ApJ, 345, 245 [ADS]

Carpenter, J. M. 2001, AJ, 121, 2851 [ADS]

Casewell, S. L., Dobbie, P. D., Hodgkin, S. T., Moraux, E., Jameson, R. F., Hambly, N. C., Irwin, J., & Lodieu, N. 2007, MNRAS, 378, 1131 [ADS]

Chabrier, G. 2001, ApJ, 554, 1274 [ADS]

—. 2002, ApJ, 567, 304 [ADS]

Chabrier, G. 2005, in Astrophysics and Space Science Library, Vol. 327, The Initial Mass Function 50 Years Later, 41 [ADS]

Chabrier, G. & Baraffe, I. 2000, ARA&A, 38, 337 [ADS]

Chabrier, G., Baraffe, I., Allard, F., & Hauschildt, P. 2000, ApJ, 542, 464 [ADS]

Chabrier, G., Johansen, A., Janson, M., & Rafikov, R. 2014, ArXiv e-prints [ADS]

Chauvin, G., Lagrange, A.-M., Dumas, C., Zuckerman, B., Mouillet, D., Song, I., Beuzit, J.-L., & Lowrance, P. 2004, A&A, 425, L29 [ADS]

Chiu, K., Fan, X., Leggett, S. K., Golimowski, D. A., Zheng, W., Geballe, T. R., Schneider, D. P., & Brinkmann, J. 2006, AJ, 131, 2722 [ADS]

Choi, J.-Y., Shin, I.-G., Han, C., Udalski, A., Sumi, T., Gould, A., Bozza, V., Dominik, M., Fouqué, P., Horne, K., Szymański, M. K., Kubiak, M., Soszyński, I., Pietrzyński, G., Poleski, R., Ulaczyk, K., Pietrukowicz, P., Kozłowski, S., Skowron, J., Wyrzykowski, Ł., OGLE Collaboration, Abe, F., Bennett, D. P., Bond, I. A., Botzler, C. S., Chote, P., Freeman, M., Fukui, A., Furusawa, K., Itow, Y., Kobara, S., Ling, C. H., Masuda, K., Matsubara, Y., Miyake, N., Muraki, Y., Ohmori, K., Ohnishi, K., Rattenbury, N. J., Saito, T., Sullivan, D. J., Suzuki, D., Suzuki, K., Sweatman, W. L., Takino, S., Tristram, P. J., Wada, K., Yock, P. C. M., MOA Collaboration, Bramich, D. M., Snodgrass, C., Steele, I. A., Street, R. A., Tsapras, Y., RoboNet Collaboration, Alsubai, K. A., Browne, P., Burgdorf, M. J., Calchi Novati, S., Dodds, P., Dreizler, S., Fang, X.-S., Grundahl, F., Gu, C.-H., Hardis, S., Harpsøe, K., Hinse, T. C., Hornstrup, A., Hundertmark, M., Jessen-Hansen, J., Jørgensen, U. G., Kains, N., Kerins, E., Liebig, C., Lund, M., Lunkkvist, M., Mancini, L., Mathiasen, M., Penny, M. T., Rahvar, S., Ricci, D., Scarpetta, G., Skottfelt, J., Southworth, J., Surdej, J., Tregloan-Reed, J., Wambsganss, J., Wertz, O., MiNDSTEp Consortium, Almeida, L. A., Batista, V., Christie, G., DePoy, D. L., Dong, S., Gaudi, B. S., Henderson, C., Jablonski, F., Lee, C.-U., McCormick, J., McGregor, D., Moorhouse, D., Natusch, T., Ngan, H., Pogge, R. W., Tan, T.-G., Thornley, G., Yee, J. C., $\mu$FUN Collaboration, Albrow, M. D., Bachelet, E., Beaulieu, J.-P., Brillant, S., Cassan, A., Cole, A. A., Corrales, E., Coutures, C., Dieters, S., Dominis Prester, D., Donatowicz, J., Greenhill, J., Kubas, D., Marquette, J.-B., Menzies, J. W., Sahu, K. C., Zub, M., & PLANET Collaboration. 2012, ApJ, 756, 48 [ADS]

Cignoni, M., Degl'Innocenti, S., Prada Moroni, P. G., & Shore, S. N. 2006, A&A, 459, 783 [ADS]

Clarke, J. R. A., Pinfield, D. J., Gálvez-Ortiz, M. C., Jenkins, J. S., Burningham, B., Deacon, N. R., Jones, H. R. A., Pokorny, R. S., Barnes, J. R., & Day-Jones, A. C. 2010, MNRAS, 402, 575 [ADS]

Cruz, K. L., Kirkpatrick, J. D., & Burgasser, A. J. 2009, AJ, 137, 3345 [ADS]

Cruz, K. L., Reid, I. N., Kirkpatrick, J. D., Burgasser, A. J., Liebert, J., Solomon, A. R., Schmidt, S. J., Allen, P. R., Hawley, S. L., & Covey, K. R. 2007, AJ, 133, 439 [ADS]

Cruz, K. L., Reid, I. N., Liebert, J., Kirkpatrick, J. D., & Lowrance, P. J. 2003, AJ, 126, 2421 [ADS]

Cushing, M. C., Kirkpatrick, J. D., Gelino, C. R., Griffith, R. L., Skrutskie, M. F., Mainzer, A., Marsh, K. A., Beichman, C. A., Burgasser, A. J., Prato, L. A., Simcoe, R. A., Marley, M. S., Saumon, D., Freedman, R. S., Eisenhardt, P. R., & Wright, E. L. 2011, ApJ, 743, 50 [ADS]

Cushing, M. C., Marley, M. S., Saumon, D., Kelly, B. C., Vacca, W. D., Rayner, J. T., Freedman, R. S., Lodders, K., & Roellig, T. L. 2008, ApJ, 678, 1372 [ADS]

Cushing, M. C., Rayner, J. T., & Vacca, W. D. 2005, ApJ, 623, 1115 [ADS]

Dahn, C. C., Harris, H. C., Vrba, F. J., Guetter, H. H., Canzian, B., Henden, A. A., Levine, S. E., Luginbuhl, C. B., Monet, A. K. B., Monet, D. G., Pier, J. R., Stone, R. C., Walker, R. L., Burgasser, A. J., Gizis, J. E., Kirkpatrick, J. D., Liebert, J., & Reid, I. N. 2002, AJ, 124, 1170 [ADS]

Day-Jones, A. C., Marocco, F., Pinfield, D. J., Zhang, Z. H., Burningham, B., Deacon, N., Ruiz, M. T., Gallardo, J., Jones, H. R. A., Lucas, P. W. L., Jenkins, J. S., Gomes, J., Folkes, S. L., & Clarke, J. R. A. 2013, MNRAS, 430, 1171 [ADS]

Day-Jones, A. C., Pinfield, D. J., Napiwotzki, R., Burningham, B., Jenkins, J. S., Jones, H. R. A., Folkes, S. L., Weights, D. J., & Clarke, J. R. A. 2008, MNRAS, 388, 838 [ADS]

Day-Jones, A. C., Pinfield, D. J., Ruiz, M. T., Beaumont, H., Burningham, B., Gallardo, J., Gianninas, A., Bergeron, P., Napiwotzki, R., Jenkins, J. S., Zhang, Z. H., Murray, D. N., Catalán, S., & Gomes, J. 2011, MNRAS, 410, 705 [ADS]

de Bruijne, J. H. J. 1999, MNRAS, 306, 381 [ADS]

Deacon, N. R. & Hambly, N. C. 2006, MNRAS, 371, 1722 [ADS]

—. 2007, A&A, 468, 163 [ADS]

Deacon, N. R., Nelemans, G., & Hambly, N. C. 2008, A&A, 486, 283 [ADS]

Delfosse, X., Forveille, T., Beuzit, J.-L., Udry, S., Mayor, M., & Perrier, C. 1999a, A&A, 344, 897 [ADS]

Delfosse, X., Tinney, C. G., Forveille, T., Epchtein, N., Borsenberger, J., Fouqué, P., Kimeswenger, S., & Tiphène, D. 1999b, A&AS, 135, 41 [ADS]

Delgado-Donate, E. J., Clarke, C. J., & Bate, M. R. 2003, MNRAS, 342, 926 [ADS]

Delorme, P., Delfosse, X., Albert, L., Artigau, E., Forveille, T., Reylé, C., Allard, F., Homeier, D., Robin, A. C., Willott, C. J., Liu, M. C., & Dupuy, T. J. 2008a, A&A, 482, 961 [ADS]

Delorme, P., Gagné, J., Girard, J. H., Lagrange, A. M., Chauvin, G., Naud, M.-E., Lafrenière, D., Doyon, R., Riedel, A., Bonnefoy, M., & Malo, L. 2013, A&A, 553, L5 [ADS]

Delorme, P., Gagné, J., Malo, L., Reylé, C., Artigau, E., Albert, L., Forveille, T., Delfosse, X., Allard, F., & Homeier, D. 2012a, A&A, 548, A26 [ADS]

Delorme, P., Lagrange, A. M., Chauvin, G., Bonavita, M., Lacour, S., Bonnefoy, M., Ehrenreich, D., & Beust, H. 2012b, A&A, 539, A72 [ADS]

Delorme, P., Willott, C. J., Forveille, T., Delfosse, X., Reylé, C., Bertin, E., Albert, L., Artigau, E., Robin, A. C., Allard, F., Doyon, R., & Hill, G. J. 2008b, A&A, 484, 469 [ADS]

Dieterich, S. B., Henry, T. J., Jao, W.-C., Winters, J. G., Hosey, A. D., Riedel, A. R., & Subasavage, J. P. 2014, AJ, 147, 94 [ADS]

Dorschner, J., Begemann, B., Henning, T., Jaeger, C., & Mutschke, H. 1995, A&A, 300, 503 [ADS]

Dupuy, T. J. & Liu, M. C. 2011, ApJ, 733, 122 [ADS]

—. 2012, ApJS, 201, 19 [ADS]

Dupuy, T. J., Liu, M. C., & Ireland, M. J. 2009, ApJ, 692, 729 [ADS]

Emerson, J. P. & Sutherland, W. 2002, in Society of Photo-Optical Instrumentation Engineers (SPIE) Conference Series, Vol. 4836, Survey and Other Telescope Technologies and Discoveries, 35–42 [ADS]

Epchtein, N., Deul, E., Derriere, S., Borsenberger, J., Egret, D., Simon, G., Alard, C., Balázs, L. G., de Batz, B., Cioni, M.-R., Copet, E., Dennefeld, M., Forveille, T., Fouqué, P., Garzón, F., Habing, H. J., Holl, A., Hron, J., Kimeswenger, S., Lacombe, F., Le Bertre, T., Loup, C., Mamon, G. A., Omont, A., Paturel, G., Persi, P., Robin, A. C., Rouan, D., Tiphène, D., Vauglin, I., & Wagner, S. J. 1999, A&A, 349, 236 [ADS]

EROS Collaboration, Goldman, B., Delfosse, X., Forveille, T., Afonso, C., Alard, C., Albert, J. N., Andersen, J., Ansari, R., Aubourg, É., Bareyre, P., Bauer, F., Beaulieu, J. P., Borsenberger, J., Bouquet, A., Char, S., Charlot, X., Couchot, F., Coutures, C., Derue, F., Ferlet, R., Fouqué, P., Glicenstein, J. F., Gould, A., Graff, D., Gros, M., Haissinski, J., Hamilton, J. C., Hardin, D., de Kat, J., Kim, A., Lasserre, T., Lesquoy, É., Loup, C., Magneville, C., Mansoux, B., Marquette, J. B., Martín, E. L., Maurice, É., Milsztajn, A., Moniez, M., Palanque-Delabrouille, N., Perdereau, O., Prévot, L., Regnault, N., Rich, J., Spiro, M., Vidal-Madjar, A., Vigroux, L., & Zylberajch, S. 1999, A&A, 351, L5 [ADS]

Faherty, J. K., Burgasser, A. J., Cruz, K. L., Shara, M. M., Walter, F. M., & Gelino, C. R. 2009, AJ, 137, 1 [ADS]

Faherty, J. K., Burgasser, A. J., Walter, F. M., Van der Bliek, N., Shara, M. M., Cruz, K. L., West, A. A., Vrba, F. J., & Anglada-Escudé, G. 2012, ApJ, 752, 56 [ADS]

Faherty, J. K., Burgasser, A. J., West, A. A., Bochanski, J. J., Cruz, K. L., Shara, M. M., & Walter, F. M. 2010, AJ, 139, 176 [ADS]

Faherty, J. K., Cruz, K. L., Rice, E. L., & Riedel, A. 2013a, Mem. Soc. Astron. Italiana, 84, 955 [ADS]

Faherty, J. K., Rice, E. L., Cruz, K. L., Mamajek, E. E., & Núñez, A. 2013b, AJ, 145, 2 [ADS]

Fan, X., Knapp, G. R., Strauss, M. A., Gunn, J. E., Lupton, R. H., Ivezić, Ž., Rockosi, C. M., Yanny, B., Kent, S., Schneider, D. P., Kirkpatrick, J. D., Annis, J., Bastian, S., Berman, E., Brinkmann, J., Csabai, I., Federwitz, G. R., Fukugita, M., Gurbani, V. K., Hennessy, G. S., Hindsley, R. B., Ichikawa, T., Lamb, D. Q., Lindenmeyer, C., Mantsch, P. M., McKay, T. A., Munn, J. A., Nash, T., Okamura, S., Pauls, A. G., Pier, J. R., Rechenmacher, R., Rivetta, C. H., Sergey, G., Stoughton, C., Szalay, A. S., Szokoly, G. P., Tucker, D. L., York, D. G., & SDSS Collaboration. 2000, AJ, 119, 928 [ADS]

Finch, C. T., Henry, T. J., Subasavage, J. P., Jao, W.-C., & Hambly, N. C. 2007, AJ, 133, 2898 [ADS]

Fitzpatrick, E. L. 1999, PASP, 111, 63 [ADS]

Fortney, J. J., Baraffe, I., & Militzer, B. 2011, Giant Planet Interior Structure and Thermal Evolution, 397–418 [ADS]

Fraunhofer, J. 1817, Annalen der Physik, 56, 282

Frommhold, L. 2006, Collision-induced Absorption in Gases [ADS]

Gagné, J., Lafrenière, D., Doyon, R., Malo, L., & Artigau, É. 2014, ApJ, 783, 121 [ADS]

Gálvez-Ortiz, M. C., Clarke, J. R. A., Pinfield, D. J., Jenkins, J. S., Folkes, S. L., Pérez, A. E. G., Day-Jones, A. C., Burningham, B., Jones, H. R. A., Barnes, J. R., & Pokorny, R. S. 2010, MNRAS, 409, 552 [ADS]

Geballe, T. R., Knapp, G. R., Leggett, S. K., Fan, X., Golimowski, D. A., Anderson, S., Brinkmann, J., Csabai, I., Gunn, J. E., Hawley, S. L., Hennessy, G., Henry, T. J., Hill, G. J., Hindsley, R. B., Ivezić, Ž., Lupton, R. H., McDaniel, A., Munn, J. A., Narayanan, V. K., Peng, E., Pier, J. R., Rockosi, C. M., Schneider, D. P., Smith, J. A., Strauss, M. A., Tsvetanov, Z. I., Uomoto, A., York, D. G., & Zheng, W. 2002, ApJ, 564, 466 [ADS]

Gizis, J. E. 2002, ApJ, 575, 484 [ADS]

Gizis, J. E., Faherty, J. K., Liu, M. C., Castro, P. J., Shaw, J. D., Vrba, F. J., Harris, H. C., Aller, K. M., & Deacon, N. R. 2012, AJ, 144, 94 [ADS]

Gizis, J. E., Monet, D. G., Reid, I. N., Kirkpatrick, J. D., Liebert, J., & Williams, R. J. 2000, Astron. J., 120, 1085

Gizis, J. E., Reid, I. N., Knapp, G. R., Liebert, J., Kirkpatrick, J. D., Koerner, D. W., & Burgasser, A. J. 2003, AJ, 125, 3302 [ADS]

Golimowski, D. A., Leggett, S. K., Marley, M. S., Fan, X., Geballe, T. R., Knapp, G. R., Vrba, F. J., Henden, A. A., Luginbuhl, C. B., Guetter, H. H., Munn, J. A., Canzian, B., Zheng, W., Tsvetanov, Z. I., Chiu, K., Glazebrook, K., Hoversten, E. A., Schneider, D. P., & Brinkmann, J. 2004, AJ, 127, 3516 [ADS]

Gomes, J. I., Pinfield, D. J., Marocco, F., Day-Jones, A. C., Burningham, B., Zhang, Z. H., Jones, H. R. A., Spaandonk, L. v., & Weights, D. 2013, MNRAS, 431, 2745 [ADS]

Gorlova, N. I., Meyer, M. R., Rieke, G. H., & Liebert, J. 2003, ApJ, 593, 1074 [ADS]

Grether, D. & Lineweaver, C. H. 2006, ApJ, 640, 1051 [ADS]

Grossman, A. S. 1970, ApJ, 161, 619 [ADS]

Grossman, A. S., Mutschlecner, J. P., & Pauls, T. A. 1970, ApJ, 162, 613 [ADS]

Guenther, E. W. & Wuchterl, G. 2003, A&A, 401, 677 [ADS]

Hawley, S. L., Covey, K. R., Knapp, G. R., Golimowski, D. A., Fan, X., Anderson, S. F., Gunn, J. E., Harris, H. C., Ivezić, Ž., Long, G. M., Lupton, R. H., McGehee, P. M., Narayanan, V., Peng, E., Schlegel, D., Schneider, D. P., Spahn, E. Y., Strauss, M. A., Szkody, P., Tsvetanov, Z., Walkowicz, L. M., Brinkmann, J., Harvanek, M., Hennessy, G. S., Kleinman, S. J., Krzesinski, J., Long, D., Neilsen, E. H., Newman, P. R., Nitta, A., Snedden, S. A., & York, D. G. 2002, AJ, 123, 3409 [ADS]

Hayashi, C. & Nakano, T. 1963, Progress of Theoretical Physics, 30, 460 [ADS]

Hearnshaw, J. B. 1986, The analysis of starlight: One hundred and fifty years of astronomical spectroscopy (Cambridge and New York: Cambridge University Press) [ADS]

Helling, C., Ackerman, A., Allard, F., Dehn, M., Hauschildt, P., Homeier, D., Lodders, K., Marley, M., Rietmeijer, F., Tsuji, T., & Woitke, P. 2008, MNRAS, 391, 1854 [ADS]

Hewett, P. C., Warren, S. J., Leggett, S. K., & Hodgkin, S. T. 2006, MNRAS, 367, 454 [ADS]

Heyer, M., Krawczyk, C., Duval, J., & Jackson, J. M. 2009, ApJ, 699, 1092 [ADS]

Howard, A. W., Marcy, G. W., Johnson, J. A., Fischer, D. A., Wright, J. T., Isaacson, H., Valenti, J. A., Anderson, J., Lin, D. N. C., & Ida, S. 2010, Science, 330, 653 [ADS]

Hubbard, W. B. 1977, Icarus, 30, 305 [ADS]

Jao, W.-C., Henry, T. J., Subasavage, J. P., Brown, M. A., Ianna, P. A., Bartlett, J. L., Costa, E., & Méndez, R. A. 2005, AJ, 129, 1954 [ADS]

Joergens, V. 2006, A&A, 446, 1165 [ADS]

—. 2008, A&A, 492, 545 [ADS]

Joergens, V. & Guenther, E. 2001, A&A, 379, L9 [ADS]

Kendall, T. R., Jones, H. R. A., Pinfield, D. J., Pokorny, R. S., Folkes, S., Weights, D., Jenkins, J. S., & Mauron, N. 2007, MNRAS, 374, 445 [ADS]

Kirkpatrick, J. D. 2005, ARA&A, 43, 195 [ADS]

Kirkpatrick, J. D., Barman, T. S., Burgasser, A. J., McGovern, M. R., McLean, I. S., Tinney, C. G., & Lowrance, P. J. 2006, ApJ, 639, 1120 [ADS]

Kirkpatrick, J. D., Cruz, K. L., Barman, T. S., Burgasser, A. J., Looper, D. L., Tinney, C. G., Gelino, C. R., Lowrance, P. J., Liebert, J., Carpenter, J. M., Hillenbrand, L. A., & Stauffer, J. R. 2008, ApJ, 689, 1295 [ADS]

Kirkpatrick, J. D., Cushing, M. C., Gelino, C. R., Griffith, R. L., Skrutskie, M. F., Marsh, K. A., Wright, E. L., Mainzer, A., Eisenhardt, P. R., McLean, I. S., Thompson, M. A., Bauer, J. M., Benford, D. J., Bridge, C. R., Lake, S. E., Petty, S. M., Stanford, S. A., Tsai, C.-W., Bailey, V., Beichman, C. A., Bloom, J. S., Bochanski, J. J., Burgasser, A. J., Capak, P. L., Cruz, K. L., Hinz, P. M., Kartaltepe, J. S.,

Knox, R. P., Manohar, S., Masters, D., Morales-Calderón, M., Prato, L. A., Rodigas, T. J., Salvato, M., Schurr, S. D., Scoville, N. Z., Simcoe, R. A., Stapelfeldt, K. R., Stern, D., Stock, N. D., & Vacca, W. D. 2011, ApJS, 197, 19 [ADS]

Kirkpatrick, J. D., Gelino, C. R., Cushing, M. C., Mace, G. N., Griffith, R. L., Skrutskie, M. F., Marsh, K. A., Wright, E. L., Eisenhardt, P. R., McLean, I. S., Mainzer, A. K., Burgasser, A. J., Tinney, C. G., Parker, S., & Salter, G. 2012, ApJ, 753, 156 [ADS]

Kirkpatrick, J. D., Henry, T. J., & Liebert, J. 1993, ApJ, 406, 701 [ADS]

Kirkpatrick, J. D., Looper, D. L., Burgasser, A. J., Schurr, S. D., Cutri, R. M., Cushing, M. C., Cruz, K. L., Sweet, A. C., Knapp, G. R., Barman, T. S., Bochanski, J. J., Roellig, T. L., McLean, I. S., McGovern, M. R., & Rice, E. L. 2010, ApJS, 190, 100 [ADS]

Kirkpatrick, J. D., Reid, I. N., Liebert, J., Cutri, R. M., Nelson, B., Beichman, C. A., Dahn, C. C., Monet, D. G., Gizis, J. E., & Skrutskie, M. F. 1999, ApJ, 519, 802 [ADS]

Kirkpatrick, J. D., Reid, I. N., Liebert, J., Gizis, J. E., Burgasser, A. J., Monet, D. G., Dahn, C. C., Nelson, B., & Williams, R. J. 2000, Astron. J., 120, 447

Kirkpatrick, J. D., Schneider, A., Fajardo-Acosta, S., Gelino, C. R., Mace, G. N., Wright, E. L., Logsdon, S. E., McLean, I. S., Cushing, M. C., Skrutskie, M. F., Eisenhardt, P. R., Stern, D., Baloković, M., Burgasser, A. J., Faherty, J. K., Lansbury, G. B., Rich, J. A., Skrzypek, N., Fowler, J. W., Cutri, R. M., Masci, F. J., Conrow, T., Grillmair, C. J., McCallon, H. L., Beichman, C. A., & Marsh, K. A. 2014, ApJ, 783, 122 [ADS]

Knapp, G. R., Leggett, S. K., Fan, X., Marley, M. S., Geballe, T. R., Golimowski, D. A., Finkbeiner, D., Gunn, J. E., Hennawi, J., Ivezić, Z., Lupton, R. H., Schlegel, D. J., Strauss, M. A., Tsvetanov, Z. I., Chiu, K., Hoversten, E. A., Glazebrook, K., Zheng, W., Hendrickson, M., Williams, C. C., Uomoto, A., Vrba, F. J., Henden, A. A., Luginbuhl, C. B., Guetter, H. H., Munn, J. A., Canzian, B., Schneider, D. P., & Brinkmann, J. 2004, AJ, 127, 3553 [ADS]

Koike, C., Kaito, C., Yamamoto, T., Shibai, H., Kimura, S., & Suto, H. 1995, Icarus, 114, 203 [ADS]

Kumar, S. S. 1963, ApJ, 137, 1121 [ADS]

Kurosawa, R., Harries, T. J., & Littlefair, S. P. 2006, MNRAS, 372, 1879 [ADS]

Kurucz, R. L. 1993, IAU Commission on Close Binary Stars, 21, 93 [ADS]

La Barbera, F., Ferreras, I., Vazdekis, A., de la Rosa, I. G., de Carvalho, R. R., Trevisan, M., Falcón-Barroso, J., & Ricciardelli, E. 2013, MNRAS, 433, 3017 [ADS]

Lawrence, A., Warren, S. J., Almaini, O., Edge, A. C., Hambly, N. C., Jameson, R. F., Lucas, P., Casali, M., Adamson, A., Dye, S., Emerson, J. P., Foucaud, S., Hewett, P., Hirst, P., Hodgkin, S. T., Irwin, M. J., Lodieu, N., McMahon, R. G., Simpson, C., Smail, I., Mortlock, D., & Folger, M. 2007, MNRAS, 379, 1599 [ADS]

Leggett, S. K., Cushing, M. C., Saumon, D., Marley, M. S., Roellig, T. L., Warren, S. J., Burningham, B., Jones, H. R. A., Kirkpatrick, J. D., Lodieu, N., Lucas, P. W., Mainzer, A. K., Martín, E. L., McCaughrean, M. J., Pinfield, D. J., Sloan, G. C., Smart, R. L., Tamura, M., & Van Cleve, J. 2009, ApJ, 695, 1517 [ADS]

Leggett, S. K., Geballe, T. R., Fan, X., Schneider, D. P., Gunn, J. E., Lupton, R. H., Knapp, G. R., Strauss, M. A., McDaniel, A., Golimowski, D. A., Henry, T. J., Peng, E., Tsvetanov, Z. I., Uomoto, A., Zheng, W., Hill, G. J., Ramsey, L. W., Anderson, S. F., Annis, J. A., Bahcall, N. A., Brinkmann, J., Chen, B., Csabai, I., Fukugita, M., Hennessy, G. S., Hindsley, R. B., Ivezić, Ž., Lamb, D. Q., Munn, J. A., Pier, J. R., Schlegel, D. J., Smith, J. A., Stoughton, C., Thakar, A. R., & York, D. G. 2000, ApJ, 536, L35 [ADS]

Leggett, S. K., Saumon, D., Marley, M. S., Geballe, T. R., Golimowski, D. A., Stephens, D., & Fan, X. 2007, ApJ, 655, 1079 [ADS]

Leggett, S. K., Saumon, D., Marley, M. S., Lodders, K., Canty, J., Lucas, P., Smart, R. L., Tinney, C. G., Homeier, D., Allard, F., Burningham, B., Day-Jones, A., Fegley, B., Ishii, M., Jones, H. R. A., Marocco, F., Pinfield, D. J., & Tamura, M. 2012, ApJ, 748, 74 [ADS]

Lépine, S., Rich, R. M., & Shara, M. M. 2007, ApJ, 669, 1235 [ADS]

Li, X., Harrison, J. F., Gustafsson, M., Wang, F., Abel, M., Frommhold, L., & Hunt, K. L. C. 2012, in American Institute of Physics Conference Series, Vol. 1504, American Institute of Physics Conference Series, 100–135 [ADS]

Liebert, J., Kirkpatrick, J. D., Cruz, K. L., Reid, I. N., Burgasser, A., Tinney, C. G., & Gizis, J. E. 2003, AJ, 125, 343 [ADS]

Linsky, J. L. 1969, ApJ, 156, 989 [ADS]

Liu, M. C., Delorme, P., Dupuy, T. J., Bowler, B. P., Albert, L., Artigau, E., Reylé, C., Forveille, T., & Delfosse, X. 2011, ApJ, 740, 108 [ADS]

Liu, M. C., Leggett, S. K., & Chiu, K. 2007, ApJ, 660, 1507 [ADS]

Liu, M. C., Magnier, E. A., Deacon, N. R., Allers, K. N., Dupuy, T. J., Kotson, M. C., Aller, K. M., Burgett, W. S., Chambers, K. C., Draper, P. W., Hodapp, K. W., Jedicke, R., Kaiser, N., Kudritzki, R.-P., Metcalfe, N., Morgan, J. S., Price, P. A., Tonry, J. L., & Wainscoat, R. J. 2013, ApJ, 777, L20 [ADS]

Lodders, K. 1999, ApJ, 519, 793 [ADS]

Lodieu, N. 2013, MNRAS, 431, 3222 [ADS]

Lodieu, N., Caux, E., Monin, J.-L., & Klotz, A. 2002a, A&A, 383, L15 [ADS]

Lodieu, N., Dobbie, P. D., Cross, N. J. G., Hambly, N. C., Read, M. A., Blake, R. P., & Floyd, D. J. E. 2013, MNRAS, 435, 2474 [ADS]

Lodieu, N., Dobbie, P. D., Deacon, N. R., Hodgkin, S. T., Hambly, N. C., & Jameson, R. F. 2007, MNRAS, 380, 712 [ADS]

Lodieu, N., Dobbie, P. D., & Hambly, N. C. 2011, A&A, 527, A24 [ADS]

Lodieu, N., Hambly, N. C., Jameson, R. F., & Hodgkin, S. T. 2008, MNRAS, 383, 1385 [ADS]

Lodieu, N., Scholz, R.-D., & McCaughrean, M. J. 2002b, A&A, 389, L20 [ADS]

Lodieu, N., Scholz, R.-D., McCaughrean, M. J., Ibata, R., Irwin, M., & Zinnecker, H. 2005, A&A, 440, 1061 [ADS]

Lodieu, N., Zapatero Osorio, M. R., Rebolo, R., Martín, E. L., & Hambly, N. C. 2009, A&A, 505, 1115 [ADS]

Looper, D. L., Gelino, C. R., Burgasser, A. J., & Kirkpatrick, J. D. 2008a, ApJ, 685, 1183 [ADS]

Looper, D. L., Kirkpatrick, J. D., & Burgasser, A. J. 2007, AJ, 134, 1162 [ADS]

Looper, D. L., Kirkpatrick, J. D., Cutri, R. M., Barman, T., Burgasser, A. J., Cushing, M. C., Roellig, T., McGovern, M. R., McLean, I. S., Rice, E., Swift, B. J., & Schurr, S. D. 2008b, ApJ, 686, 528 [ADS]

Lucas, P. W. & Roche, P. F. 1998, MNRAS, 299, 699 [ADS]

Lucas, P. W., Roche, P. F., Allard, F., & Hauschildt, P. H. 2001, MNRAS, 326, 695 [ADS]

Lucas, P. W., Roche, P. F., & Tamura, M. 2005, MNRAS, 361, 211 [ADS]

Lucas, P. W., Tinney, C. G., Burningham, B., Leggett, S. K., Pinfield, D. J., Smart, R., Jones, H. R. A., Marocco, F., Barber, R. J., Yurchenko, S. N., Tennyson, J., Ishii, M., Tamura, M., Day-Jones, A. C., Adamson, A., Allard, F., & Homeier, D. 2010, MNRAS, 408, L56 [ADS]

Ludwig, H.-G., Allard, F., & Hauschildt, P. H. 2002, A&A, 395, 99 [ADS]

Luhman, K. L. 2007, ApJS, 173, 104 [ADS]

—. 2012, ARA&A, 50, 65 [ADS]

—. 2013, ApJ, 767, L1 [ADS]

Luhman, K. L., Mamajek, E. E., Allen, P. R., & Cruz, K. L. 2009, ApJ, 703, 399 [ADS]

Luhman, K. L., McLeod, K. K., & Goldenson, N. 2005, ApJ, 623, 1141 [ADS]

Ma, B. & Ge, J. 2014, MNRAS, 439, 2781 [ADS]

Madhusudhan, N., Burrows, A., & Currie, T. 2011, ApJ, 737, 34 [ADS]

Mainzer, A. K., Bauer, J., Grav, T., Masiero, J., Cutri, R. M., McMillan, R. S., Walker, R., Dailey, J., Nugent, C. R., Conrow, T., & Wright, E. 2012, in AAS/Division for Planetary Sciences Meeting Abstracts, Vol. 44, AAS/Division for Planetary Sciences Meeting Abstracts, 102.07 [ADS]

Malo, L., Artigau, É., Doyon, R., Lafrenière, D., Albert, L., & Gagné, J. 2014, ArXiv e-prints [ADS]

Malo, L., Doyon, R., Lafrenière, D., Artigau, É., Gagné, J., Baron, F., & Riedel, A. 2013, ApJ, 762, 88 [ADS]

Mamajek, E. E. 2013, ArXiv e-prints [ADS]

Marcy, G. W. & Butler, R. P. 2000, PASP, 112, 137 [ADS]

Marley, M. S., Fortney, J. J., Hubickyj, O., Bodenheimer, P., & Lissauer, J. J. 2007, ApJ, 655, 541 [ADS]

Marley, M. S., Seager, S., Saumon, D., Lodders, K., Ackerman, A. S., Freedman, R. S., & Fan, X. 2002, ApJ, 568, 335 [ADS]

Marocco, F., Andrei, A. H., Smart, R. L., Jones, H. R. A., Pinfield, D. J., Day-Jones, A. C., Clarke, J. R. A., Sozzetti, A., Lucas, P. W., Bucciarelli, B., & Penna, J. L. 2013, AJ, 146, 161 [ADS]

Marocco, F., Day-Jones, A. C., Lucas, P. W., Jones, H. R. A., Smart, R. L., Zhang, Z. H., Gomes, J. I., Burningham, B., Pinfield, D. J., Raddi, R., & Smith, L. 2014, MNRAS, 439, 372 [ADS]

Marocco, F., Smart, R. L., Jones, H. R. A., Burningham, B., Lattanzi, M. G., Leggett, S. K., Lucas, P. W., Tinney, C. G., Adamson, A., Evans, D. W., Lodieu, N., Murray, D. N., Pinfield, D. J., & Tamura, M. 2010, A&A, 524, A38 [ADS]

Marois, C., Macintosh, B., Barman, T., Zuckerman, B., Song, I., Patience, J., Lafrenière, D., & Doyon, R. 2008, Science, 322, 1348 [ADS]

Martìn, E. L. 2000, in Very Low-Mass Stars and Brown Dwarfs, 119 [ADS]

Martín, E. L., Barrado y Navascués, D., Baraffe, I., Bouy, H., & Dahm, S. 2003, ApJ, 594, 525 [ADS]

Martín, E. L., Brandner, W., Bouvier, J., Luhman, K. L., Stauffer, J., Basri, G., Zapatero Osorio, M. R., & Barrado y Navascués, D. 2000, ApJ, 543, 299 [ADS]

Martín, E. L., Brandner, W., Bouy, H., Basri, G., Davis, J., Deshpande, R., & Montgomery, M. M. 2006, A&A, 456, 253 [ADS]

Martín, E. L., Phan-Bao, N., Bessell, M., Delfosse, X., Forveille, T., Magazzù, A., Reylé, C., Bouy, H., & Tata, R. 2010, A&A, 517, A53 [ADS]

Masson, J., Teyssier, R., Mulet-Marquis, C., Hennebelle, P., & Chabrier, G. 2012, ApJS, 201, 24 [ADS]

Maxted, P. F. L. & Jeffries, R. D. 2005, MNRAS, 362, L45 [ADS]

Maxted, P. F. L., Jeffries, R. D., Oliveira, J. M., Naylor, T., & Jackson, R. J. 2008, MNRAS, 385, 2210 [ADS]

Mayor, M., Pepe, F., Queloz, D., Bouchy, F., Rupprecht, G., Lo Curto, G., Avila, G., Benz, W., Bertaux, J.-L., Bonfils, X., Dall, T., Dekker, H., Delabre, B., Eckert, W., Fleury, M., Gilliotte, A., Gojak, D., Guzman, J. C., Kohler, D., Lizon, J.-L., Longinotti, A., Lovis, C., Megevand, D., Pasquini, L., Reyes, J., Sivan, J.-P., Sosnowska, D., Soto, R., Udry, S., van Kesteren, A., Weber, L., & Weilenmann, U. 2003, The Messenger, 114, 20 [ADS]

McLean, I. S., McGovern, M. R., Burgasser, A. J., Kirkpatrick, J. D., Prato, L., & Kim, S. S. 2003, ApJ, 596, 561 [ADS]

Metchev, S. A., Kirkpatrick, J. D., Berriman, G. B., & Looper, D. 2008, ApJ, 676, 1281 [ADS]

Mihalas, D. & Binney, J. 1981, Galactic astronomy: Structure and kinematics (W. H. Freeman and Co.) [ADS]

Miller, G. E. & Scalo, J. M. 1979, ApJS, 41, 513 [ADS]

Monet, D. G., Dahn, C. C., Vrba, F. J., Harris, H. C., Pier, J. R., Luginbuhl, C. B., & Ables, H. D. 1992, Astron. J., 103, 638

Morgan, W. W., Keenan, P. C., & Kellman, E. 1943, An atlas of stellar spectra, with an outline of spectral classification [ADS]

Morley, C. V., Fortney, J. J., Marley, M. S., Visscher, C., Saumon, D., & Leggett, S. K. 2012, ApJ, 756, 172 [ADS]

Murray, D. N., Burningham, B., Jones, H. R. A., Pinfield, D. J., Lucas, P. W., Leggett, S. K., Tinney, C. G., Day-Jones, A. C., Weights, D. J., Lodieu, N., Pérez Prieto, J. A., Nickson, E., Zhang, Z. H., Clarke, J. R. A., Jenkins, J. S., & Tamura, M. 2011, MNRAS, 414, 575 [ADS]

Nakajima, T., Oppenheimer, B. R., Kulkarni, S. R., Golimowski, D. A., Matthews, K., & Durrance, S. T. 1995, Nature, 378, 463 [ADS]

Newton, I. 1705, Oticks: Or, A Treatise of the Reflections, Refractions, Inflections and Colours of Light (London: Royal Society)

Nielsen, E. L., Liu, M. C., Wahhaj, Z., Biller, B. A., Hayward, T. L., Boss, A., Bowler, B., Kraus, A., Shkolnik, E. L., Tecza, M., Chun, M., Clarke, F., Close, L. M., Ftaclas, C., Hartung, M., Males, J. R., Reid, I. N., Skemer, A. J., Alencar, S. H. P., Burrows, A., de Gouveia Dal Pino, E., Gregorio-Hetem, J., Kuchner, M., Thatte, N., & Toomey, D. W. 2012, ApJ, 750, 53 [ADS]

Nissen, P. E. 2004, Origin and Evolution of the Elements, 154 [ADS]

Noll, K. S., Geballe, T. R., Leggett, S. K., & Marley, M. S. 2000, ApJ, 541, L75 [ADS]

Oppenheimer, B. R., Kulkarni, S. R., Matthews, K., & van Kerkwijk, M. H. 1998, ApJ, 502, 932 [ADS]

Ordal, M. A., Bell, R. J., Alexander, Jr., R. W., Long, L. L., & Querry, M. R. 1985, Appl. Opt., 24, 4493 [ADS]

Padoan, P. & Nordlund, Å. 2002, ApJ, 576, 870 [ADS]

—. 2004, ApJ, 617, 559 [ADS]

Park, H., Han, C., Gould, A., Udalski, A., Sumi, T., Fouqué, P., Choi, J.-Y., Christie, G., Depoy, D. L., Dong, S., Gaudi, B. S., Hwang, K.-H., Jung, Y. K., Kavka, A., Lee, C.-U., Monard, L. A. G., Natusch, T., Ngan, H., Pogge, R. W., Shin, I.-G., Yee, J. C., The $\mu$FUN Collaboration, Szymański, M. K., Kubiak, M., Soszyński, I., Pietrzyński, G., Poleski, R., Ulaczyk, K., Pietrukowicz, P., Kozłowski, S., Skowron, J., Wyrzykowski, Ł., The OGLE Collaboration, Abe, F., Bennett, D. P., Bond, I. A., Botzler, C. S., Chote, P., Freeman, M., Fukui, A., Fukunaga, D., Harris, P., Itow, Y., Koshimoto, N., Ling, C. H., Masuda, K., Matsubara, Y., Muraki, Y., Namba, S., Ohnishi, K., Rattenbury, N. J., Saito, T., Sullivan, D. J., Sweatman, W. L., Suzuki, D., Tristram, P. J., Wada, K., Yamai, N., Yock, P. C. M., Yonehara, A., & The MOA Collaboration. 2014, ApJ, 787, 71 [ADS]

Patience, J., King, R. R., de Rosa, R. J., & Marois, C. 2010, A&A, 517, A76 [ADS]

Pearson, K. 1895, Proceedings of the Royal Society of London, 58, 240

Pinfield, D. J., Burningham, B., Lodieu, N., Leggett, S. K., Tinney, C. G., van Spaandonk, L., Marocco, F., Smart, R., Gomes, J., Smith, L., Lucas, P. W., Day-Jones, A. C., Murray, D. N., Katsiyannis, A. C., Catalan, S., Cardoso, C., Clarke, J. R. A., Folkes, S., Gálvez-Ortiz, M. C., Homeier, D., Jenkins, J. S., Jones, H. R. A., & Zhang, Z. H. 2012, MNRAS, 422, 1922 [ADS]

Pinfield, D. J., Burningham, B., Tamura, M., Leggett, S. K., Lodieu, N., Lucas, P. W., Mortlock, D. J., Warren, S. J., Homeier, D., Ishii, M., Deacon, N. R., McMahon, R. G., Hewett, P. C., Osori, M. R. Z., Martin, E. L., Jones, H. R. A., Venemans, B. P., Day-Jones, A. C., Dobbie, P. D., Folkes, S. L., Dye, S., Allard, F., Baraffe, I., Barrado Y Navascués, D., Casewell, S. L., Chiu, K., Chabrier, G., Clarke, F., Hodgkin, S. T., Magazzù, A., McCaughrean, M. J., Nakajima, T., Pavlenko, Y., & Tinney, C. G. 2008, MNRAS, 390, 304 [ADS]

Pinfield, D. J., Dobbie, P. D., Jameson, R. F., Steele, I. A., Jones, H. R. A., & Katsiyannis, A. C. 2003, MNRAS, 342, 1241 [ADS]

Pinfield, D. J., Jones, H. R. A., Lucas, P. W., Kendall, T. R., Folkes, S. L., Day-Jones, A. C., Chappelle, R. J., & Steele, I. A. 2006, MNRAS, 368, 1281 [ADS]

Quanz, S. P., Goldman, B., Henning, T., Brandner, W., Burrows, A., & Hofstetter, L. W. 2010, ApJ, 708, 770 [ADS]

Queloz, D., Mayor, M., Weber, L., Blécha, A., Burnet, M., Confino, B., Naef, D., Pepe, F., Santos, N., & Udry, S. 2000, A&A, 354, 99 [ADS]

Rappaport, S. & Joss, P. C. 1984, ApJ, 283, 232 [ADS]

Rebolo, R., Martin, E. L., Basri, G., Marcy, G. W., & Zapatero-Osorio, M. R. 1996, ApJ, 469, L53 [ADS]

Rebolo, R., Zapatero Osorio, M. R., & Martín, E. L. 1995, Nature, 377, 129 [ADS]

Reid, I. N., Burgasser, A. J., Cruz, K. L., Kirkpatrick, J. D., & Gizis, J. E. 2001a, AJ, 121, 1710 [ADS]

Reid, I. N., Cruz, K. L., Burgasser, A. J., & Liu, M. C. 2008a, AJ, 135, 580 [ADS]

Reid, I. N., Cruz, K. L., Kirkpatrick, J. D., Allen, P. R., Mungall, F., Liebert, J., Lowrance, P., & Sweet, A. 2008b, AJ, 136, 1290 [ADS]

Reid, I. N. & Gizis, J. E. 1997, AJ, 113, 2246 [ADS]

Reid, I. N., Gizis, J. E., & Hawley, S. L. 2002a, AJ, 124, 2721 [ADS]

Reid, I. N., Gizis, J. E., Kirkpatrick, J. D., & Koerner, D. W. 2001b, AJ, 121, 489 [ADS]

Reid, I. N., Kirkpatrick, J. D., Liebert, J., Burrows, A., Gizis, J. E., Burgasser, A., Dahn, C. C., Monet, D., Cutri, R., Beichman, C. A., & Skrutskie, M. 1999, ApJ, 521, 613

Reid, I. N., Kirkpatrick, J. D., Liebert, J., Gizis, J. E., Dahn, C. C., & Monet, D. G. 2002b, AJ, 124, 519 [ADS]

Reid, N. 1992, MNRAS, 257, 257 [ADS]

Reipurth, B. & Clarke, C. 2001, AJ, 122, 432 [ADS]

Reylé, C., Delorme, P., Willott, C. J., Albert, L., Delfosse, X., Forveille, T., Artigau, E., Malo, L., Hill, G. J., & Doyon, R. 2010, A&A, 522, A112 [ADS]

Rocha-Pinto, H. J., Scalo, J., Maciel, W. J., & Flynn, C. 2000a, ApJ, 531, L115 [ADS]

—. 2000b, A&A, 358, 869 [ADS]

Rodríguez, L. F., Loinard, L., D'Alessio, P., Wilner, D. J., & Ho, P. T. P. 2005, ApJ, 621, L133 [ADS]

Roellig, T. L., Van Cleve, J. E., Sloan, G. C., Wilson, J. C., Saumon, D., Leggett, S. K., Marley, M. S., Cushing, M. C., Kirkpatrick, J. D., Mainzer, A. K., & Houck, J. R. 2004, ApJS, 154, 418 [ADS]

Rojas-Ayala, B., Covey, K. R., Muirhead, P. S., & Lloyd, J. P. 2010, ApJ, 720, L113 [ADS]

Sahlmann, J., Ségransan, D., Queloz, D., Udry, S., Santos, N. C., Marmier, M., Mayor, M., Naef, D., Pepe, F., & Zucker, S. 2011, A&A, 525, A95 [ADS]

Salpeter, E. E. 1955, ApJ, 121, 161 [ADS]

Saumon, D., Chabrier, G., & van Horn, H. M. 1995, ApJS, 99, 713 [ADS]

Saumon, D. & Marley, M. S. 2008, ApJ, 689, 1327 [ADS]

Saumon, D., Marley, M. S., Abel, M., Frommhold, L., & Freedman, R. S. 2012, ApJ, 750, 74 [ADS]

Schlegel, D. J., Finkbeiner, D. P., & Davis, M. 1998, ApJ, 500, 525 [ADS]

Schmidt, S. J., West, A. A., Burgasser, A. J., Bochanski, J. J., & Hawley, S. L. 2010a, AJ, 139, 1045 [ADS]

Schmidt, S. J., West, A. A., Hawley, S. L., & Pineda, J. S. 2010b, AJ, 139, 1808 [ADS]

Scholz, R.-D. 2010, A&A, 510, L8 [ADS]

Scholz, R.-D., McCaughrean, M. J., Lodieu, N., & Kuhlbrodt, B. 2003, A&A, 398, L29 [ADS]

Scholz, R.-D., McCaughrean, M. J., Zinnecker, H., & Lodieu, N. 2005, A&A, 430, L49 [ADS]

Scholz, R.-D. & Meusinger, H. 2002, MNRAS, 336, L49 [ADS]

Seager, S., Whitney, B. A., & Sasselov, D. D. 2000, ApJ, 540, 504 [ADS]

Seifahrt, A., Mugrauer, M., Wiese, M., Neuhäuser, R., & Guenther, E. W. 2005, Astronomische Nachrichten, 326, 974 [ADS]

Seifried, D., Banerjee, R., Pudritz, R. E., & Klessen, R. S. 2013, MNRAS, 432, 3320 [ADS]

Skemer, A. J., Close, L. M., Szűcs, L., Apai, D., Pascucci, I., & Biller, B. A. 2011, ApJ, 732, 107 [ADS]

Skrutskie, M. F., Cutri, R. M., Stiening, R., Weinberg, M. D., Schneider, S., Carpenter, J. M., Beichman, C., Capps, R., Chester, T., Elias, J., Huchra, J., Liebert, J., Lonsdale, C., Monet, D. G., Price, S., Seitzer, P., Jarrett, T., Kirkpatrick, J. D., Gizis, J. E., Howard, E., Evans, T., Fowler, J., Fullmer, L., Hurt, R., Light, R., Kopan, E. L., Marsh, K. A., McCallon, H. L., Tam, R., Van Dyk, S., & Wheelock, S. 2006, AJ, 131, 1163 [ADS]

Smart, R. L., Lattanzi, M. G., Bucciarelli, B., Massone, G., Casalegno, R., Chiumiento, G., Drimmel, R., Lanteri, L., Marocco, F., & Spagna, A. 2003, A&A, 404, 317 [ADS]

Smart, R. L., Lattanzi, M. G., Jahreiß, H., Bucciarelli, B., & Massone, G. 2007, A&A, 464, 787 [ADS]

Smart, R. L., Tinney, C. G., Bucciarelli, B., Marocco, F., Abbas, U., Andrei, A., Bernardi, G., Burningham, B., Cardoso, C., Costa, E., Crosta, M. T., Daprá, M., Day-Jones, A., Goldman, B., Jones, H. R. A., Lattanzi, M. G., Leggett, S. K., Lucas, P., Mendez, R., Penna, J. L., Pinfield, D., Smith, L., Sozzetti, A., & Vecchiato, A. 2013, MNRAS, 433, 2054 [ADS]

Stamatellos, D. 2013, in European Physical Journal Web of Conferences, Vol. 47, European Physical Journal Web of Conferences, 8001 [ADS]

Stamatellos, D. & Whitworth, A. P. 2009, MNRAS, 400, 1563 [ADS]

Stassun, K. G., Mathieu, R. D., & Valenti, J. A. 2006, Nature, 440, 311 [ADS]

Stauffer, J. R., Hamilton, D., & Probst, R. G. 1994, AJ, 108, 155 [ADS]

Stephens, D. C. 2003, in IAU Symposium, Vol. 211, Brown Dwarfs, 355 [ADS]

Stephens, D. C. & Leggett, S. K. 2004, PASP, 116, 9 [ADS]

Stephens, D. C., Leggett, S. K., Cushing, M. C., Marley, M. S., Saumon, D., Geballe, T. R., Golimowski, D. A., Fan, X., & Noll, K. S. 2009, ApJ, 702, 154 [ADS]

Sterzik, M. F. & Durisen, R. H. 2003, A&A, 400, 1031 [ADS]

Stone, R. C. 2002, PASP, 114, 1070 [ADS]

Straka, W. C. 1971, ApJ, 165, 109 [ADS]

Sudarsky, D., Burrows, A., & Pinto, P. 2000, ApJ, 538, 885 [ADS]

Sumi, T., Kamiya, K., Bennett, D. P., Bond, I. A., Abe, F., Botzler, C. S., Fukui, A., Furusawa, K., Hearnshaw, J. B., Itow, Y., Kilmartin, P. M., Korpela, A., Lin, W., Ling, C. H., Masuda, K., Matsubara, Y., Miyake, N., Motomura, M., Muraki, Y., Nagaya, M., Nakamura, S., Ohnishi, K., Okumura, T., Perrott, Y. C., Rattenbury, N., Saito, T., Sako, T., Sullivan, D. J., Sweatman, W. L., Tristram, P. J., Udalski, A., Szymański, M. K., Kubiak, M., Pietrzyński, G., Poleski, R., Soszyński, I., Wyrzykowski, Ł., Ulaczyk, K., & Microlensing Observations in Astrophysics (MOA) Collaboration. 2011, Nature, 473, 349 [ADS]

Teixeira, R., Ducourant, C., Chauvin, G., Krone-Martins, A., Song, I., & Zuckerman, B. 2008, A&A, 489, 825 [ADS]

Testi, L., D'Antona, F., Ghinassi, F., Licandro, J., Magazzù, A., Maiolino, R., Mannucci, F., Marconi, A., Nagar, N., Natta, A., & Oliva, E. 2001, ApJ, 552, L147 [ADS]

Tinney, C. G., Burgasser, A. J., & Kirkpatrick, J. D. 2003, AJ, 126, 975 [ADS]

Tokunaga, A. T. & Kobayashi, N. 1999, AJ, 117, 1010 [ADS]

Torres, G. 1999, PASP, 111, 169 [ADS]

Tsuji, T. 2000, in Very Low-Mass Stars and Brown Dwarfs, 156 [ADS]

Tsuji, T. 2002, ApJ, 575, 264 [ADS]

—. 2005, ApJ, 621, 1033 [ADS]

Tsuji, T. & Nakajima, T. 2003, ApJ, 585, L151 [ADS]

Tsuji, T., Nakajima, T., & Yanagisawa, K. 2004, ApJ, 607, 511 [ADS]

van Dokkum, P. G. & Conroy, C. 2010, Nature, 468, 940 [ADS]

Vernet, J., Dekker, H., D'Odorico, S., Kaper, L., Kjaergaard, P., Hammer, F., Randich, S., Zerbi, F., Groot, P. J., Hjorth, J., Guinouard, I., Navarro, R., Adolfse, T., Albers, P. W., Amans, J.-P., Andersen, J. J., Andersen, M. I., Binetruy, P., Bristow, P., Castillo, R., Chemla, F., Christensen, L., Conconi, P., Conzelmann, R., Dam, J., de Caprio, V., de Ugarte Postigo, A., Delabre, B., di Marcantonio, P., Downing, M., Elswijk, E., Finger, G., Fischer, G., Flores, H., François, P., Goldoni, P., Guglielmi, L., Haigron, R., Hanenburg, H., Hendriks, I., Horrobin, M., Horville, D., Jessen, N. C., Kerber, F., Kern, L., Kiekebusch, M., Kleszcz, P., Klougart, J., Kragt, J.,

Larsen, H. H., Lizon, J.-L., Lucuix, C., Mainieri, V., Manuputy, R., Martayan, C., Mason, E., Mazzoleni, R., Michaelsen, N., Modigliani, A., Moehler, S., Møller, P., Norup Sørensen, A., Nørregaard, P., Péroux, C., Patat, F., Pena, E., Pragt, J., Reinero, C., Rigal, F., Riva, M., Roelfsema, R., Royer, F., Sacco, G., Santin, P., Schoenmaker, T., Spano, P., Sweers, E., Ter Horst, R., Tintori, M., Tromp, N., van Dael, P., van der Vliet, H., Venema, L., Vidali, M., Vinther, J., Vola, P., Winters, R., Wistisen, D., Wulterkens, G., & Zacchei, A. 2011, A&A, 536, A105 [ADS]

Vrba, F. J., Henden, A. A., Luginbuhl, C. B., Guetter, H. H., Munn, J. A., Canzian, B., Burgasser, A. J., Kirkpatrick, J. D., Fan, X., Geballe, T. R., Golimowski, D. A., Knapp, G. R., Leggett, S. K., Schneider, D. P., & Brinkmann, J. 2004, AJ, 127, 2948 [ADS]

Whitworth, A. P. & Stamatellos, D. 2006, A&A, 458, 817 [ADS]

Whitworth, A. P. & Zinnecker, H. 2004, A&A, 427, 299 [ADS]

Wright, E. L., Eisenhardt, P. R. M., Mainzer, A. K., Ressler, M. E., Cutri, R. M., Jarrett, T., Kirkpatrick, J. D., Padgett, D., McMillan, R. S., Skrutskie, M., Stanford, S. A., Cohen, M., Walker, R. G., Mather, J. C., Leisawitz, D., Gautier, III, T. N., McLean, I., Benford, D., Lonsdale, C. J., Blain, A., Mendez, B., Irace, W. R., Duval, V., Liu, F., Royer, D., Heinrichsen, I., Howard, J., Shannon, M., Kendall, M., Walsh, A. L., Larsen, M., Cardon, J. G., Schick, S., Schwalm, M., Abid, M., Fabinsky, B., Naes, L., & Tsai, C.-W. 2010, AJ, 140, 1868 [ADS]

York, D. G., Adelman, J., Anderson, Jr., J. E., Anderson, S. F., Annis, J., Bahcall, N. A., Bakken, J. A., Barkhouser, R., Bastian, S., Berman, E., Boroski, W. N., Bracker, S., Briegel, C., Briggs, J. W., Brinkmann, J., Brunner, R., Burles, S., Carey, L., Carr, M. A., Castander, F. J., Chen, B., Colestock, P. L., Connolly, A. J., Crocker, J. H., Csabai, I., Czarapata, P. C., Davis, J. E., Doi, M., Dombeck, T., Eisenstein, D., Ellman, N., Elms, B. R., Evans, M. L., Fan, X., Federwitz, G. R., Fiscelli, L., Friedman, S., Frieman, J. A., Fukugita, M., Gillespie, B., Gunn, J. E., Gurbani, V. K., de Haas, E., Haldeman, M., Harris, F. H., Hayes, J., Heckman, T. M., Hennessy, G. S., Hindsley, R. B., Holm, S., Holmgren, D. J., Huang, C.-h., Hull, C., Husby, D., Ichikawa, S.-I., Ichikawa, T., Ivezić, Ž., Kent, S., Kim, R. S. J., Kinney, E., Klaene, M., Kleinman, A. N., Kleinman, S., Knapp, G. R., Korienek, J., Kron, R. G., Kunszt, P. Z., Lamb, D. Q., Lee, B., Leger, R. F., Limmongkol, S., Lindenmeyer, C., Long, D. C., Loomis, C., Loveday, J., Lucinio, R., Lupton, R. H., MacKinnon, B., Mannery, E. J., Mantsch, P. M., Margon, B., McGehee, P., McKay, T. A., Meiksin, A., Merelli, A., Monet, D. G., Munn, J. A., Narayanan, V. K., Nash, T., Neilsen, E., Neswold, R., Newberg, H. J., Nichol, R. C., Nicinski, T., Nonino, M., Okada, N., Okamura, S., Ostriker, J. P., Owen, R., Pauls, A. G., Peoples, J., Peterson, R. L., Petravick, D., Pier, J. R., Pope, A., Pordes, R., Prosapio, A., Rechenmacher, R., Quinn, T. R., Richards, G. T., Richmond, M. W., Rivetta, C. H., Rockosi, C. M., Ruthmansdorfer, K., Sandford, D., Schlegel, D. J., Schneider, D. P., Sekiguchi, M., Sergey, G., Shimasaku, K., Siegmund, W. A., Smee, S., Smith, J. A., Snedden, S., Stone, R., Stoughton, C., Strauss, M. A., Stubbs, C., SubbaRao, M., Szalay, A. S., Szapudi, I., Szokoly, G. P., Thakar, A. R., Tremonti, C., Tucker, D. L., Uomoto, A., Vanden Berk, D., Vogeley, M. S., Waddell, P., Wang, S.-i., Watanabe, M., Weinberg, D. H., Yanny, B., & Yasuda, N. 2000, AJ, 120, 1579 [ADS]

Zapolsky, H. S. & Salpeter, E. E. 1969, ApJ, 158, 809 [ADS]

Zhang, Z. H., Pinfield, D. J., Burningham, B., Jones, H. R. A., Day-Jones, A. C., Marocco, F., Gomes, J., & Galvez-Ortiz, M. C. 2013a, in European Physical Journal Web of Conferences, Vol. 47, European Physical Journal Web of Conferences, 6007 [ADS]

Zhang, Z. H., Pinfield, D. J., Burningham, B., Jones, H. R. A., Gálvez-Ortiz, M. C., Catalán, S., Smart, R. L., Lépine, S., Clarke, J. R. A., Pavlenko, Y. V., Murray, D. N., Kuznetsov, M. K., Day-Jones, A. C., Gomes, J., Marocco, F., & Sipőcz, B. 2013b, MNRAS, 434, 1005 [ADS]

Zhang, Z. H., Pinfield, D. J., Day-Jones, A. C., Burningham, B., Jones, H. R. A., Yu, S., Jenkins, J. S., Han, Z., Gálvez-Ortiz, M. C., Gallardo, J., García-Pérez, A. E., Weights, D., Tinney, C. G., & Pokorny, R. S. 2010, MNRAS, 404, 1817 [ADS]